



**Superconducting proximity effect
in ferromagnetic and diamagnetic
nanowire-structures**

DISSERTATION

zur Erlangung des Doktorgrades
der Naturwissenschaften

vorgelegt beim Fachbereich Physik
der Johann Wolfgang Goethe Universität
in Frankfurt am Main

von

Maksym Kompaniets
aus Mariupol, Ukraine

Frankfurt am Main (2015)

(D 30)

vom Fachbereich Physik der
Johann Wolfgang Goethe-Universität als Dissertation angenommen.

Dekan: Prof. Dr. Rene Reifarth

Gutachter: Prof. Dr. Michael Huth

Gutachter: Prof. Dr. Wolfgang Ensinger

Datum der Disputation:

Zusammenfassung

Der elektrische Widerstand ist eine Hauptquelle für die Wärmeerzeugung und die Ladedauer in integrierten Schaltungen. Die Verringerung des elektrischen Widerstands ist daher von großer Bedeutung für energieeffiziente und schnelle Rechneranwendungen. Die Entwicklung von hochauflösenden Nanofabrikationstechniken, wie Elektronenstrahlolithographie und maskenloser Strukturierung durch fokussierte Teilchenstrahlen, ermöglichten eine rasche Miniaturisierung von integrierten Schaltungen, wodurch auch die Verwendung von Nanodrähten in elektronischen Geräten, insbesondere supraleitenden, stark vorangeschritten ist [1, 2]. Zu beispielhaften Phänomenen, die man in supraleitenden Nanodrähten beobachten kann, gehören die thermisch aktivierten [3, 4] und Quantenphasenschlüpfe [3, 5], der Minigap Zustand [6] und der Proximity-Effekt [7, 8]. Der letztgenannte Effekt steht im Fokus der vorliegenden Arbeit.

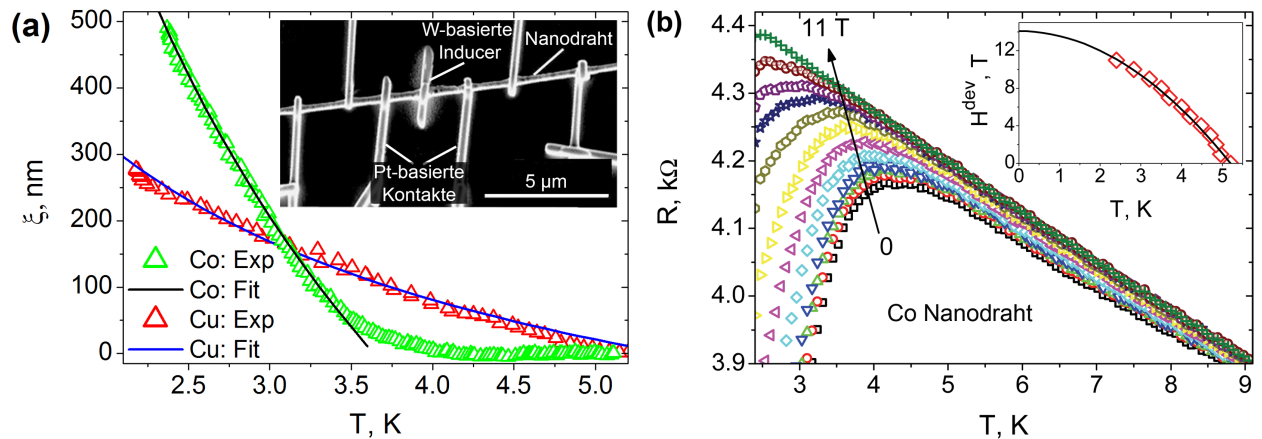
Obwohl der Proximity-Effekt in jedem Schaltungselement auftritt, welches in Kontakt mit einem supraleitenden (S) Bereich steht, hängt die Ausdehnung des Proximity-Effekts vom Material des nicht-supraleitenden Bereichs ab. Zum Beispiel, bei einem Supraleiter – normal Metall (S/N) Interface dringen die Cooper-Paare in N ein und führen dort zu supraleitendem Verhalten auf einer Länge ξ_N von $\simeq 1 \mu\text{m}$ [7, 9]. Eine andere Situation tritt ein, wenn N durch einen Ferromagneten (F) ersetzt wird [7]. Bei einem Großteil der Supraleiter ist die Wellenfunktion der Cooper-Paare ein Singulett, weil sie von zwei Elektronen mit entgegengesetzten Spins gebildet wird. Das Austauschfeld h_{ex} von F führt jedoch zu einer Ausrichtung der beiden Spins in die gleiche Richtung. Dies führt zu einem stark paarbrechenden Effekt und bewirkt einen raschen, exponentiell schwingungsgedämpften Zerfall des supraleitenden Ordnungsparameters in F über eine Distanz ξ_F . Dieser Effekt ist kurzreichweitig mit einer Spin-Singulett Zerfalldistanz von $\xi_F \simeq 1 \text{ nm}$, wie experimentell gezeigt wurde [10, 11]. In bestimmten Fällen wird jedoch die Supraleitung nicht durch den Ferromagnetismus unterdrückt, da die Anwesenheit von F ebenfalls zu Spin-Triplet Supraleitung führen kann. Im Spin-Triplet Zustand wird ein Cooper-Paar von zwei Elektronen mit parallelen Spins gebildet, wodurch es unempfindlich hinsichtlich des Austauschfeldes wird. Somit kann die Supraleitung in F auch auf Distanzen bestehen bleiben, die vergleichbar mit ξ_N sind. Wie theoretisch von Bergeret [12] gezeigt wurde, ist eine lokale Inhomogenität der Magnetisierung in der Nähe der S/F Grenzschicht für die Spin-Triplet Paarung in S/F Strukturen erforderlich. Die Inhomogenitäten des Austauschfeldes können entweder intrinsisch zu F (Domäne) sein und sind somit durch ein externes magnetisches Feld modifizierbar, oder auch durch Materialinhomogenitäten hervorgerufen werden. Diese Materialinhomogenitäten

können z.B. durch experimentelle Manipulation eingebaut werden, was durch ein Kontaktierungsverfahren erreicht werden kann [13–15].

Die aktuelle Suche nach dem experimentellen Nachweis des langreichweitigen Spin-Triplet Proximity-Effekts wird von der Möglichkeit getrieben den Null-Widerstand Suprastrom von S mit der Spinausrichtung von F zu kombinieren, was von hoher Relevanz für Entwicklungen in der spinabhängigen Elektronik ist [16, 17]. Obwohl der langreichweitige Spin-Triplet Proximity-Effekt bereits in (Multi-) Sandwich Heterostrukturen von Dünnschichten [18–20], keilförmigen Schichten [21], Josephson-Kontakten [22, 23] und komplexeren Geometrien [24–28] beobachtet wurde, ist die Arbeit von Wang [14] die einzige Veröffentlichung über den Nachweis eines langreichweitigen Spin-Triplet Proximity-Effekts in ferromagnetischen Nanodrähten. In dieser Arbeit wurden einkristalline Co-Nanodrähte verwendet und es konnte gezeigt werden, dass ein Nanodraht mit 40 nm Durchmesser einen verschwindenden Widerstand auf einer Länge von 600 nm erreicht.

Im Rahmen dieser Arbeit wird eine experimentelle Untersuchung der Proximity-Effekt induzierten Supraleitung in einkristallinen Cu und polykristallinen Co Nanodrähten und einer nanogranularen Co Nanodrahtstruktur in Kontakt mit einer supraleitenden Elektrode (“Inducer”), realisiert durch einen konventionellen W-basierten Singulett Supraleiter, vorgestellt. Die kristallinen Nanodrähte wurden durch elektrochemische Abscheidung in mittels Schwerionen geätzten Polycarbonat Templaten gewachsen. Die nanogranulare Co Struktur wurde durch fokussierte Elektronenstrahl induzierte Abscheidung (Focused Electron Beam Induced Deposition - FEBID) hergestellt, während der amorphe W-basierte “Inducer” durch fokussierte Ionenstrahl induzierte Abscheidung (Focused Ion Beam Induced Deposition - FIBID) hergestellt wurde. Für die elektrischen Widerstandsmessungen wurden Pt-basierte Spannungskontakte durch FIBID in unterschiedlichen Entfernungen über die innere “Inducer” Elektrode deponiert, was es ermöglicht den Proximity-Effekt über eine Länge von 2-12 μm zu untersuchen. Bis zu 30% Widerstandsabfälle in Bezug auf den Normalzustandswert wurden für die kristalline Cu und Co Nanodrähte beobachtet, wenn die Temperatur unterhalb des T_c der “Inducer” Elektrode (5.2 K) abgesenkt wurde. Im Gegensatz dazu wurde für die nanogranulare Co Nanodrahtstruktur ein um eine Größenordnung kleinerer relativer Widerstandsabfall im Vergleich zum Normalzustandswert festgestellt. Die Analyse der Widerstandsdaten zeigt, dass die supraleitende Proximity-Länge in kristallinem Cu und Co etwa 1 μm bei 2.4 K beträgt, was eine langreichweitige proximity-induzierte Spin-Triplet Supraleitung im Co Nanodraht bestätigt. Interessanterweise ist die Proximity-Länge größer als die durchschnittliche Korngröße des polykristallinen Co Nanodrahts. Diese Ergebnisse zeigen, dass der langreichweitige Triplet-Zustand ein robustes Merkmal dieser ferromagnetischen Nanodrähte zu sein

scheint, was großes Potential für Anwendungen liefert. Des Weiteren ist der langreichweitige Proximity-Effekt unempfindlich gegen magnetische Felder bis zu 11 T, was ein Anzeichen von Spin-Triplet Paarung sein kann. Die experimentellen Ergebnisse deuten darauf hin, dass die starke magnetische Inhomogenität des Systems sowohl durch das Vorhandensein der anti-ferromagnetischen Co_3O_4 Phase als auch durch die Manipulation durch FEBID hervorgerufen wird. Im Gegensatz dazu wird im nanogranularen Co Nanodraht die proximity-induzierte Supraleitung durch die dominierende Cooper-Paar Streuung stark unterdrückt, welche aus der intrinsischen Mikrostruktur des FEBID Deponats resultiert.



(a) Temperaturabhängigkeit der Supraleitende Proximity-Länge in kristallinen Cu und Co Nanodrähte. (b) Stabilität der Proximity-Induzierte Supraleitung im Co-Nanodraht gegen magnetische Felder bis zu 11 T.

Des Weiteren wird im Rahmen dieser Arbeit gezeigt, dass die Einflüsse der intrinsischen Mikrostruktur als auch die durch FEBID geschädigten Bereiche entscheidend für die supraleitenden Eigenschaften der Nanodrähte sind. Die verschiedenen mikrostrukturellen Eigenschaften der Proben erlaubten es qualitativ verschiedene Fälle von proximity-induzierter Supraleitung in Koexistenz mit anderen Effekten zu untersuchen. Insbesondere war es möglich einen großen Widerstandsbeitrag der Ionenstrahl beschädigten Bereiche im Fall von hochwertigen Cu Nanodrähten, ein lokalisierungsartigen Tieftemperatur Transport in polykristallinem Co Nanodraht aufgrund eines großen spezifischen Widerstands der Korngrenzen und einen starken paarbrechenden Effekt aufgrund der symmetrieverändernden Streuung der Wellenfunktion in der nanogranularen Co Struktur zu identifizieren und zu quantifizieren. Ein weiterer interessanter Effekt ist eine beobachtete Widerstandsanomalie in einem Cu Nanodraht, in der Nähe der Übergangstemperatur der supraleitenden “Inducer” Elektrode.

Darüberhinaus werden erste Ergebnisse eines neuen experimentellen Ansatzes basierend auf der Verwendung eines bleihaltigen FEBID Supraleiters zur Untersuchung des klas-

sischen (Spin-Singulett) supraleitenden Proximity-Effekts durch elektrische Widerstandsmessungen in dieser Arbeit vorgestellt. Die Verwendung von FEBID anstelle von FIBID ist von Vorteil, da Ätzprozesse verursacht durch auf den Nanodraht auftreffende Ionen vermieden werden. Dadurch kann der Einfluss der Herstellung der Inducer Elektrode auf die elektrischen Eigenschaften des Nanodrahts reduziert werden. Ein mittels supraleitenden Pb-FEBID Inducer-Elektroden kontaktierter kristalliner Au Nanodraht erreicht bei tiefen Temperaturen Null-Widerstand über einer Distanz von bis zu $1\ \mu\text{m}$, was darauf hindeutet, dass die räumliche Ausdehnung der Proximity-Effekt induzierten Supraleitung in diesem Au Nanodraht mindestens $500\ \text{nm}$ beträgt. Dieses Ergebnis verdeutlicht das Potential der Pb-basierten FEBID Supraleiter für zukünftige Anwendungen. Bei der Verwendung des Pb-basierten FEBID Supraleiters als Inducer Elektrode und Au Nanodraht als nicht supraleitendes Objekt müssen darüber hinaus Interdiffusionseffekte zwischen Au und Pb berücksichtigt werden, die zur Bildung einer intermetallischen AuPb Verbindung mit anderen strukturellen und elektrischen Eigenschaften führen können.

Bei der Betrachtung der langreichweitigen proximity-induzierten Supraleitung muss betont werden, dass die Singulett-zu-Triplet Umwandlung im ferromagnetischen Co Nanodraht spontan und zufällig auftrat, was die Reproduzierbarkeit stark einschränkt. Das zweite Ziel dieser Arbeit war deshalb die Entwicklung von nanodrahtförmigen Strukturen mit kontrollierbaren magneto-Transport Eigenschaften, die es ermöglichen den langreichweitigen Spin-Triplet Suprastrom im Ferromagneten zu manipulieren. Dies erfolgt größtenteils mittels Schichtheterostrukturen in vertikaler Richtung. Ein komplementärer Ansatz der eine kontrollierte Einstellung der magnetischen Eigenschaften von Co/Pt Heterostrukturen auf der Mesoskala in lateraler Richtung erlaubt, wird ebenfalls in dieser Arbeit vorgestellt. Mithilfe einer in-situ Nachbearbeitung der mittels FEBID hergestellten Pt- und Co-basierten Nanostreifen war es möglich lokal das Koerzitivfeld und die Remanenz einzustellen. Während einzelne Co-FEBID Nanostreifen keine Hysterese zeigen, wurde ein hartmagnetisches Verhalten bei nachbearbeiteten Co/Pt Nanostreifen mit Koerzitivfeldern bis zu $850\ \text{Oe}$ gefunden. Der beobachtete Effekt wurde auf die lokal kontrollierte Bildung der CoPt $L1_0$ Phase, welche durch Transmissionselektronenmikroskopie nachgewiesen wurde, zurückgeführt.

In dieser Arbeit wurde der supraleitende Proximity-Effekt mittels elektrischen Widerstandsmessungen in verschiedenen diamagnetischen und ferromagnetischen Nanodrähten untersucht. Die verschiedenen mikrostrukturellen Eigenschaften der Nanodrähte erlaubten qualitativ verschiedene Fälle der proximity-induzierten Supraleitung in Koexistenz mit anderen Effekten zu analysieren. Das wichtigste Ergebnis ist der experimentelle Nachweis des langreichweitigen Spin-Triplet Proximity-Effekts in ferromagnetischen polykristallinen

Nanodrähten. Basierend auf den bisher durchgeführten Experimenten kann in Zukunft der konventionelle Pb-basierte FEBID Singulett Supraleiter als “Inducer” in Kontakt mit Co und Co/Pt segmentierten Nanodrähten mit kontrollierbaren magneto-transport Eigenschaften zur Erzeugung und Manipulation der langreichweitigen Spin-Triplet Supraströme angewendet werden.

Contents

1	Introduction	21
2	Theoretical background	27
2.1	Normal conductivity	27
2.1.1	Hall effect (HE). Anisotropic magneto-resistance (AMR)	27
2.1.2	Bloch–Grüneisen formula. Matthiessen’s rule	33
2.2	Superconducting proximity effect	35
2.2.1	Basics of superconductivity. Singlet versus triplet state	35
2.2.2	Proximity effect at the superconductor/normal metal (S/N) interface	38
2.2.3	Proximity effect at the superconductor/ferromagnet (S/F) interface .	41
2.2.4	Proximity effect at the superconductor/ferromagnet (S/F) interface – nonuniform magnetization	46
2.2.5	Andreev reflection as the microscopic mechanism of the superconduct- ing proximity effect	52
3	Methods and techniques	55
3.1	Fabrication of samples and auxiliary electrodes	55
3.1.1	Electrochemical deposition (ECD) of crystalline Cu and Co nanowires	55
3.1.2	Pre-forming of contact pads and nanowires by lithography in conjunc- tion with lift-off	63
3.1.3	DC magnetron sputtering of Cr/Au contacts and Au nanowires . . .	68
3.1.4	Focused electron/ion beam-induced processing (FEBIP/FIBIP) . . .	71
3.2	Compositional, microstructural, and morphological characterization	77
3.2.1	Energy-dispersive X-ray (EDX) spectroscopy	77
3.2.2	X-ray diffraction (XRD) analysis	80
3.2.3	Scanning electron microscopy/focused ion beam (SEM/FIB)	82
3.2.4	Scanning transmission electron microscopy (STEM)	86
3.2.5	Atomic force microscopy (AFM)	87

3.3	Electrical transport and magneto-transport measurements	88
3.3.1	DC electrical transport measurements	89
3.3.2	AC electrical magneto-transport measurements	93
4	Proximity effect in single-crystal Cu nanowires	97
4.1	Transport properties of Cu nanowires	97
4.2	Resistance peak anomaly	101
4.3	Arrhenius analysis of resistance drops	102
4.4	Resistance contribution of ion-beam-damaged areas	103
4.5	Quantification of proximity length in Cu nanowire	105
4.6	Rigidity of the proximity effect in Cu nanowire against magnetic fields	108
5	Proximity effect in polycrystalline and nanogranular Co nanowires	111
5.1	Transport properties of Co nanowire and Co-FEBID structure	111
5.2	Rigidity of the proximity effect in Co nanowire against magnetic fields	114
5.3	Origins of magnetic inhomogeneities in Co nanowire	116
5.4	Quantification of proximity length for Co nanowire and Co-FEBID	117
5.5	Different conductivity regimes in Co nanowire	119
5.6	Spin-dependent scattering at grain boundaries	120
6	Tunable magnetism by post-processing of Co/Pt-FEBID structures	123
6.1	Preparation and post-processing of Co/Pt-FEBID structures	123
6.2	Characterization of Co/Pt-FEBID structures	126
6.2.1	Material composition analysis	126
6.2.2	Microstructural characterization	126
6.3	Electrical transport properties of Co/Pt-FEBID structures	130
6.4	Magnetic properties of CoPt-FEBID samples	131
6.4.1	Hall effect	131
6.4.2	Magnetoresistance	134
6.5	Laterally controlled magnetic structure for spin-triplet proximity-induced su- perconductivity	134
6.6	Post-growth purification of Co-FEBID and Pt-FEBID structures	136
6.6.1	Post-growth purification of Co-FEBID	137
6.6.2	Post-growth purification of Pt-FEBID	143

7	FEBID superconductor for proximity effect investigations in nanowires	149
7.1	Sample preparation	149
7.2	Transport measurements	152
7.2.1	Magneto-transport properties of Pb-FEBID nanowire	152
7.2.2	Proximity effect-induced superconductivity in the Au-NW	154
7.3	Room temperature alloying at the Au/Pb interface	158
8	Conclusions	161
	Appendices	165
A	Determination of crystallite sizes in Co_3O_4	165
B	Quantification of the resistance contribution of ion-damaged areas	165
C	CoPt binary alloy phase diagram, crystal structure and magnetic properties .	167
	Bibliography	168
	List of publications	191
	Curriculum vitae	193

List of Figures

2.1	(a) Typical geometry of Hall effect measurements. (b) Dependence of the Hall resistivity ρ_{Hall} on the applied external magnetic field H	28
2.2	(a) Typical geometry of anisotropic magnetoresistance (AMR) measurements. (b) Dependence of the anisotropic magnetoresistance relative change on the direction of magnetization M	31
2.3	Singlet and triplet states that can be occupied by a Cooper pair	37
2.4	Schematic representation of the superconducting order-parameter behavior at the S/N interface	38
2.5	Experimental evidence of the superconducting proximity effect of an S/N junction observed in Au and Zn and Sn nanowires	42
2.6	Schematic representation of the superconducting order parameter behavior at the S/F interface with uniform magnetization	42
2.8	Experimental evidence of oscillations of T_c as a function of F-layer thickness observed in S/F multilayers	45
2.9	Schematic representation of the superconducting-order parameter behavior near the S/F interface where the average interface magnetization is misaligned with the bulk magnetization of F	48
2.11	Experimental evidence of long-range superconducting proximity effect	51
2.12	Schematic representation of the Andreev reflection in the case of S/N and S/F interfaces	53
3.1	Irradiation and subsequent chemical etching process of polycarbonate membranes	58
3.2	Schematic representation of the etching process in a PC membrane	59
3.3	Schematic representation of the setup used for the electrochemical deposition of Cu and Co nanowires in ion-track etched polycarbonate templates	59
3.4	Typical $I(t)$ curve of four different nanowire deposition regimes in ion-track etched polycarbonate templates	60

3.5	Schematic representation of the electrochemical deposition of nanowires in ion-track etched polycarbonate templates	61
3.7	UV lithography in conjunction with lift-off	65
3.8	E-beam lithography in conjunction with lift-off	67
3.9	Principle of the DC magnetron sputtering process	69
3.10	Schematic representation of the FEBID process	72
3.11	FEBID/FIBID precursors used in this work	75
3.12	Principle of energy-dispersive X-ray spectroscopy (EDX)	78
3.13	Excitation and emission process in an atom	79
3.14	Penetration of electrons into Cu and Co nanowires, Pt-FIBID and W-FIBID electrodes, calculated by the simulation program Casino	79
3.15	Principle of the X-ray diffraction method	81
3.16	Bragg X-ray scans of Cu and Co nanowires embedded in a polymer template	83
3.17	Schematic representation of the main SEM components	84
3.18	Photograph of the FEI Nova NanoLab 600 SEM	86
3.19	Schematic representation of the components of an atomic force microscope	88
3.20	Photographs of a custom-built carrier chip and a temperature-controlled carrier chip and a carrier chip holder	89
3.21	Schematic representation of the four-terminal arrangement used for electrical resistance measurements of nanowires	90
3.22	Schematic representation of a typical ^4He cryostat internal design	92
3.23	Schematic representation of the setup used for magnetoresistance and Hall effect measurements	95
4.1	SEM images of Cu nanowires. The 4-probe and 8-probe geometries used for electrical resistance measurements on Cu nanowires	98
4.2	Cooling curve $R(T)$ and low-temperature resistance data for Cu-NW1	99
4.3	Cooling curve $R(T)$ and low-temperature resistance data for Cu-NW2	100
4.4	Arrhenius plots of the PE-induced resistance drops with the deduced activation energies U for the three sections of Cu nanowire	103
4.5	(a) Dependence of the Cu nanowire resistance on the measured section length L . Variation of the crossover temperature T^* versus L . (b) The nanowire resistance as a function of length without contributions of the defect-rich contact areas. The relative proximity-induced resistance drops ΔR versus the nanowire section length L	104

4.6	Sketch of the resistance model used for quantifying the changes in the nanowire resistivity due to the generation of defects during the FEBID processing . . .	105
4.7	Resistance model used for the quantification of the proximity length in the nanowires	107
4.8	Temperature dependence of the proximity lengths ξ for Cu nanowires	107
4.9	Temperature dependence of the resistance of the Cu nanowire for a set of applied magnetic fields from 0 to 10 T	109
4.10	Magnetoresistance of the Cu nanowire measured at different temperatures . .	110
5.1	SEM images of the fabricated Co and Co-FEBID nanowires, and corresponding 8-probe geometries used for electrical resistance measurements	112
5.2	Cooling curve $R(T)$ of the Co nanowire. Proximity effect induced resistance drops for the three sections of the Co nanowire	113
5.3	Cooling curve $R(T)$ for the L_1 section of the Co-FEBID structure. The low-temperature, relative resistance changes for the three sections of the Co-FEBID structure	114
5.4	Temperature dependence of the resistance of the L_1 (a) and L_2 (b) sections of the Co nanowire for a set of applied magnetic fields from 0 to 11 T	116
5.5	Temperature dependence of the proximity length for the Co nanowire.	118
5.6	Temperature dependence of the resistance of the L_1 , L_2 and L_3 sections of the Co nanowire for a set of different currents from 5 nA to 20 μ A. Current dependence of the resistance of the L_2 section of the Co nanowire at three different temperatures	120
5.7	Color diagram which represents switching between different conductivity regimes in the Co-NW	121
6.1	Preparation and post-processing of the Co/Pt heterostructure	124
6.2	SEM images of the Co/Pt heterostructure	124
6.3	Quantified material composition in the Co and the Co/Pt heterostructure . .	127
6.4	TEM micrograph of the Co/Pt heterostructure	128
6.5	Cross-sectional and lower layer in-plane EDX spectrograms for the Co/Pt heterostructure	128
6.6	Nano-diffractograms of the upper and lower layer of the Co/Pt heterostructure	129
6.7	Cooling $R(T)$ curves for the Co/Pt heterostructures	130
6.8	Hall voltage cycling at 10 K for the Co/Pt heterostructures	131

6.9	Correlation between the magnetization saturation field and the Co to Pt ratio for the Co/Pt heterostructures	133
6.10	Isothermal Hall voltage cycling for the Co/Pt heterostructure	133
6.11	Temperature dependences of the remanence magnetization M_r/M_s and the coercive field H_c for the Co/Pt heterostructure	134
6.12	Magnetoresistance cycling at 10 K for the Co/Pt heterostructures	135
6.13	Ferromagnetic multi-segmented nanowire structure for spin-triplet proximity-induced superconductivity investigations	136
6.14	Schematics of the preparation and purification of the Co-FEBID samples . .	137
6.15	Quantified material composition in the as-deposited and purified Co-FEBID samples	138
6.16	Cross-sectional TEM micrographs of the as-deposited and purified Co-FEBID samples and the corresponding EELS–STEM spectrograms	139
6.17	Cooling curves for the as-deposited and purified Co-FEBID samples	140
6.19	EDX spectra of the as-grown and as-purified Pt-FEBID samples	145
6.20	Schematic representation of the catalytic purification process of the Pt-FEBID samples	146
7.1	Sample layout for the Pb-FEBID superconductor and Au nanowire used for the study of the “classical” proximity effect-induced superconductivity	151
7.2	Quantified material composition in Au nanowire and Pb-FEBID deposit . . .	152
7.3	Temperature dependence of the normalised resistance of the Pb-FEBID nanowire for a set of applied magnetic fields	153
7.4	Temperature dependence of the normalised resistance for the L ₂₀₀ and L ₄₀₀ sections of the Au-NW for a set of different currents	155
7.5	Temperature dependence of the normalised resistance of the L ₇₀₀ Au-NW section for a set of applied magnetic fields directed perpendicular and parallel to the nanowire axis	156
7.6	Temperature dependence of the normalised resistance of the L ₁₅₀₀ Au-NW section for a set of applied magnetic fields	157
7.7	Temperature dependence of the normalised resistance of the L ₅₀₀₀ Au-NW section for a set of applied magnetic fields	158
7.8	AuPb binary phase diagram	159
8.1	XRD data in the vicinity of Co ₃ O ₄ peaks accompanied by Gaussian fits. . . .	165
8.3	CoPt binary alloy phase diagram	167

List of Tables

2.1	Summary table of superconducting order parameters and characteristic proximity length scales of S/N and S/F proximity effect	51
3.1	Structural and compositional parameters of all samples investigated in this work	80
4.1	Structural and compositional parameters of Cu-NW1 and Cu-NW2	98
5.1	Structural and compositional parameters of the Co and Co-FEBID nanowires	113
6.1	Geometric dimensions, composition, and magnetic properties of the Co/Pt heterostructure	126
7.1	Structural parameters of the Au-NW and Pb-FEBID inducer-electrodes . . .	151

Abbreviations

AC	A lternating C urrent
AFM	A tomical F orce M icroscopy
AMR	A nisotropic M agneto R esistance
DC	D irect C urrent
ECD	E lectro C hemical D eposition
EDX	E nergy- D ispersive X -ray
EELS	E lectron E nergy L oss S pectroscopy
FEED	F ocused E lectron B eam I nduced D eposition
FIB	F ocused I on B eam
FIBID	F ocused I on B eam I nduced D eposition
GIS	G as I njection S ystem
HE	H all E ffect
MR	M agneto R esistance
NW	N ano W ire
PE	P roximity E ffect
PC	P oly C arbonate
PVD	P hysical V apor D eposition
RT	R atio T ransformer
SAED	S electd A rea E lectron D iffraction
SEM	S canning E lectron M icroscopy
STEM	S canning T ransmission E lectron M icroscopy
TEM	T ransmission E lectron M icroscopy
UHV	U ltra H igh V acuum
UV	U ltra V iolet
XRD	X - R ay D iffraction

Chapter 1

Introduction

Some fundamental demands for modern electronic devices include: miniaturization, high clock frequencies, and low power consumption. The electrical resistance of a material is an obstacle to achieve these demands; therefore, the ability to controllably reduce it is of primary importance for various applications. In particular, low dissipation levels and high clock frequencies are at present accomplished with superconducting circuits, whereby the lateral dimension of the conductor is typically on the mesoscale and in the nanometer range. Accordingly, given that a superconductor can be in electrical contact with a normal metal or a ferromagnet, the investigation of the superconducting proximity effect [7–9, 13] and spin-dependent transport [29, 30] in nanowires and structures — the objects this work is concerned with — represents a challenging research area from the viewpoint of both basic research and the development of applications.

The superconducting proximity effect (PE) can appear in any circuit element which comes in contact with a superconducting (S) region, whereby its spatial extent depends on the material from which the non-superconducting part is made. In the case of a superconductor (S) in contact with a normal metal (N), the superconducting PE is characterized by the appearance of superconducting correlations in N at a temperature-dependent distance of $\xi_N \simeq 1 \mu\text{m}$ far below the critical temperature T_c of S, due to the injection of Cooper pairs from S into N. The length ξ_N is called the proximity length and the proximity effect in S–N systems is comprehensively addressed in Refs. [7, 8]. The Cooper pairs are pairs of electrons with opposite spins and, provided that N is replaced by a ferromagnet (F), the exchange field h_{ex} of F tends to align both spins in the same direction. This results in a strong pair-breaking effect which causes a rapid decay of the superconducting order parameter in F over a distance $\xi_F \simeq 1 \text{ nm}$. This length is known as the spin-singlet proximity length and as the value of ξ_F suggests, the PE in S–F structures is a short-ranged effect. However, in Ref. [12] it has been shown that under certain circumstances the presence of F may lead

to triplet superconducting pairing [9, 13, 16] and superconductivity in F can survive over a distance comparable with ξ_N [10, 11]. This is due to the fact that triplet Cooper pairs are formed by electrons with collinear spins, which makes them insusceptible to the exchange field. A necessary condition for the spin-triplet pairing to appear is a local inhomogeneity of the magnetization in the vicinity of the S/F interface [13]. Inhomogeneity of the exchange field can be either intrinsic to F, or can be caused by a material inhomogeneity as a result of experimental manipulations, such as contacting procedures [13]. The current quest for experimental evidence of the long-range spin-triplet PE is motivated by the possibility of combining the zero-resistance supercurrents of S with the spin alignment of F, which would have strong implications for spintronics [16, 17].

In the last decade, the study of the spin-singlet PE at an S/N interface as well as the long-range PE at an S/F interface has become a matter of extensive research, both theoretically [16, 31, 32] and experimentally [14, 18, 21, 33–39]. In particular, some theoretical works have largely been focused on clarifying the role of local magnetic inhomogeneities near an S/F interface [12, 16], while others dealt with developing new types of spin-valves based on S/F multilayers [40], and studying new types of Josephson junctions based on S/F/S trilayers [32, 41]. Experimentally, to elaborate these and other related problems, most of the studies utilized (multi-) sandwich heterostructures of flat films [18–20], wedge-shaped layers [21, 37], Josephson junctions [22, 23] and more complex geometries [24–28]. In particular, flat geometries are well-suited for observing the variation of the critical temperature T_c of S with the thickness of F, while wedged layers [21, 37] have been used for investigations of the triplet spin-valve effect caused by a non-collinear alignment of the magnetization of F layers. Other experiments [14, 38, 39] have been carried out in the nanowire geometry where marked drops in the nanowire resistance $R(T)$ were observed when sweeping the temperature below T_c of S. So, Wang *et al.* [14] have reported a long-range spin-triplet PE in single-crystal Co nanowires. It was found [14] that a wire of 40 nm diameter attained a zero-resistance state over a length of at least 600 nm.

In this work, an extensive study of the superconducting PE (along with accompanying complementary effects) was performed on crystalline Co, Cu, Au and nanogranular Co nanowires. The focused ion beam-induced deposition (FIBID) technique was employed for the preparation of auxiliary contacts and superconducting inducer electrodes to the nanowires. A proximity-induced superconductivity manifests itself via resistance drops just below the transition temperature T_c of the superconducting inducer. For this, the standard 4-probe geometry has been used together with a modified geometry supplemented by additional pairs of voltage leads for the transport measurements [42]. This allows for probing the

proximity effect at different distances from the superconducting inducer electrode (2-12 μm) and, thereby, for judging the impact of the defect-rich contact regions on the conductance properties of the nanowires. It should also be noted that the arrangement used represents an exemplary layout occurring in electrical circuits. At the same time, it substantiates the natural geometry for in-circuit nanowires with a wide range of tunable geometric, microstructural, and compositional properties fabricated by well-established preparation techniques [43–48].

In brief, the key finding of this work is a long-range PE in polycrystalline Co nanowires (chapter 5). It was found that the proximity length is approximately 1 μm at 2.4 K and the PE is unsusceptible to magnetic fields up to 11 T (the upper critical field of the inducer electrode at 2.4 K). Additionally, a weak localization-like low-temperature transport in the polycrystalline Co nanowire was observed, owing to a large resistance contribution from the grain boundaries. Similar to the Co nanowires, the PE in single-crystal, Cu nanowires is characterized by a proximity length of the order of 1 μm . Moreover, it was possible to identify and quantify a large resistance contribution of the ion beam-damaged regions in the Cu nanowires (chapter 4). By contrast, the long-ranged PE was not observed in the nanogranular Co nanowires due to the dominating Cooper pair scattering caused by its intrinsic microstructure (chapter 5). Finally, preliminary results of the approach using a Pb superconductor prepared by focused electron beam induced deposition (FEBID) for studying of the PE in Au nanowires are presented in the last chapter of this work (chapter 7). The replacement of FIBID by FEBID is advantageous with regard to the exchange of heavy ions by less destructive electrons, whereas optimization of the Pb-FEBID process on submicron dimensions has to remain for further elaboration.

A considerable part of this work is devoted to the study of materials with controllable magneto-transport properties. Controlling magneto-transport properties on the nanometer scale is essential for basic research in micro-magnetism [49] and spin-dependent transport [18], as well as for various applications [50–53]. In particular, the ability to tune the magnetization is the basic property needed for the realization of stacked nanomagnets [54], pinning of magnetic domain walls [55] and Abrikosov vortices [56, 57], magnetic sensing [51, 52] and storage [50, 53], and spin-triplet proximity-induced superconductivity [9, 13–15]. This has been accomplished to a very high degree by means of layered heterostructures in the vertical dimension, which can be prepared by thin film techniques or by an alternative approach – as used in this work – by direct writing of metal-based layers by FEBID [58, 59]. The resolution of FEBID is better than 10 nm laterally and 1 nm vertically [58, 59] and, thus, its proven applications range from photomask repair [60] to fabrication of nanowires [42, 61], nanopores [62], and magnetic [51, 52] and strain sensors [63] as well as direct-write super-

conductors [64].

In general, FEBID structures prepared with organo-metallic precursors are nanogranular metals. In these materials, metallic grains of a few nm in diameter are embedded in a carbonaceous matrix, due to an incomplete dissociation of the precursor molecules. Owing to the sensitivity of the matrix to post-processing treatments, the compositional, structural, and, hence, electrical [65, 66] and magnetic [67, 68] properties of metal-based layers fabricated by FEBID can be substantially modified either in situ or ex situ. Exemplary purification treatments of samples include annealing in a reactive atmosphere [69], electron irradiation [65, 66], or a combination of both [68, 70–72]. For instance, the tunability of the electrical properties of FEBID structures has been recently shown for the Pt(C) [65] and Pt(Si) [73] systems which undergo a metal-insulator transition (MIT) when irradiated by electrons. Also, by simultaneously using two precursor gases, binary CoPt alloys have been prepared [74]. After electron irradiation these alloys showed hardened F properties due to the formation of the CoPt $L1_0$ phase in the entire sample volume, while their resistivity was in the $m\Omega\text{cm}$ range. Recently, two fundamental findings were made in our group which were applied in this work. First, it has been shown [75] that a post-growth purification of Pt-FEBID by using pulsed oxygen flux cycles at a sample temperature of 150 °C results in a Pt resistivity of less than an order of magnitude larger than the bulk value of $10.4 \mu\Omega\text{cm}$ [76]. Second, it has been found [68] that via post-growth heating and electron irradiation of Co-FEBID layers in H_2 atmosphere, their conducting and magneto-transport properties can be drastically modified. It is thus generally accepted that the FEBID technique can accomplish the aforementioned goal to provide tunability of the electrical and magnetic properties of multi-component systems.

Multi-component systems are known to exhibit different properties with respect to the pristine materials they are made from. This is because the resulting system can combine different (and sometimes competing) features of its components as well as exhibit new unforeseen phenomena in its constituents. Of particular interest are new properties and the ability to controllably tune these properties when the sizes of the system under study are scaled down to the meso and nm range. That is, when the spatial extent in one or several dimensions is comparable with the characteristic length scales determining its physical properties. Roughly, one can categorize multi-component systems into two types: (i) multinary alloys which are a single phase over the entire volume and (ii) multilayer heterostructures, where one can discriminate the different phases of the constituent materials along with (most commonly) a new intermixed phase at their interface. It is multi-component systems with reduced dimensionality which determine the electronic functionality of devices today.

As such, the most interesting and complex aspects of such systems are their electro- and magneto-transport properties as well as the challenge of their local tunability, ideally across the MIT and adjusting the magnetic hardness. The ferromagnetic state is of particular interest since the ability to switch the magnetization is the basic property needed for tuning the local magnetic inhomogeneity of F on the lateral mesoscale. This property is required for supporting triplet superconductivity in superconductor/F heterostructures [15] and for tuning the electrical properties of the system as well. At the same time, the hardening of the magnetic properties is equally important for basic research, since it can be coupled with the MIT in artificial nanosolids.

Finally, Co/Pt multilayer heterostructures prepared by FEBID were chosen as the prospective materials with controllable magneto-transport properties. Other issues that were addressed in this work include: How to tune the magnetic properties of one layer (Co) while keeping the high conductive properties of the other layer (Pt) and development of recipes for post-growth treatments for the fabrication of the desired magnetic state. In chapter 6 an approach to the laterally resolved adjustment of the magnetic properties of CoPt-FEBID bilayers with a thickness in the nm range is presented. The approach is based on post-growth treatments of the bilayers using a combination of in situ heating in a local reactive gas atmosphere (H_2 and O_2) and electron beam irradiation of the as-deposited layers. It has been demonstrated that the appropriately processed samples combine the high conducting properties of Pt with the soft ferromagnetic behavior of Co, which can be tuned into the hard-ferromagnetic regime of the CoPt $L1_0$ phase formed at their interface, whose presence has been revealed by transmission electron microscopy.

Chapter 2

Theoretical background

2.1 Normal conductivity

2.1.1 Hall effect (HE). Anisotropic magneto-resistance (AMR)

The Hall effect [77, 78] and anisotropic magnetoresistance [79, 80] are spin-dependent electronic transport phenomena, which can be used for investigating the properties of magnetic materials. They are similar in that they both occur when a current-carrying conductor is subjected to a magnetic field. Magneto-transport measurements based on these effects allow for the magnetization direction, demagnetization and magnetization saturation fields, as well as coercive fields of samples under investigation to be determined. In this work, both the Hall effect and magnetoresistance measurements were used for characterization of post-processed Co and Co/Pt heterostructures prepared by focused electron beam induced deposition (FEBID) (see chapter 6).

Hall effect (HE)

The Hall effect [77] (HE) is a phenomenon caused by the influence of the magnetic field, B , on the charge carriers, q , flowing in a conductor with a drift velocity, v , through the Lorentz force, $\vec{F} = q\vec{v} \times \vec{B}$. The Lorentz force will deflect the charge carriers toward one side of the conductor, thus resulting in accumulation of charges along one side and creating a transverse electric field, E_y , which counteracts the force of the magnetic field [see Fig. 2.1(a)]. Most conducting materials experience such an effect. Generally, for the sample geometry shown in Fig. 2.1(a), the Hall resistivity is given by:

$$\rho_{xy} = \frac{E_y}{J_x}, \quad (2.1)$$

with electric field, E_y , directed in the y -direction for a given current density, J_x , directed in the x -direction ($J_x = nqv_x$, n - number of carriers per unit volume), and magnetic field, H_z , directed perpendicular to the sample surface.

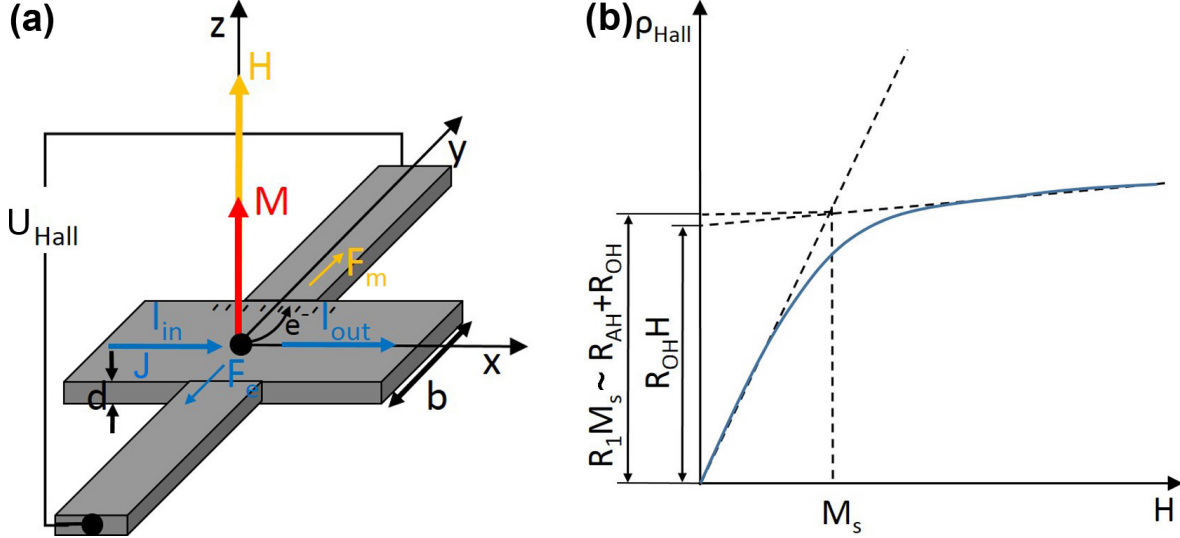


Figure 2.1: (a) Schematic representation of the geometry used for the Hall effect measurements. By passing an electric current, J , through the sample, a magnetic field, H , directed perpendicular to the sample surface will exert a transverse force, F_m , on the moving charge carriers pushing them to one side of the sample. Thus, the accumulated charge will try to compensate for the magnetic influence with force F_e , producing a voltage, U_{Hall} , between the two sides of the sample, which can be measured. (b) Dependence of the Hall resistivity, ρ_{Hall} , on the applied external magnetic field, H . For most ferromagnetic materials, it consists of the ordinary (R_{OH}) and anomalous (R_{AH}) contributions.

For most magnetic materials, the Hall effect is commonly determined as the sum of the ordinary HE (OHE, Lorentz force-induced contribution) and the anomalous HE contribution (AHE, proportional to the sample magnetization, M). In this way, the Hall resistivity is given as:

$$\rho_{Hall} = \rho_{xy} = \rho_{OH} + \rho_{AH} = R_{OH}B_z + \mu_0 R_{AH}M_z = \mu_0 [R_{OH}H_z + (R_{OH}(1 - N) + R_{AH})M_z], \quad (2.2)$$

where H_z is the applied magnetic field¹, M_z is the magnetization along the field direction z , $0 \leq N \leq 1$ is the demagnetization factor, and R_{OH} and R_{AH} are the ordinary and the anomalous Hall coefficients, respectively. R_{OH} can be determined from the slope of the ρ_{Hall} curve in the linear regime above the saturation field H_s . $R_1 = R_{OH} + R_{AH}$ can be deduced from the low-field data, ($H < H_s$) by extrapolating the slope through the zero field point,

¹The relationship between the external magnetic flux density B (the magnetic induction) and internal magnetic field H_{int} of the sample, taking into account the impact of demagnetization factor N is given as $B = \mu_0(H_{int} + M) = \mu_0(H - NM + M) = \mu_0H + \mu_0(1 - N)M$.

$H = 0$, as shown in Fig. 2.1(b). The intersection point of the two fits corresponds to the anisotropy field, NM_s , where N is the demagnetization factor and M_s is the saturation magnetization. Then, Eq. (2.2) can be rewritten as follows:

$$\rho_{Hall} = \rho_{xy} = \begin{cases} R_{OH}H_z + \mu_0 R_{AH}M_z, & \text{for } H < H_s, \\ R_{OH}H_z + \mu_0 R_{AH}M_{z,s}, & \text{for } H \geq H_s. \end{cases}$$

The Hall resistivity is proportional to the Hall voltage, which can be measured between the Hall contacts located perpendicular to the direction of the current flow [see Fig. 2.1(a)], and is given as:

$$\rho_{Hall} = \rho_{xy} = U_{Hall} \frac{d}{I}, \quad (2.3)$$

where d is the thickness of the sample, and I is the current passing through the sample.

The anomalous Hall effect (AHE) is a spin-dependent phenomenon, which generates a voltage proportional to the magnetization across a magnetic sample carrying a current [78, 81, 82]. The effect in ferromagnetic materials usually originates from the extrinsic and intrinsic contributions. The extrinsic contributions are related to the variations in the asymmetric spin-orbit scattering, which break the spatial symmetry in the trajectory of scattered electrons. Here, it should be noted that the scattering is responsible for both the AHE resistivity and longitudinal resistivity (ρ_{xx}); therefore, an interrelation between these two parameters usually exists. There are two main extrinsic scattering mechanisms that can contribute to the AHE. These are skew scattering and side jump. The skew scattering [83] is characterized by a constant spontaneous angle, Θ_S , at which the scattered carriers are deflected from their original trajectories. R_{AHE} is directly proportional to ρ_{xx} :

$$R_{AHE} \propto \rho_{xx}. \quad (2.4)$$

The side jump mechanism [84] is quantum mechanical in nature and leads to a constant lateral displacement, Δy , of the charge trajectory at the point of scattering. It results in a quadratic power law relationship between R_{AHE} and ρ_{xx} :

$$R_{AHE} \propto \rho_{xx}^2. \quad (2.5)$$

In this way, the AHE caused by extrinsic contributions is a superposition of two mechanisms and can be written as:

$$R_{AHE} = A\rho_{xx} + B\rho_{xx}^2, \quad (2.6)$$

where the first term is related to the skew scattering and the second to the side jump mechanism. This relationship can be rewritten as:

$$R_{AHE} = \alpha \rho_{xx}^n, \quad (2.7)$$

with $n = 1$ for the skew scattering and $n = 2$ for the side jump mechanism, while $1 < n < 2$ corresponds to a superposition of both mechanisms.

The AHE can also be a result of the previously mentioned intrinsic contribution [78, 85]. The origin of this contribution is from the anomalous velocity, which electrons obtain when an external magnetic field is applied to a conductor. This anomalous velocity, related to their Berry's phase [85] curvature, is perpendicular to the electric field, can therefore contribute to the AHE. For ferromagnetic conductors, the currents caused by the anomalous velocity do not sum to zero over all occupied band states, implying a contribution to the Hall conductivity, σ_{xy} . The intrinsic contribution to the AHE depends only on the band structure, and it is independent of scattering contributions ($\sigma_{xy} \sim \tau^0 = \text{const}$, where τ is the scattering time $\Rightarrow \sigma_{xy} \neq f(\rho_{xx})$). When the conductivity tensor is inverted, the intrinsic AHE yields a contribution to $\rho_{xy} \sim \sigma_{xy}/\sigma_{xx}^2$ and consequently

$$\rho_{xy} \sim \sigma_{xy} \rho_{xx}^2. \quad (2.8)$$

In principle, the quadratic power law relation is valid in the clean limit. For elevated resistivity values (bad metal regime), the dependence has the form of $\rho_{xy} \sim \sigma_{xy} \rho_{xx}^\gamma$, with $\gamma \approx 1.6 - 1.8$ [68, 78, 86].

Anisotropic magneto-resistance (AMR)

The anisotropic magneto-resistance (AMR) [87, 88] effect arises in some ferromagnetic materials due to the dependence of the resistivity on the angle between the direction of the current flow and the direction of the magnetization. The microscopic origin of the effect lies in the spin-orbit coupling. When the direction of the magnetization changes, the electron cloud around each nucleus can be slightly deformed, resulting in changes in the amount of scattering of the conduction electrons passing through the material. Thus, if the magnetic field, H , and magnetization, M , are oriented transverse to the current flow, J , this results in electron orbits oriented in the plane of the current flow, that is, the scattering cross-section is small, and thus the resistance is at a minimum [see Fig. 2.2(b), red curve]. By contrast, if the applied magnetic field and magnetization are parallel to the current flow, this results in

electron orbits oriented perpendicular to the current flow, that is, the scattering cross-section is larger, and thus the resistance is at a maximum [see Fig. 2.2(b), black curve]. As a result, by controlling the magnetization direction (the angle between the magnetization direction and current flow), the electron orbit orientation with respect to the current flow direction can be changed, causing an increase/decrease of the resistance value. The geometry used for the AMR measurements is shown in Fig. 2.2(a).

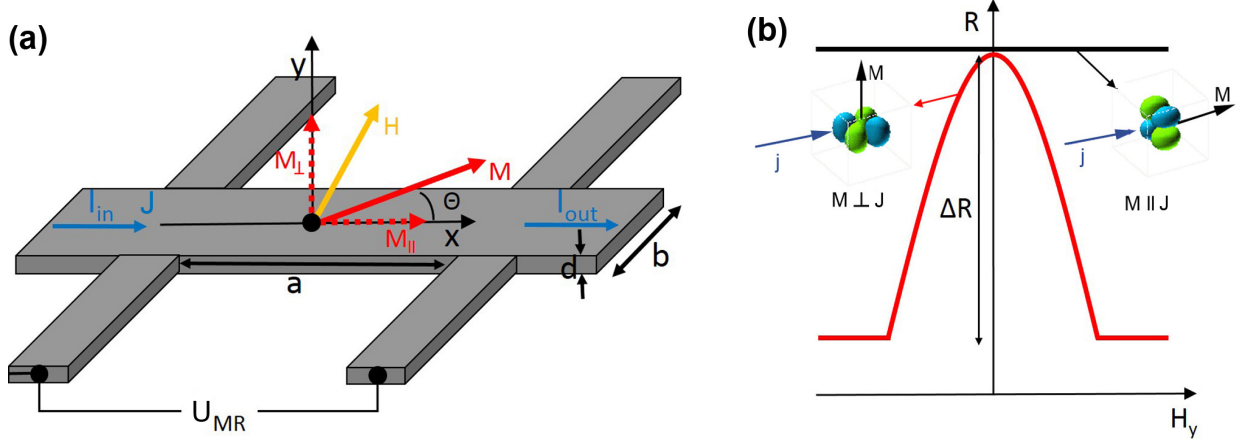


Figure 2.2: (a) Schematic representation of the geometry used for the anisotropic magneto-resistance (AMR) measurements. By passing a current, J , through the sample and varying the direction of magnetization, M , changes in the sample resistance are observed. (b) The dependence of the anisotropic magneto-resistance relative to the change in the direction of magnetization, M , for two extreme cases: (i) black curve – magnetization is directed parallel to the current flow, (ii) red curve – magnetization is directed perpendicular to the current flow.

For example, the magnetization, M , of a thin strip of ferromagnetic material is usually directed along the “easy axis” in the strip plane and parallel to the strip’s long axis. This provides spontaneous magnetization along this axis in a single domain state. If the strip of material is set in a random, multidomain state, with a specific magnetization direction for each domain, then a single domain state can be achieved by applying a strong magnetic field along the strip in order to magnetize it. Then, by applying a magnetic field, H , directed perpendicular to the “easy axis”, magnetization, M , rotates around its initial orientation by some angle, Θ , and a decrease in the resistance results.

The relationship between the resistivity and the direction of magnetization, that is, the angle Θ , is given by the Voight–Thomson formula as:

$$\rho(\Theta) = \rho_{\parallel} \cos^2 \Theta + \rho_{\perp} \sin^2 \Theta = \rho_{\parallel} - \Delta\rho \sin^2 \Theta, \quad (2.9)$$

where ρ_{\perp} and ρ_{\parallel} are the transverse and parallel components of the resistivity, respectively,

Θ is the angle between the magnetization vector and the current flow direction, and $\Delta\rho = \rho_{\parallel} - \rho_{\perp}$.

The measured, relative change in resistance caused by the applied magnetic field is given as:

$$\frac{\Delta R(H)}{R_0} = -\frac{\Delta\rho}{\rho} \sin^2 \Theta, \quad (2.10)$$

where R_0 is the resistance at $H = 0$, and $\Delta R(H) = R(H) - R_0$ is the change of the resistance at a certain magnetic field $H \neq 0$. The quantity $\Delta\rho/\rho = \rho_{\parallel} - \rho_{\perp}/\rho_{\parallel}$ is the magneto-resistivity coefficient of the material. It is worth noting that the change in resistance is caused by the sample magnetization direction, M , rather than the applied external magnetic field, H , the role of which is to change this direction.

In order to determine the dependence of the sample resistance on the applied external magnetic field [$\Delta R(H)/R_0$], the relation between the angle Θ and the external magnetic field should be defined. This can be done by using the expression for the free energy of a ferromagnetic system with uniaxial anisotropy [89, 90], which has the following form:

$$E = E_{mag} + E_k = -\mu_0 M_s (H_y \sin \Theta + H_x \cos \Theta) + \frac{1}{2} \mu_0 M_s H_k \sin^2 \Theta, \quad (2.11)$$

where H_x and H_y are the components of the vector of the external magnetic field applied in the $x - y$ plane. H_k is the anisotropy field ($H_k = 2K_u/M_s$, where K_u is an anisotropy constant) and M_s is the saturation magnetization. The first term represents the magneto-static energy, while the second term accounts for the anisotropy energy.

If the anisotropy axis is directed along the x -axis, the external magnetic field is applied perpendicular to it along the y -axis ($H_y \neq 0, H_x = 0$), minimizing of Eq. (2.11) through $\partial E/\partial \Theta = 0$ results in:

$$\sin \Theta = \frac{H_y}{H_k}. \quad (2.12)$$

As result, Eq. (2.10) based on Eq. (2.12) can be rewritten as follows:

$$\frac{\Delta R(H)}{R_0} = -\frac{\Delta\rho}{\rho} \left(\frac{H_y}{H_k} \right)^2 \quad \Rightarrow \quad R(H) = R_0 - R_0 \frac{\Delta\rho}{\rho} \left(\frac{H_y}{H_k} \right)^2. \quad (2.13)$$

As can be seen from Eq. (2.13), the dependence of the AMR on the applied magnetic field for ferromagnetic materials follows a parabolic behavior [see Fig. 2.2(b), red curve], as expected for coherent rotation of the magnetization of the sample. At larger magnetic fields, when magnetization saturation is achieved, no changes in AMR take place.

2.1.2 Bloch–Grüneisen formula. Matthiessen’s rule

In this work, the evaluation of the quality of the nanowires, which were prepared by various techniques (see chapters 4 and 6), was performed by means of the Bloch–Grüneisen theory, which is comprehensively addressed in Refs. [91, 92]. It was found that over the entire temperature range between 25 – 295 K, the temperature dependence the resistance of the nanowires can be well fitted by the Bloch–Grüneisen formula.

The Bloch–Grüneisen formula describes the temperature dependence of the electrical resistivity, $\rho(T)$, of metallic crystalline solids. The temperature-dependent electrical resistivity arises mainly from electron–phonon interaction and can be explained in the framework of the Boltzmann transport theory [91]. Typically, the electrical resistivity, ρ , is an increasing function of temperature, with a linear dependence in the high temperature range, whereas in the low temperature range, $\rho(T)$ follows a power law function of temperature. Mathematically, the Bloch–Grüneisen formula is given as:

$$\rho(T) = \rho_0 + \rho_n = \rho_0 + K(T/\Theta_D)^n \int_0^{\Theta_D/T} dx \frac{x^n}{(e^x - 1)(1 - e^{-x})}, \quad (2.14)$$

where ρ_0 is the temperature-independent resistivity caused by scattering of the electron waves by static defects that disturb the periodicity of the lattice. The second term is the temperature-dependent part of the resistivity. Here, T is the temperature, and Θ_D is the Debye temperature. K is a constant, $K \propto \lambda_{tr}\omega_D/\omega_p^2$, where λ_{tr} is the electron–phonon constant, ω_D is the Debye frequency and ω_p^2 is the plasma frequency [93]. K is commonly used as the fitting parameter, as is Θ_D , and is chosen such that the best possible fit of the experimental data is achieved. In Eq. (2.14), n is an integer, which determines the power law assigned to the prevailing scattering mechanism in the sample. It has the following interpretation:

- $n = 5$: implies that the resistance is due to the umklapp scattering of electrons by phonons (as for simple metals);
- $n = 3$: implies that the resistance is due to $s - d$ electron scattering (as for transition metals);
- $n = 2$: implies that the resistance is due to electron–electron interaction.

Due to the significantly reduced dimensionality of crystalline nanowires, the temperature-independent residual resistivity, ρ_0 , is determined not only by the material quality (defect scattering), but also largely by size effects, arising from surface scattering and internal grain

boundary scattering. When the nanowire width/diameter becomes comparable to the bulk electronic mean free path, l , (or even smaller), its electrical resistivity increases. This effect has been studied in thin films by Fuchs and Sondheimer (FS-theory) [94–96]. They showed that due to the diffuse scattering at the film boundaries, the mean free path becomes severely reduced, resulting in an increase of the resistivity. Scattering at the film surface is coined as diffusive, if the reflected electron acquires a random direction of momentum, thus reducing the net current flow. This is in contrast to specular scattering where the reflected electron has a conserved component of momentum along the applied electric field [94].

The problem becomes more complicated for polycrystalline nanowires because of additional contributions arising from internal grain boundary scattering. In their theoretical work, Mayadas and Shatzkes (MS-theory) [97, 98] predict an enhancement of the resistivity due to the grain boundary scattering imposed on the weaker FS size effect in thin films. The main conclusion of the MS-theory is that by reduction of film thickness, a decrease of the mean grain size takes place, leading to the existence of more grain boundaries and hence, an increase in the resistivity. Moreover, analysis has shown that the effect of scattering on the grain boundary greatly exceeds the effect of surface scattering. Additionally, in the experimental work by Durkan and Wellan [94] the following conclusions for polycrystalline nanowires with dimensions comparable to the electronic mean free path were made: First, the grain boundary scattering is the dominant source of resistivity when the nanowire width is comparable to the mean grain size. Second, the surface scattering (FS term) becomes equivalent to the grain boundary scattering (MS term), when the nanowire width is less than ≈ 0.5 times the mean grain size. In this case, Matthiessen’s rule can be used in which the total resistivity is a sum of the FS and MS terms.

Matthiessen’s rule states that if more than one source of scattering is simultaneously present in the system, then the total resistivity can be approximated by summing up all resistivity contributions. This rule is applicable to the Bloch–Grüneisen formula, where temperature-dependent terms with an appropriate value of n can be summed to determine the total resistivity. Or, as previously shown, it can be used for the determination of the temperature-independent total residual resistivity when more than one scattering source is present. Additionally, the Bloch–Grüneisen formula [Eq. (2.14)] itself follows Matthiessen’s rule, since the total electrical resistivity of most metals is the sum of the temperature-dependent and temperature-independent terms (and both terms are independent of each other).

However, in some cases, Matthiessen’s rule is not applicable: in particular, when the presence of one scattering mechanism alters the way in which the other scattering mechanism

functions. It breaks down also for two independent sources of scattering (*a*) and (*b*) in the relaxation time approximation when τ depends on the electron wave vector \mathbf{k} . For the case when the relaxation time for each scattering component is independent of \mathbf{k} , Matthiessen's rule requires that

$$1/\tau = 1/\tau_a + 1/\tau_b. \quad (2.15)$$

The conductivity, σ , is proportional to the average of the relaxation time, $\bar{\tau}$. Thus, the resistivity, ρ , is proportional to $1/\bar{\tau}$, and by application of the Matthiessen's rule

$$1/\bar{\tau} = 1/\bar{\tau}_a + 1/\bar{\tau}_b. \quad (2.16)$$

However, in accordance with Eq. (2.15) the following relation results:

$$\overline{(1/\tau)} = \overline{(1/\tau_a)} + \overline{(1/\tau_b)}, \quad (2.17)$$

which is not equivalent to Eq. (2.16) unless τ_a and τ_b are independent of \mathbf{k} .

2.2 Superconducting proximity effect

2.2.1 Basics of superconductivity. Singlet versus triplet state

On one hand, the phenomenology of superconductivity can be simply explained as a phenomenon of zero resistivity where the expulsion of a magnetic field can occur for certain materials below some critical temperature, T_c . On the other hand, superconductivity is a complex, macroscopic quantum coherence effect. The nature of the effect is that below T_c , electrons close to the Fermi level begin to pair into Cooper pairs [99]. For conventional superconductors this pairing is a result of small attractive forces between the electrons induced by lattice vibrations. Single electrons are fermions and must obey the Pauli exclusion principle, whereas the Cooper pairs behave in a different manner. Rather, the Cooper pairs are bosons and can condense into the same state. The resulting condensate of Cooper pairs is characterised by a ground state with gapped single particle excitations.

The Cooper pairs can exist in a spin-singlet or a spin-triplet state. Spin-singlet pairing is found in conventional low T_c *s*-wave superconductors (for example Nb, Pb or In) and unconventional high T_c *d*-wave superconductors (for example cuprates, such as Ba-La-Cu-O [100]). The singlet state (see Fig. 2.3, singlet) of a two-electron system is a set of possible states where the total spin is 0, and both the magnitude and the z component of the spin

vector are zero. Thus the only possible eigenstate of S and S_z is:

$$|0, 0\rangle = (\uparrow\downarrow - \downarrow\uparrow)/\sqrt{2}.$$

In this case, the order parameter $\Delta_{\alpha\beta}$ is represented in the form $\Delta_{\alpha\beta} = \Delta \cdot (i\sigma_3)_{\alpha\beta}$ (σ_3 is the Pauli matrix in the spin space, α and β are spin indices) [13, 101]. The difference between the s - and d -wave superconductors is determined by a different dependence of the order parameter Δ on the Fermi momentum $\mathbf{p}_F = \hbar\mathbf{k}_F$. Thus, for isotropic singlet conventional superconductors Δ does not depend on \mathbf{k} [$\Delta^s(\mathbf{k}_F) = \Delta_0$], for anisotropic conventional superconductors Δ is dependent on the \mathbf{k}_F direction, but it does not change sign as a function of the momentum \mathbf{k}_F orientation in space. At the same time, for unconventional d -wave superconductors, the order parameter $\Delta^d(\mathbf{k}_F)$ may have either positive or negative sign depending on the direction [$\Delta^d(\mathbf{k}_F) = \Delta_0(k_x^2 + k_y^2)$]. The Pauli principle requires the function $\Delta(\mathbf{k}_F)$ to be an even function of \mathbf{k}_F [$\Delta(\mathbf{k}_F) = \Delta(-\mathbf{k}_F)$].

Another type of pairing, spin-triplet pairing, was found in materials with strong electronic correlations, such as heavy fermion intermetallic compounds [102], in superconductor Sr_2RuO_4 [103], and unconventional organic superconductors, such as $(\text{TMTSF})_2\text{PF}_6$ in high magnetic fields [104], as well as superconductor/ferromagnet (S/F) structures [105]. The triplet state (see Fig. 2.3, triplet) of a two-electron system with total spin 1 has three possible eigenstates, S_z , equal to 1, 0, or -1 :

$$\begin{aligned} |1, 1\rangle &= \uparrow\uparrow \\ |1, 0\rangle &= (\uparrow\downarrow + \downarrow\uparrow)/\sqrt{2}. \\ |1, -1\rangle &= \downarrow\downarrow \end{aligned}$$

In the spin-triplet state, the condensate function $\langle\psi_\alpha(r, t)\psi_\beta(r', t')\rangle$ must be an odd function with respect to the permutations $\alpha \leftrightarrow \beta$, $r \leftrightarrow r'$ at equal times ($t = t'$). The spin-triplet pairing means that the spins of Cooper pairs are parallel to each other and the transposition of the spin indices does not change the condensate function. Provided this function remains finite at $t = t'$ it must change the sign under transposition of the coordinates r and r' . So it has to be an odd function of the orbital momentum, that is, the orbital angular momentum L is an odd number ($L = 1, 3$, etc.) The condensate function depends on the direction in the space, and thus the superconducting condensate is sensitive to the presence of non-magnetic impurities. The d - and p -wave superconductivity will be suppressed by impurities along with the order parameter $\Delta_{\alpha\beta} = \sum_{\mathbf{k}} \Delta_{\alpha\beta}(\mathbf{k}_F) \sim \sum_{\mathbf{k}} \langle\psi_\alpha(r, t)\psi_\beta(r', t)\rangle_{\mathbf{k}}$. Such sensitivity to

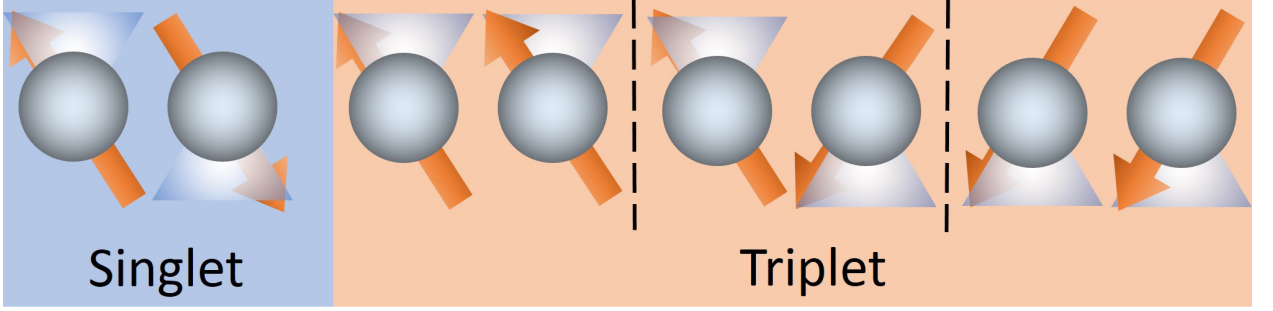


Figure 2.3: Singlet and triplet states that can be occupied by a Cooper pair.

impurities makes difficult to observe this superconducting state experimentally.

However, another nontrivial possibility for the spin-triplet pairing exists. Nothing forbids the condensate function $\langle \psi_\alpha(r, t) \psi_\beta(r', t) \rangle$ to change sign under the transposition $t \leftrightarrow t'$. In the frequency representation, this property is realized if the condensate function $\langle \psi_\alpha(r, \tau) \psi_\beta(r', \tau') \rangle_{k, \omega}$ is odd function of the frequency ω . However, if it is odd in frequency, it may be even in the momentum. In this way, the correlation function $\langle \psi_\alpha(r, \tau) \psi_\beta(r', \tau') \rangle_{k, \omega}$ equals to zero at coinciding times, and therefore the Pauli principle for the equal-time correlation functions is not violated. The order parameter $\Delta(\omega) \propto \sum_{\omega, k} \langle \psi_\alpha(r, \tau) \psi_\beta(r', \tau') \rangle_{k, \omega}$ is also odd function of ω , that is, $\Delta(\omega) = -\Delta(-\omega)$. In contrast to the “conventional” triplet pairing, the odd triplet superconductivity is not sensitive to non-magnetic impurities.

This new, unconventional state, the so-called odd-frequency triplet superconductivity, can be observed only in the S/F proximity structures, and its main properties are:

- It contains a spin-triplet component, in particular, equal-spin pair amplitudes with non-zero total spin projections $S_z = \pm 1$ are involved, which are insensitive to an exchange field in ferromagnet resulting in a long-range proximity effect in S/F structures.
- In the diffusive limit, the condensate function has an *s*-wave symmetry. Thereby, it is *even* in the momentum \mathbf{p} (under the interchange of the spatial coordinates of the two electrons), and therefore is not sensitive to non-magnetic impurities.
- The triplet pair amplitude is also *even* with regard to interchange of electron spins.
- Consequentially, to obey the Pauli principle, the triplet condensate function must be *odd* with regard to interchanging time coordinates (under time reversal), that is *odd* in frequency.

2.2.2 Proximity effect at the superconductor/normal metal (S/N) interface

If a superconductor (S) is placed in contact with a normal metal (N), the Cooper pairs penetrate the N, inducing superconducting correlations which decay over some distance. This proximity effect is comprehensively addressed in Refs. [7, 8]. The characteristic decay distance is called the proximity length and its typical value is approximately $\xi_N \simeq 1 \mu\text{m}$ at low temperatures [7, 9]. For many years, the study of the classical proximity effect at the S/N interface has been a matter of extensive research, both theoretically [106–108] and experimentally [38, 39, 106, 109, 110]. In particular, it was shown that for the S/N geometry, N shows superconductor-like properties, including magnetic screening [111] and modification of the density of states [112].

The proximity effect (PE) refers in general to all changes of the superconducting properties of a system that consists of an S metal in good electrical contact with an N metal (see Fig. 2.4). These changes take place on both sides of the S/N interface within some characteristic distance. On one side, the penetration of the Cooper pairs into N will induce superconductivity in this region. On the other side, the leakage of Cooper pairs from S to N also results in a decrease of their density in S close to the S/N boundary over the characteristic correlation (coherence) length, ξ_S , usually leading to reduction of the order parameter Δ and the transition temperature of S in comparison with bulk values far away from the boundary.

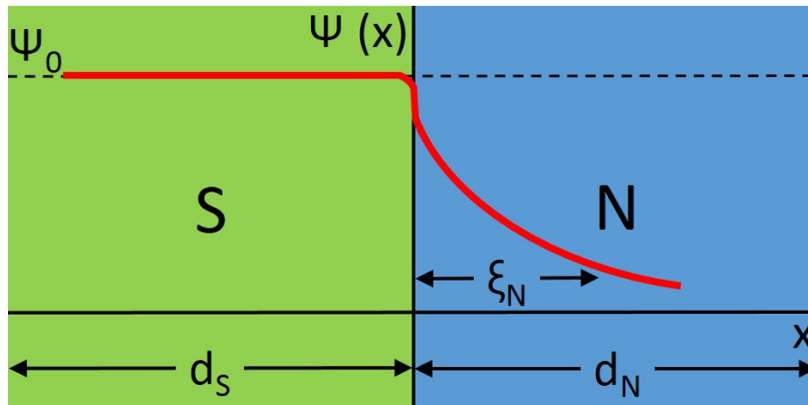


Figure 2.4: Schematic representation of the superconducting order-parameter behavior at the S/N interface. In N, it decays exponentially $\psi(x) \approx \psi_0 \exp(-x/\xi_N)$ and can penetrate through N over a large distance. The penetration depth, ξ_N , is an increasing function of decreasing temperature ($\xi_N \approx 1/\sqrt{T}$).

The decay of the superconducting correlations over some distance into N implies that some fraction of N close to the S/N boundary will become superconducting. The study of the PE was started by Cooper [113] who made the theoretical assumption that zero-momentum

electron pairs (the Cooper pairs) are able to retain their coherence over a microscopic distance, even if they penetrate into materials with a pairing potential $V = 0$ ($T_c = 0$). He supposed that the electron pairs experience an effective attractive potential, which is simply the spatial average of the potentials on both sides of the S/N interface. Cooper's theory was formulated in the thin film limit, namely that the thicknesses of S and N, given by d_S and d_N , respectively, must be much smaller than the characteristic lengths, ξ_S and ξ_N . Later, this theory was further developed without these limitations by de Gennes and Guyon [114] and then extended by de Gennes [7] and Werthamer [115], where the characteristic lengths of the proximity problem were also introduced. Since the PE relates to the problem of inhomogeneous superconductors, all of these works are based on the Gor'kov equations for inhomogeneous superconductivity [116].

In the case of a homogeneous superconductor, in accordance with BCS theory [99], the ordering is expressed as a correlation in the occupation of the one-electron states at $k \uparrow$ and $-k \downarrow$ in momentum space, and the gap parameter $\Delta(\mathbf{k})$ is assumed to be homogeneous in the sample. In the case of an inhomogeneous superconductor (and PE in particular) the ordering is a function of position and is determined as a condensation (probability) amplitude by:

$$F(\mathbf{r}) = \langle \psi \uparrow(\mathbf{r}) \psi \downarrow(\mathbf{r}) \rangle, \quad (2.18)$$

where $\psi \uparrow(\mathbf{r})$ and $\psi \downarrow(\mathbf{r})$ are the one-electron annihilation operators (the bracket indicates a thermal average), and $|F(\mathbf{r})|^2$ is then essentially the probability of finding two electrons in the condensed state at a point \mathbf{r} , therefore, it represents the superfluid density.

By analogy with BCS, the order parameter for an inhomogeneous system is defined by:

$$\Delta(\mathbf{r}) = V(\mathbf{r}) F(\mathbf{r}), \quad (2.19)$$

where $V(\mathbf{r})$ is the attractive interaction between the electrons at a point \mathbf{r} . In contrast to a spatially homogeneous superconductor, where Δ is independent of position, here $\Delta(\mathbf{r})$ varies with position. For small $\Delta(\mathbf{r})$ close to T_c of the S/N junction, the Gor'kov self-consistent, linear equation can be reduced to an integral equation:

$$\Delta(\mathbf{r}) = V(\mathbf{r}) \int K(\mathbf{r}, \mathbf{r}') \Delta(\mathbf{r}') d^3 \mathbf{r}', \quad (2.20)$$

where the kernel $K(\mathbf{r}, \mathbf{r}')$ is a temperature-dependent function. De Gennes solved Eq. (2.20) [7] in one dimension for the case of a S/N proximity junction with negligible pair interaction in N ($V_N = 0$). Under these conditions, $\Delta(\mathbf{r})$ vanishes in N, but the condensation amplitude,

$F(\mathbf{r}) = \Delta(\mathbf{r})/V(\mathbf{r})$, has a tail in N, and $F(\mathbf{r})$ is an integral only over S. The solution was found for the clean ($l_N \gg \xi_N$, the elastic mean free path is much larger than the coherence length) and dirty ($l_N \ll \xi_N$, the elastic mean free path is much smaller than the coherence length) limits. For the clean limit F has the asymptotic form:

$$F_N(x) \propto \psi(x) \exp(-xK_N) \quad (x \gg K_N^{-1}), \quad (2.21)$$

where $\psi(x)$ is a slowly varying function of x and

$$K_N^{-1} = \boxed{\frac{\hbar v_F}{2\pi k_B T}} = \xi_N \quad (\text{clean limit}). \quad (2.22)$$

K_N^{-1} represents the penetration depth of the electron pairs into N and is equal to the proximity length, ξ_N . For $x \approx K_N^{-1}$ the shape of $F_N(x)$ is not a simple exponential function.

For the dirty limit an asymptotic form holds, and

$$K_N^{-1} = \sqrt{D_N v_F} = \sqrt{\frac{\hbar v_F l_N}{6\pi k_B T}} = \boxed{\sqrt{\frac{\hbar D_N}{2\pi k_B T}}} = \xi_N \quad (\text{dirty limit}). \quad (2.23)$$

Here v_F is the Fermi velocity, k_B is the Boltzmann constant, and \hbar is Plank's constant $h/2\pi$. The quantity $v_F l_N/3$ is the diffusion coefficient D_N of the electrons in the normal conductor.

In this way, a finite Cooper pair density is induced in N, where it decays with a characteristic length ξ_N deep from the S/N interface. As $T \rightarrow 0$, $\xi_N(T)$ diverges in the clean and dirty limits. Furthermore, at the interface, the wave function ψ can change abruptly. The magnitude of this change depends on the transmission at the S/N interface. For this reason, care should be taken during the preparation of S/N junctions. In the ideal case, the metal surfaces should be clean, free of oxides and other contaminants. In addition, interdiffusion effects between S and N, resulting in alloying at the interface, should be avoided. This problem is considered in more detail in chapter 7. This can be achieved by proper selection of the S and N metals.

To solve the PE problem discussed herein, appropriate boundary conditions for the gap function must be defined. These boundary conditions at the S/N interface ($x = 0$) were introduced by de Gennes as follows:

$$\frac{F_S(0)}{N_S} = \frac{F_N(0)}{N_N} \quad (2.24)$$

and

$$v_{FS}l_S \left. \frac{dF_S(x)}{dx} \right|_0 = v_{FN}l_N \left. \frac{dF_N(x)}{dx} \right|_0, \quad (2.25)$$

where N_S and N_N are the density of states of the superconductor and normal metal at the Fermi level, respectively. Here positive values of x correspond to the N side. The condition (2.24) is valid both for the clean and dirty limits, whereas condition (2.25) can be used only for characterization of the dirty limit.

Among a large number of experimental works recently published regarding the classical PE, the works of Wang *et al.* [38] and Liu *et al.* [39] are notable. These works are the most relevant for the work presented herein, as these are based on nanowire structures (made of Au, Zn, and Sn) used for PE investigations. Reported penetration lengths of the superconducting phase from S into N (i.e., the proximity length) were in the micrometer range. In the first work, the PE in \varnothing 70 nm, single crystal, Au nanowires was studied as a function of nanowire length, magnetic field, and excitation current [see Fig. 2.5(a)]. For these purposes, resistance versus temperature measurements [$R(T)$] in a 4-probe geometry with superconducting W-based current and voltage electrodes were used. A sharp, superconducting transition was found for short nanowires ($\approx 1 \mu\text{m}$), whereas a nonzero, residual resistance was observed for longer nanowires ($\approx 2 \mu\text{m}$). However, two sharp transitions were observed for nanowires with intermediate lengths ($\approx 1.2 \mu\text{m}$). For this case, it was proposed that the normal and superconducting regions are separated by the so-called minigap phase, originated from a coexistence of proximity-induced superconductivity with a normal region near the center of the nanowire.

In the work of Liu *et al.* [39], a long-range PE effect was observed in single crystal, superconducting nanowires made of Zn and Sn with lengths up to $6 \mu\text{m}$. The same approach as that applied by Wang was used, where the PE was revealed via $R(T)$ measurements. It was shown that superconductivity in the nanowires can be strongly suppressed when non-superconducting (Au) voltage electrodes were used. In contrast, when the electrodes were made of a superconductor (Pb) with T_c higher than the T_c of the nanowires, the nanowires became completely superconducting at the T_c of the electrodes [see Fig. 2.5(b)]. In addition, by means of $I - V$ measurements, evidence was provided that the PE occurs along the entire length of the nanowires.

2.2.3 Proximity effect at the superconductor/ferromagnet (S/F) interface

The spatial extent of the PE is dependent on the non-superconducting part of the material. Thus, another situation prevails when N is replaced by a ferromagnet (F) [7]. For most

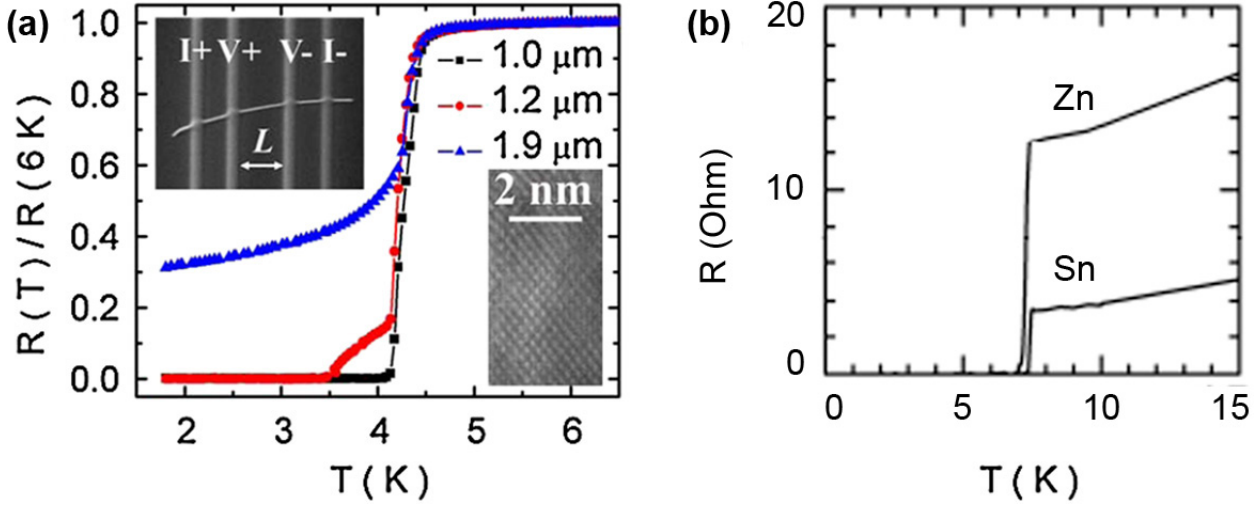


Figure 2.5: Experimental evidence of the proximity effect of an S/N junction observed in (a) Au [38] and (b) Zn and Sn [39] nanowires. The nanowires were contacted in a 4-probe geometry with superconducting current and voltage electrodes used to perform resistance versus temperature $R(T)$ measurements. The effect was revealed via the complete or partial vanishing of the nanowire ohmic resistance at $T < T_c$ of the superconducting electrodes.

superconductors, the wavefunction of the Cooper pairs is singlet. The exchange field h_{ex} of F tends to align both spins in the same direction. This results in a strong pair-breaking effect and causes a rapid, exponential, oscillatory decay of the superconducting-order parameter in F over a distance ξ_F (see Fig. 2.6). This effect is short-ranged, with a spin-singlet decay length of $\xi_F \simeq 1$ nm, as experimentally shown [10, 11]. This effect is considered in more detail in this subsection.

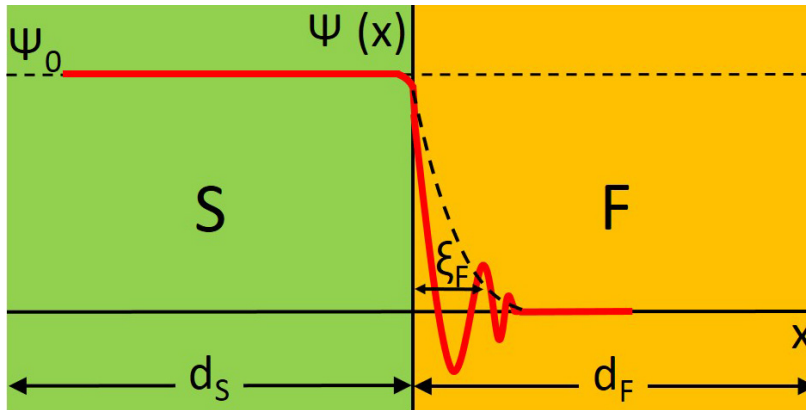


Figure 2.6: Schematic representation of the superconducting-order parameter behavior at the S/F interface with uniform magnetization. In F, it is an exponentially-damped, oscillatory function $\psi(x) \approx \psi_0 \cos(x/\xi_F) \exp(-x/\xi_F)$ and can penetrate only a few nm through F due to the exchange interaction in F. The penetration depth ξ_F is a function of the exchange energy, E_{ex} ($\xi_F \approx \sqrt{\hbar D_F / E_{ex}}$).

The origin of the damped, oscillatory decay of the singlet Cooper pair wavefunction in the ferromagnetic layer of an S/F system is attributed to the effect that was theoretically

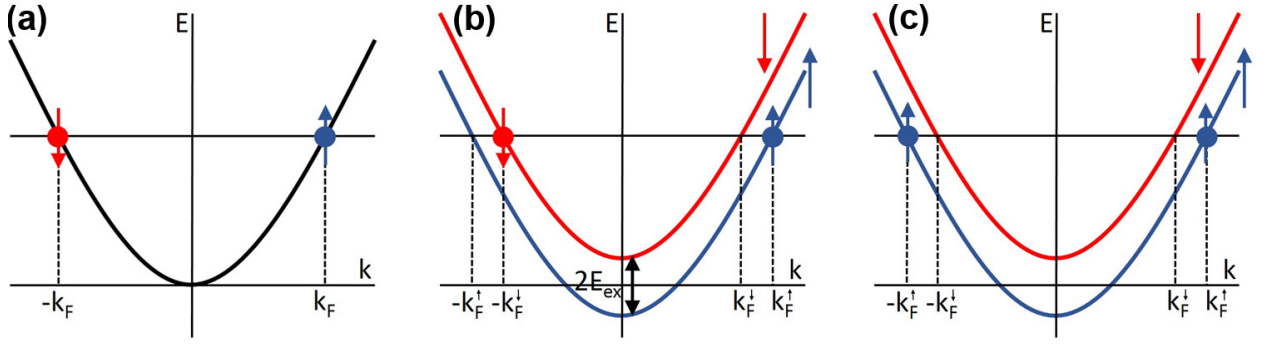


Figure 2.7: (a) Cooper pair at zero magnetic field formed by two electrons with opposite momenta ($\pm k_F$) and opposite spins ($\uparrow\downarrow$), where the total momentum of the pair is 0 (singlet pairing). (b) Under influence of the exchange field, h_{ex} , due to the exchange splitting both electronic bands are shifted with respect to each other by an amount of $2E_{ex}$, resulting in a nonzero center-of-mass momentum Q of the Cooper pairs. (c) In addition, Cooper pairs can be formed by electrons with collinear spins (triplet pairing), which makes them insusceptible to the exchange field, h_{ex} .

predicted by Fulde and Ferrell [117] and Larkin and Ovchinnikov [118] (the so-called FFLO state). They found a nonuniformity of the superconductivity in a pure ferromagnetic superconductor at low temperatures, where superconducting-order parameter modulations are caused by the Zeeman splitting of the electron levels under a magnetic field acting on the electron spins. A singlet Cooper pair at zero magnetic field² (or an S/N system, where no exchange interaction takes place) is usually formed by two electrons with opposite momentum ($\pm k_F$) and opposite spin ($\uparrow\downarrow$), and the total momentum of the pair is 0 [see Fig. 2.7(a)]. However, due to the exchange splitting in F, the electron band for spin up (\uparrow , blue) will be shifted with respect to the band for spin down (\downarrow , red) by the amount of $2E_{ex}$ [see Fig. 2.7(b)] [17]. The electrons with spin moments parallel to the exchange field h_{ex} lower their kinetic energy, while the electrons with antiparallel spin moments increase their energy by the same amount. As pairing occurs between (essentially) equal-energy electrons, the resulting momentum of the Cooper pair at the Fermi energy will be nonzero, $\pm Q = 2E_{ex}/\hbar v_F \neq 0$, where v_F is the Fermi velocity. This causes spatial oscillations of the superconducting-order parameter proportional to e^{iQx} with a period $2\pi/Q \propto \pi v_F/h_{ex}$. For a ferromagnetic superconductor, the direction of the vector \mathbf{Q} is determined by the crystal anisotropy, whereas for S/F systems, \mathbf{Q} is always perpendicular to the S/F interface.

Interestingly, due to its very high sensitivity to impurity scattering, the FFLO state has thus far not been experimentally detected in bulk ferromagnetic superconductors. However,

²I.e., not an applied external magnetic field, H , which acts on the orbital states of the paired electrons, but rather h_{ex} , which acts on electron spins. The exchange field inside a ferromagnet can be as high as 10^3 T.

the FFLO state was experimentally observed in S/F systems as the spatial oscillations of the electronic density of states [119], a non-monotonic dependence of T_c (of S/F bilayers and multilayers) on the F layer thickness [$T_c(d_F)$] [34, 120], and by the realization of π -Josephson junctions in S/F/S systems [36, 121, 122]. One example of experimental evidence of the non-monotonic variation of T_c versus F layer thickness d_F obtained by Jiang *et al.* on Nb/Gd multilayers [120] is shown in Fig. 2.8(a). These results gave the first evidence of the predicted π -phase in S/F multilayers, where the order parameter in neighboring S layers can have an intrinsic phase difference [123]. The latter effect was seen in so-called Josephson π -junctions based on S/F/S structures. Usually, at equilibrium conditions a phase difference φ between two superconductors of an S/N/S Josephson junction is equal to 0. The energy E of the Josephson coupling is given as $E = (\hbar I_c/e)[1 - \cos \varphi]$, where I_c is the Josephson critical current, and the current-phase relation is $I(\varphi) = I_c \sin \varphi$. For an S/N/S junction, the constant $I_c > 0$, whereas the minimum energy of the junction is achieved at $\varphi = 0$. This is in contrast to an S/F/S Josephson junction, where the equilibrium phase difference in S on the both sides of the junction would be π . For this junction, the constant $I_c > 0$ becomes negative, and transition from the 0 to the π state results in a sign change of the critical current, though the experimentally measured critical current is always positive and equal to $|I_c|$. The non-monotonic behavior of the Josephson critical current I_c as a function of d_F [see Fig. 2.8(b)] or T was detected in S/F/S junctions, where the vanishing of I_c indicates the transition from the 0 to π state.

One can use two approaches to describe the FFLO state, that is, to solve the PE problem for the S/F system. The first approach corresponds to the situation when a very weak ferromagnet with an extremely small exchange interaction ($h_{ex} \approx T_c$) is placed in contact with a superconductor. In this case, the theory based on the introduction of the generalized Ginzburg–Landau functional proposed by de Gennes [126] can be used. The second approach corresponds to the experimental situation when the exchange field of the ferromagnet is much larger than the T_c of a superconductor ($h_{ex} \gg T_c$), and the gradient of the superconducting-order parameter variation is also large. In this case, the microscopic theory should be used [9]. The most convenient treatment is to apply the Bogoliubov–de Gennes equations or the Green’s functions using the quasi-classical Eilenberger [127] or Usadel [128] equations. In principle, the solutions to both cases show that the superconducting-order parameter in presence of the exchange field in the dirty limit ($l_F \ll \xi_F$) is an exponentially-damped, oscillatory function:

$$\psi(x) \approx \psi_0 \exp(-x/\xi_{F1}) \cos(x/\xi_{F2}). \quad (2.26)$$

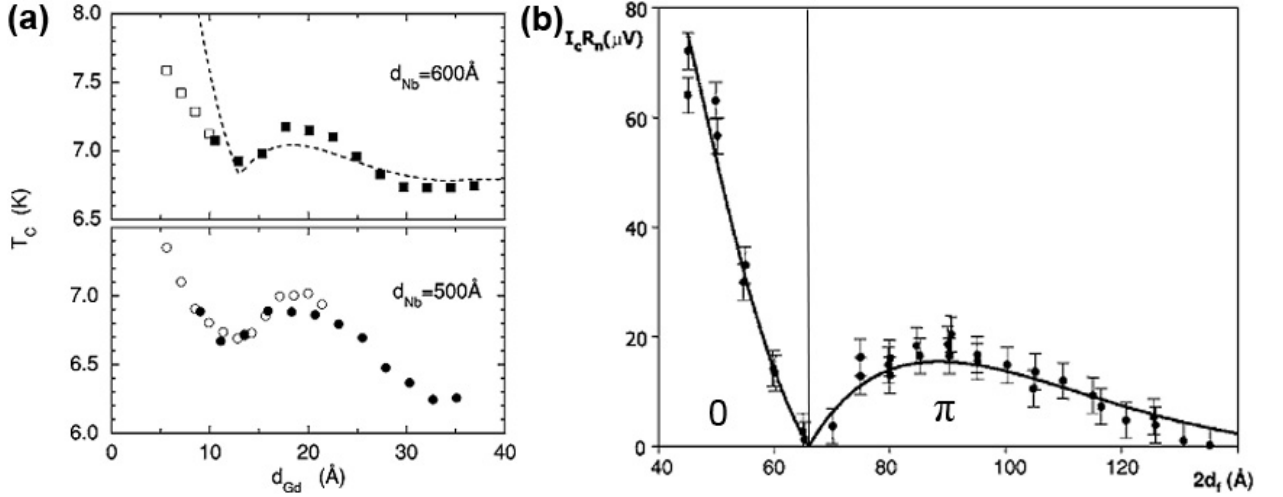


Figure 2.8: (a) Experimental evidence of oscillations of T_c as a function of F (Gd)-layer thickness (d_{Gd}) observed by Jiang *et al.* [120] in S/F (Nb/Gd) multilayers for two different thicknesses of S (Nb): upper graph for $d_{Nb} = 600 \text{ Å}$ and lower graph for $d_{Nb} = 500 \text{ Å}$. The dashed line in the upper graph is a fit to the theory of Radovic *et al.* [124]. (b) Experimental data of the characteristic voltage, given by the product of the S/F/S junction critical current, I_c , and normal state resistance, R_n , versus F (PdNi)-thickness, d_F , measured by Kontos *et al.* [121]. The solid line is a fit to the theory of Buzdin *et al.* [125].

The expression for the proximity length is:

$$\xi_F^{-1} = \xi_{F1}^{-1} + i\xi_{F2}^{-1}, \quad (2.27)$$

where ξ_{F1} is the characteristic correlation decay length, and ξ_{F2} is the characteristic oscillation length of the superconducting-order parameter in F.

In the dirty limit, the scale of ξ_{F1} and ξ_{F2} for “strong” ferromagnets is the same and it is rather short-ranged. It corresponds to:

$$\xi_{F1} = \xi_{F2} = \xi_F = \sqrt{\frac{\hbar D_F}{E_{ex}}} \quad (\text{dirty limit}). \quad (2.28)$$

Here, D_F is the diffusion coefficient in the ferromagnet.

In the case of a “strong” ferromagnet in the clean limit ($l_F \gg \xi_F$), the damped oscillatory behavior of the superconducting-order parameter remains, while the damping is non-exponential and much weaker ($\sim 1/x$) [129]:

$$\psi(x) \approx (1/x) \exp(-x/\xi_{F1}) \sin(x/\xi_{F2}). \quad (2.29)$$

In contrast to the dirty limit, the characteristic correlation decay (ξ_{F1}) and oscillation (ξ_{F2})

lengths are not the same [101] and equal to:

$$\xi_{F1} = \boxed{\frac{v_{Ff}}{2\pi T}}, \quad \xi_{F2} = \boxed{\frac{\hbar v_{Ff}}{E_{ex}}} \quad (\text{clean limit}). \quad (2.30)$$

2.2.4 Proximity effect at the superconductor/ferromagnet (S/F) interface – nonuniform magnetization

In the previous subsection 2.2.3, it was noted that the existing exchange field h_{ex} in F tends to align both spins of a singlet Cooper pair in the same direction, resulting in strong pair-breaking effects. This scenario is valid for large values of h_{ex} , whereas below a certain value of h_{ex} , the singlet Cooper pair can survive in the FFLO state, manifested in the rapid exponential oscillatory decay of the superconducting-order parameter in F over a distance ξ_F . However, under some circumstances, superconductivity is not necessarily suppressed by ferromagnetism: the presence of F may lead to a triplet pairing, which can penetrate F for long distances (even as far as spin-singlet pairs can penetrate N). This case is considered in more detail in this subsection.

It is obvious that if a Cooper pair can be formed of two electrons with equal spins ($\uparrow\uparrow$ or $\downarrow\downarrow$), then it will not be affected by h_{ex} in F. Moreover, the electrons of this resulting Cooper pair with $\uparrow\uparrow$ or $\downarrow\downarrow$ spins can pair with equal and opposite momenta $k_{F\uparrow}$ and $-k_{F\uparrow}$, and this will not lead to a nonzero center-of-mass momentum, as it does in the FFLO state. In this framework, the question arises of how to generate such Cooper pairs with spin equal electrons. The answer was first outlined in the theoretical works by Bergeret *et al.* [12] and Kadigrobov *et al.* [130]. It was shown that a local inhomogeneity of the magnetization in the vicinity of the interface of the S/F structures could lead to a conversion of the “classical” spin-singlet Cooper pairs into a new unconventional state with spin-equal pairing. Moreover, in the same works it was theoretically revealed that in the superconducting PE, the equal-spin correlations can persist in F on a length scale typical for non-magnetic materials, but anomalously large for ferromagnets. Here one remark can be done. Since the electron transport in F usually takes place in the dirty limit, and the pair amplitude must be isotropic in space (unchanged), then it must be *even* under interchange of the spatial coordinates of the Cooper pair electrons. Since a Cooper pair is in the equal-spin triplet state, it must be *even* with respect to interchange the electron spins. Consequently, to obey the Pauli principle, the pair wave-function must be *odd* with respect to interchange the time coordinates of the two electrons, thus providing discussed in subsection 2.2.1 “*odd-frequency*” triplet pairing.

The presence of the magnetic inhomogeneity at the S/F interface (the so-called “spin-

mixer”) is a necessary condition for observation of this type of triplet pairing. The process of singlet-to-triplet conversion can be described by considering the FFLO state, which necessarily involves formation of $\uparrow\downarrow + \downarrow\uparrow$ spin-zero triplet pairs in S. For strongly spin-polarized ferromagnets, a spin-zero triplet amplitude $\uparrow\downarrow + \downarrow\uparrow$ (total spin $S_z = 0$) will be generated in S by the strong interface-spin polarization and it can coexist with the singlet amplitude in S. However, both amplitudes do not survive in F and are damped in an oscillatory fashion over a short length of the order ξ_F . However, if the average interface magnetization is misaligned with the bulk magnetization of F, disordered interface moments can transform $\uparrow\downarrow + \downarrow\uparrow$ ($S_z = 0$) into the $\uparrow\uparrow$ or $\downarrow\downarrow$ ($S_z = \pm 1$) triplet amplitudes in F (depending on the magnetization direction), as is shown in Fig. 2.9. Singlet pairs are rotationally invariant, that is, they are the same regardless of how they are viewed in spin-space (that is, of the quantization direction), and anyway does not survive. In contrast, triplet pairs can exist in three different states and each state can be transformed into one another if one would change the quantization direction. For example, if an interface region between bulk S and F is magnetized in the y -direction, then opposite-spin pairs $(\uparrow\downarrow + \downarrow\uparrow)_y$ with respect to the y -axis will be generated. But they are equivalent to spin-equal triplet pairs $i(\uparrow\uparrow + \downarrow\downarrow)_z$ in F magnetized in the z -direction. This makes the coexistence of superconductivity with ferromagnetism energetically compatible. Bergeret *et al.* [12] have shown that the spin-triplet components with $S_z = \pm 1$ can survive and penetrate F over large distances of the order ξ_N :

$$\xi_F^T \approx \xi_N \approx \sqrt{\frac{\hbar D_F}{2\pi k_B T}}, \quad (2.31)$$

where D_F is the diffusion coefficient in the ferromagnet.

Next, basing on Refs. [12, 13, 41, 101] the generation mechanism of the odd-frequency spin-triplet superconductivity induced by nonuniform magnetization in S/F structures is considered. As it has been already mentioned above, a homogeneous h_{ex} of F can contribute to the formation of the spin-triplet component with the projection $S_z = 0$ of the condensate function. But for the long range proximity effect in S/F structures spin-triplet components with $S_z = \pm 1$ are required. Here, some examples of the S/F structures for which all components of the triplet state can be induced are presented. The common property of these is that the magnetization is nonuniform. First, consider a triple-layer S/F/S structure shown in Fig. 2.10(a). The main feature of this structure is that the magnetizations of two F layers are inclined at the angles $\pm\alpha$ with respect to the z -axis. Each of F layers generates the $S_z = 0$ spin-triplet components in the direction of h_{ex} which will overlap in S. Thus, if the magnetizations of two F are collinear to each other (parallel or antiparallel), the total pro-

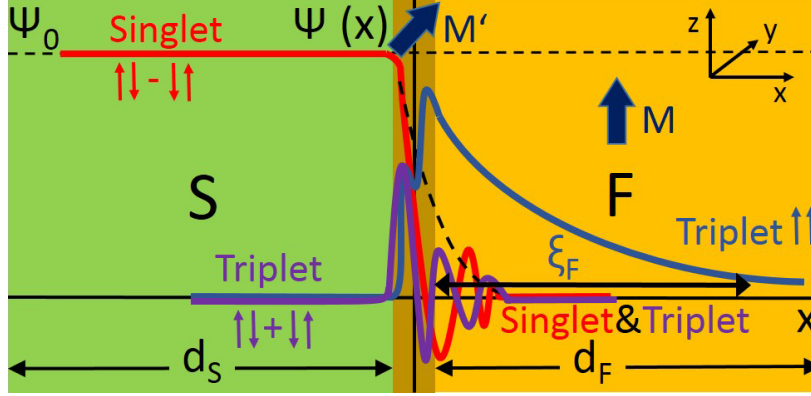


Figure 2.9: Schematic representation of the superconducting-order parameter behavior near the S/F interface where the average interface magnetization is misaligned with the bulk magnetization of F. Singlet (red) and spin-zero triplet ($\uparrow\downarrow + \downarrow\uparrow$) (purple) FFLO amplitudes are damped in an oscillatory fashion over a short distance of the order ξ_F in F and become shorter as the exchange field h_{ex} increases. At the same time, non-zero, spin-triplet amplitudes $\uparrow\uparrow$ or $\downarrow\downarrow$ ($S = \pm 1$) (blue) can be generated at the S/F interface, which can penetrate and survive in F over long distances. The penetration depth is $\xi_F^T \approx \xi_N \approx 1/\sqrt{T}$.

jection remains zero. At the same time, if the magnetizations are not collinear, the $S_z = 0$ components from each F will have non-zero projections onto the other. In S, the superposition of the spin-triplet components from the different F layers should have all possible projections of spin, also $S_z = \pm 1$. Here one remark should be given. The thickness of the S layer should not be larger than the coherence length $\xi_S \approx \sqrt{D_S/\pi T_c}$ in S (D_S – the diffusion coefficient in S) since the triplet component decays in S on the length of the order of ξ_S . But, on the other hand, if the S layer is too thin then the T_c can be suppressed. Thus, by spatial “rotation” of the spin basis by means of layered ferromagnets with respect to that in S the spin-triplet component can be generated which can penetrate into F over long distances.

Above, an example was presented of how long range spin-equal triplet component can be produced in S/F structures under artificial experimental conditions. However, intrinsic properties of ferromagnets such as domain walls can be used as a source of “natural” magnetic inhomogeneities. For example, they can arise near the interface between grain boundaries of polycrystalline ferromagnets [15], or near the interface between S and F in S/F structures [12, 13]. The latter one is considered here in more detail [see Fig. 2.10(c)]. The structure consists of an S/F bilayer with an uniform magnetization in the F-layer. The magnetization vector $\mathbf{M} = M_0(0, \sin \alpha(x), \cos \alpha(x))$ rotates in F layer starting from the S/F interface ($x = 0$), whereas the rotation angle has a piecewise dependence on x : for $0 < x < w$ $\alpha(x) = Qx$ and for $x > w$ $\alpha(x) = Qw$, where Q is the wave vector which describes the spatial structure of the domain wall (the x -axis is perpendicular to the S/F interface). The vector \mathbf{M} is aligned parallel to the z -axis at the S/F interface and rotates by the angle $\alpha(w)$ over the

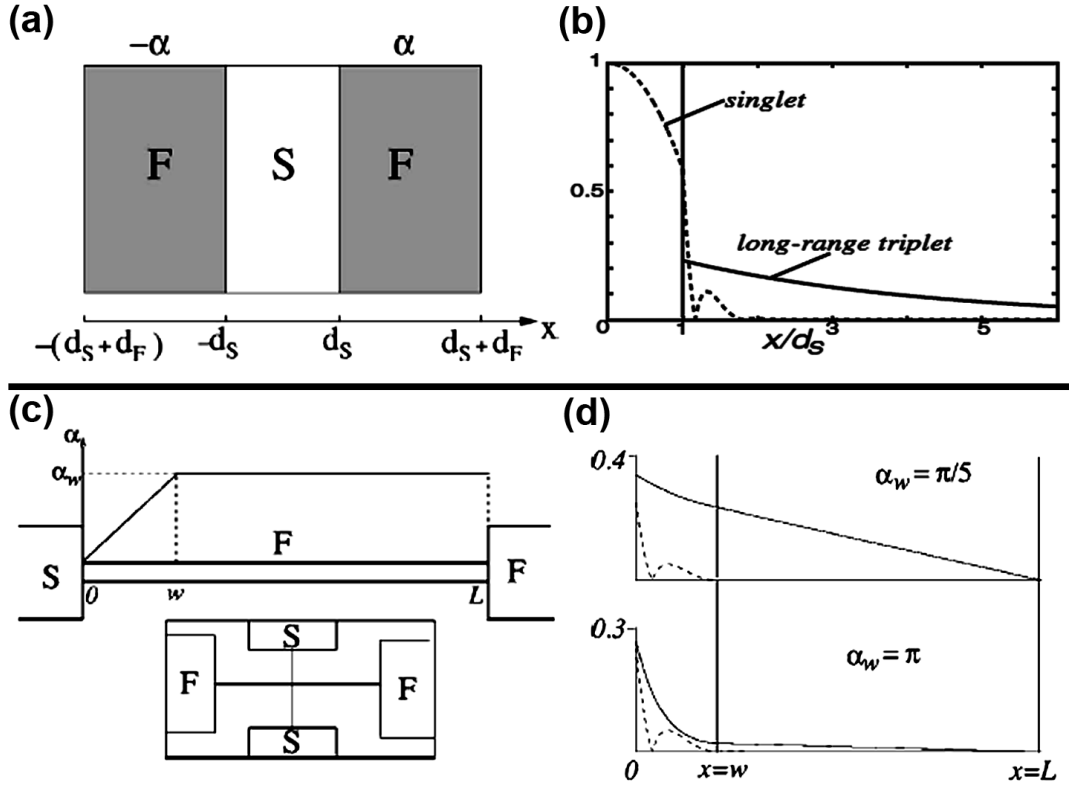


Figure 2.10: (a) Schematic representation of a S/F/S triple layer structure where the magnetizations of the left and right F layers are inclined at the angles $\pm\alpha$ with respect to the z -axis, and (b) corresponding spatial dependence of the spin-singlet (dashed line) and long-range triplet (solid line) components [41]. (c) Schematic representation of an S/F structure with a Bloch-type domain wall, and (d) corresponding spatial dependence of the spin-singlet (dashed line) and long-range triplet (solid line) components of the condensate function for different values of angle α_w [12].

length w . Accordingly, a Bloch-type domain wall can be built. Outside of the domain wall ($w < x < \infty$) the orientation of the magnetization \mathbf{M} is fixed. By application of the Usadel equation (the problem was considered in the dirty limit) it was shown in Ref. [12] that for such kind of structure the equal spins triplet component can be generated in the domain wall which can further penetrate in F over a long distance of the order of ξ_N , whereas the spin singlet component in F is short ranged (of the order of ξ_F) [see Fig. 2.10(d)]. Interestingly, although the amplitudes of both components can be comparable, the penetration length of the triplet component is always larger.

Currently, the quest for experimental evidence of the long-range spin-triplet proximity effect is motivated by the possibility of combining the zero-resistance supercurrents of S with the spin alignment of F, which would have strong implications for spintronics [16, 17, 131]. The theory (briefly described above) has undergone subsequent development during the last decade. For example, it was predicted that the role of potential “spin-mixers” can be played

by the intrinsic properties of F. These can be magnetic domain walls [132, 133], or intrinsic inhomogeneities of rare earth ferromagnets (such as Ho) [12, 134]. Also, “spin-mixers” can be implemented by means of ferromagnetic multilayers [32, 135], or inhomogeneities originating from experimental manipulations, such as the contacting procedures of the samples [13].

So far, the long-range spin-triplet superconducting PE was observed in (multi-) sandwich heterostructures of flat films [18–20], in wedge-shaped layers [21], Josephson junctions [22, 23] and more complex geometries [24–28]. In particular, flat geometries are well-suited for observation of the variation in the critical temperature T_c of S as a function of the thickness of F (as was discussed in the previous subsection 2.2.3). Wedged layers [21, 37] were used for investigations of the spin-valve effect caused by a non-collinear alignment of the magnetization of F layers. Other experiments [14, 38, 39] were carried out in the nanowire-based geometries, where marked drops in the nanowire resistance $R(T)$ were observed at a temperature below the T_c of S. The work of Wang *et al.* [14] appears to be the first report on the long-range PE in ferromagnetic nanowires. In this work, single-crystal, \varnothing 40 nm, Co nanowires were contacted with superconducting, W-based voltage electrodes for 4-probe $R(T)$ measurements, as shown in the inset of Fig. 2.11(a). In this experiment, the nanowire maintained a zero-resistance state over a length of at least 600 nm [see Fig. 2.11(a)]. The role of the “spin-mixers” was assigned to the defects produced in the vicinity to the electrode–nanowire interface due to the application of the focused ion beam-induced deposition of W (W-FIBID) for the preparation of superconducting electrodes, as a result of bombardment with high-energy Ga^+ ions ($E = 30$ keV) and local heating of the nanowire. Nevertheless, this experiment is referred to as a “hard to reproduce” experiment, because singlet–triplet conversion occurs randomly/spontaneously, and the proposed conversion mechanism is uncertain.

On the other hand, the conversion can be controlled, as was demonstrated by Khaire *et al.* [22] by application of sophisticated multilayered structures shown in the inset of Fig. 2.11(b). This structure was made of two weakly spin-polarized ferromagnets X (PdNi or CuNi) to provide singlet–triplet amplitude conversion, and two strongly spin-polarized ferromagnetic layers made of Co to transport the long-range triplet supercurrent between the singlet superconducting Nb electrodes. Here, the controlled misalignment of the magnetization of the X layers with respect to the Co layers plays a crucial role. The dependence of the Josephson supercurrent on the Co layer thickness $I_c(D_{Co})$ is shown in the main panel of Fig. 2.11(b). With increasing thickness of the Co layer, the maximum supercurrent in the junction decays very slowly (red cycles). This is in a sharp contrast to the fast decay of the supercurrent when the X layers are absent (black squares). This finding gives evidence of a reliable way to

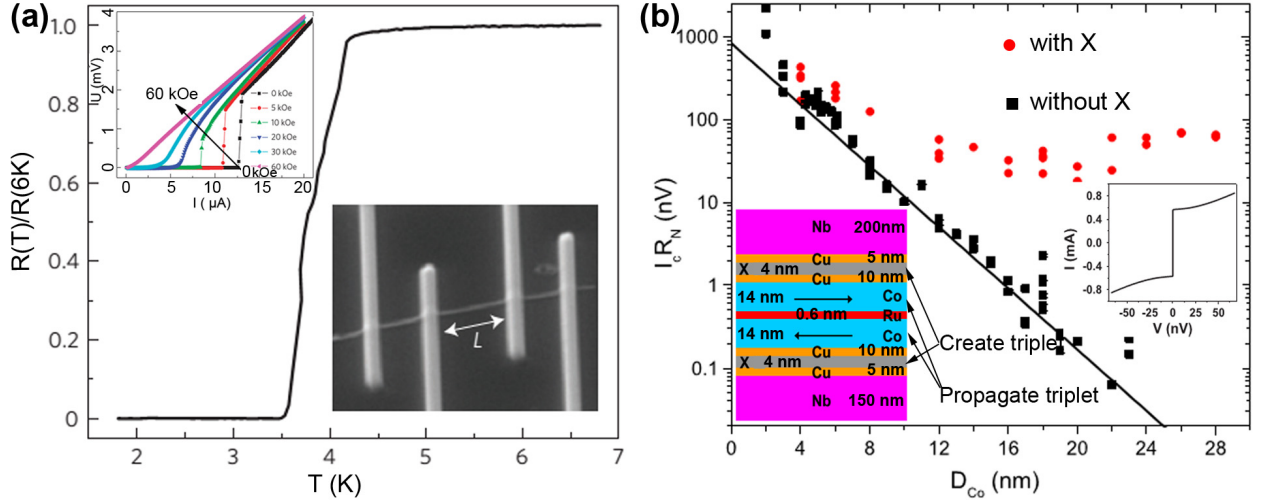


Figure 2.11: (a) Zero-resistance state of single-crystal Co nanowire below 3.5 K contacted with superconducting, W-based electrodes ($T_c \approx 5$ K) [14]. The distance between the inner voltage electrodes was about 600 nm suggesting that the spatial extent of the PE-induced superconductivity in the nanowire is at least 300 nm. Upper-left inset: $V(I)$ curves of the nanowire obtained at different perpendicular magnetic fields at 1.8 K. (b) Product of the critical current times the normal state resistance, $I_c R_N$, as a function of total Co thickness measured over the multilayered junction, shown in the left inset [22]. Here the X layers were made of a weakly spin-polarised ferromagnet, and served as singlet–triplet state converters. The critical current decays slowly over the junction for the X layers (red cycles), whereas it decays very fast without X layers (black squares). $I(V)$ characteristic of the junction at $H = 0$ represented in the right inset.

produce and manipulate long-range spin-triplet supercurrents. In perspective, the approach can be applied to multisegmented, ferromagnetic nanowires for transporting spin-polarised supercurrents over rather long distances. Here, each segment is made of selected materials and serves a particular function.

Interface	Order parameter	Proximity length
S/N	$\psi_N(x) \propto \psi_0 \exp(-\frac{x}{\xi_N})$	$\xi_N = \frac{\hbar v_F}{2\pi k_B T}$ (clean limit) $\xi_N = \sqrt{\frac{\hbar D_N}{2\pi k_B T}}$ (dirty limit)
S/F (uniform magnetization)	$\psi_F(x) \propto \frac{1}{x} \exp(-\frac{x}{\xi_{F1}}) \sin(\frac{x}{\xi_{F2}})$ $\psi_F(x) \propto \psi_0 \exp(-\frac{x}{\xi_{F1}}) \cos(\frac{x}{\xi_{F2}})$	$\xi_{F1} = \frac{\hbar v_F}{2\pi k_B T}$, $\xi_{F2} = \frac{\hbar v_F}{E_{ex}}$ (clean limit) $\xi_{F1} = \xi_{F2} = \xi_F = \sqrt{\frac{\hbar D_F}{E_{ex}}}$ (dirty limit)
S/F (nonuniform magnetization)	$\psi_F^{triplet}(x) \propto \psi_N(x)$ $\psi_F^{singlet}(x) \propto \psi_F(x)$	$\xi_F^{triplet} = \sqrt{\frac{\hbar D_F}{2\pi k_B T}}$ (dirty limit) $\xi_F^{singlet} = \sqrt{\frac{\hbar D_F}{E_{ex}}}$ (dirty limit)

Table 2.1: Summary table of superconducting order parameters and characteristic proximity length scales of S/N and S/F proximity effect.

2.2.5 Andreev reflection as the microscopic mechanism of the superconducting proximity effect

The microscopic characteristic of the superconducting proximity effect was described by Andreev [136] within the framework of the so-called Andreev reflection. It was proposed as a mechanism describing how single-electron states of a normal metal can be converted into Cooper pairs in a superconductor, and explained the transformation of the dissipative electrical current into the dissipationless supercurrent. The Andreev reflection both, for S/N and S/F interfaces, is considered in this subsection.

Before discussing the Andreev reflection phenomenon, a term known as spin polarization must be introduced. It is defined as:

$$P = \frac{N_{\uparrow}(E_F) - N_{\downarrow}(E_F)}{N_{\uparrow}(E_F) + N_{\downarrow}(E_F)}, \quad (2.32)$$

where $N_{\sigma}(E_F)$ is the spin-dependent density of states (DOS) at the Fermi level. For a normal metal $P = 0$, because $N_{\uparrow}(E_F) = N_{\downarrow}(E_F)$. In a ferromagnet, the spin sub-bands are shifted with respect to each other because of the exchange interaction, and $0 \leq P \leq 1$.

In the case of a S/N interface, an incident electron from the N-side with energy below the superconducting gap Δ can penetrate into S only under the condition that it must find the second electron of opposite spin to form a Cooper pair. As result, a hole is formed that moves from the interface towards N (Andreev reflection). The hole and incident electron belong to the opposite spin sub-bands [see Fig. 2.12(a)]. The result of such a double-charge transfer is the appearance of the sub-gap conductance, which is twice the normal state conductance. Detailed theory behind this phenomenon was presented by Blonder, Tinkham, and Klapwijk [137]. In the case of a S/F interface, when complete spin polarization $P = 100\%$ takes place, an incident electron from F with spin up (\uparrow) and energy below the superconducting gap Δ cannot form a Cooper pair because of the lack of states with spin down (\downarrow) in F to provide a second electron for the pair [see Fig. 2.12(b)]. Consequently, Andreev reflection is suppressed. The influence of the spin polarization in a ferromagnet on the sub-gap conductance of the S/F interface was first presented by de Jong and Beenakker [138].

According to de Jong and Beenakker [138], consider a description of the conductance through a ballistic S/F point contact. A ferromagnet is contacted through a small area with a superconductor. Under the conditions when the transverse dimension of the contact area is much smaller than the mean free path and the interface is clean, the conductance is determined only by the scattering process at the S/F interface. Using scattering channels,

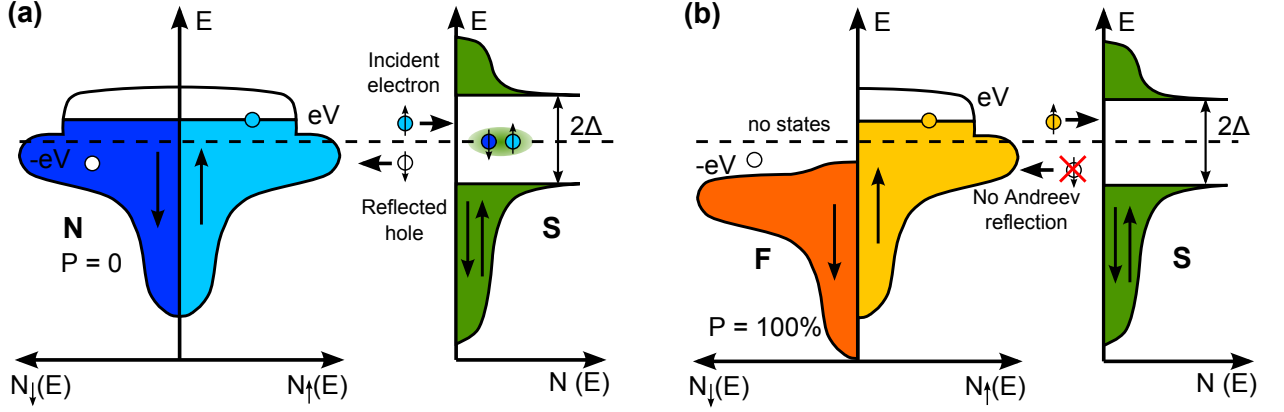


Figure 2.12: Schematic representation of the Andreev reflection in the case of (a) a S/N interface, when the spin polarization $P = 0$, and (b) a S/F interface, when the spin polarization $P = 100\%$, and reflection is not possible.

which are sub-bands that cross a Fermi level, the ballistic conductance at $T = 0$ of the normal metal/ferromagnet (N/F) interface is given by the Landauer formula [139]:

$$G_{NF} = \frac{e^2}{h} N, \quad (2.33)$$

where $N = N_{\uparrow} + N_{\downarrow}$ is the total number of scattering channels of spin-up (N_{\uparrow}) and spin-down (N_{\downarrow}) channels, and spin polarization gives $N_{\uparrow} > N_{\downarrow}$.

In the case, when a superconductor is placed in contact with a non-polarized metal (S/N interface), all electrons are Andreev-reflected as holes. This gives a double contribution to the number of scattering channels and the conductance itself, since for each Andreev reflection $2e$ are transferred. For the spin-polarized metal where $N_{\uparrow} > N_{\downarrow}$, all spin spin-down electrons are reflected as spin-up holes. However, only a fraction $N_{\uparrow}/N_{\downarrow} < 1$ of the spin-up (N_{\uparrow}) channels can be Andreev-reflected, because the DOS in the spin-down sub-band is smaller than the DOS in the spin-up sub-band, whereas in the spin-down (N_{\downarrow}) channels, all electrons will be Andreev-reflected. Thus, the resulting sub-gap conductance of the S/F contact is given as:

$$G_{SF} = \frac{e^2}{h} (2N_{\downarrow} + 2N_{\uparrow} \frac{N_{\downarrow}}{N_{\uparrow}}) = 4 \frac{e^2}{h} N_{\downarrow}. \quad (2.34)$$

By comparing Eqs. (2.33) and (2.34), one can see that G_{SF} can be either larger or smaller than G_{NF} , depending on the $N_{\downarrow}/N_{\uparrow}$ ratio.

This Andreev reflection approach at the S/F interface was successfully applied by Soulen *et al.* [140] to analyse the spin polarization of different metals by means of a superconducting point contact. For example, it was shown that for Co $P = 42\%$, while for CrO_2 $P = 90\%$. Today, Andreev point contact spectroscopy in comparison to spin-polarized electron

tunnelling spectroscopy [141] gives the possibility of measuring the spin polarization in a much broader range of metals.

Chapter 3

Methods and techniques

Before presenting the main results of this work, it is necessary to provide a description of how these results were experimentally obtained. Therefore, this chapter introduces and defines the parameters used for the fabrication and characterization of the samples. The chapter begins with an extensive description of the various sample fabrication techniques. It is followed by a section describing the main methods used for structural characterization of the samples. In the last section, in situ and low-temperature techniques used to perform electrical transport and magnetotransport measurements are discussed.

3.1 Fabrication of samples and auxiliary electrodes

The techniques used for the fabrication of the nanowires for the study of the superconducting proximity effect are introduced in this section. Namely, these techniques are (i) electrochemical deposition (ECD) in heavy-ion-track etched polycarbonate templates for fabrication of crystalline Cu and Co nanowires, (ii) DC Magnetron sputtering in conjunction with electron beam lithography for fabrication of crystalline Au nanowires, and (iii) focused electron beam induced deposition (FEBID) for fabrication of nanogranular, Co-based nanowires, Pb-based superconducting nanowires and electrodes and Co/Pt heterostructures. In addition, focused ion beam induced deposition (FIBID) of Pt- and W-based structures used for contacting the nanowires for electrical transport measurements and fabrication of the superconducting floating electrodes, respectively, is presented.

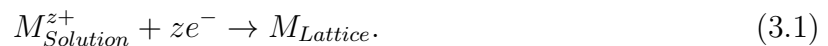
3.1.1 Electrochemical deposition (ECD) of crystalline Cu and Co nanowires

The preparation of crystalline Cu and Co nanowires was performed in collaboration with Cornelia Neetzel from the Materials Analysis group of Prof. Dr. W. Ensinger at the Department of Materials Science of TU Darmstadt within the framework of the collaboration

project NanoBiC.

The nanowires were grown by ECD in heavy-ion-track etched polycarbonate (PC) templates [43, 44, 48, 142]. In general, this is a well-known technique and belongs to the category of bottom-up deposition processes. In this technique, structural growth arises from an electrically conductive film deposited on one side of the template allowing the nanowires to grow through the insulating pores to the other side. Currently, it is one of the most widely used techniques for obtaining one-dimensional nanostructures with precisely controllable geometrical (transversal and longitudinal) and compositional properties. They can be prepared as either solid cylinders with controllable length and diameter [143, 144], multilayered cylinders with layers of variable composition and thickness [145], or hollow nanotubes of controllable diameter and wall thickness [146–148].

The ECD of metals and alloys involves the reduction of metal ions from aqueous, organic or fused-salt electrolytes [149]. In this work, deposition was performed only with aqueous solutions. The reduction of metal ions M^{z+} in aqueous solution is represented by:



This can be experimentally accomplished by means of an electrodeposition process in which z electrons (e^{-}) are provided by an external power supply. The deposition reaction represented by Eq. (3.1) is a reaction of charged particles at the interface between a solid metal electrode and a liquid solution. The two types of charged particles, metal ions and electrons, can cross the interface.

The complete ECD process for the fabrication of nanowires in heavy-ion-track etched PC templates is a many-step procedure. It includes (i) irradiation of the PC membranes with heavy ions to form latent tracks, (ii) etching of the irradiated membranes to obtain pores of desired form and size to be used as subsequent templates for nanowire deposition, (iii) ECD of the actual nanowires, and (iv) decomposition of PC template resulting in individual nanowires for further applications. In the following subsections, details of each of these steps are briefly given.

Irradiation

The ECD of nanowires was performed in heavy-ion-track etched polycarbonate membranes irradiated at the linear accelerator facility (UNILAC) at Helmholtzzentrum für Schwerionenforschung (GSI) in Darmstadt. Heavy ions, for example, ^{238}U , ^{197}Au or ^{206}Pb , can be accelerated along the 120 m linear track to a specific energy of up to 11.4 MeV/nucleon.

The heavy ions collide with the PC membrane of thickness between 30 μm and 120 μm , penetrating it completely, and leaving behind latent damage tracks with a diameter typically of several nanometers. During the irradiation process, the majority of the delivered energy is absorbed by the PC membrane. Each individual ion induces excitation and stimulates the ionization process during the penetration step. Consequently, fragmentation and radical reactions take place, causing formation of hydroxyl and alkyne groups. Through specific adjustments of the ion beam parameters, in particular the beam current, the fluence can be varied to a great extent ranging from one individual ion track to an ion track density of 10^{10} cm^{-2} . The tracks are typically parallel to one another and stochastically distributed. The templates for nanowire deposition used in this work typically had a thickness of 30 – 60 μm and a fluence of 10^7 - 10^8 ions/ cm^{-2} was used.

The PC templates used in this work exhibit high chemical stability against acids and neutral aqueous solutions, whereas they can be slowly decomposed in strong alkaline solutions. In organic solutions, such as dichloromethane (DCM), the templates will be quickly decomposed. The PC templates used in this work were purchased from Bayer Material Science (Makrolon $\text{\textcircled{R}}$). This thermoplastic polymer is stable up to temperature of 130 $^{\circ}\text{C}$ and has insulating electrical properties. Furthermore, the handling of this material is straightforward due to its excellent elasticity.

Etching

The ion tracks formed during the irradiation process cannot be directly used for the deposition of nanowires for two reasons. First, remnants of the PC fragments remain inside the tracks and must be removed. Second, the unetched tracks do not have the ideal cylindrical form and their diameters, which will eventually determine the diameter of the nanowires, are too small for handling and application in experiments. Therefore, the ion tracks formed after the irradiation step should be transformed to nanopores by application of a special etching process. The etching process is dependent on the following reaction parameters:

- Concentration of etching solution,
- Temperature,
- Use of etching supplements and their concentration,
- Etching time.

From the combination and variation of all of these parameters, various geometries such as cylindrical, conical and bi-conical pores can be obtained. Since this work was focused

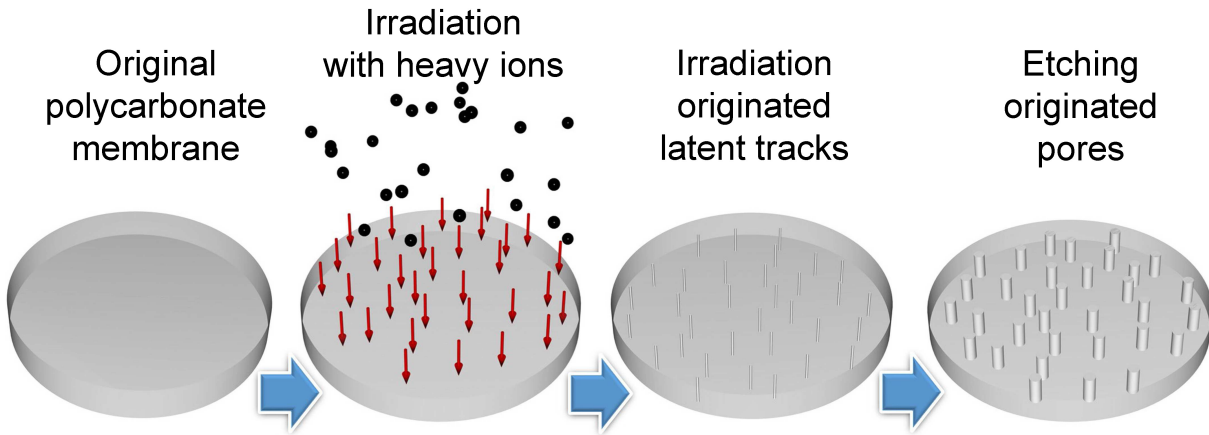


Figure 3.1: Schematic diagram of the irradiation and subsequent chemical etching process of polycarbonate membranes.

on the fabrication of cylindrical nanowires, only the cylindrical nanopore geometry was considered. For the production of cylindrical pores, the as-irradiated PC templates were mounted into a specially constructed teflon holder and immersed in 6M sodium hydroxide at a constant bath temperature of 50 °C under continuous stirring. The resulting diameter of the pores was varied between 35 – 350 nm, according to a previously determined etching rate of 35 nm/min [46]. Using this template-assisted, ECD method, nanowires with a diameter as small as 30 nm can be grown. After the etching process, the template is removed from the etching solution, cleaned with Milli-Q water and finally air dried. The schematic diagram of the irradiation and subsequent etching process is presented in Fig. 3.1.

The etching consists of two kinetic processes which simultaneously take place. The etching rate of the irradiated track areas, r_{track} , is higher than the non-irradiated remainder of the polycarbonate membrane, $r_{membrane}$. Thus two different etching rates arise, the relation of which determines the geometry of the pores. The etching process occurring along the ion track in a PC membrane is represented in Fig. 3.2. The opening angle of the pore is given by Eq. (3.2) [142, 150, 151]. It is evident that angle α in Eq. (3.2) decreases when $r_{track} > r_{membrane}$. Under these conditions, the preferred, almost cylindrical pore geometry can be obtained if the etching process takes place uniformly and simultaneously from both sides of the foil, where the desired diameter of these pores depends only on the etching time.

$$\alpha = \arcsin \left(\frac{r_{membrane}}{r_{track}} \right). \quad (3.2)$$

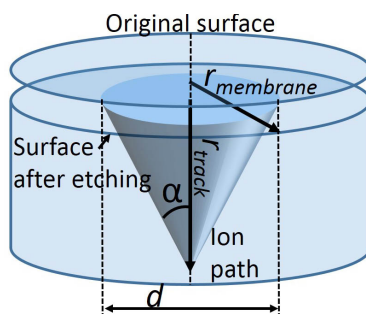


Figure 3.2: Schematic representation of the etching process in a PC membrane.

Electrochemical deposition

The PC template can be used for the ECD of nanowires only after irradiation and etching. Before the deposition process, one side of the template is usually covered with a 50 nm thick Au film, which serves as a cathode during the subsequent potentiostatic deposition of nanowires. For this purpose a Q300T dual target sputtering system was used with the following sputtering parameters: $I = 40$ mA, working distance $l = 7.5$ cm, deposition time $t = 6$ min.

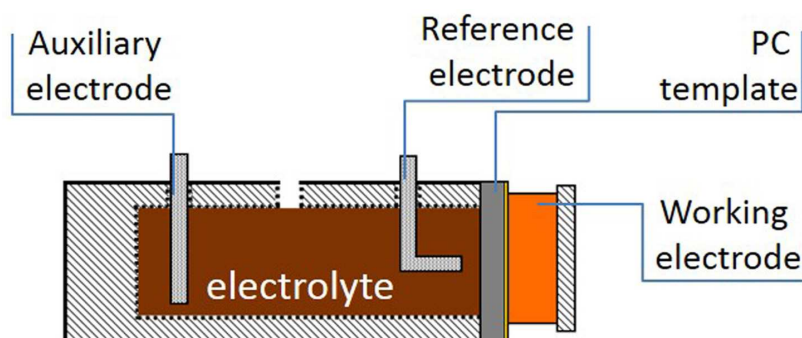


Figure 3.3: Schematic representation of the setup used for the electrochemical deposition of Cu and Co nanowires in ion-track etched polycarbonate templates by using three electrodes (auxiliary, reference, and working electrode).

For the next step, the template was mounted in the custom built electrochemical cell with a three-electrode assembly using Ag/AgCl as a reference electrode and a glassy carbon wire as an auxiliary electrode (see Fig. 3.3). The sputtered Au film is placed in contact with a Cu working electrode. For the ECD process, the electrochemical cell is filled with the correspondingly chosen electrolyte and an appropriate deposition potential is applied. The nanowires are grown from the bottom side (sputtered Au film) to the top side of the template at a temperature which is favorable for each respective material. The electrochemical deposition was performed and controlled with the aid of a commercially available potentiostat (Solartron Analytical ModuLab System). Details of the setup can be found in [43, 44].

The whole deposition process is controlled by chronoamperometric monitoring during the potentiostatic growth of the nanowires. Fig. 3.4 illustrates a typical current versus time curve $I(t)$ of the ECD process. The initial high current density decreases after several seconds to an almost constant, low value (section A of the curve). This is attributed to the formation of the diffusion layer and marks the beginning of the deposition. Section B corresponds to the direct homogeneous growth of the nanowires inside the pores of the template with nearly constant current. The end of the deposition process corresponds to an increase of the current density indicated by section C. Here the nanowires have reached the top side of the template and the first caps have begun to grow on the top of the nanowires. If the process were not terminated at this point, the growth of the caps on the top of the nanowires would continue, and eventually a continuous layer would be formed over the whole top side of the template (section D). Controlling the $I(t)$ curve during the growth stage allows the deposition to be stopped after a given time to obtain nanowires of a desired length.

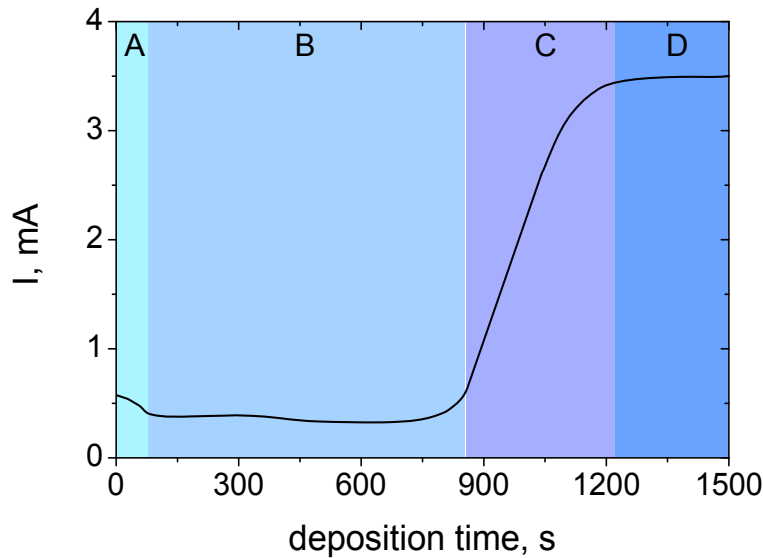


Figure 3.4: Typical $I(t)$ curve of four different nanowire deposition regimes in ion-track etched polycarbonate templates. In section A the nanowire deposition process begins. Section B corresponds to the actual continuous growth of the nanowires inside the pores of the template with almost constant current density. In section C, the nanowires reach the top side of the template, and the first caps are formed on the top of the nanowires. This corresponds to the increase in the current caused by the increased surface. In section D, the caps grow further and eventually form a continuous layer. The diagram is reproduced after [48].

The integral of the $I(t)$ curve on the segment between the beginning of the deposition and the transition to section C corresponds to the total charge Q_{exp} applied during the deposition process. In the case of complete pore filling, an estimated total charge Q_{theo} can

be calculated by Faraday's law:

$$Q_{theo} = \frac{z \cdot F \cdot m}{M}, \quad (3.3)$$

where z is the number of electrons transferred per ion during the reaction, F is the Faraday constant, m is the total mass and M is the molar mass of the deposited material. Thus, the ratio Q_{exp}/Q_{theo} may serve as an indicator of the deposition process efficiency, or the homogeneity of the nanowire growth within the pores over the whole template. When $Q_{exp} < Q_{theo}$, this suggests that the deposition did not take place in all of the pores simultaneously and the density of the full-grown nanowires is lower than that of the pores.

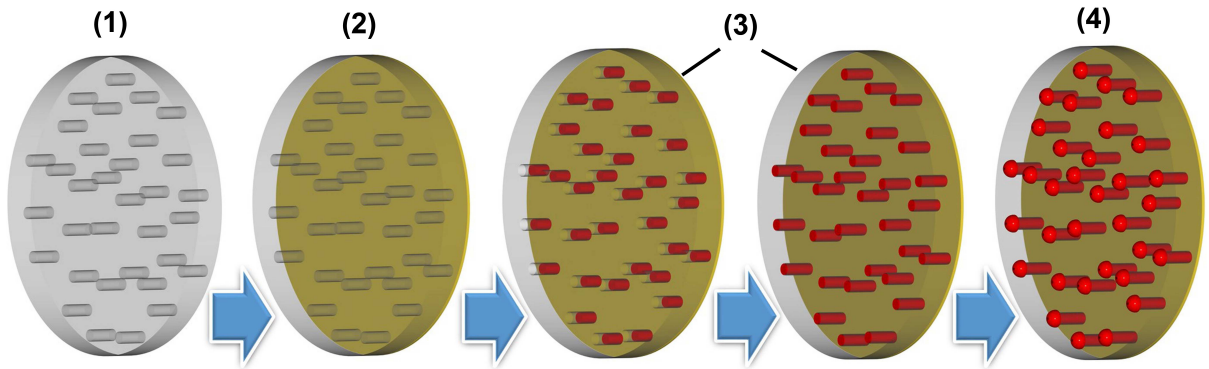


Figure 3.5: Schematic representation of the ECD process used to form nanowires in ion-track etched polycarbonate templates (left to right). After irradiation, the ion tracks of the PC membrane are etched (1) to obtain pores of a desired diameter, used for deposition of the nanowires. After the etching step, a thin Au film is sputter-deposited onto one side of the template (2), which serves as a cathode. Next, the deposition process (3) takes place within the pores, and is controlled by chronoamperometric monitoring [$I(t)$ curve] and is terminated as soon as caps begin to grow (4) on the top of the nanowires. When the deposition is complete, the PC template (containing the embedded nanowires) is dissolved in DCM effectively freeing individual nanowires.

The schematic representation of the ECD process used to form nanowires in heavy-ion-track etched polycarbonate templates is shown in Fig. 3.5. Employing this method, crystalline Cu and Co nanowires were synthesized. For both types of nanowires, the resulting diameter was approximately 300 nm with a length between 30 – 60 μm .

The growth of Cu nanowires was performed in an aqueous electrolyte solution of the following composition:

- $c(\text{CuSO}_4 \cdot 7\text{H}_2\text{O}) = 210 \text{ g/L}$
- $c(\text{H}_2\text{SO}_4) = 2.1 \text{ mL/L}$

A high concentration of CuSO_4 provides a sufficiently high supply of ions inside the pores during the deposition. Addition of sulfuric acid increases the conductivity of the solution and lowers the cathode overvoltage. The temperature of the deposition process was held at a constant value of $50\text{ }^\circ\text{C}$ set by a heating plate. The deposition was performed at a constant potential of 110 mV , and the $I(t)$ curve was monitored to control the progressive growth of the nanowires within the pores.

The deposition of Co nanowires was carried out using a pulsed deposition method with a $5\text{ s on}/5\text{ s off}$ time, at -1.1 V versus Ag/AgCl electrode. The deposition was performed in aqueous electrolyte with the following composition:

- $c(\text{CoSO}_4 \cdot 7\text{H}_2\text{O}) = 350\text{ g/L}$
- $c(\text{H}_3\text{BO}_3) = 40\text{ g/L}$

In the last step, the PC template is dissolved in dichloromethane (CH_2Cl_2 , DCM). The result is a colloidal solution with a large number of free-floating nanowires. A small drop of the DCM solution containing the dispersed nanowires is placed onto an insulating substrate and once dried, the substrate containing many individual nanowires can be used for further application. In Fig. 3.6 SEM micrographs of single Cu and Co nanowires "released" from the PC template are presented.

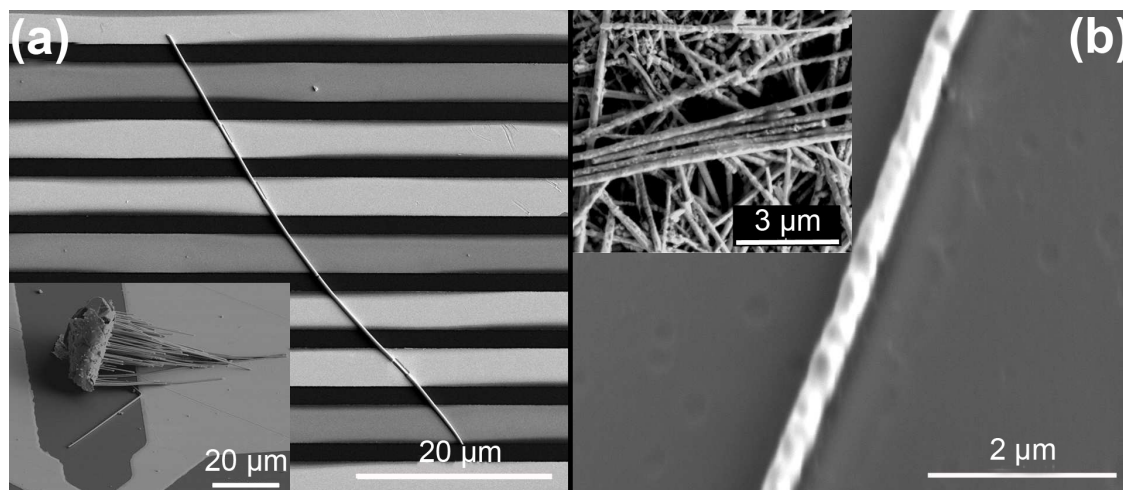


Figure 3.6: SEM micrographs of the crystalline Cu (a) and Co (b) nanowires prepared by ECD used in this work. Nanowires with lengths of approximately $50\text{ }\mu\text{m}$ and diameters of approximately 300 nm resulted. For the Co nanowires, one can distinguish individual crystallites with a size of $200 - 400\text{ nm}$. Inset of (a): cluster of Cu nanowires attached to the Au film. Inset of (b): A cluster of Co nanowires formed due to the magnetic attraction between the nanowires.

Notably, the nanowires prepared by ECD in this work were of extraordinarily high mechanical stability. The PC template dissolution procedure in DCM is sometimes accompanied

by application of few-second pulses from an ultrasound bath in order to detach the nanowires from the starting Au film. This allows for transfer of the nanowires to the substrate but may lead to strong mechanical stresses. Considering the average length of the intact nanowire, only seldom broken nanowires fragments were found. The nanowires were often found bent along the wire axis, suggesting that the nanowires have a very high plasticity.

3.1.2 Pre-forming of contact pads and nanowires by lithography in conjunction with lift-off

The preparation of Au/Cr contact pads and Au nanowires by lithography in conjunction with lift-off on 3 different types of substrates is described in this subsection. The substrates were *p*-doped Si(100)/SiO₂(285 nm) for operation with individual Cu and Co nanowires (see chapters 4, 5), Si/SiO₂(10 nm)/Si₃N₄(100 nm) for FEBID of Co and Pb nanowires and fabrication of Au nanowires (see chapters 5, 7), and *c*-cut (0001) Al₂O₃ for FEBID of Co/Pt multilayered heterostructures (see chapter 6). All of the substrates are commercially available (CrysTec GmbH) and their working surfaces were epitaxially polished by the supplier. The as-supplied substrates were cut from wafers of 10 × 10 mm² with a thickness of approximately 450 μm.

Cr/Au contact pads with a thickness of 3/50-100 nm were prepared by ultraviolet (UV) lithography in conjunction with lift-off, whereas electron beam lithography (EBL) in conjunction with lift-off was used for the preparation of rectangular-shaped Au nanowires with a thickness of approximately 60 nm.

UV lithography in conjunction with lift-off

Lift-off is a commonly used technique for the structuring of thin films deposited by various techniques. First, a pattern with a specific design is defined on a pristine substrate using a UV-light-sensitive material (photoresist) via photolithography. This results in selective covering of the substrate with the photoresist. Then, a thin film is deposited over the entire substrate, covering both the photoresist and the resist-free areas of the substrate. During the actual lift-off step, the photoresist under the film is dissolved and removed with a special solvent, thus partially lifting the film away from the substrate, whereas the rest of the film deposited directly on the substrate remains intact. The lift-off process used in this work consists of 9 steps, as described in detail next.

- [1] *Surface preparation.* Firstly, the as-supplied substrates are covered with wax to protect them during transportation and storage. This protective layer must be removed before

use. Secondly, because of the sensitivity of the lift-off process, care must be taken when preparing the substrate surfaces. Typical surface contaminants such as dust, and organic and inorganic residues must be removed. The surface is then prepared for the resist adhesion and subsequent deposition of a film. The exact cleaning procedure may vary among different laboratories, but what is important is that this is carried out in a reproducible manner. For the substrates used in this work, a consistent cleaning procedure in acetone (10 min), bi-distilled deionized water (5 min), and isopropyl alcohol (5 min) accompanied by ultrasound was employed.

- [2] *Resist coating.* The cleaned substrate surface should then be covered with a UV photoresist. This was realized by a method known as spin coating. The surface, coated with several drops of the photoresist, is rapidly spun, resulting in uniform spreading, where the excess is spun off. In this work, an image reversal, UV photoresist AR-4040 (ALLRESIST GmbH) was used. The parameters for the spin coating were: 3 s duration, 2000 rotations per minute (rpm), followed by 57 s at 6000 rpm. This results in a photoresist thickness of $\approx 1.2 \mu\text{m}$. In general, an image reversal photoresist is the best choice for the lift-off process. It attains a reproducible undercut, which helps to prevent the photoresist sidewalls from being covered with further deposited material and makes the subsequent lift-off step easier.
- [3] *Pre-bake.* The pre-bake procedure is required to evaporate the excess solvent and to harden the photoresist. For this purpose, the coated substrate was placed on a hotplate heated to 85°C for 2 min.
- [4] *Photomask alignment and exposure.* A photomask is used as a tool which uses light to transfer a desired pattern onto the surface of a substrate. It creates a shadow causing photomask-patterned regions where no light reaches the substrate. In the lift-off process, the unexposed areas correspond to the available region where the desired material is deposited. The photoresist is covered with a photomask and subjected to UV light. During the exposure, the photomask should be properly aligned and placed in contact with the substrate surface. In this work, the exposed UV dose was $60 \text{ mJ}/\text{cm}^2$ [see Fig. 3.7(4)].
- [5] *Post-bake.* A post-bake, or image reversal bake, is required to convert the exposed photoresist areas and make them insoluble in the developer, while the unexposed areas remain unmodified (in preparation for the next step). The post-bake parameters, specifically the baking temperature and time, define the photoresist profile. For ex-

ample, a low bake temperature will convert only the strongly exposed photoresist, resulting in a pronounced undercut. In contrast, a high temperature bake will convert the weakly exposed photoresist in addition, making the undercut less pronounced, however, this results in a photoresist profile which is more steep. The optimal post-bake temperature for photoresist AR-4040 was found to be 115 °C, applied for 5 min [see Fig. 3.7(5)].

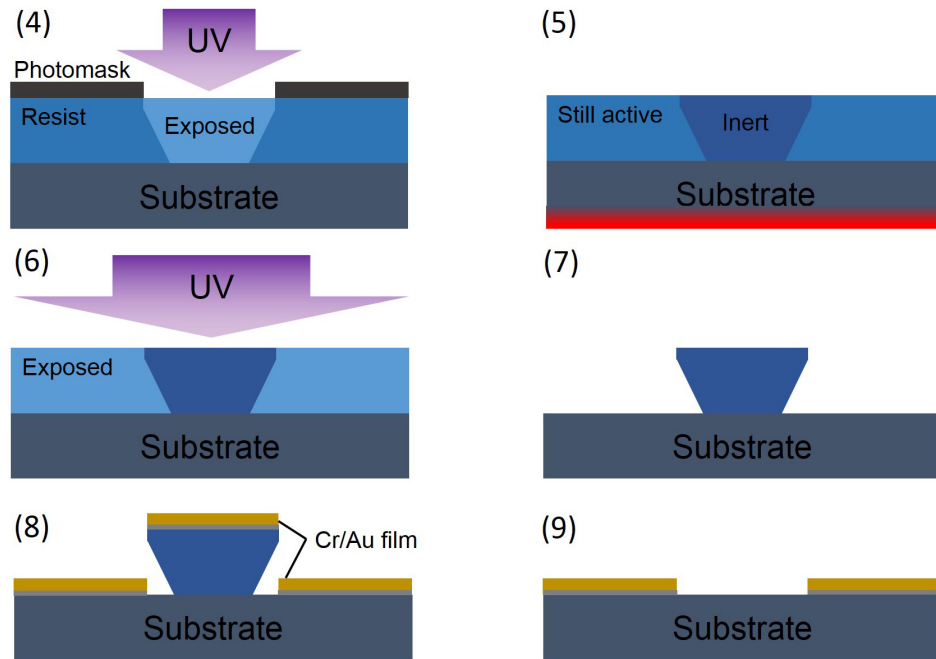


Figure 3.7: (4) Exposure of the photoresist region which will remain on the substrate. (5) Image reversal bake required to make the exposed photoresist insoluble in the developer. (6) Flood exposure required to develop the unexposed photoresist. (7) Development of the photoresist resulting in the desired pattern with a typical undercut. (8) Sputter deposition of a thin film of a selected material. One part of the material is sputtered above the photoresist, while another part directly on the substrate surface. (9) Removal of the photoresist rests. The material above the photoresist will be lifted-off, while the rest will remain in place, resulting in the desired pattern.

[6] *Flood exposure without photomask.* In this step, the entire photoresist film is exposed without a photomask. This is required in order to make the photoresist areas up to now unexposed developable in the next step. Although there is no UV dose limitation for this exposure step, it should be high enough to completely expose the entire thickness of the photoresist all the way through to the substrate. The flood exposure dose used in this work was 3 times higher than that used for the first irradiation step with a photomask (180 mJ/cm²) [see Fig. 3.7(6)].

[7] *Development.* During the development process, special chemicals are applied to the

photoresist. The photoresist areas subjected to the highest UV dose undergo polymerization, resulting in chemical insensitivity to the developer. In contrast, non-polymerized areas of the photoresist will be decomposed by the developer, resulting in selective removal of the photoresist in the areas where the contact pads will be deposited. The development rate depends on the post-bake parameters, whereas the development time determines the undercut profile. In this work, a solution of the developer AR-300 – 35 (ALLRESIST GmbH) mixed 1:1 with bi-distilled, deionized water was used for the development process for approximately 60 s. The development process was then stopped with pure, bi-distilled water [see Fig. 3.7(7)].

[8] *Material sputter deposition.* In this step, the sputter deposition of a thin film of a selected material will be performed over the whole substrate surface. Here, one part of the sputtered material will cover the patterns which were revealed on the substrate after the previous development step, while another part will be deposited on the raised area above the photoresist. [see Fig. 3.7(8)].

[9] *Removal.* After the sputtering of the thin film, the next step involves the removal of the remaining layer of the developed photoresist using a chemical solvent. The film is thin enough to allow the solvent/remover to seep underneath the film and dissolve the photoresist. The material above the photoresist will be removed (lifted-off), while the rest of the sputtered material which is directly on the substrate remains in place. The solvent/remover used in this work was AR-300 – 70 (ALLRESIST GmbH) applied for typically 1.5 hours at 60 °C. Additionally, ultrasound was applied to the substrate for 3 – 5 min to remove the lifted-off material [see Fig. 3.7(9)].

E-beam lithography in conjunction with lift-off

For the preparation of the fine Au nanowires used in this work, electron beam lithography (EBL) was used in conjunction with lift-off. UV lithography used for the preparation of the Cr/Au contact pads is only applicable down to minimal feature size of about 0.7 μm under optimal processing conditions. However, the desired dimensions of the Au nanowires was 200 nm or less. For this reason, EBL was chosen over standard UV lithography. In contrast to UV lithography, in EBL, the chemical modification of the polymer resist is caused by electron irradiation.

The principle of EBL in conjunction with lift-off is very similar to the conventional lift-off process based on UV lithography. Therefore, in this subsection the basic steps are only

roughly described, but with a focus on the main distinguishing points. A schematic representation of the EBL process is shown in Fig. 3.8. A pre-cleaned substrate is first spin-coated with the electron-beam (e-beam) resist, which is sensitive to exposure by electrons. The e-beam resist used in this work was the positive working copolymer, AR-617.03 (ALLRESIST GmbH). Patterns with a pronounced undercut are possible by using this resist as a two-layer system, which is advantageous for lift-off. The sensitivity of the resist increases with an increase of the soft-bake temperature. Thus, a resist treated at 200 °C is approximately 20% more sensitive as compared to resist treated at 180 °C. Therefore, a first, bottom resist layer was tempered at 200 °C. Then, a second spin-coating step was applied wherein the resist was treated at 180 °C. The parameters for the spin coating used for application of the e-beam resist on the substrate were 3 s at 1000 rpm followed by 57 s at 6000 rpm, resulting in a photoresist thickness of approximately 90 nm.

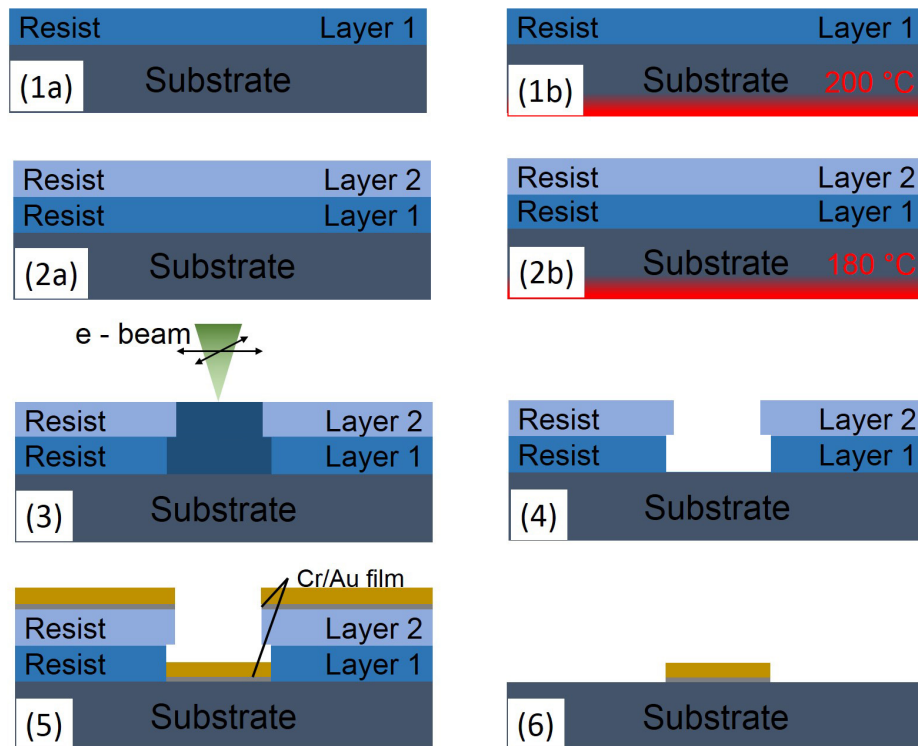


Figure 3.8: (1a) Coating of the substrate with a first layer of the e-beam resist and (1b) subsequent soft baking. (2a) Coating of the substrate with a second layer of the e-beam resist and (2b) subsequent soft baking. Strong undercut patterns are possible by using the e-beam resist as a two-layered system. (3) Electron beam exposure required to render the exposed e-beam resist developable. (4) Development of the e-beam resist resulting in the desired pattern with a typical lateral undercut. (5) Sputter deposition of a thin film of a selected material. One part of the material is sputtered on the raised area above the e-beam resist, while another part is sputtered directly on the substrate surface. (6) Removal of the e-beam resist rests. The material above the resist will be lifted-off, while the rest remains in place, forming the desired pattern of deposited material.

The next step was the exposure of the e-beam resist to electrons. For this, the substrates coated with the resist were mounted in a scanning electron microscope (SEM) (FEI, Nova NanoLab 600, for details see subsection 3.2.3). The exposure was performed by scanning in raster mode by means of a focused beam of electrons across a predefined pattern. The pattern was manually set via the SEM software or a bitmap image file. The e-beam resist is comprised of macromolecules that are modified upon exposure to high energy electrons, resulting in a changed sensitivity of the irradiated areas during the subsequent development step. In contrast to photolithography (where a large area of the substrate is simultaneously exposed), in EBL, localized exposure is possible, whereby the minimum exposure area is determined by the e-beam diameter (≥ 0.1 nm here). In this work, the EBL e-beam parameters were 20 kV/60 pA, the pitch was 30 nm, the dwell time was 5 μ s and the process pressure was 3.5×10^{-6} mbar. The exposure dose can be adjusted accordingly, which is of major importance for the two-layer systems employed in this work. The total exposure dose was controlled by the number of e-beam scans/passes across a selected pattern. After accurate calibration of the exposure dose on a series of test samples, the optimal number of passes was found to be 7 for the nanowire fabrication and 2 for the auxiliary contacts in the vicinity of the nanowire (for details see chapter 7).

After exposure, the exposed regions corresponding to those where the e-beam resist becomes soluble will be developed by means of special chemicals (developer + terminator). Due to differentiation processes, the bottom layer is attacked faster by the chemicals, and structures with a pronounced undercut can be obtained. Both layers are developed in one step by immersing the substrate in the developer, AR-600 – 56 (ALLRESIST GmbH), mixed at a ratio of 9 : 1 with the terminating solution, AR-600 – 60 (ALLRESIST GmbH), for approximately 60 s. The development process was then terminated by exposure of the substrate in the pure terminator solution, AR-600 – 60, for approximately 20 s, followed by rinsing with bi-distilled, deionized water. The resulting patterned e-beam resist serves as a shadow mask for the subsequent sputter deposition of the selected material. Finally, by means of lift-off, the material above the resist will be removed, while the rest remains intact, forming final desired structures.

3.1.3 DC magnetron sputtering of Cr/Au contacts and Au nanowires

For the deposition of thin films (from which Cr/Au contact pads and Au nanowires were subsequently fabricated) DC magnetron sputtering was used. This method belongs to the category of physical vapor deposition (PVD) processes and is often used for the deposition

of thin films onto various surfaces, for example, the semiconducting or insulating substrates in this work. In this technique, the atoms of a desired material can be ejected from the solid target and condensed onto surfaces [152–154].

In the basic sputtering process, the target (cathode) (the source of the material to be deposited) is bombarded with energetic ions, typically inert gas ions such as argon [see Fig. 3.9(a)]. By applying a DC voltage between the target and the substrate, argon is ionized (Ar^+), and these resulting ions are accelerated toward the target. The bombardment process causes the ejection of atoms from the target surface. Simultaneously, a cold gas-like phase consisting of ions and electrons (i. e., a plasma) will be generated. The ejected atoms traverse some distance until they reach the anode and condense on the substrate surface. During this process, the atoms on the substrate begin to bind with one another at the atomic level, forming tightly bound, atomic layers. Depending on the sputtering time, a set of atomic layers can be deposited resulting in a thin film with controllable properties.

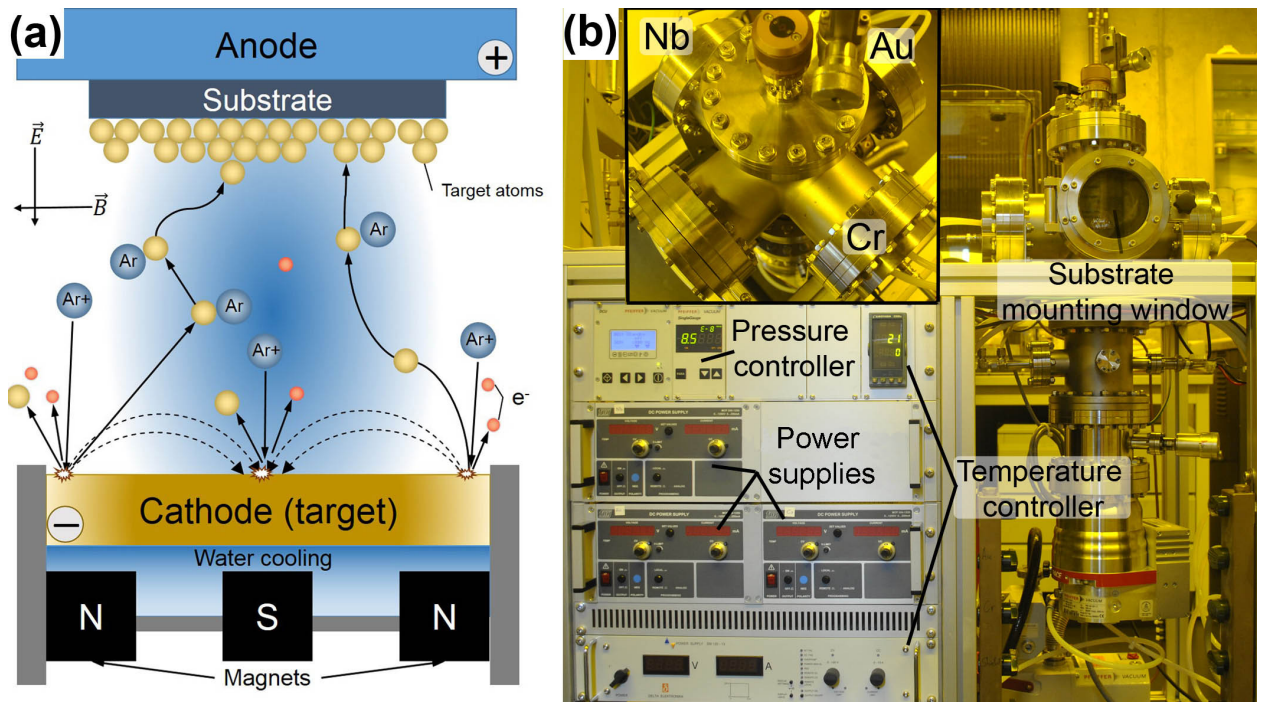


Figure 3.9: (a) Principle of the DC magnetron sputtering process. Inert gas atoms, such as Ar, can be ionized by application of a strong potential difference between the cathode and anode. These ions are further accelerated toward a target (cathode) and after collision with it, atoms of the target material are ejected from the surface layer and accelerate toward the substrate. On the substrate, the atoms form a set of layers, thus building up a thin film. (b) Photograph of the custom-built, DC magnetron sputtering setup used in this work.

The main difference between magnetron sputtering and “classical” sputtering is the application of a magnetic field to maintain the plasma near the target, thereby increasing the efficiency and the quality of process [152]. Thus, secondary electrons emitted from the target

surface during the ion bombardment process also play an important role. In the magnetron sputtering process, permanent magnets (as a part of the sputtering cathode) make use of the fact that the magnetic field configured parallel to the target surface can maintain secondary electron motion in the vicinity of the target. The magnets are arranged in such a way that one pole is positioned at the central axis of the target and another pole is formed by a ring of magnets around the outer edge of the target [see Fig. 3.9(a)]. Electrons in the magnetic field are trapped in cycloids and circulate over the target's surface, substantially increasing the probability of the ionizing electron–atom collision to occur. The increased ionization efficiency results in a dense plasma in the vicinity of the target. This leads to increased ion bombardments of the target, giving higher sputtering rates onto the substrate. In addition, the increased ionization efficiency allows the whole process to be performed at a lower operating pressure (typically 10^{-3} mbar compared to 10^{-2} mbar) and a lower operating voltage (typically -500 V compared to $-2 \div 3$ kV) than in the “classical” sputtering mode.

The sputtered film properties are usually controlled by the sputtering parameters: sputter current and voltage, pressure, and substrate temperature. The sputter current mainly determines the sputtering rate, while the sputter voltage determines the energy with which sputtering atoms will escape from the target as well as the sputter yield, which is the number of sputtered particles per incoming ion. The substrate temperature, as well as the target–substrate distance, has a strong impact on the film texture, crystallinity, and surface morphology [154].

In this work, a custom-built, DC magnetron sputtering setup (as shown in Fig. 3.9(b)) was used for the sputter deposition of the thin films. This setup is comprised of a UHV chamber made of stainless steel, supplied with a source of Ar gas (99.999% purity) as the sputter gas, and equipped with 2-inch Cr, Au and Nb targets of 99.996% purity. The substrate (with a pattern formed prior to this step by photo- or e-beam lithography) is mounted on a suitable substrate holder and transferred into the chamber. The setup chamber with the mounted substrate is usually evacuated for ≥ 5 hours. A background pressure in the range of 8.6×10^{-8} – 1.6×10^{-7} mbar indicates a suitable vacuum. During the evacuation and sputtering process, the substrate is kept at room temperature. Then, Ar gas is fed into the chamber, and a current is applied between the cathode and anode by a DC power supply. By the gas pressure, p , and the cathode–anode distance, d , is determined the breakthrough voltage, U_D , at which a sustainable, glow discharge (plasma) forms. This voltage is determined as $U_D = A \cdot pd / (\ln(pd)) + B$, where A and B are material constants. The electrode distance, d , is kept constant, while the pressure, p , can be directly controlled by means of the fine-dosage valve. Thus, by increasing the pressure, the number of gas ions increases, thereby

enhancing the ionization probability and the gas conductivity, resulting in a reduction of the breakthrough voltage. At some ionization rate, a stable burning plasma is established, whereby a sufficient number of ions is available for sputtering the material.

For the sputtering of Cr, a potential of $\approx 350 - 370$ V at an Ar gas pressure of 2.0×10^{-2} mbar was required to form a stable plasma and a homogeneous deposition process. These parameters resulted in a sputtering rate of ≈ 0.1 nm/s. For the sputtering of Au, the voltage was $\approx 650 - 670$ V at a gas pressure of 7.0×10^{-3} mbar. The sputtering rate for Au was ≈ 0.3 nm/s. The current value was set at 10 mA and was held constant during the process both, for Cr and Au. The film thickness was inferred from the sputtering time after accurate calibration of the deposition rate on a number of Cr and Au films. The thickness of the sputtered films was verified by means of atomic force microscopy inspection.

3.1.4 Focused electron/ion beam-induced processing (FEBIP/FIBIP)

Focused electron beam-induced deposition (FEBID) is a process of decomposing gaseous molecules using a focused beam of highly energetic electrons, which leads to the deposition of non-volatile fragments onto a nearby substrate. In this way, mask-less "bottom-up" writing is performed for predefined, free-standing patterns with resolution in the micro- to nano-meter range. Focused ion beam-induced deposition (FIBID) is based on the same principles as FEBID with the major difference that the highly energetic electrons are replaced by ions, which unlike electrons in FEBID serve as the structural and compositional foundation for the final, deposited structures. Generally, both processes take place in a vacuum chamber of a scanning electron microscope (SEM) equipped with a focused ion beam (FIB). Detailed recent reviews of FEBID and FIBID processes and related techniques can be found in [58, 59, 155]. The FEBID/FIBID techniques are particularly suitable for the preparation of mesoscopic, hybrid structures of dimensions down to 10 nm laterally and 1 nm vertically [58, 59]. Well-established applications range from photomask repair [60], fabrication of nanowires [42, 61] and nanopores [62] to magnetic [51, 52] and tunable strain sensors [63].

The basic concepts of FEBID and FIBID techniques are reviewed in this subsection. A discussion regarding the precursor gases applied in this work is also provided.

FEBID

The principle of FEBID is schematically shown in Fig. 3.10. The precursor gas is supplied to the SEM chamber in the vicinity of the substrate surface by a gas injection system (GIS). The precursor molecules will adsorb, desorb and diffuse onto the substrate surface. Given optimal

conditions applied during the deposition process, the surface will be covered homogeneously and permanently with precursor gas molecules. Further, by rastering over the substrate surface with the electron beam, the adsorbed precursor molecules will be excited and as a result dissociated. During the dissociation process, decomposition of the precursor molecules to volatile and non-volatile components takes place. The volatile components will be pumped away from the SEM chamber, while the non-volatile components are deposited. Scanning takes place over a predefined area, resulting in deposits that can be freely configured in a desired spatial geometry. At the end of the deposition process, the precursor flux and the electron beam scanning will be stopped. The adsorbed precursor molecules will be desorbed from the substrate surface and only the deposits where rastering by the electron beam took place remain. In the FEBID process (in particular during the decomposition of the precursor molecules), not only the primary electrons from the incident electron beam contribute, but also the backscattered and secondary electrons [see Fig. 3.17(b)] generated after interaction of the primary electrons with the atoms of the substrate subsurface layer [156, 157].

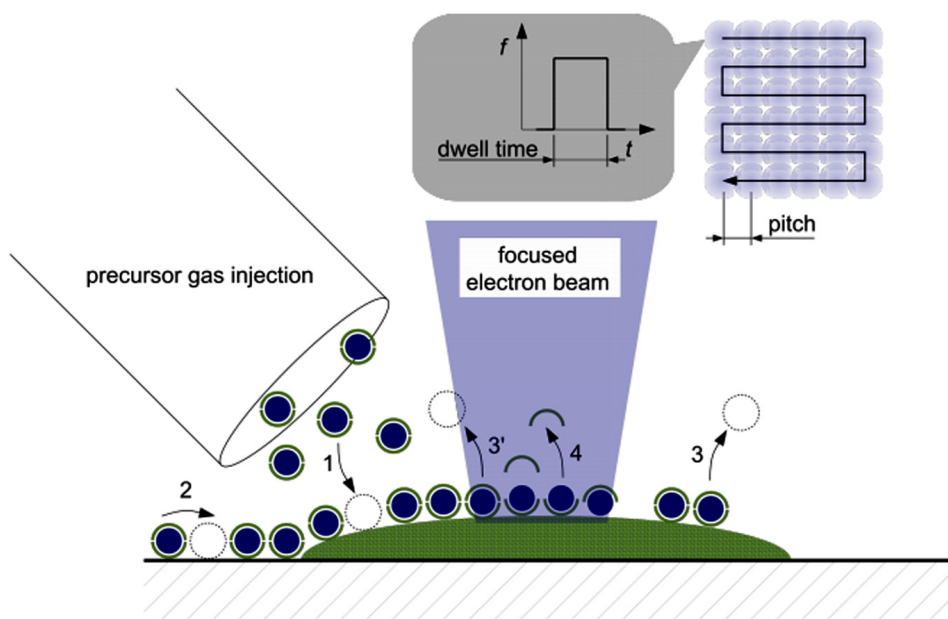


Figure 3.10: Schematic representation of the FEBID process. The precursor molecules (metal–organic compounds: metal (blue), organic ligands (green)) supplied by the GIS in the vicinity of the substrate surface are adsorbed onto the surface. Surface diffusion (2), followed by thermally induced desorption (3) and electron-stimulated desorption (3') take place. Within the focus of the electron beam, adsorbed precursor molecules are (partially) dissociated, followed by desorption of volatile organic ligands (4). Upper right: For pattern definition, the electron beam is moved in a raster fashion over the surface and settles on each dwell point for a specified dwell time. After one raster sequence is completed, the process is repeated until a predefined number of repeated loops is reached. Figure is reproduced after [59].

Basic relevant FEBID parameters are the primary beam energy, E , the beam current, I , the distance between successive dwell points of the electron beam, the so-called pitch, p , and the time period over which the electron beam is held at each dwell point, the dwell time, t_D . The typical beam energy varies between 1 – 30 keV, while beam current varies between 5 pA – 24 nA. A typical pitch is between 10 – 100 nm. As for dwell time, it can be as short as 50 ns, or as long as 100 ms. The variation and combination of the given FEBID parameters have a significant impact on precursor decomposition efficiency, deposition rate, and metal content of the resulting deposits. Regarding the deposition efficiency, additional details such as the type of substrate used (different backscattered electrons and secondary emission), the substrate (process) temperature, the precursor flux, or purity of the vacuum during the process also have an impact on the process [69, 158].

In many cases, the as-deposited FEBID structures (for many of the available precursors) result in nanogranular materials. They consist of crystalline, metallic inclusions (approximately 3 – 10 nm in diameter) embedded in an amorphous, carbon-rich, dielectric matrix. Other species, such as oxygen from the precursor molecules, are also incorporated into the deposits along with the metal. The metal content of these nanogranular materials is strongly dependent upon the applied precursor gas and the deposition parameters, and is often less than 40 at. %, the remainder being mostly carbon and oxygen. Only in very few cases [159, 160], for the $\text{Co}_2(\text{CO})_8$ precursor gas by careful optimization of deposition parameters up to 95 at. % metal purity was reported for Co structures. However, in contrast to the deposition by focused ion beam (which notably affects [161, 162] the underlying matter due to the destructive heavy ions), FEBID has a much weaker impact on the structural properties (and thus, the conducting properties) of the material due to the small electron mass.

FIBID

The principles of FIBID are similar to those of FEBID with the major difference being that the focused electron beam is replaced by a focused ion beam. A liquid-metal ion source of Ga^+ is typically used as the source of ions. Generally, the metal content of the structures prepared by FIBID is higher than that of FEBID since the precursor gas molecule dissociation with heavy ions is more efficient. Also, the deposition rate in the FIBID process is several times higher than that in FEBID. In addition to the primary ions, secondary electrons and ions generated from the substrates contribute to the deposition process. A typical metal content for FIBID deposits is around 40 – 50 at. % (depending on the precursor gas and

the deposition parameters), the rest consisting mostly of carbon, oxygen and gallium. This is reflected in the conductive properties of as-deposited FIBID structures, the resistivity of which is often several orders of magnitude smaller than FEBID structures [163].

Although this process presents many advantages, several disadvantages limit FIBID applications. Firstly, Ga^+ ions introduce additional gallium contamination into the deposits. Secondly, the damage induced by the heavy ions is significant. Often, the surface of the substrate is destroyed by ion irradiation before the deposition takes place [161, 162]. As the gallium ion beam causes amorphization, implantation and vacancy generation in the area near the surface of the exposed region, in this work, imaging with the ion beam was kept to a minimum. Also, the angular spread of secondary electrons is larger than in FEBID, thus resulting in lower spatial resolution.

By analogy with FEBID, the main parameters that govern the FIBID process are the primary beam energy, E , the beam current, I , the dwell time, t_D , and the pitch, p .

In general, FIBID deposits, similar to FEBID structures prepared with organo-metallic precursors, are nano-granular metals. In some cases, for example for W-based FIBID structures, they have an amorphous microstructure [164].

FEBID/FIBID precursors

Among the variety of metal-based deposits that can be prepared by the FEBID/FIBID techniques, Pt, Co, W and Pb are particularly attractive for potential applications. For example, Pt is an oxidation resistant conductor, Co is a soft ferromagnet, while W and Pb are superconductors. In FEBID/FIBID the choice of the precursor material is crucial since it determines the composition of the deposited structures.

The most popular precursors for deposition of materials by FEBID/FIBID are metal carbonyls of $\text{M}(\text{CO})_x$ structure and metallocenes. Metal carbonyls are coordination complexes of transition metals with carbon monoxide ligands. Metallocenes are compounds typically consisting of two cyclopentadienyl anions (Cp , C_5H_5^-) bound to a metal center (M) in the oxidation state II, with the resulting general formula, $(\text{C}_5\text{H}_5)_2\text{M}$. Both types of precursors are commercially available, but produce significant carbon contamination in the resulting FEBID/FIBID deposits.

In this work, FEBID of Pt was used for the deposition of the multilayered Co/Pt heterostructures (see chapter 6). The precursor was trimethyl (methylcyclopentadienyl)platinum(IV) $[\text{MeCpPt}(\text{Me})_3]$ [Fig. 3.11(a)] [165], which is a whitish crystalline powder. The e-beam parameters were $E = 5$ keV, $I = 1$ nA, $p = 20$ nm, $t_D = 1$ μs . Before the deposition, the

precursor was heated to 44 °C. The metal content of the as-deposited structures from this precursor usually did not exceed $\approx 25\%$. This Pt-based precursor has wide application in the fabrication of tunable strain sensors [63], binary nanostructures [73, 74], and investigations of the effect of mesoscopic disorder on electronic properties [65].

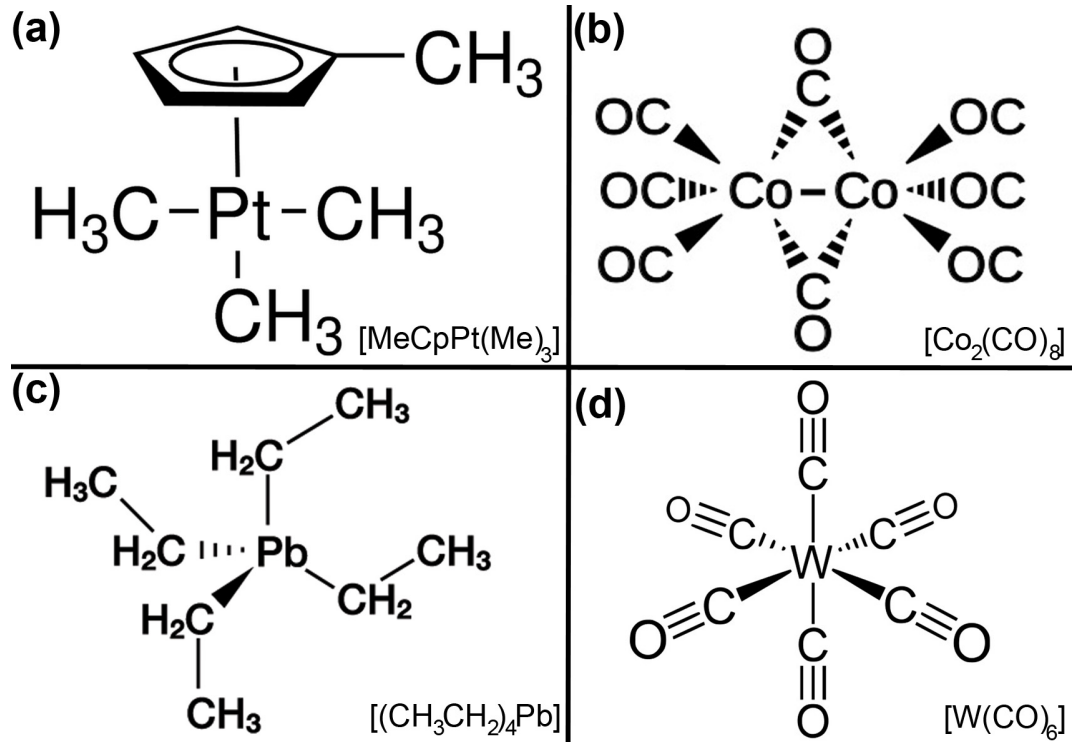


Figure 3.11: Precursor gas molecules used in this work: (a) trimethyl(methylcyclopentadienyl)platinum(IV), (b) dicobalt octacarbonyl, (c) tetraethyl lead, (d) tungsten hexacarbonyl.

FEBID of Co was used in this work for the deposition of granular Co nanowires (see chapter 5) and multilayered Co/Pt heterostructures (see chapter 6). The precursor was dicobalt octacarbonyl $[\text{Co}_2(\text{CO})_8]$ [Fig. 3.11(b)] [166] and consists of red-orange crystals, which at room temperature in air, release carbon monoxide upon decomposition. This precursor is commonly used for the fabrication of magnetic micro- and nano-structures [159, 160, 167–169]. For the deposition of the nanowires the e-beam parameters were $E = 3$ keV, $I = 90$ pA, $p = 5$ nm, and $t_D = 1$ μs , while for the deposition of the Co/Pt heterostructures, the parameters were $E = 5$ keV, $I = 1$ nA, $p = 20$ nm, and $t_D = 50$ μs . Before deposition, the precursor was heated to 27 °C. The metal content of the deposited structures did not usually exceed $\approx 80\%$. This Co-based precursor has a tendency towards spontaneous dissociation of the precursor gas molecules and autocatalytic deposition on SiO_2 substrate surfaces [45]. For this reason, $\text{Si}/\text{SiO}_2/\text{Si}_3\text{N}_4$ and Al_2O_3 were selected as working substrates instead of Si/SiO_2 .

FEBID of Pb was used for the deposition of superconducting nanowires and electrodes that induce superconducting properties in the Au nanowires (see chapter 7). The precursor was an organo–lead compound, tetraethyl lead $[(\text{CH}_3\text{CH}_2)_4\text{Pb}]$ [Fig. 3.11(c)] [170]. In contrast to the other precursors which are solids, this precursor is a colorless, oily, volatile liquid. Great care should be taken in the handling of this precursor due to its high toxicity. The e-beam parameters for this process were $E = 10$ keV, $I = 13.3$ nA, $p = 10$ nm, $t_D = 5$ μs . During the deposition the precursor was kept at room temperature. The Pb-FEBID deposit is a Pb-based superconductor with a superconducting transition temperature T_c of 6.2–7.2 K, close to that of bulk Pb ($T_c = 7.26$ K), which is strongly dependent on the deposition parameters [64]. Pb-FEBID, developed recently in our group, is the only known superconductor that can be prepared by FEBID.

FIBID of W was used for the preparation of electrodes that induce superconducting properties in Cu and Co nanowires (see chapters 4 and 5). Generally, the W-FIBID deposit is an amorphous, W-based superconductor, with additional C and Ga components [164]. It has a T_c of 4.8–5.2 K, which is strongly dependent on the deposition parameters [171] (for comparison, bulk W has $T_c = 0.012$ K). The precursor for this process was tungsten hexacarbonyl $[\text{W}(\text{CO})_6]$ [Fig. 3.11(d)] [172, 173]. It is a colorless solid, characterized as a volatile, air-stable derivative of tungsten in its zero oxidation state. The ion beam parameters for this process were $E = 30$ keV, $I = 10$ pA, $p = 18$ nm, $t_D = 200$ ns. With these FIB parameters, the resulting W-based deposits exhibit a T_c of ≈ 5.2 K, which is nearly independent of the deposit thickness in the range of 50 – 300 nm and for beam currents between 1 – 30 pA [171].

FIBID of Pt was used for the preparation of current and voltage leads to the Cu and Co nanowires (see chapters 4 and 5). The precursor gas was the same as that used for FEBID, $[\text{MeCpPt}(\text{Me})_3]$. The ion beam parameters were $E = 30$ keV, $I = 10$ pA, $p = 30$ nm, $t_D = 200$ ns. Generally, the Pt-FIBID deposit was an amorphous, Pt-based material, with additional C and Ga components [163]. A metal–insulator transition is known to occur in Pt-FIBID structures at liquid helium temperature once the deposit thickness is reduced below 50 nm [163]. Taking this into account, Pt-FIBID leads of thickness larger than 130–230 nm and a width of 100–200 nm were used in this work. Such dimensions ensure that the electrical conductivity of the deposit is in the metallic regime.

3.2 Compositional, microstructural, and morphological characterization

The primary techniques, which were used in this work for the characterization of the samples prepared by the various methods described in the previous section, are now discussed. For the compositional analysis of the materials, energy-dispersive X-ray spectroscopy (EDX) and electron energy loss spectroscopy (EELS) were used. For the crystallographic microstructural analysis, X-ray diffraction (XRD) was employed as well as selected area electron diffraction (SAED) analysis in conjunction with transmission electron microscopy (TEM). The thickness and topography of the samples under investigation was determined by means of atomic force microscopy (AFM), while for the imaging of the samples, scanning electron microscopy (SEM) was used. All of these techniques are briefly introduced together with the corresponding equipment and experimental parameters.

3.2.1 Energy-dispersive X-ray (EDX) spectroscopy

The material composition of all samples was evaluated by means of energy-dispersive X-ray spectroscopy (EDX) in an SEM. EDX [174, 175] is an analytical technique used for the elemental examination of solid samples. This technique is based on the detection of characteristic X-rays that are generated when a sample is bombarded with high-energy electrons. The X-rays are detected with an energy-dispersive spectrometer, which can discriminate X-rays with different energy levels. In principle, all elements from atomic number 4 (Be) to 92 (U) can be detected. The quantity (intensity) of X-rays emitted by each element in a sample is directly proportional to the concentration of the element (mass or atomic fraction). As result, all collected X-rays can be converted into X-ray spectra, which contain information on the concentration of each element constituting the sample.

There is a considerable overlap between functions of an SEM and an EDX spectrometer. Elemental distribution “maps” can be produced by scanning the e-beam in raster mode and displaying the intensity of a selected X-ray line. Also, images produced by the collection of electrons emitted from the sample reveal the surface topography. The SEM, which is closely related to the electron probe, is designed primarily for producing electron images, but can also be used for elemental mapping, and even point analysis if an X-ray spectrometer is added. For this reason, modern SEMs are often additionally equipped for EDX.

The basic design of an EDX spectrometer is shown in Fig. 3.12(a). It typically consists of the following key components: excitation source (e-beam) and a semiconducting X-ray

detector equipped with a field-effect-transistor preamplifier and main amplifier, which provides further amplification and fast pulse inspection functionality to reduce pile up events. A computer-assisted system is used to control these two components, allowing for automated operation. In this work, the Si(Li) sensor cooled to cryogenic temperatures with liquid nitrogen was used in EDX spectroscopy with an e-beam energy up to 20 keV. When the electron beam hits the sample, there is a high probability that X-ray photons will be generated. The generated X-ray then escapes the sample and hits the detector, creating a charged pulse. This short-lived current is then converted into a voltage pulse with an amplitude corresponding to the energy of the detected X-ray. Further, each voltage pulse can be converted into a digital signal resulting in the addition of one count to the corresponding energy channel. The collected counts form a typical EDX spectra with narrow peaks superimposed over the broad background, an example of which is shown in Fig. 3.12(b).

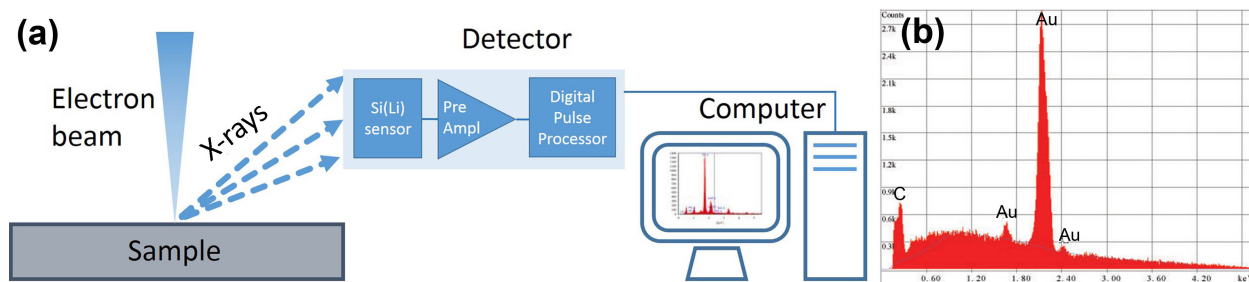


Figure 3.12: (a) Components of a modern, digital, energy-dispersive X-ray spectroscopy system. (b) A typical EDX spectrum showing the main elemental peaks superimposed over the background signal.

To stimulate the emission of characteristic X-rays from a sample, a high-energy e-beam is focused onto the sample surface to be analyzed. Electrons from the e-beam will interact with the sample atoms, stimulating the emission of electrons from the sample, as shown in Fig. 3.13. The electrons originally positioned in the inner shell (K shell) will be ejected, leading to changes in the energy state of the atom. In order for the atom to return to its lower energy state, this “vacancy” is immediately occupied by an electron coming from a higher-energy shell, emitting some energy in the form of X-rays in the process. As the energy of the emitted X-ray is directly related to the energy difference between two levels, and to the atomic structure of the element from which the X-rays were emitted, this allows the elemental composition of the sample to be determined.

An EDAX Genesis 2000 EDX spectrometer mounted directly to the SEM (FEI, Nova NanoLab 600) was used in this work to monitor the material composition. The probed sample areas were $100 \times 100 \text{ nm}^2$, while the e-beam parameters were $E = 3 - 5 \text{ keV}$ and $I = 1.6 \text{ nA}$, typically. Here the beam energy, which must be greater than twice the energy of

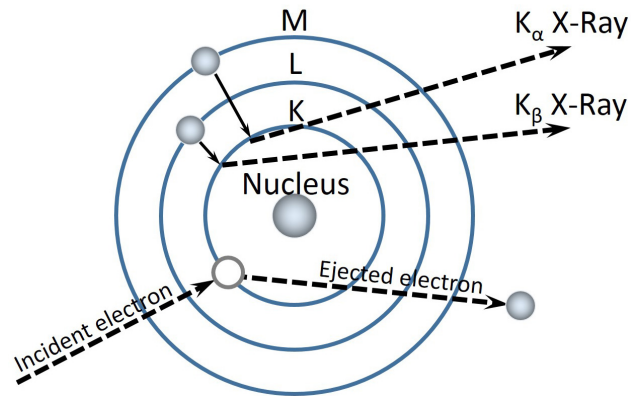


Figure 3.13: Excitation and emission process in an atom.

the characteristic X-ray photons of the material under examination, determines the effective thickness of the layer to be analyzed. It is approximately 70–80 nm for the electrochemically deposited Cu and Co nanowires, and for the Pt-FEBID/FIBID and W-FIBID electrodes (see Fig. 3.14). The penetration of the electrons into all of the examined objects was calculated by the simulation program Casino [176].

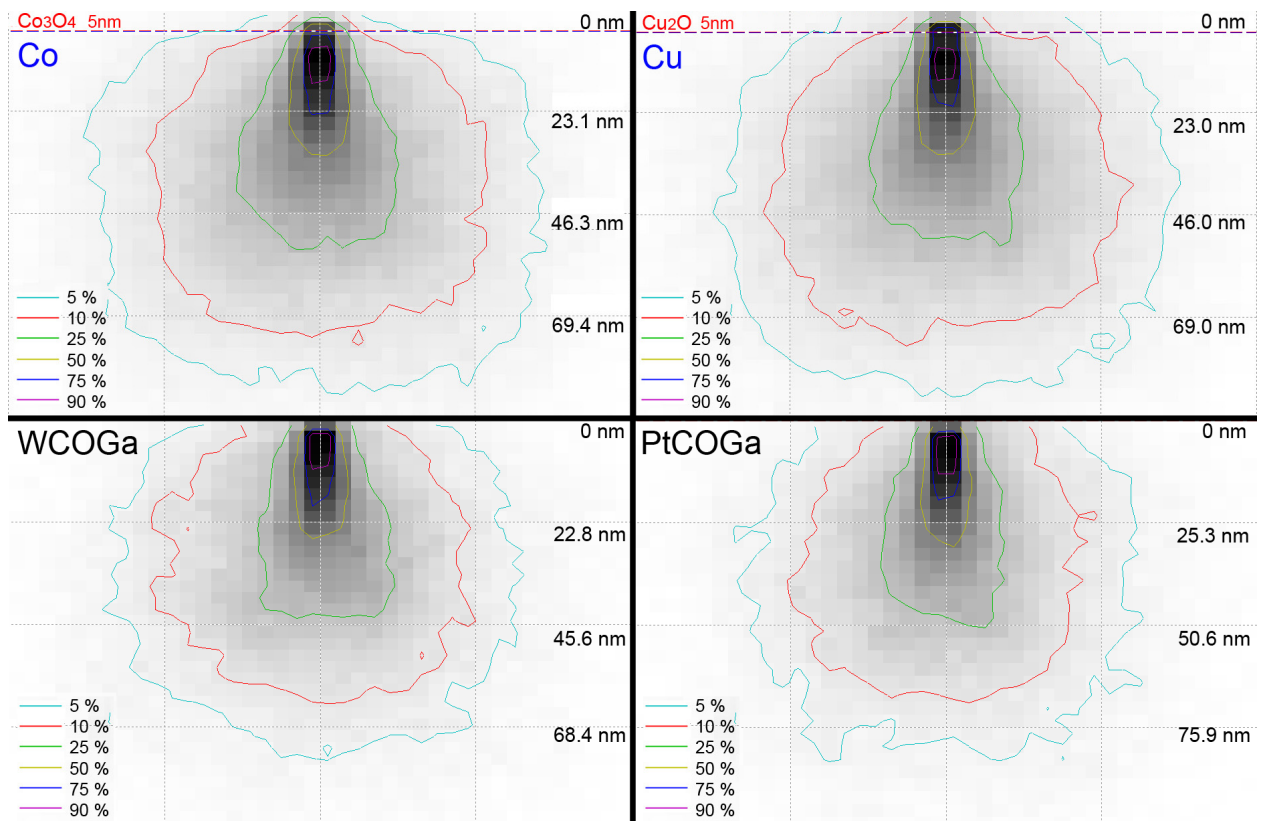


Figure 3.14: The penetration of the electrons into Cu and Co nanowires, Pt-FIBID and W-FIBID electrodes, calculated by the simulation program Casino at e-beam energy of 5 keV.

The material composition was calculated taking into account ZAF (atomic number, absorption and fluorescence) and background corrections. The software EDAXs Genesis Spec-

Object	Cross-section, nm \varnothing or $w \times d$	Metal content, at. %	O, at. %	C, at. %	Ga, at. %
Cu-NW1	\varnothing 380	95	5	0	0
Cu-NW2	\varnothing 275	95	5	0	0
Co-NW	\varnothing 280	59	41	0	0
Co-FEBID	155×255	71	14	15	0
W-FIBID	150×200	47	8	30	15
Pt-FIBID	150×180	32	5	53	10
(A) Co-FEBID purified	500×11	83	10	7	0
(B) Co/Pt	1000×21	28/14	49	9	0
(C) Co/Pt	1000×22	29/13	40	18	0
(D) Co/Pt	1000×16	15/15	57	13	0
Pb-FEBID	100×150	45	25	30	0
Au-NW	150×60	98	0	2	0

Table 3.1: The structural and compositional parameters of all samples investigated in this work. w : width; d : thickness.

trum v. 5.11 was used to analyze the material composition. The statistical error in the elemental composition was 2%. The elemental composition was quantified without a thickness correction, thus the obtained data are a qualitative indicator only. The structural and compositional parameters of all samples explored in this work are presented in Tab. 3.1.

3.2.2 X-ray diffraction (XRD) analysis

In order to determine the crystallographic microstructure of the Cu and Co nanowires X-ray diffraction (XRD) was used. In XRD, Bragg's law is applied given a monochromatic X-ray source and a variable angular position of the samples under investigation.

Bragg diffraction occurs when electromagnetic irradiation (X-rays) incident upon a crystalline sample scatter in a specular fashion, and due to the ordered arrangement of the atoms of the crystals, undergo constructive interference. At a certain defined wavelength and incident angle, the intensity peaks of scattered irradiation (so-called Bragg peaks) can be obtained in crystalline materials. When the X-rays are specularly reflected by the atoms in any one lattice plane and the reflected rays from successive lattice planes interfere constructively, sharp intensity peaks of the scattered irradiation can be observed. A typical crystalline solid is composed of parallel lattice planes formed by periodically arranged atoms and spaced at a distance, d , as shown in Fig. 8.1(a). When the scattered waves constructively interfere, they remain in phase since the path length of each wave is equal to an integer multiple, n , of the wavelength, λ . The Bragg condition defines the path difference between the two rays, which is $2\Delta = 2d \sin \Theta$, where Θ is the angle of incidence (the Bragg angle). Constructive interference between the outgoing waves is described by Bragg's law:

$$2d \sin \Theta = n\lambda. \quad (3.4)$$

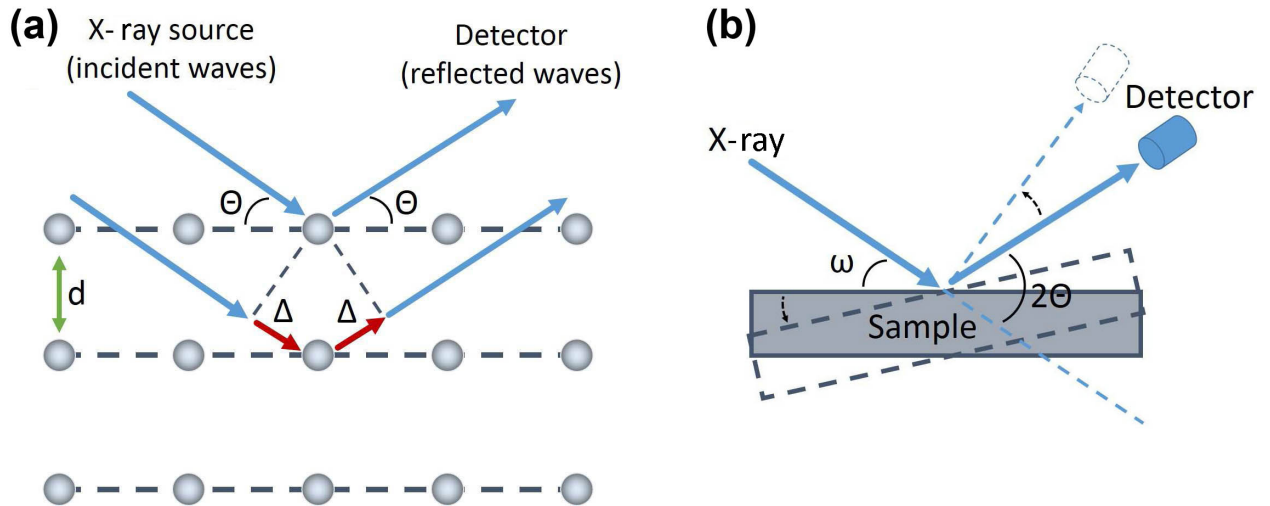


Figure 3.15: (a) Bragg reflection from a family of lattice planes, separated by a distance d . Incident and reflected rays are shown for the two neighboring planes. $2\Delta = 2d \sin \Theta$ is the geometrical path difference between the two ray paths. (b) Schematic representation of the scan principle for collection of the ω - 2Θ X-ray diffractogram.

The measurement principle is shown in Fig. 8.1(b). During the measurements, the X-ray incident angle, ω , can be varied in the range $0 - 90^\circ$ by rotating the sample. The detector follows the reflection angle, $\Theta = \omega$. Thus, the intensity, I , of the diffracted X-rays can be plotted as a function of the angle 2Θ in an ω - 2Θ scan. The X-rays, in accordance with Bragg's law (Eq. 3.4), will be diffracted at the atomic planes of a crystal, and at a given angle, an increase in the intensity I can be detected. By means of Eq. (3.4) the distance d between the crystal atomic planes with regard to the diffraction angle can be determined.

The obtained X-ray diffractograms were compared with reference diffraction patterns simulated by the crystal structure visualization software Mercury 2.3 [177], which has access to a crystallographic database. By comparing the experimental Bragg peak positions and intensities with simulated reference spectra, one can identify the crystallographic phase and its orientation.

For the determination of the mean crystallite size of polycrystalline solids (in this case nanowires) the Scherrer equation can be applied. This equation gives the direct relationship between the size of sub-micrometer crystallites of a solid and the broadening of a Bragg peak in a diffraction spectra. The Scherrer equation is:

$$\tau = \frac{K \cdot \lambda}{\Delta(2\theta) \cos \Theta}, \quad (3.5)$$

where τ is the mean size of the crystallites, K is a dimensionless shape factor, with a value close to unity (K has a typical value of ≈ 0.9 , but varies with the actual shape of the

crystallites), λ is the X-ray wavelength, $\Delta(2\theta)$ is the Bragg peak width at half the maximum intensity (FWHM), and Θ is the Bragg angle.

The microstructure of the nanowires was examined by means of XRD while still embedded in the PC template. During the growth of the nanowires, the deposition process was terminated as soon as the caps began to grow on the top of the nanowires. This precaution was taken because the crystallographic microstructure of the caps can be significantly different from the microstructure of the nanowires themselves, leading to incorrect interpretation of the diffractograms. The XRD characterization was performed in collaboration with Dr. Joachim Brötz at the Department of Material Sciences of TU Darmstadt. For these measurements, a SeifertPTS 3003 diffractometer with a Cu anode ($\lambda_{K\alpha} = 0.154$ nm) was used. Measurements were performed at an accelerating voltage of 40 kV and a current of 40 mA.

The acquired data revealed the single crystalline nature of the Cu nanowires and the polycrystalline nature of the Co nanowires. The corresponding diffractograms are presented in Fig. 3.16 (a) and (b), respectively. According to the XRD results, metallic crystalline Cu was found to grow (110)-oriented along the nanowire axis, and no other crystalline phases were detected. Cu reflexes are assigned to the face-centered-cubic phase, while Au reflexes stem from the sputtered Au film on one side of the PC template required for nanowire deposition (see section 3.1.1). The Co nanowires were found to grow polycrystalline in a hexagonal-close-packed phase and, in addition, two peaks stemming from Co_3O_4 have been observed in the X-ray diffractogram. The broadening of the Co_3O_4 peaks in the X-ray diffractogram analyzed on the basis of the Scherrer Eq. (3.5) gives 5–10 nm as an estimate for the thickness of an oxide layer or, alternatively, to the size of Co_3O_4 crystallites (see Appendix A). By using the SEM to scan along the nanowire axis, it was possible to observe individual crystallite grains with a size of 200–400 nm in the Co nanowires. In addition, EDX analysis of the Cu and Co nanowires indicate the presence of oxides, which is also known from other studies [144, 178, 179]. Furthermore, it is assumed that the 5–10 nm thick Co_3O_4 at the Co grain boundaries is responsible for the enhanced resistivity of the Co nanowire, as will be discussed in chapter 5.

3.2.3 Scanning electron microscopy/focused ion beam (SEM/FIB)

Scanning electron microscopy (SEM), which was an essential tool utilized in this work, was used for both sample fabrication and characterization. Several of the techniques previously introduced in this chapter (EBL, FEBID/FIBID, EDX spectroscopy, etc.) were used in combination with SEM.

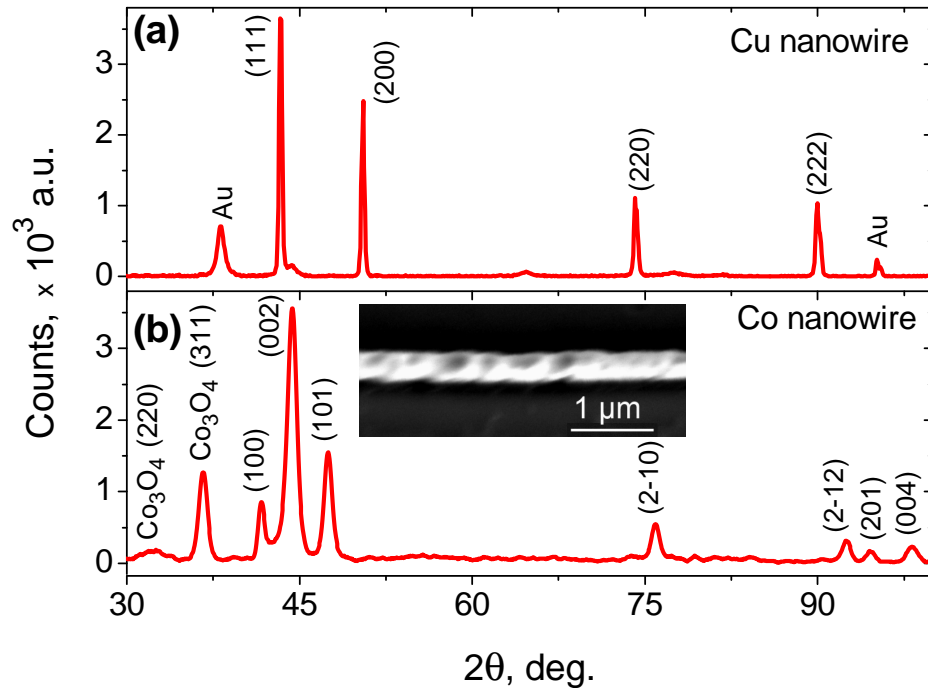


Figure 3.16: Bragg X-ray scans of (a) Cu and (b) Co nanowires embedded in a polymer template. Inset of (b): SEM image of the Co nanowire. Individual crystallites with a size of 200 – 400 nm can be distinguished.

SEM involves complex instrumentation designed for imaging objects and/or their surfaces with high spatial resolution (on the micro- and nano-meter scale), as well as analyzing compositional or structural properties of subsurface layers. The principle of operation is based on the interaction between the focused electron beam and the object under investigation.

The SEM is built around an electron column, where a stable beam of primary electrons is produced with controllable energy and current, as well as size and shape. The electron column consists of an electron source (involving a filament cathode, a Wehnelt cap and an anode), a condenser lens (required for primary electron beam focusing), an $x - y$ deflection system, and an objective lens (required for the final electron beam focusing) [see Fig. 3.17(a)] [180]. The electron column is adjacent to a working chamber, containing a stage with a sample holder and different detectors to receive signals generated upon interaction of a primary electron beam with a sample under investigation. In the column and sample chamber, vacuum conditions are monitored to prevent the defocusing of the electron beam on rest gas molecules. The electron column and the working chamber typically have independent vacuum pumping systems.

For measurement and control of the SEM, supplementary electronics are required including: the energy supply for the electron source and magnetic lenses, the scan generator and the signal amplifier for detectors.

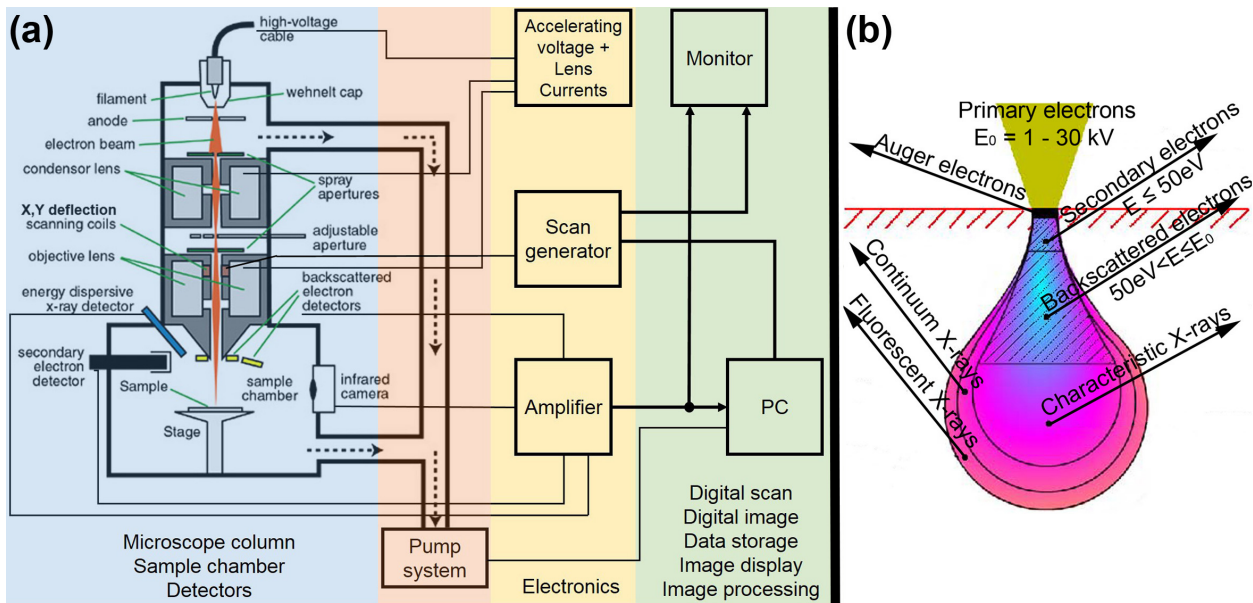


Figure 3.17: (a) Schematic representation of the main SEM components. Shown here are the electron column, a working chamber, a pump system, and supplementary measuring and control electronics. (b) Typical emissions and the interaction volume formed by the primary electron beam in the sample under investigation. The size and shape of the interaction volume is defined by the primary electron energy and the atomic number of the sample.

In SEM, electrons from thermoionic emissions from the filament cathode are accelerated toward the anode with an accelerating voltage ranging from 1 kV to 30 kV. The generated electron beam has a relatively large diameter ($10 - 50 \mu\text{m}$) to be used for scanning on the micro- and nano-meter scale. Therefore, a set of magnetic lenses (condenser and objective) is typically used for focusing to a spot with a diameter of $\approx 1 - 5 \text{ nm}$. In addition, $x - y$ deflection scanning coils are used to move the focused electron beam along the x and y axes to scan in a raster fashion over a defined area of the sample surface.

The principle of SEM is based on the interaction of the focused electron beam with the sample surface, whereby information about surface topography and composition can be obtained. The incident primary electron beam interacting with the atoms of the sample generates various interaction emission products, providing information about the sample. The main products are secondary electrons (SEs), back-scattered electrons (BSEs), Auger electrons, and a variety of X-rays [Fig. 3.17(b)]. Detectors for each type of signal are directly mounted in the SEM chamber in the vicinity of the sample. Originating from the near-surface layers by inelastic scattering, low energy ($< 50 \text{ eV}$) SEs are suitable to study the topography of the material and are typically used for imaging. BSEs have high energies, and they are reflected or back-scattered out of the sample interaction volume by elastic scattering interactions. BSEs are used for distinguishing contrast between areas of different

chemical composition, since elements with a high atomic number backscatter electrons more strongly than elements with low atomic number, and thus appear brighter in the image. The generated, characteristic X-rays are used in EDX spectroscopy for material composition determination, as is described in subsection 3.2.1).

Typically, a pear-shaped interaction volume is formed by interaction of the primary electron beam with the sample, as illustrated in Fig. 3.17(b). Its size and shape depend on the primary beam energy and the atomic number of the materials comprising the sample. This fact must be considered with regard to EDX spectroscopy and the FEBID process. In particular, in EDX spectroscopy, a properly selected electron beam energy can help to improve the measurement accuracy, for example, by avoiding overlapping signals generated from the substrate. Also, the number of secondary electrons generated from the substrate together with primary electrons has a significant impact on the precursor-gas molecule decomposition during the FEBID process. The penetration depth of the primary electrons is significant in FEBID as well as in the post-deposition treatments of the deposits (see chapter 6).

Focused ion beam (FIB) was used in conjunction with SEM, mostly for FIBID (see subsection 3.1.4) and to cut-etch any nanowires causing a short circuit between auxiliary Cr/Au contact pads. The operating principle of FIB is similar to SEM with the difference that electrons are replaced by heavy ions (typically Ga^+ ions). Due to the higher mass of the ions (as opposed to electrons), the interaction of the ion beam with the surface is significantly stronger, generally resulting in surface etching and destruction. Therefore, imaging with the ion beam was kept to a minimum in this work.

The SEM used in this work was a dual-beam (electron and ion beams) high-resolution instrument, Nova NanoLab 600 from FEI, a photograph of which is shown in Fig. 3.18. It is built on electron and ion columns mounted at 52° with respect to each other. The electron column is equipped with a high-performance, field-emission gun electron source (FEG-SEM), whereas the ion column system has a gallium, liquid metal, ion source (LMIS). Under optimal conditions and beam parameters, the minimum resolution is ≈ 1.1 nm for the electron beam and ≈ 7.0 nm for the ion beam. The instrument is equipped with a through-lens detector (TLD) for secondary and backscattered electrons and an Everhart-Thornley detector (ETD) for secondary electrons. For chemical material composition, the instrument is equipped with an EDX spectroscopy system [Si(Li) detector]. For the FEBID/FIBID processing, commercial and custom-built, multichannel gas injection systems (GIS) are assembled in the working chamber. An integrated IR-CCD camera is installed for live, in-chamber viewing. The positioning of the sample into the chamber is provided by a 5-axis, motorized $x-y-z$ -rotate-tilt stage. For operation with the ion beam, the stage is usually tilted at 52° .

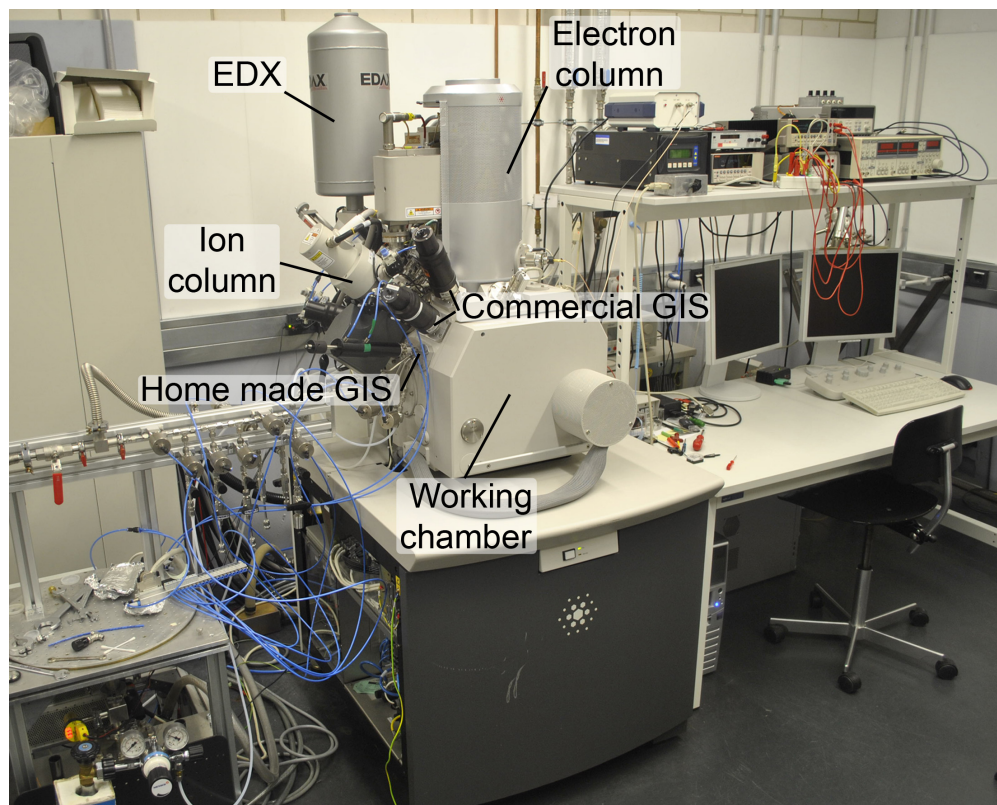


Figure 3.18: Photograph of the FEI Nova NanoLab 600 SEM.

3.2.4 Scanning transmission electron microscopy (STEM)

In order to make accurate, local analysis of the samples prepared by FEBID, and in particular, to identify microstructural, morphological and compositional modifications that have occurred in the samples after post-growth treatments, scanning transmission electron microscopy (STEM) was employed (see chapter 6). The STEM investigations were performed in collaboration with Dr. techn. H. Plank and Dr. techn. Ch. Gspan from the Institute for Electron Microscopy and Nanoanalysis (TU Graz, Austria).

The main components of the STEM [181] instrumentation, as well as their technical arrangements, are very similar to SEM. The difference is in the principle behind formation of an image. In contrast to SEM, STEM employs a focused electron beam scanning in a raster fashion over a thin sample in transmission mode. Thus, the image will be a result of the electrons passing through and interacting with a sample. The final image contrast is formed due to the various absorption of the electrons in the material, which is dependent on the microstructural and compositional homogeneity of the sample. A suitable sample thickness is ≈ 100 nm typically, but can slightly vary upon the accelerating voltage of the electron beam. Typical energies used for the electron beam in STEM ($\approx 100 - 300$ kV) are around an order of magnitude higher than in SEM.

One of the biggest advantages of STEM is the option to perform compositional and microstructural analysis, in addition to standard imaging. Most modern STEMs are equipped with supplemental equipment for EDX spectroscopy, electron energy loss spectroscopy (EELS), or selected area electron diffraction (SAED). EDX spectroscopy is briefly reviewed in subsection 3.2.1. EELS is used for compositional examination. It is based on the analysis of the kinetic energy losses experienced by electrons of the incident electron beam due to the multiple inelastic scattering events in the material. The principles of SAED are similar to X-ray diffraction and it is typically used for the identification of local crystal structure, with the advantage that the analysis can be performed on selected areas on the nanometer scale.

In this work, a high-resolution STEM (FEI, Titan G2) with a spherical aberration corrector for the electron beam (DCOR) was used for the analysis of the samples. The microscope was equipped with the following components: an X-FEG, high-brightness electron gun; a high-end, post-column, electron energy filter (Quantum ERSTM, Gatan); and four, high-sensitivity, SSD, X-ray detectors (Bruker, Super-X). The measurements were performed with an electron beam diameter smaller than 1 Å at an accelerating voltage of 300 kV.

3.2.5 Atomic force microscopy (AFM)

The determination of the diameter/thickness of the nanowires in addition to the thickness of the Cr/Au contact pads and FEBID/FIBID deposits was performed by means of non-contact atomic force microscopy (AFM). AFM allows for inspection of surface topography/morphology with a resolution on the order of fractions of a nanometer, while the investigated surface area can be on the order of a few nanometers and up to hundreds of micrometers.

The measurement principle of AFM [Fig. 3.19(a)] is based on scanning a sample surface using a cantilever with a sharp tip. When the tip is brought into close proximity to a sample surface, van der Waals interactions will take place between the atoms of the tip and atoms of the surface, resulting in deflection of the cantilever according to Hooke's law. Depending on the position, the cantilever is deflected in a different manner because of van der Waals force variations due to the topography. The magnitude of the deflection can be measured during scanning by means of a laser spot reflected from the top surface of the cantilever onto a photodiode array. In this work, AFM was performed in non-contact, dynamic mode. In this mode, the cantilever is set to vibrate with a resonance frequency. The resonance frequency is transmitted to the cantilever by a piezoelectric element. While scanning over a sample surface, the resonance frequency (as well as the amplitude and phase of vibration)

will be changed due to the tip–surface interaction via van der Waals forces. These changes can be detected and used as a signal to map the topography. In order to minimize the noise generated due to low-frequency vibrations of the environment, the resonance frequency should be relatively large, that is in the several 10 kHz range.

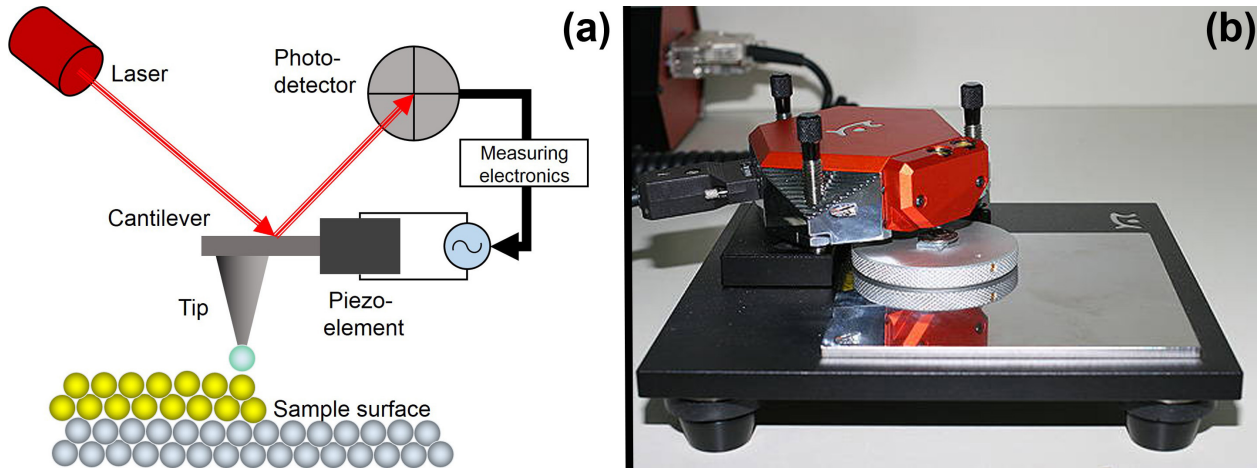


Figure 3.19: (a) Schematic representation of the working principle and main components of an atomic force microscope (AFM). (b) Photograph of the scanning head of the AFM Nanosurf EasyScan 2 .

The AFM instrumentation used in this work was a Nanosurf EasyScan 2 [Fig. 3.19(b)]. The resolution of this microscope is 1.1 nm (lateral) and 0.21 nm (vertical), and the maximum scanning area is $70 \times 70 \mu\text{m}$. During the scan, the microscope was placed on a vibration isolation table, which reduces the influence of external vibrations.

3.3 Electrical transport and magneto-transport measurements

Electrical transport measurements can reveal essential electronic properties of the studied materials. The electrical resistance was measured as a function of temperature using the standard four-terminal method, which detects the voltage changes associated with a sample. Transport measurements were made in a helium-flow cryostat equipped with a 12 T superconducting solenoid. Most of the electrical resistance measurements were taken in the direct current (DC) mode. Selected measurements, in particular magneto-transport, were performed in the alternating current (AC) mode.

To perform electrical transport and magneto-transport measurements on structures (samples) with dimensions on the micro- and even nano-meter scale, one must consider how to supply and receive the current/voltage signal from these structures. By maximizing the number of structures on one substrate, the problem of reproducibility can be eliminated to some degree. For this purpose, a custom-built carrier chip made of glass-fiber printed circuit

board (PCB) with gold-plated 24-pins was used [see Fig. 3.20(a)]. A substrate with 24, pre-formed, Cr/Au contact pads prepared by photolithography in conjunction with lift-off (see subsection 3.1.2) can be mounted on this carrier chip. Connection between the pins and contact pads was realized via a $50\ \mu\text{m}$ diameter bond wire. The carrier chip with the mounted substrate can be easily plugged into a socket fixed onto the sample holder in the SEM or sample rod in the cryostat. The contact pads are 1 mm in width along the outer perimeter of the substrate, and become smaller towards the substrate center, where the width can be reduced down to 200 nm. In this way, 24 submicron contacts in the center of the substrate establish a “working area”, where nanowires can be placed, contacted and measured, FEBID/FIBID structures can be deposited and post-processed, etc. For FEBID, a thin copper plate is usually placed between the substrate and carrier chip, which was kept at ground potential. This helps to minimize accumulation of charge carriers on the substrate and, ultimately, to prevent drift of the focused electron beam during the FEBID process.

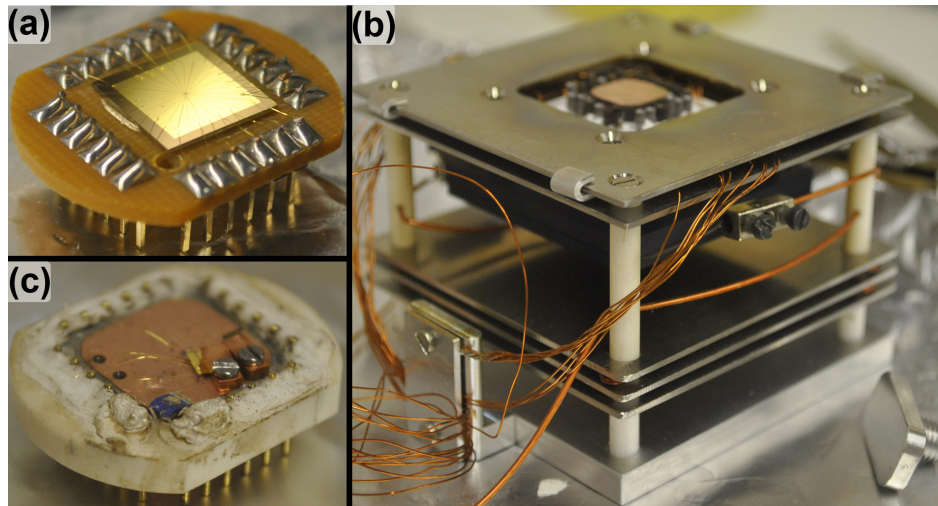


Figure 3.20: Photographs of a custom-built (a) carrier chip, (b) temperature-controlled carrier chip holder and (c) temperature-controlled carrier chip.

3.3.1 DC electrical transport measurements

The four-terminal (4-probe), electrical resistance measurement technique is schematically represented in Fig. 3.21. This was used for all samples investigated in this work. The application of this technique is associated with low sample resistivity in combination with low temperature measurement, as well as small sample dimensions. All these criteria generally shift the measured current/voltage values to the low range of $10^{-3} - 10^{-6}$ A/V, thereby causing difficulty in detection and analysis. Therefore, for the low resistivity measurements, it is important not to use the same set of auxiliary wires to carry the excitation current and

to measure the resulting voltage drop across the sample. Long wires leading into the SEM or cryostat usually have their own resistance, which can be a source of voltage not associated with the sample. In such a situation, the 4-probe technique can be particularly effective, given that no current flows along the measurement voltage leads, and only the voltage drop produced by the sample will be detected. Moreover, in the case of nanowire-shaped samples, technical realization of the 4-probe setup poses no problem due to the elongated sample geometry.

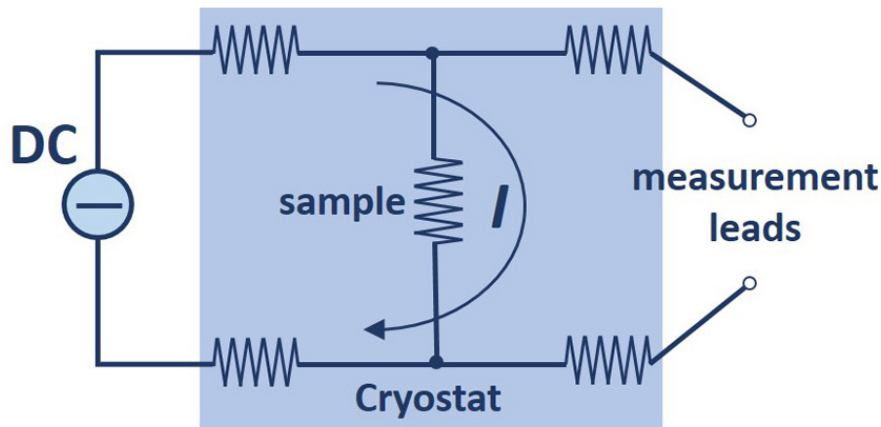


Figure 3.21: Schematic representation of the four-terminal arrangement used for electrical resistance measurements of nano wires.

For all samples investigated in this work, the 4-probe technique was used in DC current mode for the temperature-dependent resistivity measurements. A programmable DC current/voltage sourcemeter (Keithley, 2400) and a DC nano-voltmeter (Agilent, 34420A) were used. The current-reversal method was applied with the purpose to eliminate thermoelectric voltages¹. This was realized by means of reversing the polarity of the current source and averaging two measured values during the measurements.

In situ measurements

The electrical properties of the samples that were directly fabricated in the SEM should be evaluated in situ before being transferred into the cryostat for low-temperature measurements. For this purpose, a custom-built sample holder can be installed in the working chamber of the SEM. This holder can be used for both sample fabrication and characterization. The holder is a 24-pin socket, built on PCB with one additional separate pin always kept at ground potential. The 24-pin carrier chip with a mounted substrate can be plugged into

¹Parasitic voltages generated due to different Seebeck coefficients of two materials

the 24-pin socket, where the separate pin (Faraday cup) is typically used for measuring the current of the electron beam. The in situ holder can be connected through a vacuum-tight, 25-pin, D-sub connector to different instruments (e.g., DC current/voltage sourcemeter, DC nanovoltmeter, etc.) located outside of the chamber. This setup allows to perform electrical transport measurements on fabricated FEBID/FIBID structures or contacted nanowires without exposing them to air. Measurements can be recorded from the instruments via a GPIB² adapter and saved on a computer for further analysis.

For the preparation of the Co/Pt heterostructures (see chapter 6), in particular for the purification of Pt- and Co-based FEBID deposits, a custom-built temperature-controlled carrier chip holder was used, as shown in Fig. 3.20(b). It was constructed specifically to be used in the SEM working chamber, and allows for very accurate control of the sample temperature in the range of 22 °C to 350 °C. This holder is based on a resistive tungsten heating element placed in thermal contact with a massive solid copper block. The copper block can be thermally coupled with a second copper block built into the carrier chip (on the surface of which a substrate can be mechanically fixed). The heating process is manually controlled by sending a current through the heating element ($I_{max} = 1.5$ A at an applied voltage of $U = 30$ V). Furthermore, the temperature-controlled carrier chip holder allows for in situ electrical transport measurements in the SEM working chamber in analogy with the approach described in the previous paragraph.

For high-temperature measurements, the standard glass-fiber carrier chip was replaced by a ceramic carrier chip, which has a high melting point and low outgassing rate in vacuum [see Fig. 3.20(c)]. Before being used in the experiment, the carrier chip was degassed and heated at 300 °C in vacuum for a minimum of 2 hours. This was required to ensure that no residual gases from the conducting adhesive resin (Eccobond 56) contaminate the vacuum in the SEM chamber. Eccobond 56 was used for assembly of the ceramic chip components and electrical contacts.

Cryomeasurements

For the superconducting proximity effect investigations, the temperature-dependent resistance measurements, and the examination of transport and magneto-transport properties of the nanowires and FEBID structures, low-temperature measurements were required. A ⁴He bath cryostat with a dynamic variable temperature insert (VTI) from Oxford Instruments was used for this purpose (see Fig. 3.22). The VTI allows the stepwise coverage of the

²Abbreviation for General Purpose Interface Bus

temperature range between 1.4 – 300 K. A step width, that is, the average cooling/heating rate, can be set manually and was ≈ 3 K per minute. The cryostat is equipped with a superconducting magnet that enables measurement in magnetic fields up to 14 T. The simple cryostat design allows for simple and fast sample exchange. For this purpose, a sample rod (where the 24-pin socket and a temperature sensor were mounted) was used. The carrier chip with the sample can be plugged into the socket and loaded into the interior chamber of the cryostat. The socket current/voltage leads are connected to the measurement instruments (DC current/voltage sourcemeter, DC nano-voltmeter, lock-in amplifier), while the temperature sensor is connected to the temperature controller.

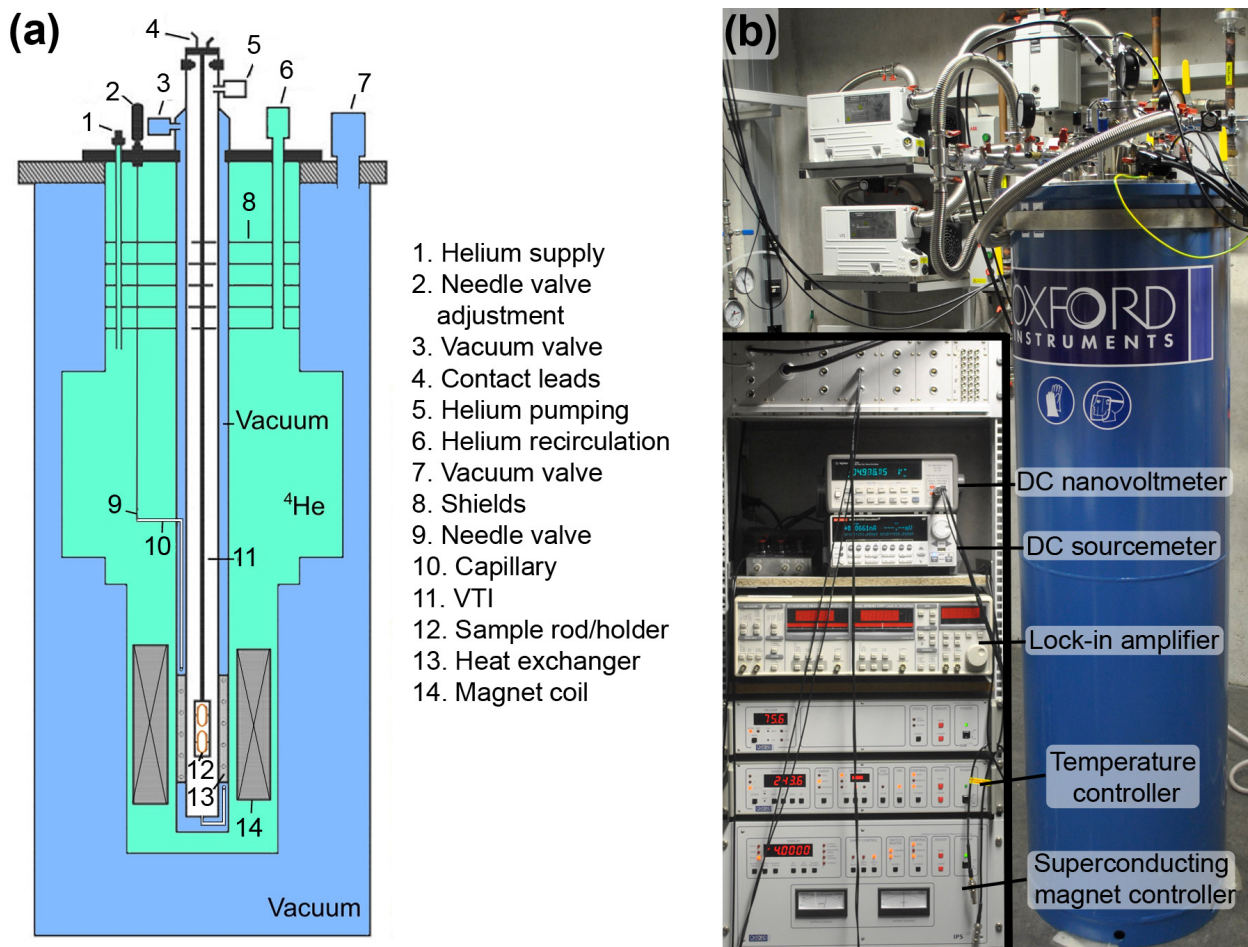


Figure 3.22: (a) Schematic representation of a typical ^4He cryostat internal design. (b) Photograph of the Oxford Instruments ^4He cryostat. Inset: Supplementary measurement and controlling instruments.

The cooling/heating of the sample in the cryostat is based on thermodynamic principles of thermal exchange between the sample and helium gas. For this, liquid helium is transferred with the help of a vacuum pump from the liquid ^4He main bath through a capillary and delivered into the sample chamber of the VTI. The liquid helium flux is controlled by a fine

gauge needle valve. During the delivery, transition of the ^4He from the liquid to the gas state takes place due to the reduced pressure in the VTI. Temperatures below 4.2 K are achieved by lowering the pressure of the ^4He gas vapor around the sample. Vaporized ^4He is pumped through the sample chamber, thus cooling the sample. Temperatures above 4.2 K are achieved by heating the evaporated ^4He gas with a heat exchanger, which surrounds the transport capillary. Precise temperature control (less than 50 mK) is realized via interplay between the helium flux rate (i.e., the position of the needle valve) and the supplied heating power. This can be performed automatically by a PID-based temperature controller.

The superconducting magnet is located at the bottom of the cryostat close to the sample chamber of the VTI, and is completely immersed in liquid ^4He to keep the magnet coils at a constant, low temperature. Thus, at 4.2 K, a magnetic field of up to ± 12 T can be generated. If a higher magnetic field is required, the magnet can be further cooled down by a λ -cooler, and a magnetic field of up to ± 14 T can be obtained. A superconducting magnet controller was used for supplying a high current to the magnet coils and for controlling the magnetic field.

3.3.2 AC electrical magneto-transport measurements

Magneto-resistance (MR) and Hall effect (HE) measurements were performed to study the magnetic properties of Co/Pt heterostructures (see section 6). The coercivity, hysteresis loop squareness and saturation fields are parameters used for the characterization of the samples. Due to the very low MR and HE signal values, the resolution of the DC technique was insufficient and not applicable. For this reason, AC measurements with a lock-in amplifier in conjunction with a differential preamplifier and a ratio transformer to null the signal at $H = 0$ were used [182].

Magneto-resistance measurements

Magneto-resistance is a small effect of the change of a material's resistance with an applied magnetic field; but, for example, for Co/Pt heterostructures it is less than 1 % of the bulk resistance. In order to detect such low signals, alternative measurement techniques must be employed. The magneto-resistance signal, $\Delta R(H)$, is imperceptible due to the relatively overwhelming bulk resistance of the sample. To amplify this small signal a resistance bridge was used, the main task of which was to null out the large resistance signal, $R(0)$, due to the bulk conductance.

The principle of the nulling out step is the following. The voltage, $V(H)$, is produced by

passing the excitation current, I , through the sample, $V(H) = IR(H)$. If a reference voltage is produced that is equal to the zero-field voltage across the sample, $V_0 = IR(0)$, then its value can be subtracted from the actual voltage, $V(H)$, across the sample to obtain $\Delta R(H)$,

$$V(H) - V_0 = IR(H) - IR(0) = I\Delta R(H). \quad (3.6)$$

This very small signal (which is directly related to the magneto-resistance) can then be amplified and analyzed as a function of the applied magnetic field, H .

The nulling procedure can only be performed if a small voltage, V_0 , which is independent of the applied magnetic field is provided. This can be achieved by using a passive adjustable voltage divider, which is driven by the same voltage that delivers the excitation current for the sample. In this work, a low-noise, variable-ratio transformer (RT) was used, which consists of inductive voltage dividers that employ tapped transformers instead of resistors to perform voltage division.

A schematic representation of the setup with the basic components used for the magneto-resistance measurements is shown in Fig. 3.23. The source of an alternating, sine wave current with known amplitude and frequency is applied to the sample by a lock-in amplifier (LIA). The current was approximated by a voltage source ($U = 1$ V, $f = 387.7$ Hz) with a serially connected load resistor ($R = 5$ M Ω), whose value is large compared to the sample resistance. To generate $V_0(t)$, the excitation voltage from the voltage source is split: one part to the load-resistor/sample circuit, and the other part to the input of the inductive divider (RT). The output voltage is some fraction of the input voltage, and that fraction can be adjusted. Each knob on the front of the RT controls one digit in that fraction. The output of the RT is sent to the B-input of the LIA, and the difference between the sample voltage and RT output voltage is measured. The RT must be adjusted until this difference is as small as possible in zero magnetic field. The voltage change in the sample due to the applied magnetic field is measured and amplified with a differential preamplifier (gain = 100) and sent to the A-input of the LIA. The differential preamplifier gain should be taken into account when calculating the change of the sample voltage, $\Delta V(H)$.

Hall effect measurements

Due to the universal geometry of the samples, it was possible to perform Hall effect measurements without the need to fabricate an additional series of samples. The same setup was used for this purpose as for the MR measurements (see Fig. 3.23). The dashed red line in Fig. 3.23 represents the contact configuration for the Hall effect measurements. For the

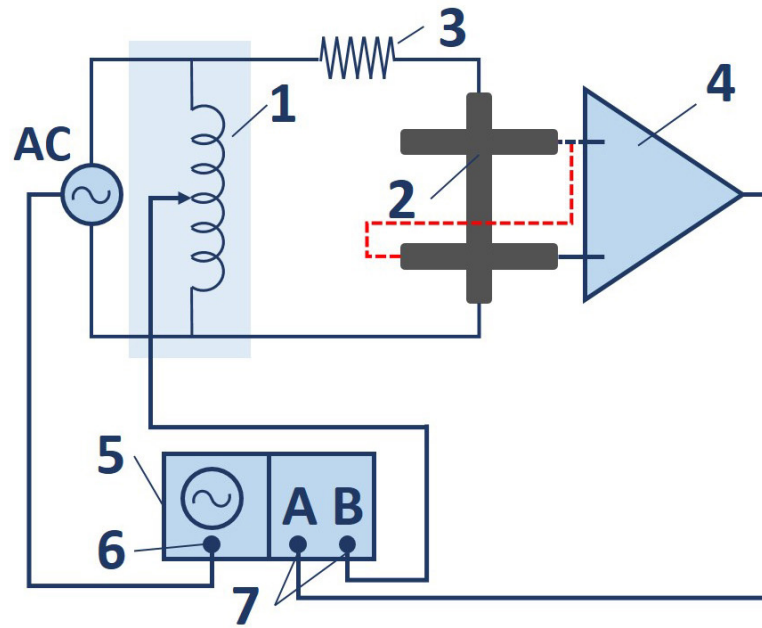


Figure 3.23: Schematic representation of the setup used for magneto-resistance and Hall effect measurements. It is based on AC measurements with a lock-in amplifier in conjunction with a differential preamplifier and a ratio transformer to null the signal at $H = 0$. The dashed red line represents the contact configuration for the Hall effect measurements. The basic components are: (1) ratio transformer, (2) sample, (3) 5 M Ω resistance, (4) differential preamplifier, SR560, (5) lock-in amplifier, SRS830 [(6) internal lock-in reference and (7) lock-in inputs].

MR as well as the HE measurements, the magnetic field was directed perpendicular to the sample surface. All measurements were performed at constant temperatures.

Chapter 4

Proximity effect in single-crystal Cu nanowires

The superconducting proximity effect in single-crystal Cu nanowires is considered in this chapter. Additionally, the overall resistance behavior during cooling of the Cu nanowires are analysed by means of the Bloch–Grüneisen formula. Next, the nanowire resistance drops and resistance peak anomaly at the phase transition of the superconductor in contact is discussed and analyzed in detail. In addition, the large resistance contribution of the ion-beam-damaged regions in the nanowires (caused by application of FIBID) is identified and quantified. Finally, a simple resistance model is introduced and used for quantifying the proximity lengths in the nanowires as a function of temperature. The results of this chapter were published in Refs. [42, 183].

4.1 Transport properties of Cu nanowires

The samples investigated in this chapter are two single-crystalline Cu nanowires prepared by electrochemical deposition. Details of preparation can be found in chapter 3 subsection 3.1.1. Throughout the chapter, the samples will be referred to as Cu-NW1 and Cu-NW2. The superconducting inducer electrode and the current and voltage leads were prepared by FIBID of W and Pt, respectively. W-FIBID is an amorphous, W-based superconductor, with contributions from C and Ga. It has a critical temperature T_c of 4.8 – 5.2 K, depending on the deposition conditions.

Transport measurements on the nanowires were performed in a helium-flow cryostat equipped with a 12 T superconducting solenoid. The electrical resistance was measured as a function of temperature in the standard 4-probe geometry (Cu-NW1) and 8-probe geometry (Cu-NW2) as shown in Fig. 4.1(a) and (b), respectively. In the 4-probe geometry,

all four electrodes were superconducting W-FIBID. In the 8-probe geometry, three pairs of Pt-FIBID voltage leads were attached at different distances L_1 , L_2 , and L_3 (see table 4.1 for distances) besides the superconducting W-FIBID inner inducer electrode. Most of the electrical resistance measurements were taken in constant DC current mode ($I_{DC} = 1\mu A \hat{=} j = 1.6 \text{ kA/cm}^2$). Selected measurements were repeated with a lock-in amplifier. The AC data were essentially the same as those measured with DC current ($I_{AC} = 0.2\mu A \hat{=} j = 0.32 \text{ kA/cm}^2$).

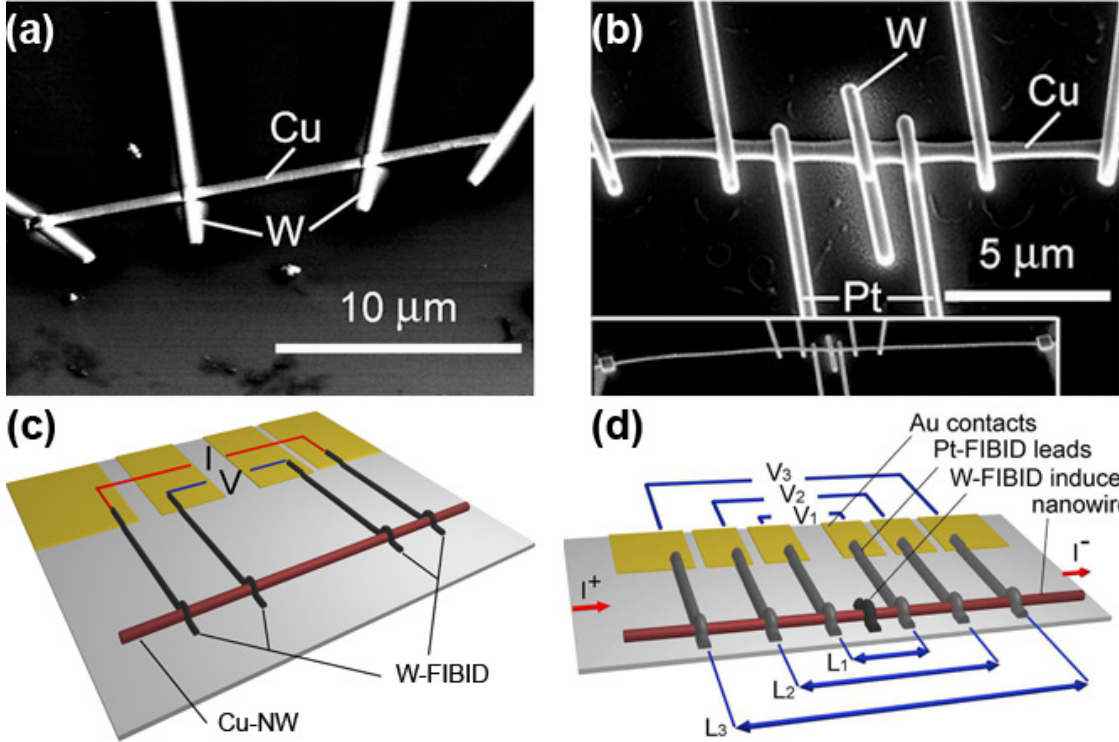


Figure 4.1: (a) SEM image of Cu-NW1 and (c) corresponding to 4-probe geometry used for electrical resistance measurements. (b) SEM image of Cu-NW2 and (d) corresponding to 8-probe geometry. The lower inset in (b) shows the current leads.

Object	Cross-section, nm	Current, μA	Microstructure	L_1 , μm	L_2 , μm	L_3 , μm	Metal content, at. %	O, at. %	C, at. %
Cu-NW1	\varnothing 380	0.2	single-crystal	7.5	\times	\times	95	5	0
Cu-NW2	\varnothing 275	1	single-crystal	2.2	4.6	9	95	5	0

Table 4.1: Structural and compositional parameters of Cu-NW1 and Cu-NW2.

The 8-probe geometry used for electrical resistance measurements [see Fig. 4.1(b,d)] is advantageous as compared to other geometries. Namely, (i) it allows for measurements of the electrical resistance of the nanowire at different distances from the inducer, thereby allowing for the evaluation of the spatial extent of the superconducting order parameter in the nanowire. (ii) The proposed geometry allows measurements to be performed on different sections of the same nanowire, eliminating the problem of reproducibility of the microstructural

sample properties. (iii) This arrangement is very sensitive to the proximity effect due to the elongated nanowire geometry with a large aspect ratio. (iv) The superconducting proximity effect can be studied on nanowires with a wide range of geometrical, microstructural, and compositional properties, as the nanowire fabrication techniques are well established [43–48].

The temperature dependence of the electrical resistance $R(T)$ of Cu-NW1 is presented in Fig. 4.2(a). In addition to a pronounced peak in the vicinity of 5 K, $R(T)$ demonstrates typical metallic behavior: The curve has a practically linear section above 100 K, a residual plateau below 25 K, and a power-law crossover in between. The room-temperature resistivity of Cu-NW1 is $\rho_{295\text{K}} = 2.2 \mu\Omega\text{cm}$, which is by 25% higher than the literature value of $1.7 \mu\Omega\text{cm}$ for bulk copper [76]. This relatively large resistivity is attributed to the presence of ion beam-damaged regions underneath the inducer and voltage electrodes. In Fig. 4.2(b), the resistance peak at $T \approx 5$ K is larger by more than a factor of 30 as compared to the resistance value at 6 K. Below 4.5 K, the resistance of Cu-NW1 drops by almost a factor of 2 as compared to $R_{6\text{K}}$ and remains at this level down to 2.4 K (the lowest temperature achievable in the experiment).

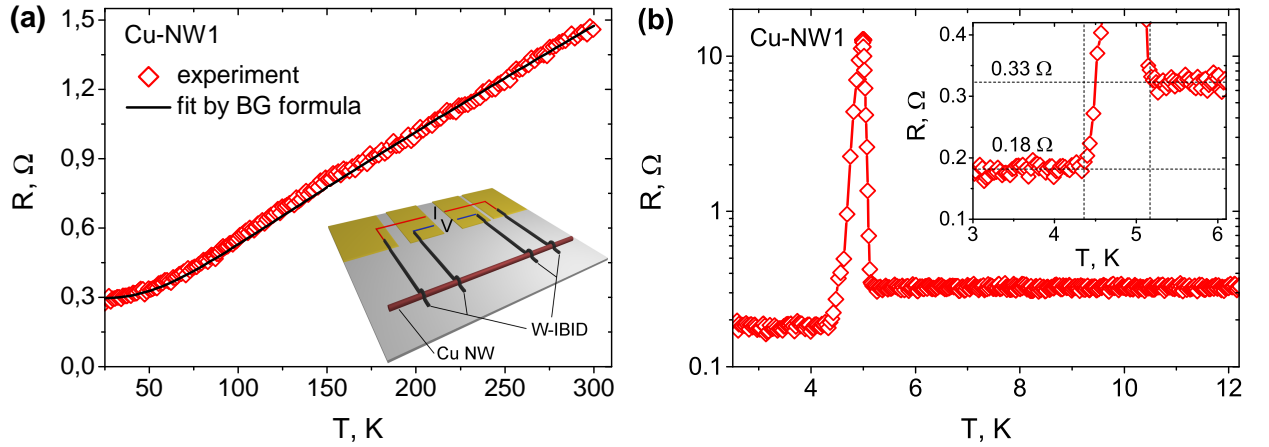


Figure 4.2: (a) The cooling curve $R(T)$ for Cu-NW1. The straight line is a fit to the Bloch-Grüneisen law by Eq. 4.1 with $n = 5$ and a Debye temperature $\Theta_D = 343$ K [76]. (b) The $R(T)$ curve for the same nanowire close to T_c of the superconducting electrodes. Below 5.2 K, an anomalous resistance peak is observed.

The $R(T)$ curve for Cu-NW2 between 15 and 295 K [see Fig. 4.3(a)] is very similar to that of Cu-NW1. The room-temperature resistivity of Cu-NW2 was evaluated by means of the resistance model discussed below in section 4.4, and it is $\rho_{295\text{K}} \approx 2.05 \mu\Omega\text{cm}$. However, in the temperature range between 2 and 15 K, the behavior of $R(T)$ for Cu-NW2 differs from that for Cu-NW1. These distinctive features are presented in Fig. 4.3(b), where $R_{15\text{K}}$ is the resistance at $T = 15$ K. Firstly, no resistance peak was observed in the vicinity of 5 K for Cu-NW2. Secondly, the behavior of the $R(T)$ curves measured for the three nanowire

sections differs substantially. With the reduction of T from 15 to 5.5 K, a residual plateau is maintained for the outer and the middle voltage leads, while for the inner leads the resistance increases by 5%. By further reducing the temperature from 5.5 to 2 K, the resistance of all the sections decreases with different slopes. Here, in contrast to the sudden resistance drop observed in Cu-NW1, the reduction of the resistance with decreasing temperature is much slower and the relative resistance changes are smaller (5-35% as compared to 45% in the case of Cu-NW1). The presence of [refer to L_1 in Fig. 4.3(b)] two different slopes in $R(T)$ below and above 3.7 K is apparent. Finally, for Cu-NW2 the $R(T)$ data were found to be independent of the current for $I < 20 \mu\text{A}$. The $R(T)$ data for the L_1 nanowire section for a set of different currents from $5 \mu\text{A}$ ($\hat{=} j = 8 \text{ kA/cm}^2$) to $20 \mu\text{A}$ ($\hat{=} j = 32 \text{ kA/cm}^2$) are presented in Fig. 4.3(c). As can be seen, the curves perfectly overlap indicating no current-induced modifications of the nanowire conducting properties. This is in contrast to the Co-NW results, which are reported in chapter 5 section 5.5.

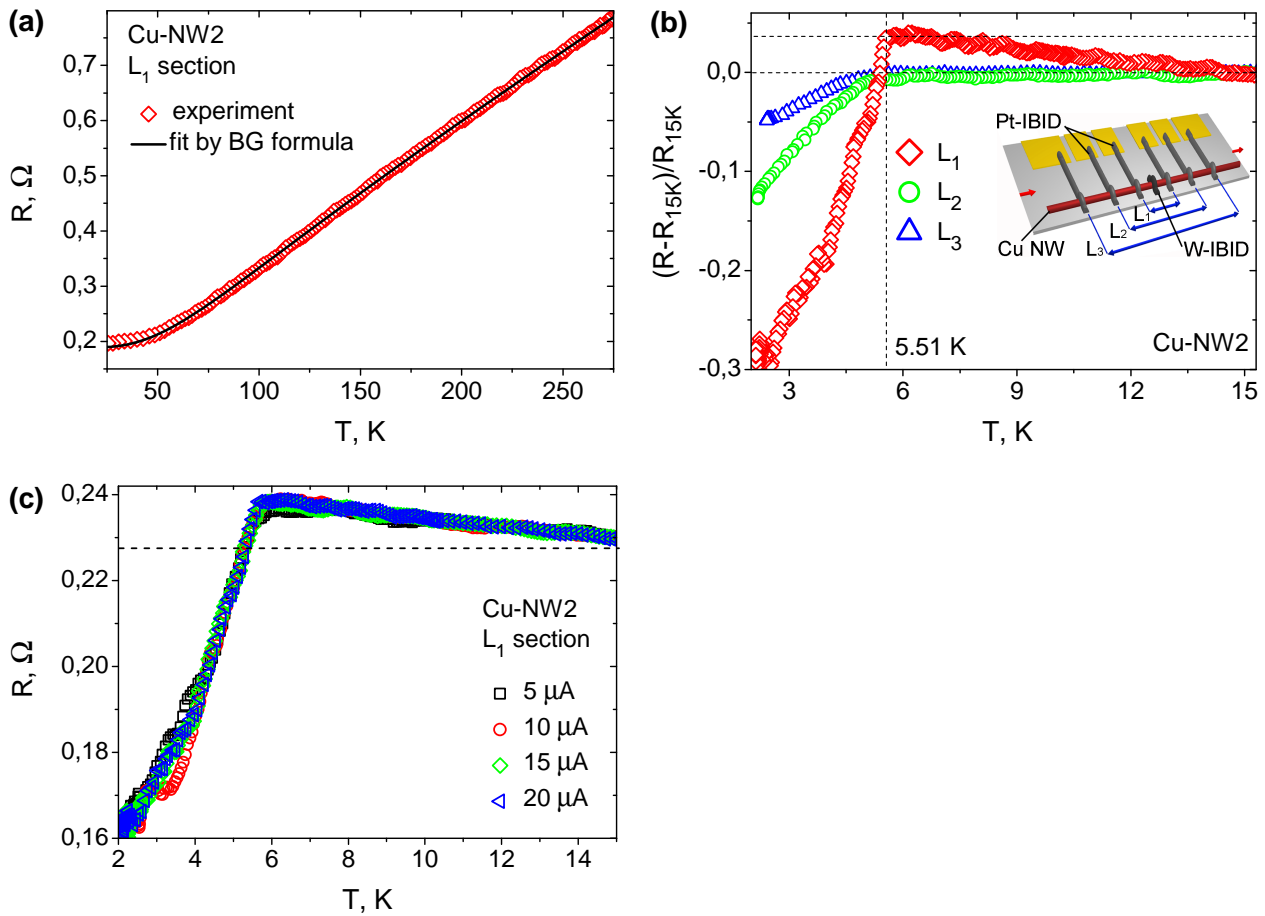


Figure 4.3: (a) The cooling curve $R(T)$ for the L_1 section of Cu-NW2. The straight line is a fit to the Bloch–Grüneisen law by Eq. 4.1. (b) The temperature dependence of the relative resistance changes $(R - R_{15\text{K}})/R_{15\text{K}}$ for the L_1 , L_2 and L_3 sections of Cu-NW2. (c) The same dependence for the L_1 section of Cu-NW2 for a set of different currents from $5 \mu\text{A}$ to $20 \mu\text{A}$.

The overall shape of the $R(T)$ curves for Cu-NW1 and Cu-NW2 can be fit rather well to the Bloch–Grüneisen formula [91, 92]:

$$R(T) = R_0 + K(T/\Theta_D)^n \int_0^{\Theta_D/T} dx \frac{x^n}{(e^x - 1)(1 - e^{-x})}, \quad (4.1)$$

where R_0 is the residual resistance, Θ_D is the Debye temperature (343 K for Cu [76]), and K is a fitting constant. In Eq. 4.1, n is an integer which determines the power law which in turn depends on the prevailing scattering mechanism in the sample. The resulting fit is shown in Fig. 4.2(a). The fitting parameter K has been chosen such that the best possible coincidence with the experimental curve is achieved for $R_{25\text{K}}$ and $R_{295\text{K}}$. The $R(T)$ curve in Fig. 4.2(a) has been fit by Eq. 4.1 with $n = 5$, which implies that the resistance is due to scattering of electrons by phonons, as expected for nonmagnetic metals [91, 92]. Taking into account the close-to-bulk resistivity value for Cu-NW1, it was concluded that this nanowire represents a high-quality reference sample. The cooling curve for Cu-NW2 is also well fit to Eq. (4.1) [see Fig. 4.3(a)] with $n = 5$, but with the lower Debye temperature $\Theta_D = 310$ K and a different residual resistivity contribution.

4.2 Resistance peak anomaly

The resistance peak anomaly in Fig. 4.2(b) is discussed in this section. A resistance peak in the vicinity of T_c of S, similar to that reported in this work, has been observed in a number of experiments [14, 184–186]. Several theoretical models to describe this result [187] have already been proposed. It is widely appreciated that the resistance anomaly and the superconducting PE are two interconnected phenomena. Specifically, the resistance peak usually appears in the vicinity of T_c and, with decreasing temperature, a PE-induced resistance drop takes place. Additionally, for both the resistance peak and drop, the existence of an S/N interface is a necessary condition. According to literature [14, 38, 188]: (i) The appearance of the resistance peak is not related to the magnetic ordering of N, as the effect has been observed for superconductors in contact with ferromagnetic Co [14] and Ni [14], as well as diamagnetic Au [38], Cu (this work), and Ag. (ii) The magnitude of the resistance peak and its form can show a large variability even if the S materials are the same. (iii) The effect depends on the length of the nanowire and the sample–contact interface(s). (iv) The effect is observed regardless of whether S is a part of the electrical circuit or if it is a floating electrode. To explain the resistance peak in Fig. 4.2(b), one can refer to the model suggested in [187], which has already been confirmed experimentally [184]. The main idea of that

model is the following: It has been proposed [184] that an increase of the resistance above the normal-state value at the onset of the superconducting transition is due to a deformed N/S boundary in the vicinity of the voltage probes. The deformed N/S boundary leads to the formation of a nonequilibrium region inside S. The formation of the latter is caused by the injection of quasiparticles from N characterized by a finite value of the electric field and a corresponding effective resistance. Although the situation in this work differs from that of the experiment in [184], some parallels can still be drawn. Here, the FIBID technique was used for contacting Cu-NW1 with two superconducting W-based electrodes. The resulting system has two N/S boundaries with deformed shapes in the vicinity of the contact regions whose asymmetry is the cause of the observed resistance peak. It is therefore suggested that the presence of only one S/N interface in Cu-NW2 is the reason why the resistance peak is absent.

4.3 Arrhenius analysis of resistance drops

The resistance drops in Cu-NW2 are analyzed in this section. As the measurements were taken at small transport currents and the results were found to be independent of the transport current magnitude for $I \leq 20 \mu\text{A}$, an Arrhenius analysis can be applied to the temperature dependence of the resistances in Fig. 4.3(b) in order to check whether some activation mechanism can be identified at $T \lesssim 5.2 \text{ K}$. The Arrhenius analysis relies upon the assumption that the resistance of the sample is independent of the transport current and is given by Arrhenius' law:

$$R = R_0 \exp\left[\frac{-U}{T}\right], \quad (4.2)$$

where R_0 is a constant and U is the activation energy of some process [161, 189].

The Arrhenius plots with $R_0 = R_{15\text{K}}$ are shown in Fig. 4.4. For each section two different activation processes can be identified. The activation energy U of the process dominating at close-to-critical temperatures is higher than that at far-subcritical temperatures. The temperature corresponding to the crossover between the two different activation processes T^* is plotted versus the nanowire section length in Fig. 4.5(a). The thermo-activated process with a lower activation energy is attributed to the resistance contribution originating from the FIBID-damaged nanowire region, while the process with higher U relates to the unaffected regions. The lower activation energy of the damaged-part contribution is caused by an irregular defect distribution. As the temperature decreases below T_c , the intact part first reaches the low-resistance state and for this part, the drop of $R(T)$ is most steep, see Fig. 4.4.

The long nonzero resistance “tail“ down to the lowest achievable temperature suggests that there is an incomplete superconducting phase coherence over the measured nanowire sections even at temperatures far below T_c of the inducer electrode. This incomplete phase coherence is likely caused by thermally induced phase slippage in inhomogeneous regions caused by the FIBID process. The shift of the crossover temperature T^* for the different sections may be explained by different ratios of the ion beam-damaged volume fraction to the total volume of the measured nanowire section. Therefore, the two effects, PE-induced superconductivity and nanopatterning-induced disorder in the ion beam-exposed regions are superimposed. The latter fact is also reflected in that the residual resistivity of Cu-NW2 at 15 K is about $0.67 \mu\Omega\text{cm}$ as compared to about $0.44 \mu\Omega\text{cm}$ for Cu-NW1. Given the impact of the contact procedure, these resistivity values speak for the high structural quality (and attest to the compositional purity, refer also to table 4.1) of both, Cu-NW2 and Cu-NW1.

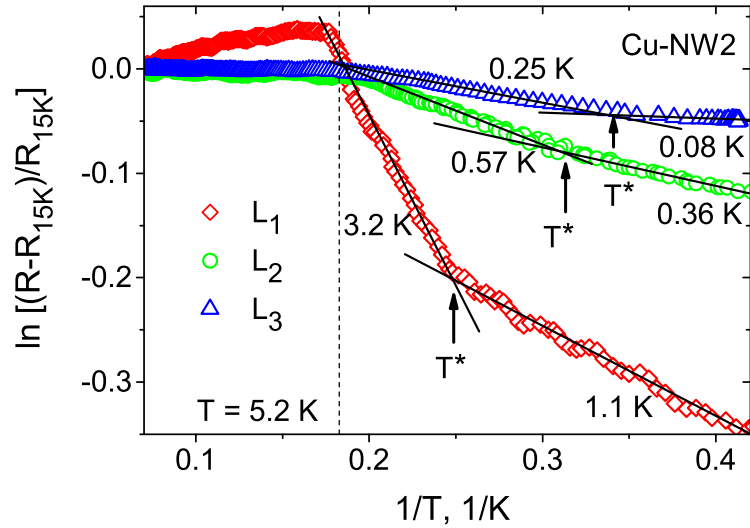


Figure 4.4: Arrhenius plots of the PE-induced resistance drops with the deduced activation energies U for the three nanowire sections of Cu-NW2. Two different activation processes can be identified for all the sections, with a crossover at $T^*(L)$.

4.4 Resistance contribution of ion-beam-damaged areas

In this section, the normal-state resistance changes in Cu-NW2 during the processing by FIBID is considered in more detail. During the FIBID process, some part of the nanowire underneath the W-based and Pt-based electrodes is irradiated by Ga ions. Using simulations by the Monte Carlo method [190], an ion penetration depth of ≈ 25 nm for an ion beam energy of 30 keV was estimated. To account for the resistance changes due to the FIBID processing, the model circuit shown in the inset of Fig. 4.6 was used. In this circuit, the

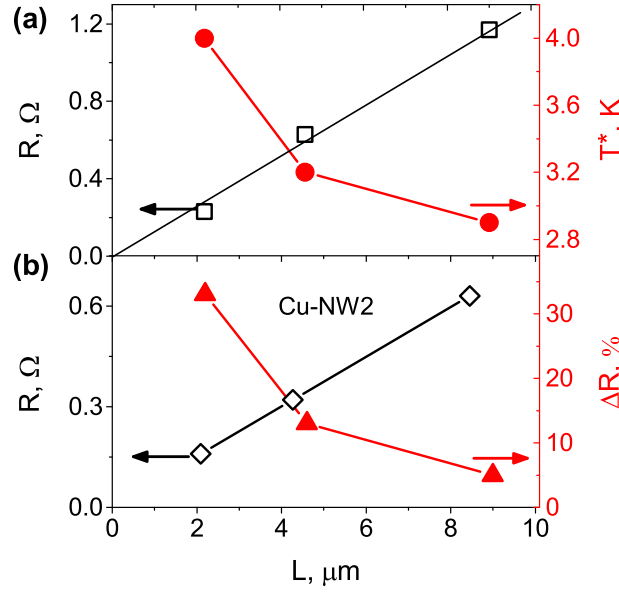


Figure 4.5: (a) Left axis: Dependence of the Cu-NW2 nanowire resistance $R_{15\text{K}}$ (\square) on the measured section length L . The straight line is a linear fit with $\rho_{15\text{K}} = 0.67 \mu\Omega\text{cm}$ for an assumed ideal wire. Right axis: Variation of the crossover temperature T^* versus L (\bullet). (b) Left axis: The nanowire resistance as a function of its length without contributions of the defect-rich contact areas (\diamond), see text for details. Right axis: The relative proximity-induced resistance drops ΔR (\blacktriangle) versus the nanowire section length L .

entire nanowire is modeled as a series of affected and unaffected parts. The unaffected part is denoted as a resistor R while the situation becomes more complicated for the part exposed to the ion beam. This is because of the strongly inhomogeneous distribution of the defects behind ions passing through the material. The distribution of defects is described by the Bragg curve [191], as is depicted in Fig. 4.6.

By using this distribution law for the irradiated nanowire regions, one can distinguish three different degrees of defects across the nanowire cross-section: (i) The defect density is virtually constant in the regions where the ballistic mode prevails in the motion of ions (red part of the Bragg curve in Fig. 4.6). (ii) An enhanced density of defects occurs corresponding to the Bragg peak in the region where the ions are stopped (green part). (iii) An undamaged, internal region of the nanowire (blue part). Each part of the Bragg curve corresponds to a nanowire region with resistance values R_1 , R_2 and R_3 , respectively, which all together define the effective resistance R' of the damaged region. As the exact geometry of the three parts of the nanowire is difficult to estimate, it was impossible to calculate the respective resistivities individually. However, it was possible to quantify the resistivity eigenvalue of the intact nanowire and the resistivity of the regions under the Pt- and W-FIBID electrodes using 25 nm as a rough estimate for the ion penetration depth. In these calculations it was assumed that the nanowire has an ideal cylindrical shape and the current distribution is

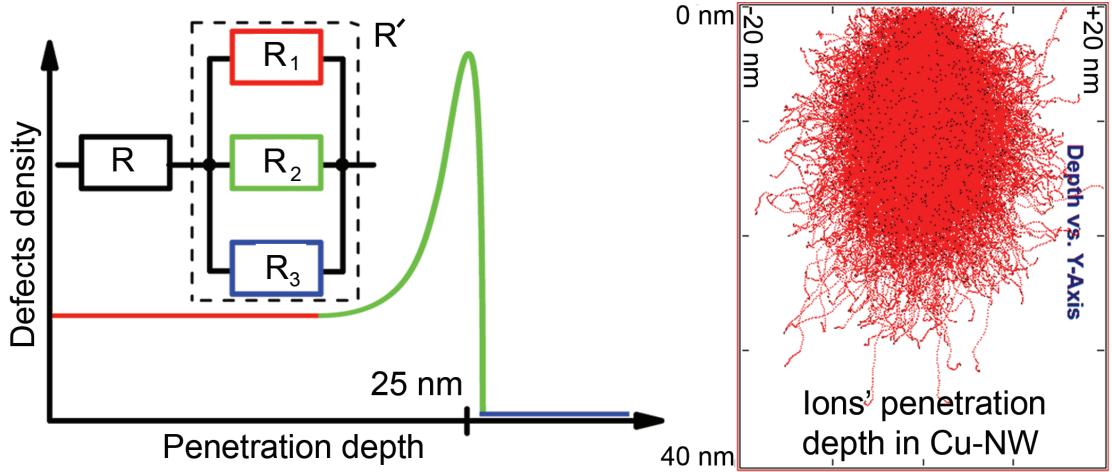


Figure 4.6: Sketch of the resistance model used for quantifying the changes in the nanowire resistivity due to the generation of defects during the FIBID processing. The distribution of defects behind the ion track follows the Bragg curve which has a plateau in the quasi-ballistic regime of the ion motion and a pronounced peak in the diffusive regime. With further increasing depth, the density of produced defects drops to zero. This corresponds to the virtually undamaged region preserved after the dominant portion of ions has been stopped at the characteristic penetration depth which is estimated as 25 nm in the present case.

homogeneous (Appendix B). The central result of the analysis is that the resistivity values for the regions underneath the Pt-based and W-based electrodes at 6 K are $\rho^* = 4.2 \mu\Omega\text{cm}$ and $\rho^{**} = 6.2 \mu\Omega\text{cm}$, respectively. This is an order of magnitude higher than the resistivity of the undamaged Cu nanowire $\rho = 0.45 \mu\Omega\text{cm}$. As a proof of the calculations on the basis of this simple model, one can refer to the resistivity of Cu-NW1 which was not exposed to FIBID over the entire measured section and has virtually the same value $\rho = 0.51 \mu\Omega\text{cm}$ at 6 K. Finally, having subtracted the calculated contributions of the ion-beam damaged regions, the nanowire resistance versus its length is plotted in Fig. 4.5(b) (left axis). One can notice a factor of two reduction of the wire resistance as compared to the as-measured values presented in Fig. 4.5(a) (left axis). From this, it can be concluded that the conducting properties of Cu-NW1 and those of the undamaged regions of Cu-NW2 are very similar and the employed model reasonably describes the changes in the conducting properties of the nanowires during processing by FIBID.

4.5 Quantification of proximity length in Cu nanowire

In this section, the resistance drops in the vicinity of T_c of the W-based inducer electrode are analyzed, and the proximity lengths for both nanowires are quantified. At this point it is important to understand, if the cause of the observed resistance drops is due to: (a) the

superconducting inducer electrode in conjunction with the near-interface region under it, or (b) as discussed below, the proximity-induced superconducting order parameter present in the bulk of the nanowire material. During the FIBID process the topmost layer of the nanowire underneath the W-based inducer electrode is irradiated by Ga ions. Using simulations by the Monte Carlo method [190], the ion penetration depth of ≈ 25 nm for an ion beam energy of 30 keV was estimated. Even assuming that the entire interface region becomes superconducting due to the presence of Ga–C–O and (together with the inducer electrode) it short-circuits the underlying section of the nanowire, the upper estimates for the resistance drop (from the geometrical considerations) is about 12% for the L_1 section of Cu-NW2. In the calculations the widths of the inducer electrodes were taken to be 10% larger than those seen in the SEM image in order to account for possible spreading of the tungsten from the inducer. Hence, since the observed resistance drops (35% for the L_1 nanowire section) are at least a factor of 3 larger than the values estimated above. It was thus concluded that the superconducting proximity effect takes place in the bulk of the nanowire material.

The treatment of the resistance data in the 8-probe geometry relies upon the model electrical circuit sketched in Fig. 4.7. A nanowire of length L in contact with a superconducting inducer located at the middle of the nanowire is considered. It is assumed that the current distribution in the cross-section of the nanowire is homogenous and it is not affected by the Pt-based voltage leads and the W-based inducer. At $T > T_c$ the nanowire can be regarded as a resistor with the normal-state resistance R_0 . By contrast, at $T < T_c$, when Cooper pairs propagate from the superconducting inducer into the nanowire, a finite fraction of the nanowire becomes superconducting. The length of the superconducting section of the nanowire is twice the proximity length 2ξ , since Cooper pairs propagate in both directions along the nanowire axis. The remaining part of the circuit of length $(L - 2\xi)$ is in the normal state with the residual resistance $R_r = R_0(L - 2\xi)/L$. According to the model circuit in Fig. 4.7, the total resistance of the measured nanowire section is $R = R_0(L - 2\xi)/L + R_s(2\xi/L)$, where the proximity length is

$$\xi = L(R_0 - R)/2R_0. \quad (4.3)$$

An analogous model can be applied to Cu-NW1 in the 4-probe geometry where Cooper pairs spread from the superconducting voltage electrodes inwards towards the nanowire. In this way, using Eq. 4.3 and the experimental data reported in Figs. 4.2(b) and 4.3(b), the proximity lengths for both nanowires can be calculated. The resulting curves $\xi(T)$ for Cu-NW1 and Cu-NW2 are shown in Figs. 4.8(a) and (b), respectively.

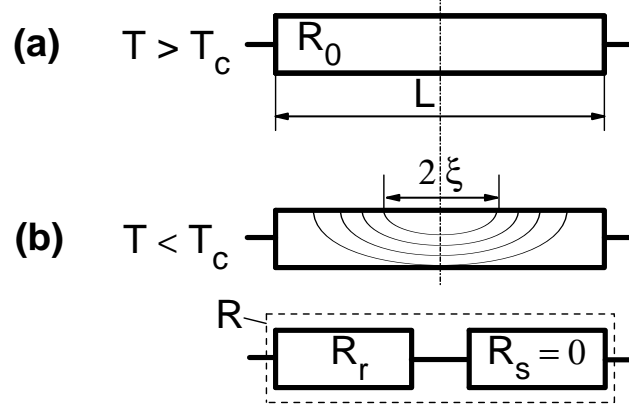


Figure 4.7: (a) At $T > T_c$ the nanowire is modeled as a resistor R_0 . (b) At $T < T_c$ the Cooper pairs propagate from the superconducting inducer into the nanowire and a finite fraction of the nanowire becomes superconducting. The spatial extent of the superconducting condensate in the nanowire at different temperatures is shown by the contour lines. Bottom panel: The model electrical circuit used for the quantification of the proximity length in the nanowires.

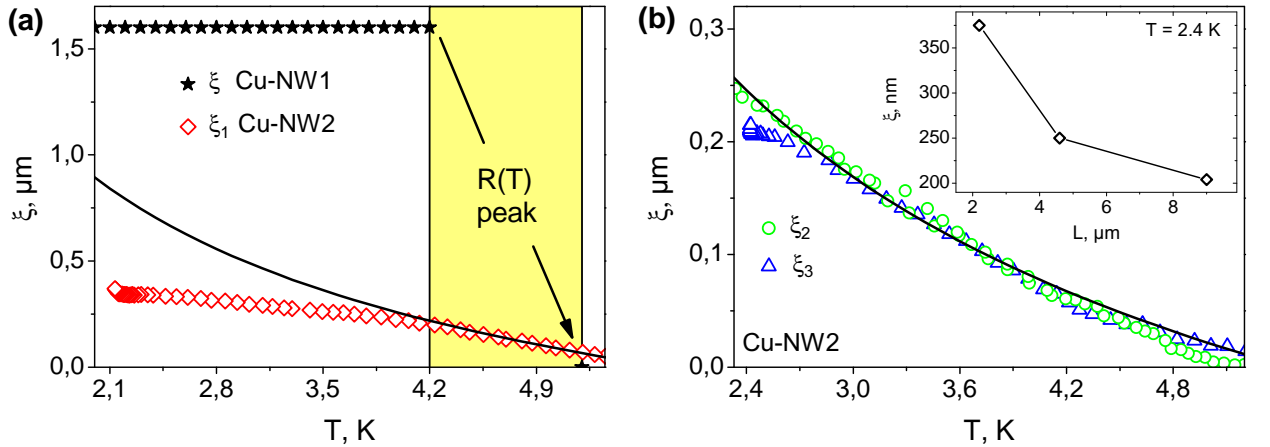


Figure 4.8: The temperature dependences of the proximity lengths for Cu-NW1 (a) and Cu-NW2 (a) and (b), respectively. The proximity lengths ξ_1 , ξ_2 and ξ_3 have been deduced by Eq. 4.3 from the $R(T)$ data measured on the sections L_1 , L_2 and L_3 , respectively. The solid lines are fits to an expression of the form $\xi(T) \propto \sqrt{1/T}$. Note a factor of two deviation of $\xi(T)$ from the fit curve in (a) for $T < 4$ K which is attributed to the enhanced degree of disorder caused by the processing by FIBID. Inset to (b): The proximity length deduced for the different measured sections at 2.4 K for Cu-NW2.

The proximity length in the Cu-NW1 at 2.4 K is $\xi = 1.6 \mu\text{m}$. This is an exemplary value for the spin-singlet proximity length in pure diamagnetic materials. In the vicinity of T_c the quantification of $\xi(T)$ is not possible as the exact shape of the resistance drop is masked by the resistance peak. The proximity length in Cu-NW2 at 2.4 K is a factor of five shorter than that in Cu-NW1 and is attributed to the degradation of the conducting properties of Cu-NW2 in the ion beam-irradiated regions. The temperature dependences $\xi_2(T)$ and $\xi_3(T)$ for Cu-NW2 in Fig. 4.8(b) can be well-fitted to an expression of the form $\xi(T) \propto \sqrt{1/T}$.

This is in good agreement with the theoretical predictions for the temperature dependence of the superconducting proximity length in the diffusive limit (details can be found in chapter 2 subsection 2.2.2). There is a notable deviation of $\xi_1(T)$ for Cu-NW2 from the fit curve below 4 K in Fig. 4.8(a) where the suppression of the proximity length is believed to be caused by the enhanced scattering of the Cooper pairs in the defect-rich regions of the nanowire.

In the inset of Fig. 4.8(b) the calculated proximity length in Cu-NW2 for the different measured sections at 2.4 K is illustrated. One can see from the data that $\xi(L)$ for Cu-NW2 decreases with increasing distance between the voltage leads. This is attributed to the increasing scattering of the Cooper pairs in the disorder-rich regions underneath the contacts as the number of contacts between the voltage leads rises.

4.6 Rigidity of the proximity effect in Cu nanowire against magnetic fields

With the aim to examine the rigidity of the superconducting PE in Cu-NW2, magnetic field measurements of $R(T)$ at different magnetic fields up to 10 T were performed. The magnetic field was directed perpendicular to the nanowire axis. The measurements were performed after the main series of measurements reported in previous sections were completed. The obtained $R(T)$ curves for the L_1 section of Cu-NW2 are presented in Fig. 4.9(a). As can be seen from the $R(T)$ curve at 0 T, the resistance drop occurs in two steps. In the first step between 5.35 K and 5.45 K, the resistance drops sharply to $\approx 95\%$ of its normal state value. At ≈ 5.1 K, a second resistance drop takes place followed by the long nonzero resistance “tail” down to the lowest achievable temperature (≈ 2 K) with two different slopes below and above 4 K. As result, two different T_c s revealed by two distinct transitions can be distinguished. It is suggested that the first resistance drop is related to the superconducting transition of the inducer electrode. The second resistance drop occurs due to the PE-induced superconductivity in the nanowire, which resulted in the emergence of a small superconducting “mini-gap” δ in the regions of the nanowire far from the superconducting inducer electrode [192]. In the meantime, the gap in the nanowire in the direct vicinity of the inducer electrode corresponds to the gap Δ of the inducer electrode (i.e., the W-FIBID superconductor). Further, by application of the magnetic field, the onset temperature of the resistance drop is shifted towards lower temperatures. Moreover, the first resistance drop vanishes at a magnetic field of about 10 T. In order to suppress the second resistance drop, magnetic fields of approximately a factor of two lower were required. As can be seen in Fig. 4.9(b), the data points $H(T)$, obtained by plotting the field values versus the tempera-

ture at which the onset of the resistance drops takes place for both cases, nicely follows the empirical law [193]:

$$H(T) = H_c(0)[1 - (T/T_c)^2], \quad (4.4)$$

where $H_c(0) = H_c^\Delta(0) = 10$ T, suggesting that this field corresponds to the upper critical field of the superconducting inducer electrode with $T_c = T_c^\Delta = 5.4$ K, whereas $H_c(0) = H_c^\delta(0) = 6.4$ T and $T_c = T_c^\delta = 5.1$ K corresponds to the PE-induced superconductivity in Cu-NW2. The resulting dependences of $H(T)$ are accompanied by fits to Eq. (4.4), which are represented in Fig. 4.9(b) by the solid lines.

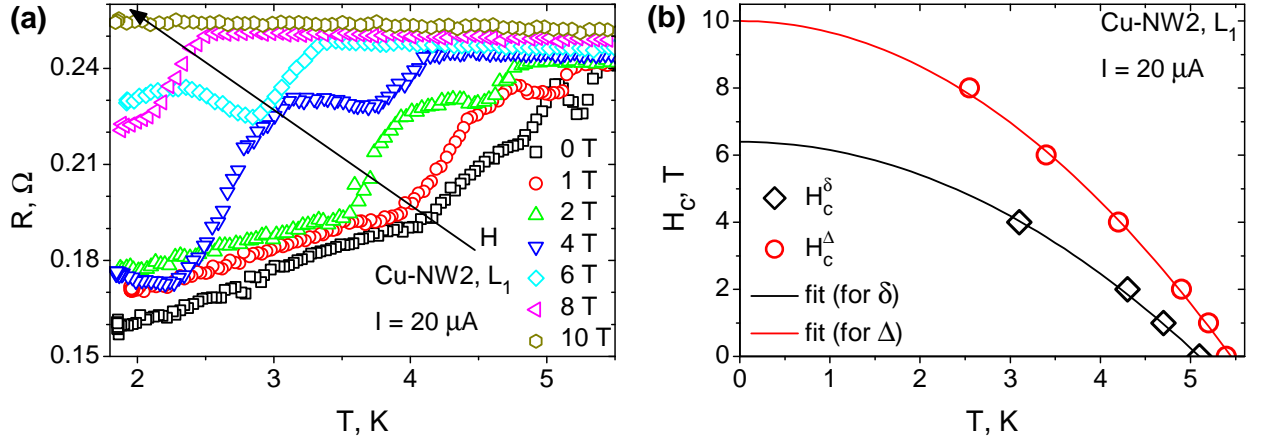


Figure 4.9: (a) Temperature dependence of the resistance of the L_1 section of Cu-NW2 for a set of applied magnetic fields from 0 to 10 T with a step width of 2 T along the arrow. (b) The temperature dependence of the magnetic field H_c corresponding to the onset of the downturn in the $R(T)$ curves in (a) for the superconducting state in the W-based inducer electrode (open red cycles) and PE-induced superconductivity in the nanowire (open black rectangles). The solid lines are fits to Eq. (4.4).

The magnetoresistance of the L_1 section of Cu-NW2 measured at several different temperatures is presented in Fig. 4.10(a). The applied magnetic field was directed perpendicular to the nanowire axis. From the evaluation of the $R(H)$ curves one can clearly identify the superconducting transition at low temperatures, which vanishes with increasing temperature. However the main focus is on the behavior of the $R(H)$ curves where the nonmonotonic resistance increase can be clearly identified. This dependence exhibits periodic oscillations, resulting in pairs of mini-resistance peaks and valleys in the $R(H)$ dependence that are symmetric with respect to $H = 0$ and vanish with increasing temperature. Furthermore, upon differentiation, resistance oscillations of smaller amplitude become evident. Thus, in Fig. 4.10(b) the numerical derivative dR/dH as a function of H at 1.8 K for positive magnetic fields is shown. For comparison, the periodic differential magnetoresistance oscillations in

Au nanowires connected to superconducting electrodes (reported by Wang *et al* [38, 194]) are presented in the inset of Fig. 4.10(b). It has been proposed that such oscillations in dR/dH are caused by (i) the induced superconductivity in the nanowire by the proximity effect (ii) accompanied by the generation and movement of superconducting vortices in response to the increasing perpendicular magnetic field across the wire. Additionally, it has been shown that the oscillation period can be approximately calculated as $B = \Phi_0/(2\pi r^2)$ (where $\Phi_0 = h/2e$ is superconducting flux quantum, r is the radius of the nanowire). However, application of this conclusion to the magnetoresistance oscillations observed for Cu-NW2 with $r = 137$ nm did not comply, for which calculated B should be 4.4 mT. This is in contrast to the measured period of oscillations shown in Fig. 4.10(b) (for magnetic field up to 5 T), which is approximately 0.5 T.

An examination of whether 300 nm-thick Cu nanowires are systematically able to generate a “mini-gap” state over the entire measured section must remain for future elaboration on a large number of samples.

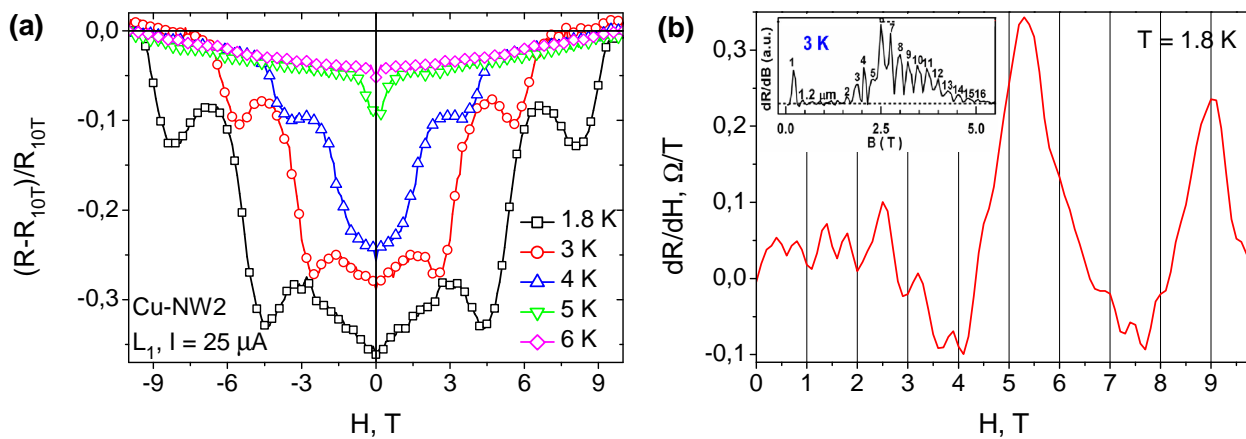


Figure 4.10: (a) Magnetoresistance of the L_1 section of Cu-NW2 measured at different temperatures. (b) Periodic oscillations of the differential magnetoresistance plotted as a function of magnetic field of the L_1 section of Cu-NW2 at 1.8 K. Inset: Periodic differential magnetoresistance oscillations in Au nanowires connected to superconducting electrodes. Such oscillations are caused by the generation and movement of superconducting vortices across the nanowire (reproduced after [194]).

Chapter 5

Proximity effect in polycrystalline and nanogranular Co nanowires

Experimental evidence of a long-range superconducting proximity effect in polycrystalline Co nanowires in contact with a superconducting, W-based, floating electrode (inducer) is reported in this chapter. For electrical resistance measurements voltage leads were connected at different distances to the Co nanowire on both sides of the superconducting inducer. A 28% reduction of the nanowire resistance was observed when sweeping the temperature to below the transition temperature of the inducer ($T_c = 5.2$ K). The analysis of the resistance data shows that the superconducting proximity length in polycrystalline Co is as large as $1 \mu\text{m}$ at 2.4 K, attesting to a long-range proximity effect. Moreover, this long-range proximity effect is not susceptible to magnetic fields up to 11 T, which is indicative of spin-triplet pairing. The presented results provide evidence that magnetic inhomogeneity of the ferromagnet enlarges the spatial extent of the spin-triplet superconducting proximity effect. At the same time, it has been found that the proximity-induced superconductivity in nanogranular, nanowire-shaped Co-FEBID structures is strongly suppressed, most likely due to the enhanced pair breaking effects. The results of this chapter were published in Refs. [15, 42, 183].

5.1 Transport properties of Co nanowire and Co-FEBID structure

The samples investigated in this chapter are one polycrystalline Co nanowire prepared by ECD and one nanogranular, nanowire-shaped Co structure prepared by FEBID of Co¹. Details of preparation can be found in chapter 3 subsections 3.1.1 and 3.1.4, respectively. Throughout this chapter, the samples will be referred to as Co-NW and Co-FEBID, respec-

¹Precursor $\text{Co}_2(\text{CO})_8$, $E = 3$ kV, $I = 90$ pA, $p = 5$ nm, $t_D = 1 \mu\text{s}$, working $P = 1.3 \times 10^{-5}$ mbar, base $P = 7 \times 10^{-6}$ mbar.

tively. The SEM images of the samples are shown in Fig. 5.1(a) and (b). The Co-FEBID sample was prepared as a rectangular, nanowire-shaped deposit supplemented with six pairs of additional transverse side branches [see Fig. 5.1(b)]. The entire sample was fabricated in one single deposition process. This ensured that the side branches could act as contact pads for the Pt-FIBID voltage leads, thereby preventing irradiation of the main deposit by the ion beam. The superconducting, inducer electrode as well as the current and voltage leads to the nanowires were prepared by FIBID of W and Pt, respectively. The W-FIBID deposit is an amorphous, W-based superconductor ($T_c = 4.8 - 5.2$ K), with contributions of C and Ga.

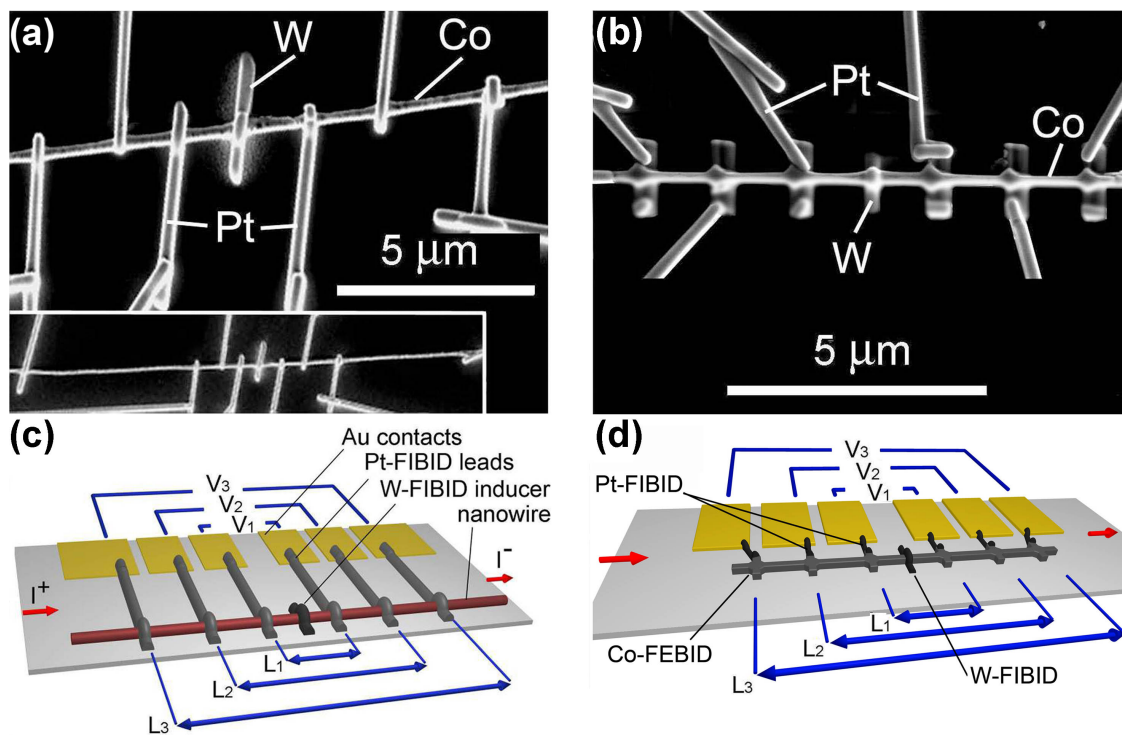


Figure 5.1: SEM images of the fabricated (a) Co-NW and (b) Co-FEBID nanowires. The lower inset in (a) depicts the current leads. (c) and (d) Corresponding 8-probe geometries used for electrical resistance measurements. Only the inner, floating electrode is made of superconducting W-FIBID, while others are of non-superconducting Pt-FIBID.

Transport measurements were performed in a helium-flow cryostat equipped with a 12 T superconducting solenoid. The electrical resistance of the Co-NW and Co-FEBID samples was measured as a function of temperature in the 8-probe geometry, as is shown in Fig. 5.1(c, d). Three pairs of Pt-FIBID voltage leads were attached at different distances, L_1 , L_2 , and L_3 (see Tab. 5.1 for values) beside the superconducting, W-FIBID inner inducer electrode. The resistance was measured in fixed-current mode with a DC current of 100 nA corresponding to a current density of 162 A/cm² for the Co-NW and 0.5 μ A corresponding to a current density of 13 kA/cm² for the Co-FEBID sample.

Object	Cross-section, nm \odot or $w \times d$	Current, μA	Microstructure	L_1 , μm	L_2 , μm	L_3 , μm	Metal con- tent, at. %	O, at. %	C, at. %
Co-NW	\odot 280	0.1	polycrystalline	3.8	7.2	12	59	41	0
Co-FEBID	155×255	0.5	nanogranular	2.1	4.8	7.5	71	14	15

Table 5.1: The structural and compositional parameters of Co-NW and Co-FEBID. w : width; d : thickness.

Figure 5.2(a) depicts the cooling curve for the L_2 section of Co-NW, which demonstrates a thermally activated behavior. The room-temperature resistivity of Co-NW $\rho_{295\text{K}} = 1771 \mu\Omega\text{cm}$ is two orders of magnitude larger than the literature value of about $5.8 \mu\Omega\text{cm}$ for bulk Co [76]. It is suggested that this high resistivity value is related to the contribution of the grain boundaries between individual Co crystallites rather than the resistivity of individual Co-crystallites. The low-temperature resistance data for the different voltage probes are presented in Fig. 5.2(b). As observable from the figure, the superconducting PE prevails over the localization behavior below 5.2 K, as the curves start to deviate from the thermally activated behavior. With further reduction of the temperature, a rapid drop of the resistance follows for the inner and the middle voltage probes, while the drop is less pronounced for the L_3 section. The largest resistance drop of about 28% with respect to the normal resistance state was observed for the L_2 section. To treat these $R(T)$ drops, the same model electrical circuit as applied to Cu nanowires and sketched in Fig. 4.7 was used. Results of this analysis are presented in section 5.4.

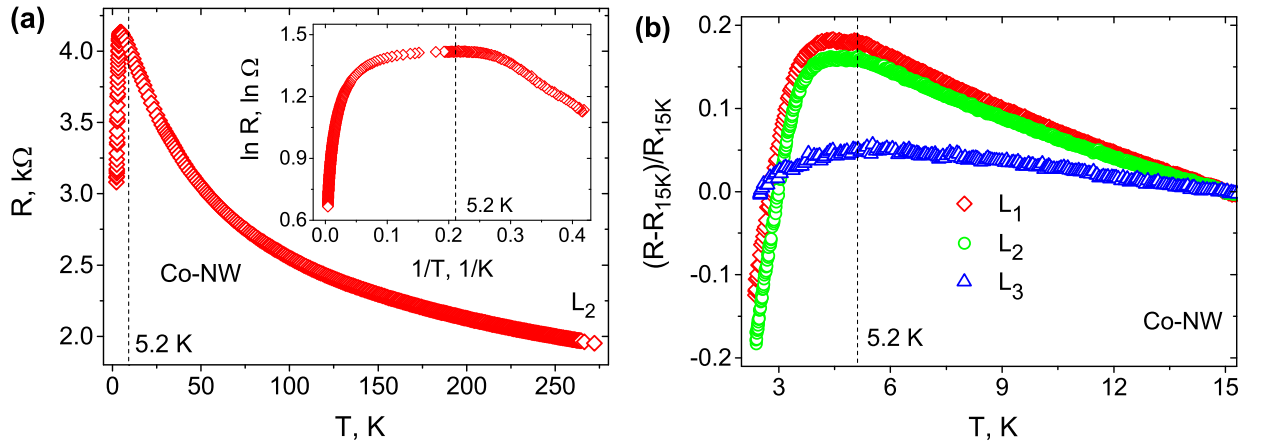


Figure 5.2: (a) Cooling curve $R(T)$ for the L_2 section of Co-NW. Inset: The same data in $\ln R$ vs. $1/T$ representation. The vertical dashed lines mark the temperature where the curves start to deviate from the localization behavior. (b) PE-induced resistance drops for the three sections of Co-NW.

The cooling curve for the L_1 section of the Co-FEBID nanowire is shown in Fig. 5.3(a). The room temperature resistivity of Co-FEBID is $\rho_{295\text{K}} = 84 \mu\Omega\text{cm}$, approximately 15 times larger than that of the reference bulk value [76]. The cooling curve has an almost linear,

metallic-like section between 295 K and 30 K and demonstrates a tendency towards localization at lower temperatures. This is followed by a resistance drop at about 4.8 K. Fig. 5.3(b) displays the low-temperature resistance data for the three pairs of potential probes. Above 4.8 K, the inner section $R(T)$ increases with decreasing temperature, while for the middle and outer sections $R(T)$ decreases with decreasing temperature, with different temperature derivatives. The relative resistance drops for the L_1 , L_2 and L_3 sections are only $\approx 5\%$ with respect to $R_{4.8K}$.

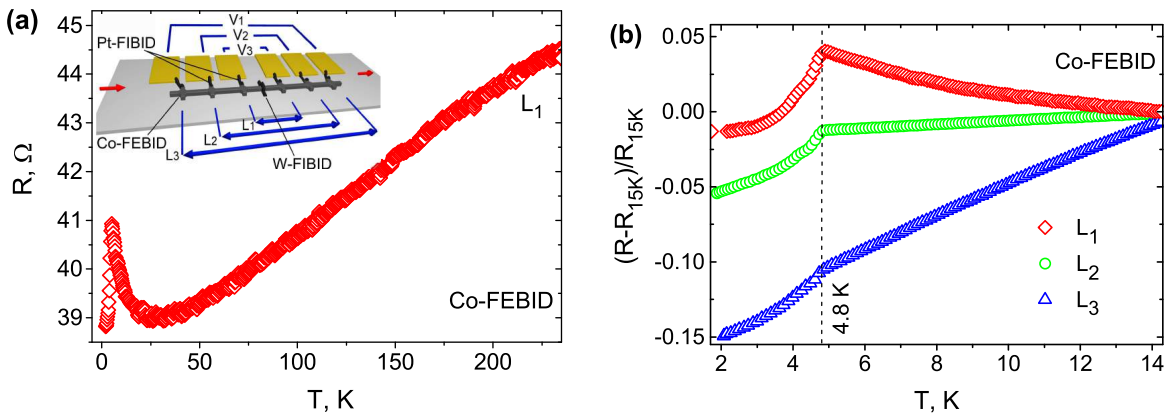


Figure 5.3: (a) Cooling curve $R(T)$ for the L_1 section of Co-FEBID. (b) The low-temperature, relative resistance changes for the three sections of the Co-FEBID structure.

5.2 Rigidity of the proximity effect in Co nanowire against magnetic fields

In section 5.1 it was shown that the resistance drops for Co-NW in the vicinity of 5 K are of the same order of magnitude as those for Cu nanowires (see chapter 4, section 4.1). The magnitude of the $R(T)$ drops clearly indicates that the superconducting PE in Co-NW is long-ranged. One explanation of the observed phenomenon is that the superconductivity in the Co nanowire may be triplet in nature. Another suggestion could be that the surface of the nanowire is not ferromagnetic and the PE is due only to the singlet effect stemming from the outermost non-ferromagnetic layer of the nanowire. Further support of the conclusion that the observed effect is triplet in nature can be obtained from its magnetic field dependence. Namely, if the pairing is spin-triplet, proximity-induced superconductivity in the ferromagnet should survive as long as the magnetization saturation field of the ferromagnet or the critical field of the superconductor is not reached, whichever is smaller. Otherwise, if the pairing is singlet, proximity-induced superconductivity is known to be suppressed in micrometer-thick

superconductors at fields substantially smaller than the upper critical field H_{c2} of the inducer electrode [110]. At the same time, reports that proximity-induced singlet superconductivity in $\simeq 50$ nm-thick nanowires can survive up to fields $H \lesssim H_{c2}$ of the W inducer were also given [14, 38]. Co-NW is a factor of five thicker than those in Refs. [14, 38], placing it between the existing reports.

Measurements of the $R(T)$ of Co-NW in magnetic fields up to 11 T were performed with the field aligned in the substrate plane at an angle of 67° with respect to the nanowire axis. The oblique angle was a result of the accidental orientation of the nanowire with regard to the pre-formed contact pads. The measured $R(T)$ curves for the L_1 and L_2 sections are presented in the main panels of Fig. 5.4(a) and Fig. 5.4(b), respectively. One can clearly see that with increasing magnetic field the temperature of the $R(T)$ maximum shifts towards lower temperatures, but the drop itself is maintained up to 11 T. It was found that the data points $H^{\text{dev}}(T)$, obtained by plotting the field values versus the temperature at which the $R(T)$ curves start to deviate from the localization behavior, nicely follows the empirical law [193]:

$$H^{\text{dev}}(T) = H_c(0)[1 - (T/T_c)^2], \quad (5.1)$$

where $H_c(0) = 14.1$ T is the upper critical field and $T_c = 5.2$ K is the superconducting transition temperature of the inducer. The resulting dependence $H^{\text{dev}}(T)$ accompanied by a fit to Eq. (5.1) for the L_1 section is shown in the inset of Fig. 5.4(a) by the solid line. For the L_2 section, the $H^{\text{dev}}(T)$ curve can also be fitted well by Eq. (5.1) with the same $H_c(0)$ and T_c , as shown in the inset of Fig. 5.4(b).

From these results it is clear that the disappearance of proximity-induced superconductivity is not due to pair-breaking effects in the Co nanowire, but rather due to the breakdown of superconductivity in the W inducer itself. Therefore, the conclusion can be made that the observed effect is related to the fact that spin-triplet pairing is unsusceptible to the magnetic field.

To conclude the presented analysis, it should be noted that both singlet and triplet Cooper pairs are sensitive to orbital depairing, whereas only singlet pairs are sensitive to spin depairing. This suggests that one of the mechanisms for the breakdown of superconductivity in Co-NW is not effective. Namely, if the spin-sensitive depairing mechanism is absent in Co-NW, the observed robustness of the PE against fields follows readily and indicates that the PE effect in Co-NW is spin-triplet in nature. A discussion of the magnetic inhomogeneity sources responsible for the observed long-range PE is presented in the next section.

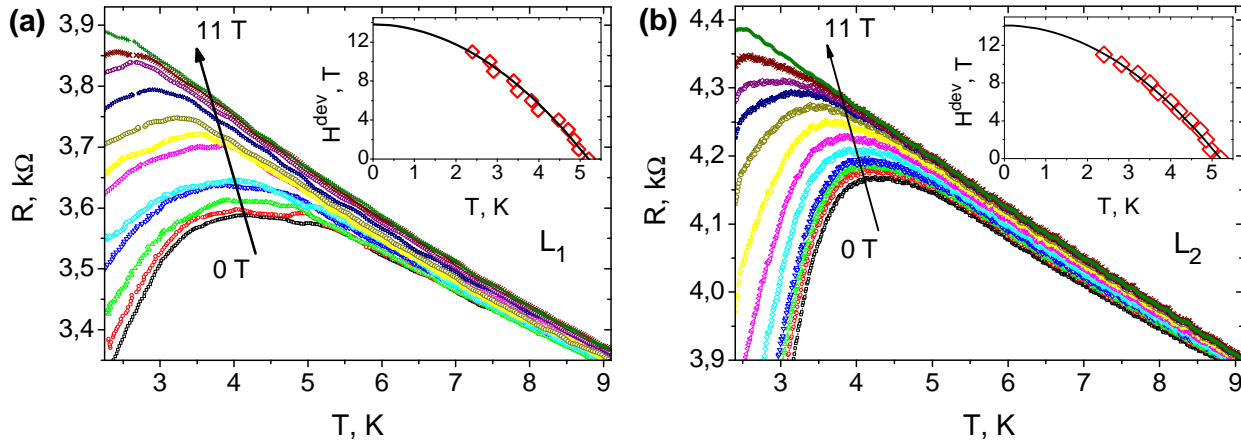


Figure 5.4: The temperature dependence of the resistance of the L_1 (a) and L_2 (b) sections of Co-NW for a set of applied magnetic fields from 0 to 11 T with a step width of 1 T along the direction of the arrow. Insets: The temperature dependence of the magnetic field H^{dev} corresponding to the onset of the downturn in the $R(T)$ curves for Co-NW in the main panels. The solid lines are fits to Eq. (5.1) with $H_c(0) = 14.1$ T for Co-NW, suggesting that this field corresponds to the (upper) critical field of the superconducting inducer electrode.

5.3 Origins of magnetic inhomogeneities in Co nanowire

As was theoretically shown by Bergeret *et al.* [12], a local inhomogeneity of the magnetization in the vicinity of the S/F interface is necessary for the spin-triplet pairing in S/F structures. In this section, the microstructural peculiarities of the explored S/F system, which made it possible to observe the long-range spin-triplet PE, are presented. Four different sources of magnetic inhomogeneity in the nanowire are considered, which can roughly be categorized according to its polycrystalline microstructure and those due to the FIBID processing:

(i) The investigated nanowire has a polycrystalline microstructure, as confirmed by both X-ray diffraction measurements and direct SEM inspection (see chapter 3 subsection 3.2.2). Accordingly, a multidomain state with domain boundaries located at the boundaries of crystallites should be assumed for its ground state. In 200 nm-thick Co nanowires, the magnetization saturates at about 1 T [195] which can be taken as a rough estimate for the 280 nm-thick Co nanowire.

(ii) Since peaks related to Co_3O_4 were observed in the X-ray diffraction data (see chapter 3, subsection 3.2.2), it is assumed that the cobalt oxide is located at the boundaries of individual crystallites. Electrically, this assumption is in line with the resistance measurements where a clear tendency towards localization behavior has been observed. This corresponds to a thermally assisted electron tunneling regime between neighboring grains separated by a cobalt oxide layer. It is this tunneling regime which causes the observed high-resistance state of the polycrystalline Co nanowire. Magnetically, Co_3O_4 is a strong

antiferromagnet with a magnetization saturation field larger than 10 T [196].

(iii) During the FEBID process, the Ga ions (30 kV) are stopped in the 30 nm thick top-most layer of the nanowire [197]. The Ga irradiation causes amorphization, implantation and vacancy generation underneath the auxiliary electrodes. This means that the nanowire leads and the nanowire-inducer interfaces have a modified bulk and surface magneto-crystalline anisotropy which causes an inhomogeneity.

(iv) In the FEBID process, Pt–Co intermixture can lead to the formation of CoPt alloy or L_{10} phase [74] at the interfaces of the Pt-based leads and the Co nanowire. The L_{10} phase is a hard ferromagnet.

Given the sources of inhomogeneity mentioned above, the magnetization saturation fields of Co and CoPt L_{10} indicate that 1-2 T should be enough to cause a magnetically homogeneous state to quench the triplet PE. At the same time, as the proximity length scale order is larger than the average grain size (i.e., Cooper pairs tunnel between grains) it is believed that the presence of the antiferromagnetic Co_3O_4 is the dominant cause for the rigidity of the PE at large magnetic fields.

5.4 Quantification of proximity length for Co nanowire and Co-FEBID

The analysis of the resistance data in the 8-probe geometry relies upon the model electrical circuit used for Cu nanowires as sketched in Fig. 4.7. Using Eq. (4.3) and the $R(T)$ data in Fig. 5.2(b) the proximity length as a function of temperature was calculated. The resulting $\xi(T)$ curves for the different measured sections of Co-NW are shown in Fig. 5.5(a). These are decreasing functions of temperature and can be fitted well to an expression of the form $\xi(T) \propto \sqrt{1/T}$ from 2.4 K to 3.6 K. This is in good agreement with the theoretical predictions [9] for the temperature dependence of the superconducting proximity length in the diffusive limit (details can be found in chapter 2, subsection 2.2.4). In the temperature range from 3.6 K to 5.2 K a fit to this law is not possible due to the crossover from proximity-induced superconductivity to the localization behavior.

Interestingly, the calculated proximity length for Co-NW at 2.4 K is 0.3-0.5 μm for the L_1 and L_3 sections and 1 μm for the L_2 section, attesting to an even more long-ranged effect as compared to Cu-NW2 (see chapter 4 section 4.5). Figure 5.5(d) illustrates the calculated proximity length in Co-NW for the different measured sections at 2.4 K. Surprisingly, in contrast to Cu-NW2 [see Fig. 4.8(b)], the dependence $\xi(L)$ for Co-NW is not monotonic in distance. The non-monotonic dependence of the proximity length on the measured nanowire

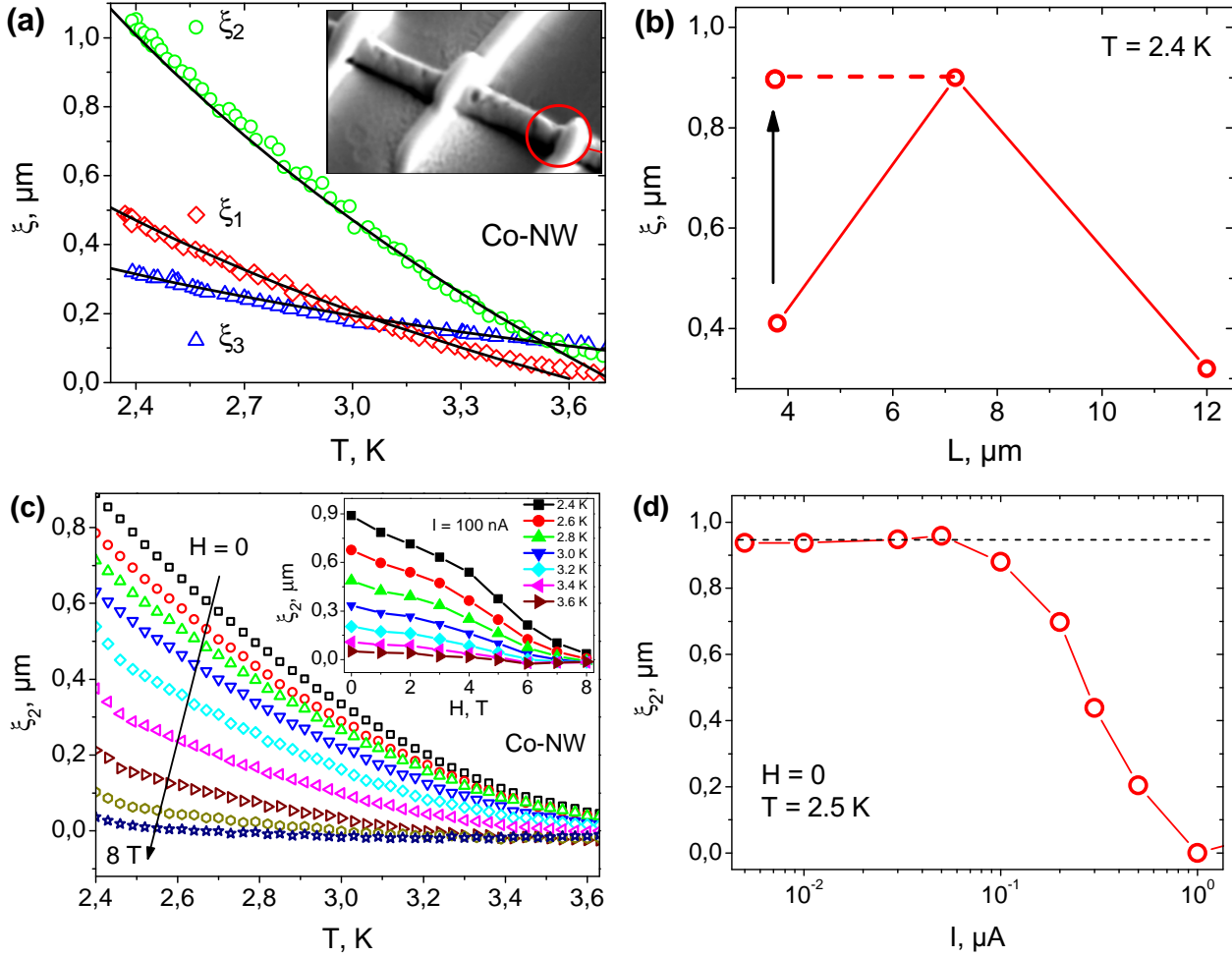


Figure 5.5: (a) The temperature dependence of the proximity length for Co-NW. The proximity lengths ξ_1 , ξ_2 and ξ_3 have been deduced by Eq. 4.3 from the $R(T)$ data measured on the sections L_1 , L_2 and L_3 , respectively. The solid lines are fits to an expression of the form $\xi(T) \propto \sqrt{1/T}$. Inset to (a): SEM image of the narrowing of Co-NW in the vicinity of one of the inner voltage leads. (b) The proximity lengths deduced for the different measured sections at 2.4 K for Co-NW. The vertical arrow points out that the experimentally measured value of the proximity length for the L_1 section in Co-NW is likely underestimated. Refer to the text for details. (c) $\xi_2(T)$ in the Co-NW for a set of magnetic fields with a step width of 1 T indicated by the black arrow. Inset to (c): The field dependence $\xi_2(H)$ in the Co-NW. (d) The current dependence of ξ_2 in the Co-NW.

section and a factor of two difference in the quantified values of ξ in Co-NW are most likely caused by the unpredictable location and formation of the boundaries between the crystallites in this nanowire. For this reason, a post-measurement inspection of the contact regions with SEM was undertaken. Under the microscope, it was found that the location of one of the inner potential probes is very close to a narrow section of Co-NW (most likely at a grain boundary) [see red circle in the inset of Fig. 5.5(a)]. As the triplet order parameter is coupled to the ferromagnetic ordering, the latter aligns the Cooper pair spins along the magnetization direction. Hence, since the direction of magnetization of neighboring domains

differs in general, the superconducting order parameter is suppressed at the grain boundary with respect to its intra-domain value. Therefore, if a contact lead is placed in the vicinity of the grain boundary, the full amplitude of the spin-triplet order parameter can not be probed. This, in turn, results in a reduction of the relative resistance drop due to the PE. In this way, the calculated proximity length for the inner voltage leads is underestimated and in fact it can be as large as $1 \mu\text{m}$, indicating that the observed superconducting PE in the Co nanowire is long-ranged.

The magnetic field and the current dependency of the spin-triplet proximity length for the L_2 section of the Co-NW $\xi_2(T)$ are shown in Fig. 5.5(c) and (d), respectively.

In contrast to Co-NW, the calculated proximity length for Co-FEBID at 2.4 K is on the order of 100 nm. According to the analysis of the microstructure and the scattering mechanisms in this sample in section 5.6, the calculated value is not related to the proximity length but rather to the length of the inducer short-circuited nanowire section, as its doubled value is very close to the width of the W-FIBID inducer electrode. That is, in the case of the nanogranular, Co-FEBID nanowire structure, it was not possible to reliably observe the PE due to spatial resolution limitations mediated by the width of the superconducting inducer electrode.

5.5 Different conductivity regimes in Co nanowire

The $R(T)$ measurements at different currents on the L_1 , L_2 and L_3 sections of the Co-NW were performed with the aim to examine the robustness of the PE effect against increasing current densities. The lowest current was 5 nA ($\hat{=}j = 8.1 \text{ A/cm}^2$) and the highest current was $20 \mu\text{A}$ ($\hat{=}j = 32.4 \text{ kA/cm}^2$). The obtained results for the L_1 , L_2 and L_3 sections are presented in Fig. 5.6(a, b, c), respectively. As can be seen, the overall tendency of the $R(I)$ dependence for all Co-NW sections is the same. For this reason, only the L_2 section is considered in more detail below.

The $R(I)$ curve for the L_2 section of the Co-NW is shown in Fig. 5.6(d). At 2.4 K, the PE-induced resistance drop is independent of the current up to $\approx 100 \text{ nA}$, while at larger currents the resistance attains its maximum value and then decreases for $I > 1 \mu\text{A}$. A decrease of the resistance at high currents was also observed at 6 K and 15 K, which are shown for reference in Fig. 5.6(d). By contrast, the Cu-NW $R(T)$ data were found to be independent of the current value up to $I = 20 \mu\text{A}$ (see Fig. 4.3).

Although temperatures below 2.4 K were not achievable in the experiment, the $R(I)$ curves in Fig. 5.6(d) suggest that the superconducting PE effect can be used for switching

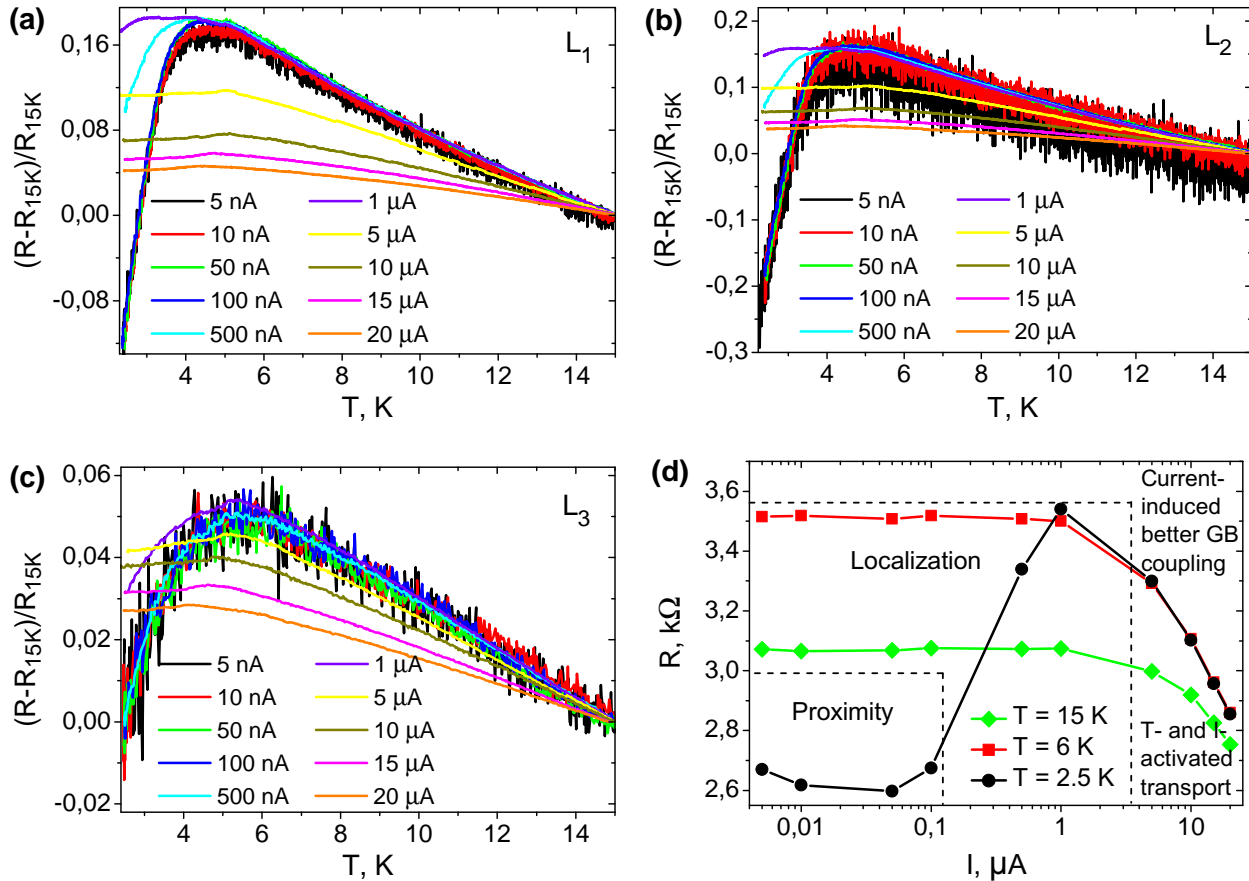


Figure 5.6: The temperature dependence of the resistance of the L_1 (a), L_2 (b) and L_3 (c) sections of the Co-NW for a set of different currents from 5 nA to 20 μ A. (d) Current dependence of the resistance of the L_2 section of the Co-NW at three different temperatures.

between different conductivity regimes in the Co-NW. Thus, a $R(T, I)$ color diagram was derived from the data to indicate these regimes, as shown in Fig. 5.7. Three main regimes can be distinguished: the proximity-induced, low-ohmic regime in the limit of weak currents and low temperatures (dark blue); the high-ohmic behavior due to the dominating grain-boundary scattering at moderate current and low temperature (red); and the metallic-like behavior in the limit of strong current and/or high temperature due to the current- and temperature-activated charge carrier transport between individual grains (light blue).

5.6 Spin-dependent scattering at grain boundaries

The driving question in the analysis of the microstructural properties of the Co-FEBID nanowire is why the PE-induced superconductivity is not present in this sample. Although there is no definite answer to this question, a possible explanation can be proposed as follows. In contrast to the case of the Co nanowires prepared by ECD, Co-FEBID sample is not a

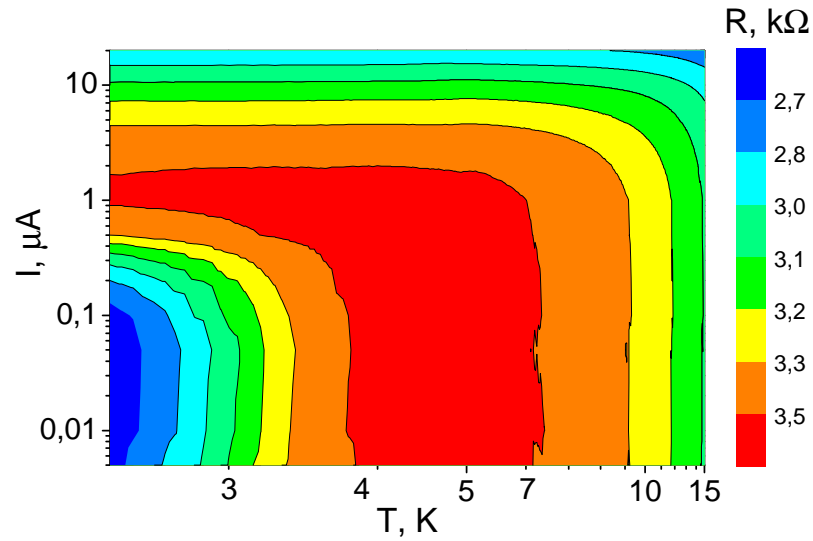


Figure 5.7: Color diagram which represents switching between different conductivity regimes in the Co-NW.

homogeneous, ferromagnetic metal. In general, structures prepared by FEBID belong to the class of disordered electronic materials with different degrees of disorder, ranging from a low impurity concentration in a well-ordered polycrystalline structure to strongly disordered amorphous materials. With regard to the microstructural and electrical transport properties, the nanogranular Co-FEBID nanowire is located between these limiting cases. Carbon and oxygen have been observed by EDX spectroscopy (see Tab. 5.1), and it is assumed that C and O are impurities responsible for suppressing the PE, since these elements represent effective scattering centers, hindering Cooper pairs from spreading through the fine-dispersed deposit.

On the microscopic level, the role of C and O with regard to the scattering process is the following. Consider a region in Co-FEBID that forms one magnetic domain and hence all spins in this region point in one direction. Then, to survive in this environment, a Cooper pair should also have spins pointing in the same direction. Adding a scattering process at the domain boundaries results in changes in the orbital momentum and, due to the spin-orbital interaction, in changes of the orientation of spins. When the spins start to reverse, this leads to the pair-breaking effect. This scenario strongly depends on the symmetry of both the scattering center and the wave function of the propagating Cooper pair. In the present case, Cooper pairs are induced from the W-based floating electrode having *s*-wave symmetry. Additionally, if they are affected by a simple *s*-wave-like scattering, meaning that the outgoing particle is also in the same relative momentum state (which is *s*-wave), then the pair-breaking effect will be zero. However, if due to the symmetry of the scattering process, the preferential scattering will be into the *p*-wave or *d*-wave-like states, then it will lead to the pair-breaking effect: very strongly, for the *p*-wave-like state, and less strongly for

the d -wave-like state.

In this way, the scattering process strongly depends on the symmetry of the electron wave function of the defects in an odd frequency, triplet superconductor. Simple spherically symmetric scatterers will not change much. However, for scatterers with an orbital shape, which is significantly different from the ferromagnetic orbital shape (Co has d -wave symmetry), this can lead to strong pair-breaking effects.

In Co-FEBID, the structure defects are O and C. Oxygen has p -wave valence orbitals, while carbon has s - p -hybrid orbitals. None has an s -wave-like symmetry. Both oxygen and carbon have small atomic radii so that both elements can be incorporated into interstitial sites of the Co hcp lattice. The resulting electron orbital symmetry will be more like in diamond (tetrahedral). As result, the preferential scattering of a Cooper pair wave function from s -wave to p -wave will take place. However, the p -wave function is odd in orbital momentum, resulting in an overall even Cooper pair function, causing the pair-breaking effect.

Chapter 6

Tunable magnetism by post-processing of Co/Pt-FEBID structures

Controlling magnetic properties on the nm-scale is essential for basic research in micro-magnetism and spin-dependent transport, as well as for various applications. This has been accomplished to a very high degree by means of layered heterostructures in the vertical dimension. This chapter presents a complementary approach that allows for controlled tuning of the magnetic properties of Co/Pt heterostructures on the lateral mesoscale. By means of in situ post-processing of Pt- and Co-based nano-stripes prepared by FEBID, it was possible to locally tune their coercive field and remanent magnetization. Whereas single Co-FEBID nano-stripes show no hysteresis, hard-magnetic behavior for post-processed Co/Pt nano-stripes with coercive fields up to 850 Oe were found. The observed effect is attributed to the locally controlled formation of the CoPt $L1_0$ phase, whose presence was revealed by transmission electron microscopy. During the writing of this thesis the results of this chapter were accepted for publication [198].

6.1 Preparation and post-processing of Co/Pt-FEBID structures

Co and Pt growth, as well as processing and imaging experiments were carried out in a dual-beam, high-resolution SEM (FEI, Nova NanoLab 600) equipped with a multi-channel GIS for FEBID. As substrates, epi-polished c-cut (0001) Al_2O_3 with Cr/Au contacts of 3/50 nm thickness prepared by photolithography in conjunction with lift-off were used (see chapter 3, subsection 3.1.2). The samples consisted of one Co-FEBID structure and three Co/Pt-FEBID nano-stripes labeled as sample A, B, C, and D, respectively (see Fig. 6.1). The Co/Pt deposits B and C bridge a 12 μm gap between the Au contacts, while samples A and D were deposited in a cross-shaped fashion, see Fig. 6.2 for an overview.

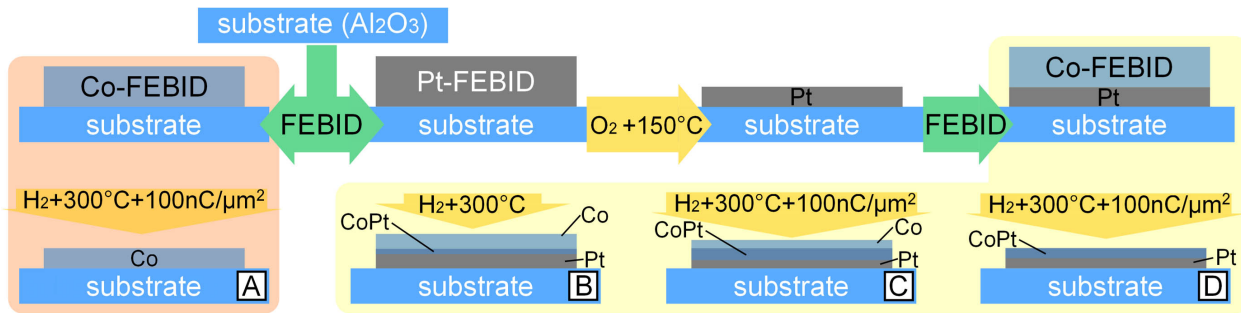


Figure 6.1: Preparation and post-processing of the samples investigated in this work. Throughout the text the samples are referred to by their labels A, B, C, and D, as indicated.

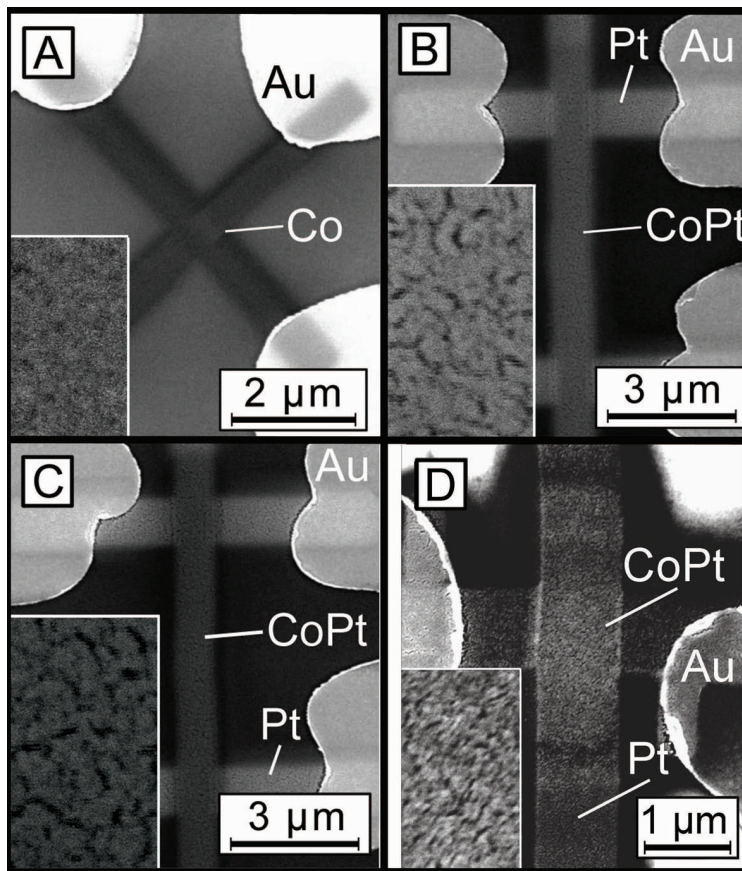


Figure 6.2: SEM images of the samples. The $500 \times 860 \text{ nm}^2$ insets show the morphology of the post-processed Co/Pt FEBID nano-strips.

FEBID of Pt was used for the fabrication of the bottom layers of all samples, with the exception of sample A¹. After the Pt deposition, the samples were heated to 150 °C in the SEM without breaking the vacuum. Once heated, the Pt-based deposits were subject to a pulsed oxygen flux fed into the vacuum chamber up to a pressure of 1.5×10^{-5} mbar through a custom-built GIS. 12 cycles of oxygen flux switched on for 5 minutes interrupted by 5-

¹Precursor $(\text{CH}_3)_3\text{Pt}(\text{CpCH}_3)$, $U = 5 \text{ kV}$, $I = 1 \text{ nA}$, $p = 20 \text{ nm}$, $t_D = 1 \text{ } \mu\text{s}$, $T_{\text{precursor}} = 44 \text{ } ^\circ\text{C}$, process $P = 9.5 \times 10^{-6}$ mbar for a needle position of the GIS at 100 μm height and 100 μm lateral shift from the writing field position.

minute turn-offs were performed. The resistance of the as-deposited Pt-based layers was $0.4 \Omega\text{cm}$ and decreased to $70\text{--}90 \mu\Omega\text{cm}$ after 10 oxygen pulses. The post-processed Pt layers exhibited a nanoporous structure and a reduction of height from $50 \pm 1.5 \text{ nm}$ to $11 \pm 1.5 \text{ nm}$, as inferred from atomic force microscopy, due to the removal of the carbonaceous matrix [75]. The void volume fraction of the very thin, purified Pt layer was estimated from a greyscale threshold analysis of the SEM image which yielded a value of 0.31 ± 0.07 .

FEBID of Co was used for the preparation of the top layers of the structures². After the deposition, all samples were heated to 300°C in the SEM without breaking the vacuum. All samples were subject to a H_2 flux fed into the SEM chamber up to a pressure of $1.5 \times 10^{-5} \text{ mbar}$. While at 300°C , samples A, C, and D were additionally irradiated with the electron beam ($E = 5 \text{ kV}$, $I = 1 \text{ nA}$, $p = 20 \text{ nm}$, $t_D = 50 \mu\text{s}$), whereas sample B was not. The irradiation dose was $100 \text{ nC}/\mu\text{m}^2$ for all irradiated samples.

The as-deposited reference sample A has a nanogranular Co microstructure with inclusions of carbon and oxygen. The employed purification procedure of heating at 300°C in H_2 atmosphere in conjunction with electron irradiation relies upon the Fischer–Tropsch reaction [68, 199]. In this chemical process, cobalt serves as a catalyst, while volatile hydrocarbons and water are produced, effectively oxidizing the carbon. Thus, in the course of the reaction, carbon is partially removed from the deposit causing a reduction of the deposit thickness (details of the purification mechanism of the Co-based deposits prepared by FEBID are presented in subsection 6.6.1).

The as-deposited Pt-FEBID layers for samples B, C, and D are also nanogranular metals. The purification mechanism for the Pt-FEBID structures relies upon the catalytic activity of Pt in oxygen atmosphere [75, 200]. When delivered close to the surface, molecular oxygen is dissociatively chemisorbed on the surface of the metallic Pt particles. Since the process takes place at 150°C , a thermally activated oxidation of carbon at the Pt/C interface occurs, leading to the formation of CO and a reorganization and coalescence of Pt nanocrystallites by surface diffusion (details of the purification mechanism of the Pt-based deposits prepared by FEBID are presented in subsection 6.6.2). The latter, in turn, results in a nanoporous morphology which is clearly seen in the SEM images of samples B, C, and D in the insets to Fig. 6.2. As shown in section 6.2 by TEM inspection, it is this nanoporosity which allows Co to penetrate into the Pt layer during the Co deposition and to form a Co/Pt alloy phase. Considering the Co-Pt binary phase diagram (see Appendix C), for a Co/Pt-ratio of 1:1,

²Precursor $\text{Co}_2(\text{CO})_8$, $U = 5 \text{ kV}$, $I = 1 \text{ nA}$, $p = 20 \text{ nm}$, $t_D = 50 \mu\text{s}$, $T_{\text{precursor}} = 27^\circ\text{C}$, process $P = 8.85 \times 10^{-6} \text{ mbar}$, base $P = 4.12 \times 10^{-6} \text{ mbar}$. A custom-built, liquid-nitrogen trap filled with zeolite powder was employed for removing the water vapor from the SEM chamber.

the CoPt L1₀ phase can form. This phase is a hard ferromagnet whose presence can explain both the reduction of the saturation field as well as the appearance of a hysteresis loop in samples B, C, and D, as reported in section 6.4.

SEM images of the fabricated samples are shown in Fig. 6.2, while their geometric dimensions, elemental composition, and magnetic properties are compiled in table 6.1.

Sample	l , μm	w , μm	d_{Co} , nm	d_{Pt} , nm	Co, at. %	Pt, at. %	C, at. %	H_c , Oe	H_s , T	M_r/M_s	Co/Pt
A	0.49	0.5	11	0	92	0	8	×	1.7	×	∞
B	5.45	1	10	11	54	27	19	770	1.5	0.15	2
C	5.35	1	11	11	49	22	29	850	1.3	0.25	2.23
D	1	1	5	11	35	35	30	420	0.5	0.18	1

Table 6.1: Geometric dimensions, composition, and magnetic properties of the samples. l : length; w : width; d_{Co} : thickness of the Co layer; d_{Pt} : thickness of the Pt layer; H_c : coercive field; H_s : saturation field; M_r/M_s : remanent magnetization.

6.2 Characterization of Co/Pt-FEBID structures

6.2.1 Material composition analysis

The material composition was inferred from energy-dispersive X-ray spectroscopy, in the same SEM without exposure of the deposits to air. The EDX parameters were 5 kV and 1.6 nA. The elemental composition was quantified without thickness correction, thus the reported data are a qualitative indicator only. The obtained material composition for all the samples is presented in Fig. 6.3. Here, the oxygen-based signal was excluded from the EDX data since its bulk part mostly stems from the substrate (Al_2O_3), and quantification was performed such that $[\text{Co}]+[\text{C}]$ and $[\text{Co}]+[\text{C}]+[\text{Pt}]$ give 100 at.%, respectively. In this way, the EDX data serve as an indicator of the Co/Pt ratio being the key parameter for the Co/Pt alloy phase formation.

6.2.2 Microstructural characterization

To gain insight into the microstructure of the purified samples and to examine whether the assumed CoPt L1₀ phase (revealed by modifications of the magnetic properties reported in section 6.4) is indeed present in sample C once its magneto-resistance measurements had been completed, sample C was inspected by scanning TEM (STEM). Before the STEM measurements, sample C was covered with a 300 nm-thick protective Pt-C layer deposited

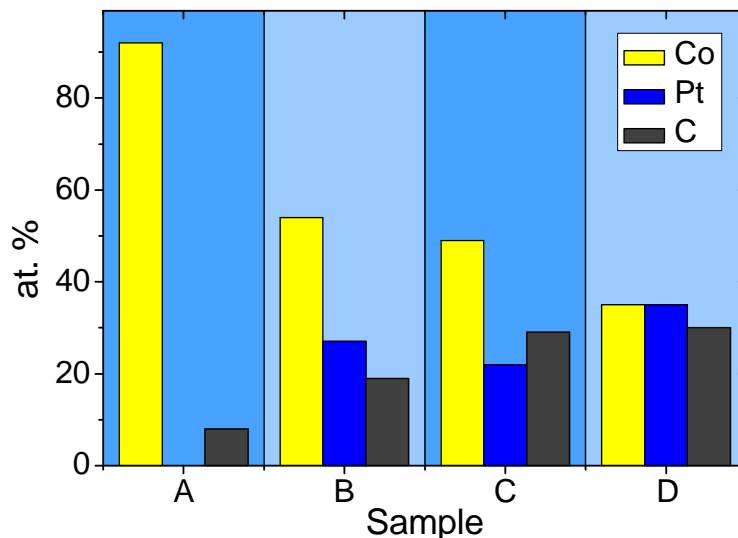


Figure 6.3: Quantified material composition in the samples, as indicated.

by FEBID. The STEM inspection was performed in a Titan G2 microscope from FEI (see chapter 3, subsection 3.2.4 for details).

A convergence angle of 1.0 mrad was used to generate electron nanodiffraction patterns in STEM mode. These diffraction patterns were recorded energy-filtered on a 16-bit CCD. To collect the nanodiffraction images over the complete layer the “diffraction spectrum image” technique was used as part of the software package Digital Micrograph (Gatan). The lateral step size from pixel to pixel was 3.7 nm. Therefore, an individual selection of the diffraction patterns from the upper and the lower layer was possible. For a comparison with the experimental nanodiffraction data from the upper and lower layer, electron diffraction simulations for the CoPt fcc- and fct-phase assuming bulk lattice constants were made with the software JEMS. The pixel time for the energy-dispersive X-ray (EDX) cross-sectional line scan was 8 seconds per spectrum and the step size was 0.8 nm. To generate the elemental signal profile, the intensity from the Pt M edge (2.05 keV) and the Co K edge (6.92 keV) was used.

Figure 6.4 presents a cross-sectional TEM image of sample C in the high angle annular dark field mode (a) and in the annular dark field mode (b). The respective spectrograms obtained by STEM-EDX along the direction depicted by the arrows in Fig. 6.4(b) are shown in Fig. 6.5. From the cross-sectional STEM-EDX spectrum in Fig. 6.5(a) it follows that the top layer of sample C predominantly consists of Co with a very minor content of Pt and C, whereby the Pt content gradually increases upon reaching the Co/Pt interface. The bottom layer largely consists of Pt with a notable content of Co down to the Al_2O_3 substrate, see the “step” in the Co signal profile in Fig. 6.5(a). From a closer look at the TEM micrograph

in Fig. 6.4, a series of light channels running through the entire thickness of the bottom layer is observable. The in-plane scan, acquired within the bottom layer and shown in Fig. 6.5(b), reveals that these light channels correspond to Co-rich areas in the Pt-rich layer. The substantial variation of the Co and Pt signals in the in-plane scan further corroborates the hypothesis that the pores emerged over the course of purification of the Pt layer have been filled with Co.

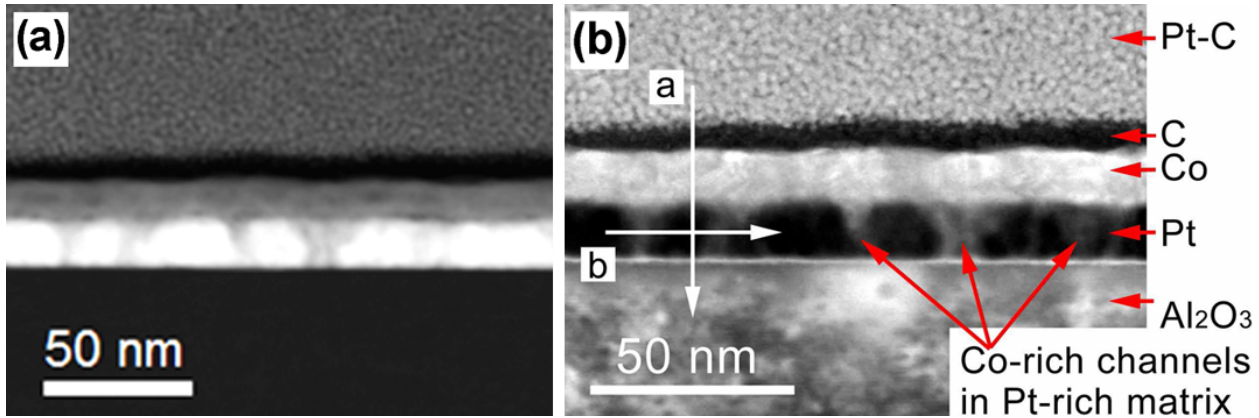


Figure 6.4: TEM micrographs of sample C acquired (a) in the high angle annular dark field mode and (b) in the annular dark field mode. In (a), elements with higher atomic numbers Z are brighter in the image. The light regions in the Pt layer in (b) correspond to Co-rich channels embedded in the Pt-rich matrix. The arrows depict the directions along which the STEM-EDX spectra in Fig. 6.5 have been acquired.

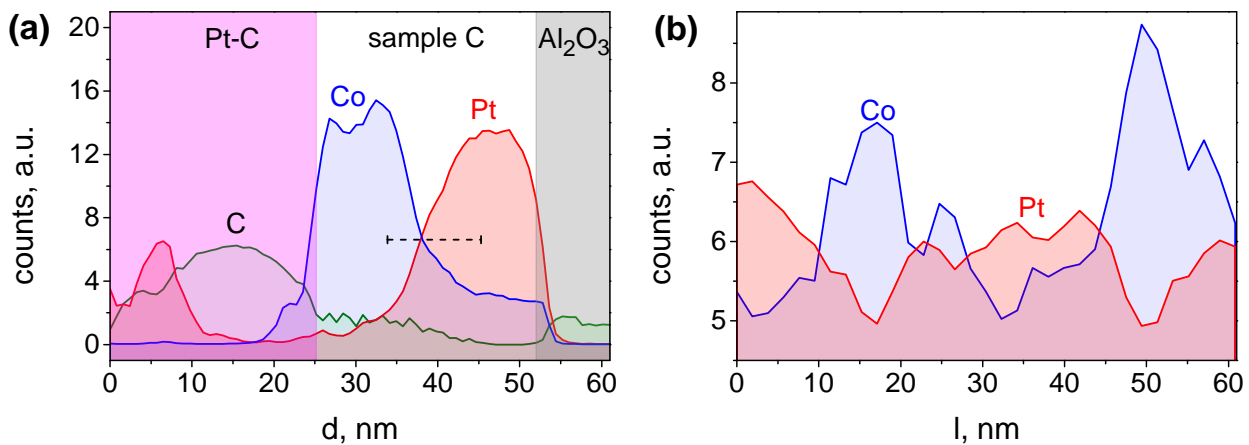


Figure 6.5: (a) Cross-sectional and (b) lower layer in-plane EDX spectrograms for sample C acquired along the respective arrows in Fig. 6.4. The dashed line in (a) sketches the choice of the thickness of the control sample D where the CoPt $L1_0$ phase is expected to be formed over nearly the entire sample volume.

The individual nanodiffraction images for the upper and the lower layer are shown in Fig. 6.6. The diffractograms are accompanied by the respective simulated diffraction patterns. Among the reflections in the upper layer [see Fig. 6.6(b)] one recognizes the intensive

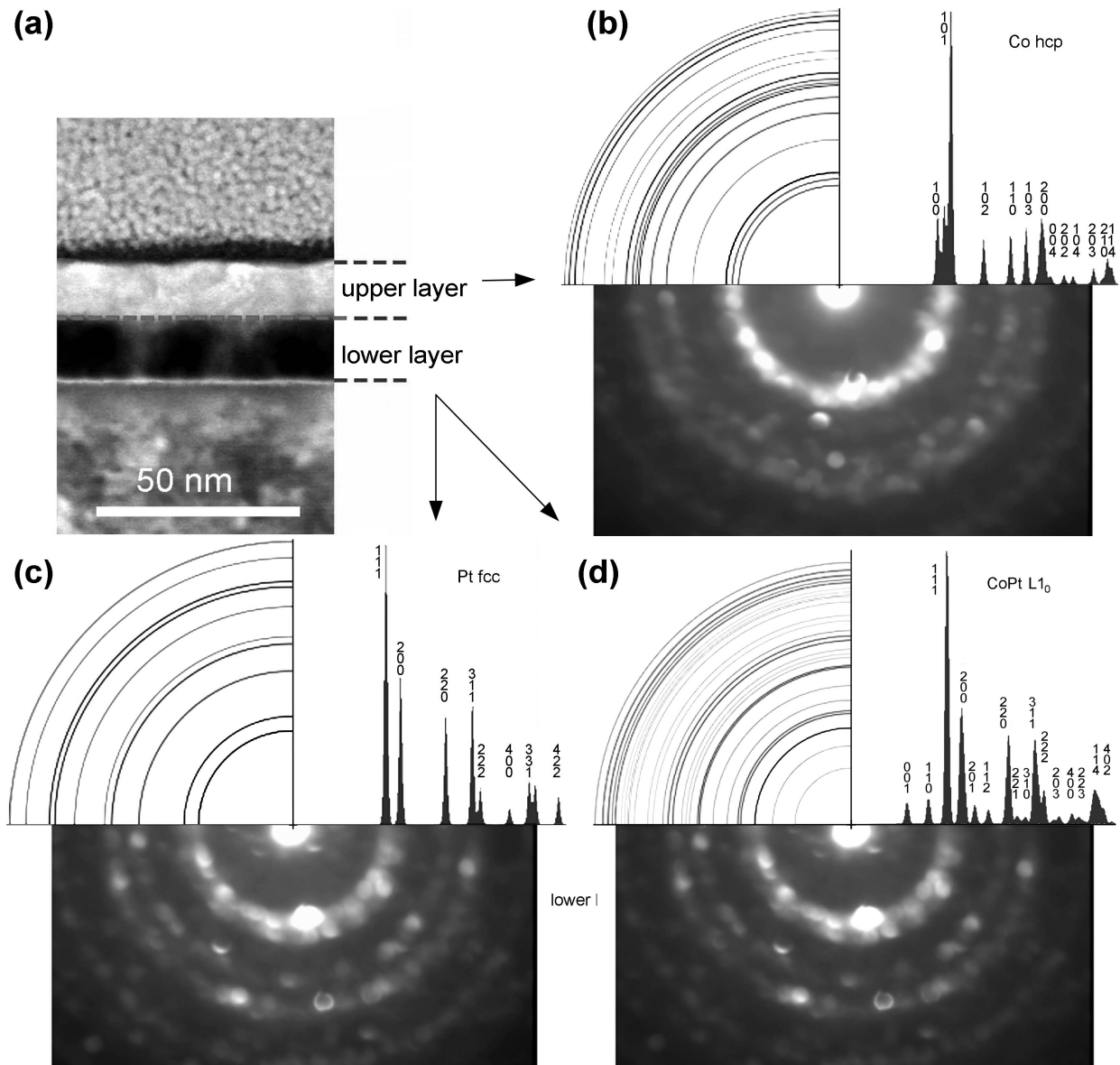


Figure 6.6: The location of the probed layers is shown in panel (a). Nano-diffractograms of the upper (b) and lower layer (c,d) of sample C alongside with the simulated diffraction patterns for a Co hcp phase (b), a Pt fcc lattice (c) and a CoPt fct phase (d).

(100)+(101) rings and clearly visible (110) and (200) rings which are the fingerprint for a Co hcp lattice. The rings (102), (103), and (114) may also be recognized, though these have a much lower intensity. The reflections for lower layer are compared with a Pt fcc lattice in Fig. 6.6(c) and a CoPt fct phase in Fig. 6.6(d). As the simulation patterns depict, the bright rings (111), (200), (220) and (311) are expected for both lattices while the main reflections are dominated by Pt. At the same time, a weak additional diffraction intensity within the innermost Pt (111) ring suggests the presence of some smaller contribution from a CoPt fct phase, thereby supporting hypotheses that the CoPt L_{10} phase is formed in the lower layer. For comparison, no such intensity is visible for Co in the upper layer. At the same time, it

is believed that no full transformation to the $L1_0$ phase took place in the lower layer, but a partial transformation on the large inner surface of the nanoporous Pt layer in which the Co deposit (and then purified Co) is located. Accordingly, the diffraction pattern of the lower layer most likely shows an overlay of the Pt and the CoPt $L1_0$ phases.

6.3 Electrical transport properties of Co/Pt-FEBID structures

The electrical resistance of the samples was measured as a function of temperature in the standard 4-probe geometry in a helium-flow cryostat equipped with a 12 T superconducting solenoid. Temperature-dependent electrical resistance measurements were performed in fixed current mode with a DC current of 200 nA corresponding to a current density of $\approx 1 \text{ kA/cm}^2$.

The temperature dependence of the electrical resistance $R(T)$ for samples B and C are metallic in nature (see Fig. 6.7). The resistivities of the samples at 10 K are $\rho_{10\text{K}} \approx 40 \mu\Omega\text{cm}$ and the room temperature-to-10 K resistance ratios are approximately 1.35. The room temperature resistivity values $\rho_{300\text{K}} \approx 55 \mu\Omega\text{cm}$ are an order of magnitude larger than the literature values for bulk Co and Pt [76] and are in agreement with the already reported values for purified individual Co [68] and Pt [75] FEBID structures.

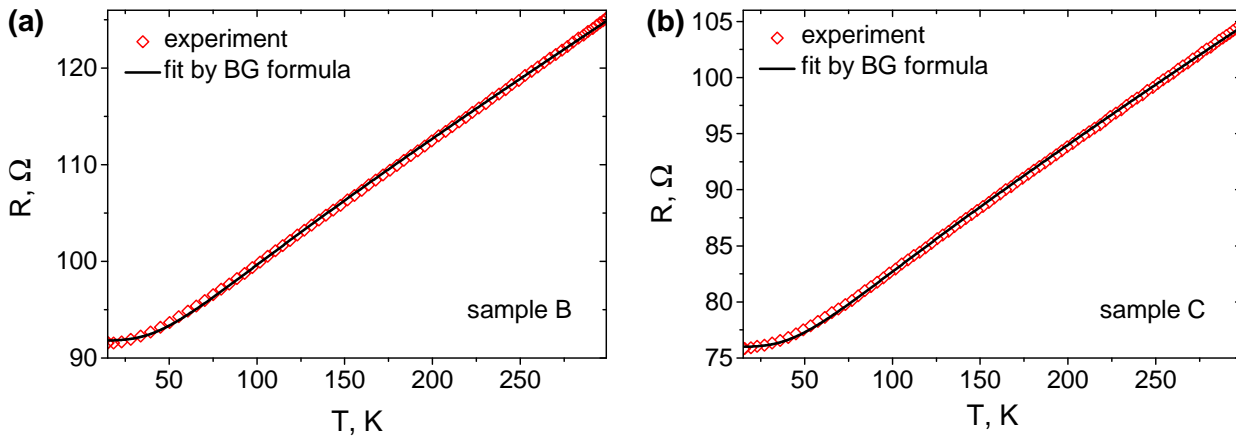


Figure 6.7: The Cooling curves $R(T)$ for samples (a) B and (b) C. The solid lines are fits to the Bloch–Grüneisen law by Eq. 2.14 with $n = 5$ and Debye temperatures $\Theta_D = 275 \text{ K}$ and $\Theta_D = 279 \text{ K}$ for samples B and C, respectively.

The $R(T)$ curves for samples B and C can be fitted rather well to the Bloch–Grüneisen formula [Eq.(2.14)]. The fitting parameter K is chosen such that the best possible coincidence with the experimental curves in Fig. 6.7(a) and (b) is achieved for $\rho_{15\text{K}}$ and $\rho_{290\text{K}}$. The $R(T)$ curve are fitted by Eq. (2.14) with $n = 5$ which implies that the resistance is due to electron–phonon scattering [91], while electron–magnon contributions ($\propto T^2$) are small. Varying the Debye temperature as a fitting parameter, the best possible coincidence of the measured

data to Eq. 2.14 is achieved with Debye temperatures $\Theta_D = 275$ K and $\Theta_D = 279$ K for samples B and C, respectively. While the Debye temperature for bulk Pt is 215 K and for bulk Co is 385 K [201], the obtained values of Θ_D for samples B and C are very close to Debye temperatures (between 280 – 295 K) of purified Co-FEBID nanostructures [68].

6.4 Magnetic properties of CoPt-FEBID samples

6.4.1 Hall effect

The central finding was the modification of the field dependence of the Hall voltage $U(H)$ measured at 10 K for all samples, see Fig. 6.8. For these measurements, a lock-in amplifier in conjunction with a differential preamplifier and a ratio transformer to null the signal at $H = 0$ were used (see chapter 3, subsection 3.3.2). The magnetic field was directed perpendicular to the sample plane and, hence, the out-of-plane magnetization was probed by the measurements.

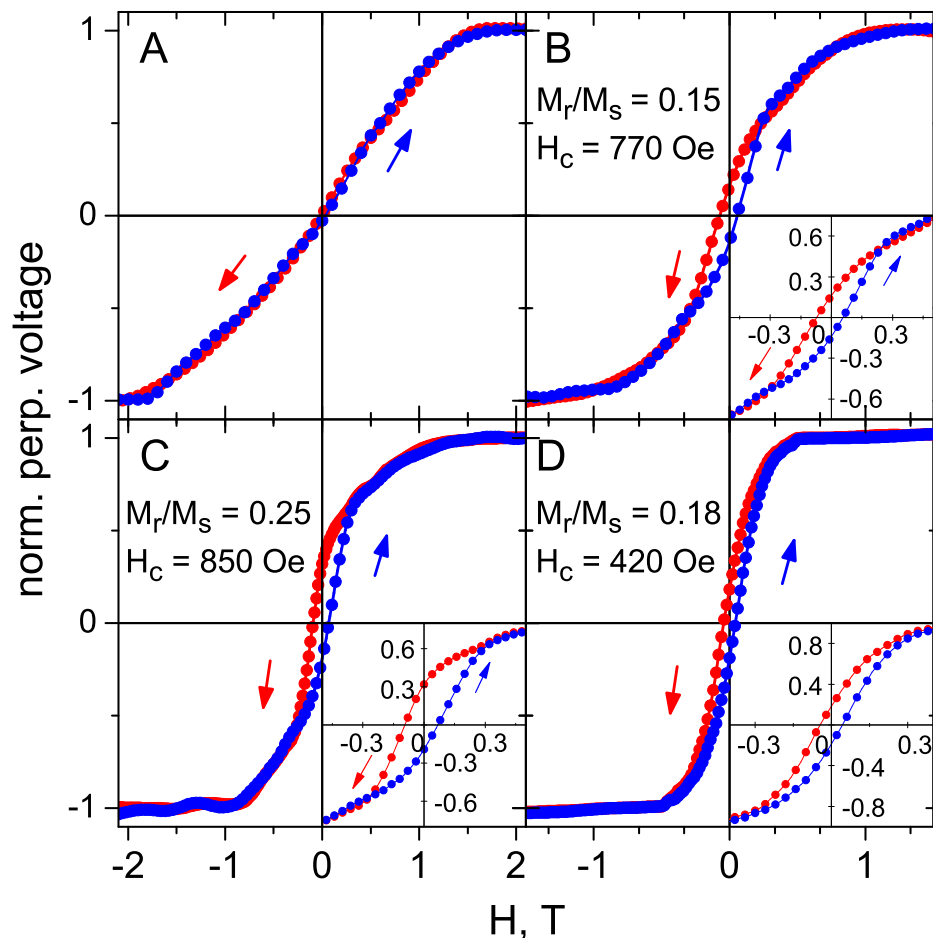


Figure 6.8: Hall voltage cycling at 10 K for all samples. Before measurements, all samples were saturated at 3 T. Note the different field range and scale for sample D.

The Co-based reference sample A shows no hysteresis, whereby $U(H)$ is nearly linear from -1.5 T to 1.5 T and saturates at $H_s = \pm 1.7$ T. The magnetic behavior of the thin polycrystalline Co stripe A is not dominated by the magnetocrystalline anisotropy, but rather by the shape anisotropy causing the magnetization to lie preferentially in the plane. Given the demagnetizing factor for the created geometry, $N \approx 1$ [202], a saturation magnetization of $M_s = H_s/N = 1.7 \text{ T} \times 10^4/4\pi = 1353 \text{ emu/cm}^3$ results for this sample, corresponding to 98% of the bulk value [203].

The $U(H)$ curve of the Co/Pt-based sample B demonstrates two distinctive features compared to sample A: Sample B shows a noticeable hysteresis loop and its saturation field H_s is by about 30% smaller than H_s for sample A. The behavior of sample B is that of a ferromagnet, with a coercive field H_c of 770 Oe and a remanent-to-saturation magnetization ratio (squareness) M_r/M_s of 0.15. The irradiated Co/Pt-based sample C exhibits an even broader hysteresis loop with $H_c = 850$ Oe and $M_r/M_s = 0.25$, respectively. Its saturation field H_s amounts to 1.3 T. Even though samples B and C demonstrate hysteresis, one can see that it is not completely open and the overall behavior of the Hall voltage curves is suggestive of a superposition of a soft and hard ferromagnetic response. In all, the following two effects have been observed in the post-processed Co/Pt samples, namely (i) a developing hysteresis and (ii) a reduction of the magnetization saturation field. These modifications of the magnetic properties are assumed to be caused by the formation of the CoPt $L1_0$ phase in the course of purification treatments, whose presence has been revealed by TEM microscopy.

As the presence of the CoPt $L1_0$ phase is confirmed by TEM inspection, it was necessary to examine the hysteresis development and the rectangular enhancement due to the presence of the CoPt $L1_0$ phase in the processed samples. For this purpose, a control sample D was prepared with the entire thickness chosen as shown by the dashed line in Fig. 6.5(a). The thickness of the Co layer in sample D was chosen such that its atomic content per volume was set to be nearly equal to that in the processed Pt layer (given the nanoporosity of the processed platinum). As a consequence of this, sample D is a nano-stripe where a full formation of the CoPt $L1_0$ phase is most favorable (the Co/Pt ratio is very close to 1:1) and this phase is expected to be formed over nearly the entire sample volume. This is in contrast to samples B and C, where the CoPt $L1_0$ phase is likely formed within an interface layer only. Figure 6.9 shows a clear correlation between the magnetization saturation field and the Co/Pt ratio. Moreover, a hard-magnetic behavior is shown for sample D in Fig. 6.8(D). The $U(H)$ curve exhibits the most open, rectangular hysteresis loop among all measured samples, with $H_c = 0.5$ T and a squareness M_r/M_s of 0.18. This provides strong evidence that the magnetic response hardening in the processed CoPt-FEBID nano-stripes is indeed

due to the CoPt $L1_0$ phase.

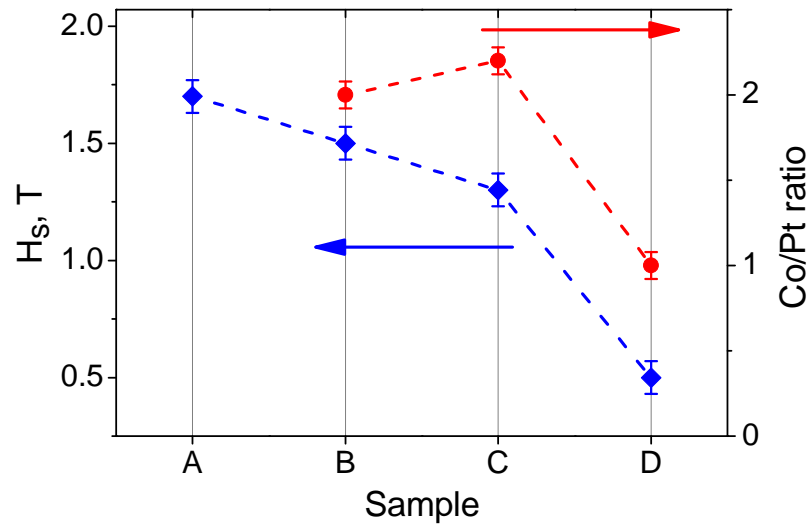


Figure 6.9: The magnetization saturation fields H_s (left axis, diamonds) and the Co/Pt ratios (right axis, circles) for the four investigated samples.

The Hall voltage cycling $U(H)$ for sample D was repeated at different temperatures up to room temperature, see Fig. 6.10. The temperature-induced reduction of the coercive field and the remanent magnetization is presented in Fig. 6.11. A linear extrapolation of the $H_c(T)$ data suggests that above 400 K sample D will behave as paramagnet, attesting to the robustness of the ferromagnetism in this sample at room temperature.

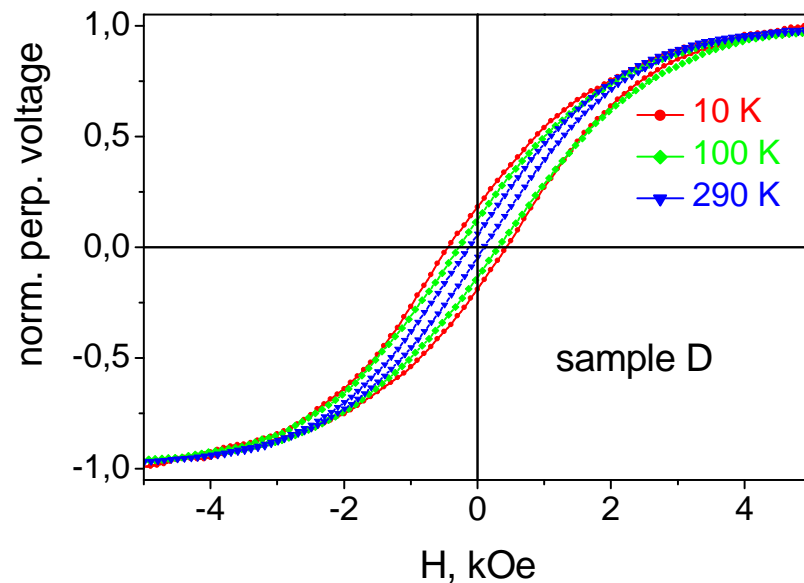


Figure 6.10: Isothermal Hall voltage cycling for sample D at a series of temperatures, as indicated.

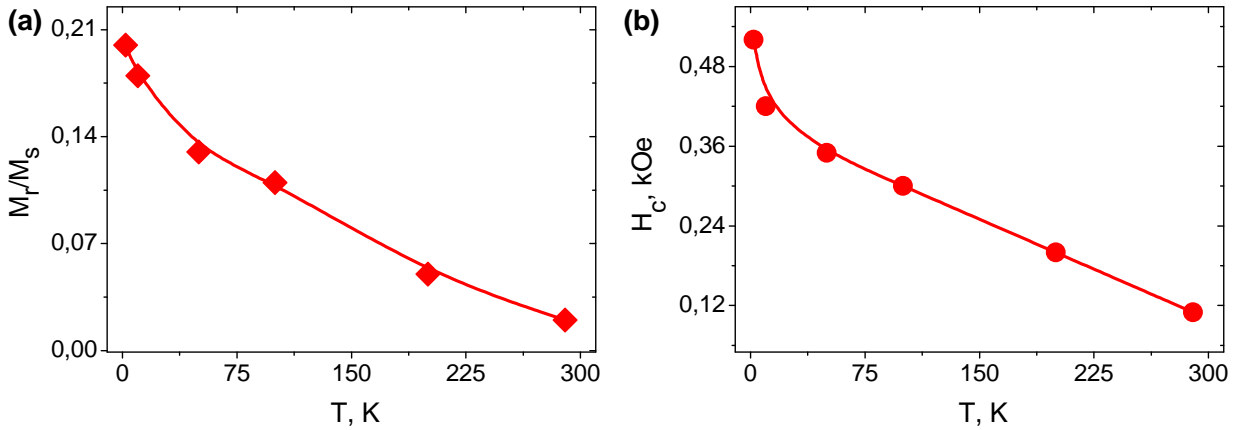


Figure 6.11: Temperature dependences of the remanence magnetization M_r/M_s (a) and the coercive field H_c (b) for sample D.

6.4.2 Magnetoresistance

Magnetoresistance (MR) measurements were performed at 10 K with magnetic fields up to ± 3 T applied perpendicular to the substrate plane. The setup used for the MR measurements was similar to that used for the Hall effect measurements (see chapter 3, subsection 3.3.2). The results for samples A, B and C are shown in Fig. 6.12. MR is defined as $100[R(H) - R(H = 0)]/R(H = 0)$, where $R(H)$ and $R(H = 0)$ are the resistances at the given magnetic field H and zero field, respectively.

The MR for all the samples appears already saturated at ± 2 T. At the same time, the value of the MR at 3 T for sample A is about a factor of four larger than that of sample B. The MR is negative for all the samples, indicative of the ferromagnetic state. The observed saturation behavior with a quadratic dependence at $H \leq H_s$ is expected for ferromagnetic materials since the electron scattering probability decreases as more magnetic moments are aligned along the direction of the external magnetic field. All the samples show a pure anisotropic MR (AMR) signal, which originates from an anisotropic electron scattering due to spin-orbit coupling. This attests to the metallic character of the samples. In addition, a notable hysteresis was detected for samples B and C when sweeping magnetic field H in \pm directions, which in addition to Hall effect measurements.

6.5 Laterally controlled magnetic structure for spin-triplet proximity-induced superconductivity

Perspectively, the advantage of controlling the magnetic structure laterally can be applied in spin-triplet proximity-induced superconductivity experiments. In particular, this can be used

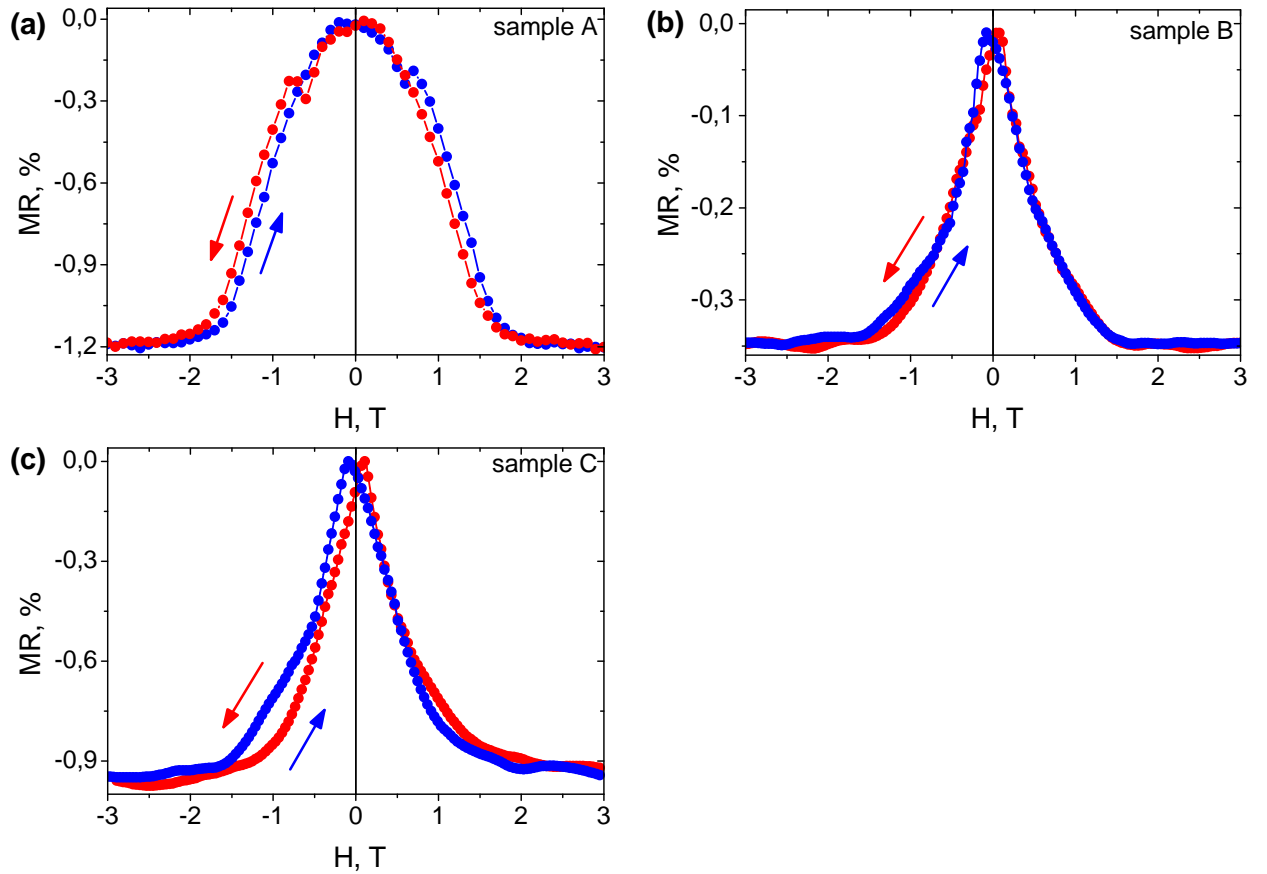


Figure 6.12: Perpendicular magnetoresistance measurements at 10 K for samples A, B and C. Before measurements, all samples were magnetized in a field of 3 T. The arrows indicate the field sweep directions. MR is defined as $100[R(H) - R(H = 0)]/R(H = 0)$.

to study the influence of controlled magnetic inhomogeneity on the singlet to triplet state conversion with a purpose to generate and inject spin-equal superconducting order parameter in ferromagnetic nanowire structures. One example of a ferromagnetic multi-segmented nanowire structure in contact with a singlet superconductor is shown in Fig. 6.13. It consists of alternating series of segments made of two different ferromagnetic materials: (i) magnetically soft ferromagnet $F^{(1)}$ with coercive field $H_c^{(1)}$ and (ii) magnetically hard ferromagnet $F^{(2)}$ with coercive field $H_c^{(2)}$. In relation to this work, as the first one can be used purified Co-FEBID with H_c value of 0.22 T [68], while as the second one can be used prepared by FEBID Co/Pt heterostructure with a tunable H_c value of 0.042 – 0.085 T depending on the post-processing conditions (see section 6.4). Now, if an external magnetic field will be applied in-plane [Fig. 6.13(a)] or out-of-plane [Fig. 6.13(b)] magnetization with the absolute value greater than $H_c^{(1)}$ and $H_c^{(2)}$ ($H > H_c^{(1)}, H_c^{(2)}$), then the nanowire will be fully magnetized in one direction. At the same time, if the direction of magnetic field will be rotated by an angle of 180 degrees, while the absolute value of magnetic field will be $H_c^{(1)} < H < H_c^{(2)}$, then the magnetization direction of the segments $F^{(1)}$ and $F^{(2)}$ will be in opposite direc-

tions. In that case, at the interface between two ferromagnets or, eventually between grain boundaries, a domain wall can be formed. This domain wall can be Bloch/Neel wall, depending upon whether the magnetization rotates parallel/perpendicular to the domain interface. As it has been shown in chapter 2 subsection 2.2.4, a “natural” magnetic inhomogeneity associated with a domain wall can be suitable for generation of the odd-frequency triplet superconducting order parameter in ferromagnet.

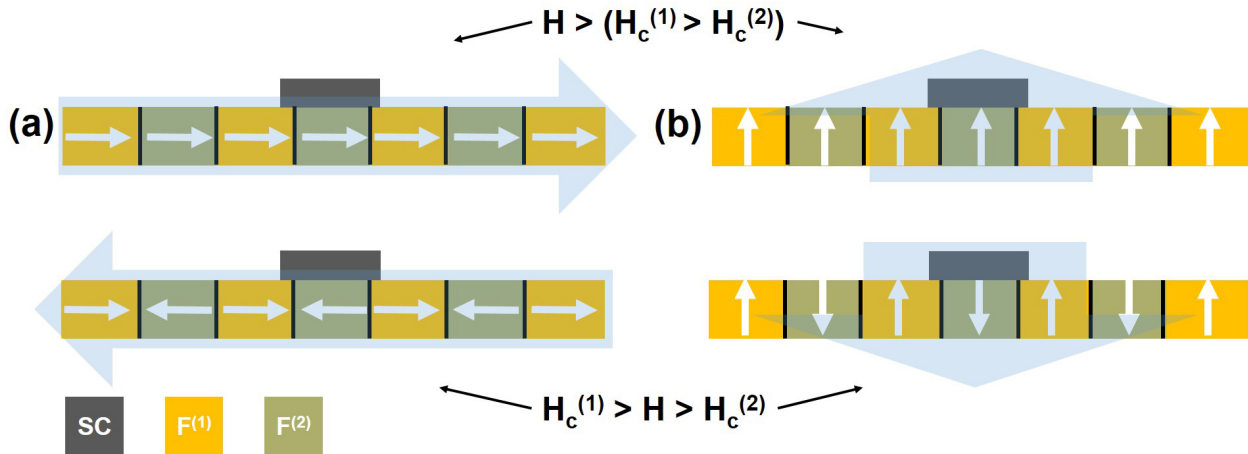


Figure 6.13: Ferromagnetic multi-segmented nanowire structure for spin-triplet proximity-induced superconductivity investigations.

6.6 Post-growth purification of Co-FEBID and Pt-FEBID structures

The local deposition of materials by means of FEBID represents a versatile approach for the fabrication of functional nanostructures [15, 51, 52, 57, 60–63]. However, a long-standing problem lies in that for most of the organo-metallic precursors used the low efficiency of the process for decomposing the precursor gas molecules gives rise to a rather large quantity of C with inclusions of oxygen in the deposits, and the metal percentage is low. For Pt-based deposits using the precursor Me_3CpMePt , strategies have been developed to obtain clean metal structures by in situ post-growth treatments using O_2 or H_2O as reactive gases [70–72]. For Co- and Fe-based deposits using the precursors $\text{Co}_2(\text{CO})_8$ and $\text{Fe}(\text{CO})_5$, respectively, several reports have been given stating metal contents well above 80 at.% in as-grown samples [167–169]. By careful optimization even up to 95 at. % metal purity was reported for Co structures in very few cases [159, 160, 204]. However, such high metal contents are by no means routinely obtained, even when special care is taken by working under optimized high-vacuum conditions. For example, H_2O removal from residual gases by Meissner traps

and pre-growth plasma cleaning of the SEM chamber can be employed.

Since the preparation of the layered Co/Pt heterostructures is directly based on the combination of the purification of Co- and Pt-based structures prepared by FEBID, in this subsection both processes are presented in more detail. Both processes are related to an in situ cleaning approach to obtain pure Co-FEBID or Pt-FEBID nanostructures.

6.6.1 Post-growth purification of Co-FEBID

A description of the purification technique used for the Co-FEBID structures is presented as a collaborative experiment with Evgenia Begun. The results of this experiment, which were applied to the design of the Co/Pt heterostructures, are presented in this subsection. Here, the basic compositional and microstructural modifications applied for the Co-FEBID structures over the course of purification, as well as changes in their conducting and magnetic properties, are presented. Also, driving elements behind the purification mechanism are proposed.

The samples are two strip-shaped Co-based deposits prepared by FEBID³. The first sample was left as-deposited for reference purposes. The second one was heated to 300 °C and underwent post-processing. Specifically, it was subject to a H₂ flux fed into the SEM chamber by a custom-built GIS positioned at a height of 100 μm and 100 μm laterally from the writing field position, at a pressure of up to 1.5×10^{-5} mbar. This was accompanied by irradiation with 5 kV/0.5 nA electrons and total dose of 100 nC/μm² (see the chart in Fig. 6.14).

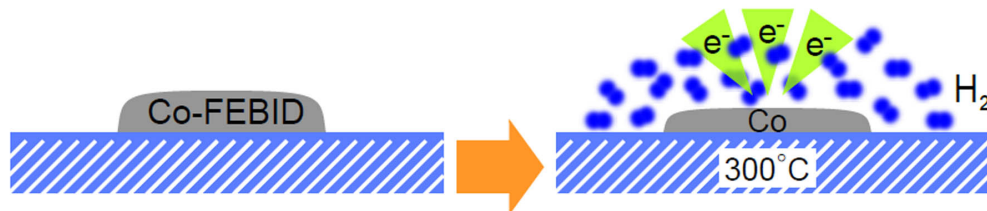


Figure 6.14: Schematics of the preparation and purification of Co-FEBID samples. Left shows the as-deposited layer, and right is the layer which underwent heating accompanied by a H₂ flux in the SEM chamber and electron irradiation. The process parameters are detailed in the text.

³Precursor $\text{Co}_2(\text{CO})_8$, $E = 5$ kV, $I = 0.5$ nA, $p = 20$ nm, $t_D = 50$ μs, $T_{\text{precursor}} = 27$ °C, process $P = 8.16 \times 10^{-6}$ mbar.

Material composition and microstructural characterization

The material composition of the samples was characterised by EDX in the same SEM, without exposure to air after deposition. The EDX parameters were 3 kV and 1.6 nA. The quantified data are presented in Fig. 6.15.

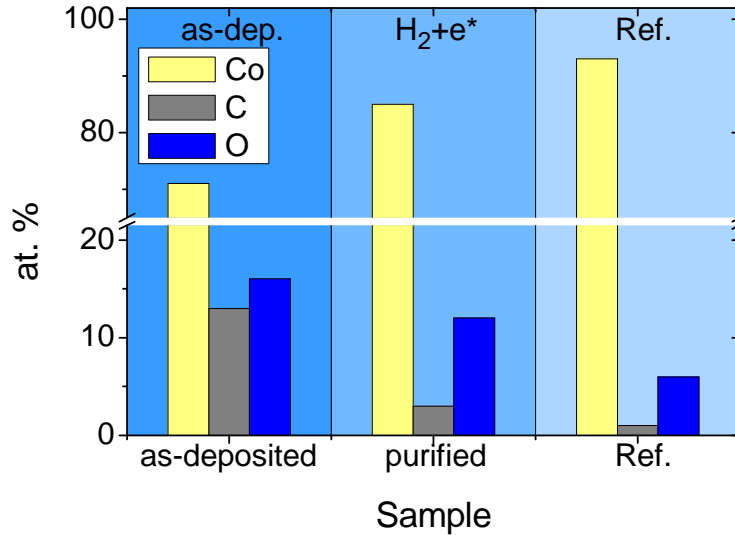


Figure 6.15: The quantified material composition in the as-deposited and purified Co-FEBID samples. In the sample caption in the right panel “Ref.” stands for the reference Co film grown by PVD.

The reference measurement made on a Co thin film⁴ has yielded 93 at. % of Co, 6 at. % of O, and 1 at. % of C. The 6 at. % of O is attributed to an oxide layer formed on the film surface. The results of the as-deposited sample are 71 at. % of Co. The purified sample exhibited a Co content of 85 at. %, 12 at. % of O, and an only a minor contribution of C at 3 at. %. Overall, the implementation of the in situ purification treatment indicates an increase in the metal content and the effective removal of carbonaceous material. The latter conclusion has been supported by a decrease of the thickness of the processed sample by about 30 % (from 48 nm to 31 nm) with respect to the as-deposited sample (confirmed by AFM).

Microstructural characterization was performed by means of TEM and STEM–EELS measurements⁵ in cooperation with H. Plank and Ch. Gspan at the Institute for Electron Microscopy and Nanoanalysis (TU Graz, Austria). For these measurements an additional

⁴The 450 nm-thick Co film was grown on a Si/SiO₂/Si₃N₄ substrate by physical vapor deposition (PVD) at a base pressure of 3×10^{-7} mbar and a growth rate of about 1 Å/sec using Co of 99.99% purity.

⁵The TEM used for these investigations was from FEI, Tecnai F20 with a Schottky gun operating at 200 kV. The EELS data were obtained with a post-column energy filter from Gatan (GATAN, USA) and a 2k CCD. For the EELS measurements, the STEM mode was used for exact positioning and correlation of the electron beam with the sample and its composition.

series of Co-FEBID samples was prepared using the same FEBID parameters as the primary samples which underwent the purification procedure according to the respective protocol shown in Fig. 6.14. After preparation, the samples were covered with a 300 nm-thick protective Pt-C layer deposited by FEBID.

The results of the TEM and STEM-EELS examination are presented in Fig. 6.16. A homogenous distribution of Co, C and O over the entire thickness was revealed for the as-deposited sample, showing only a slightly enhanced content of oxygen within the topmost, 5 nm-thick layer [see Figs. 6.16(a) and (b)]. Furthermore, a continuous fine-grained morphology was observed, which is expected for FEBID structures. However, the key finding was obtained on the purified sample. For this sample, a double-layered structure with rather well-defined interface was identified [see Figs. 6.16(b) and (d)]. The top layer appeared C- and O-free with a highly compact Co distribution and a thickness of ≈ 20 nm, while for the bottom layer a porous structure with clearly reduced O and strong variations of C has been identified.

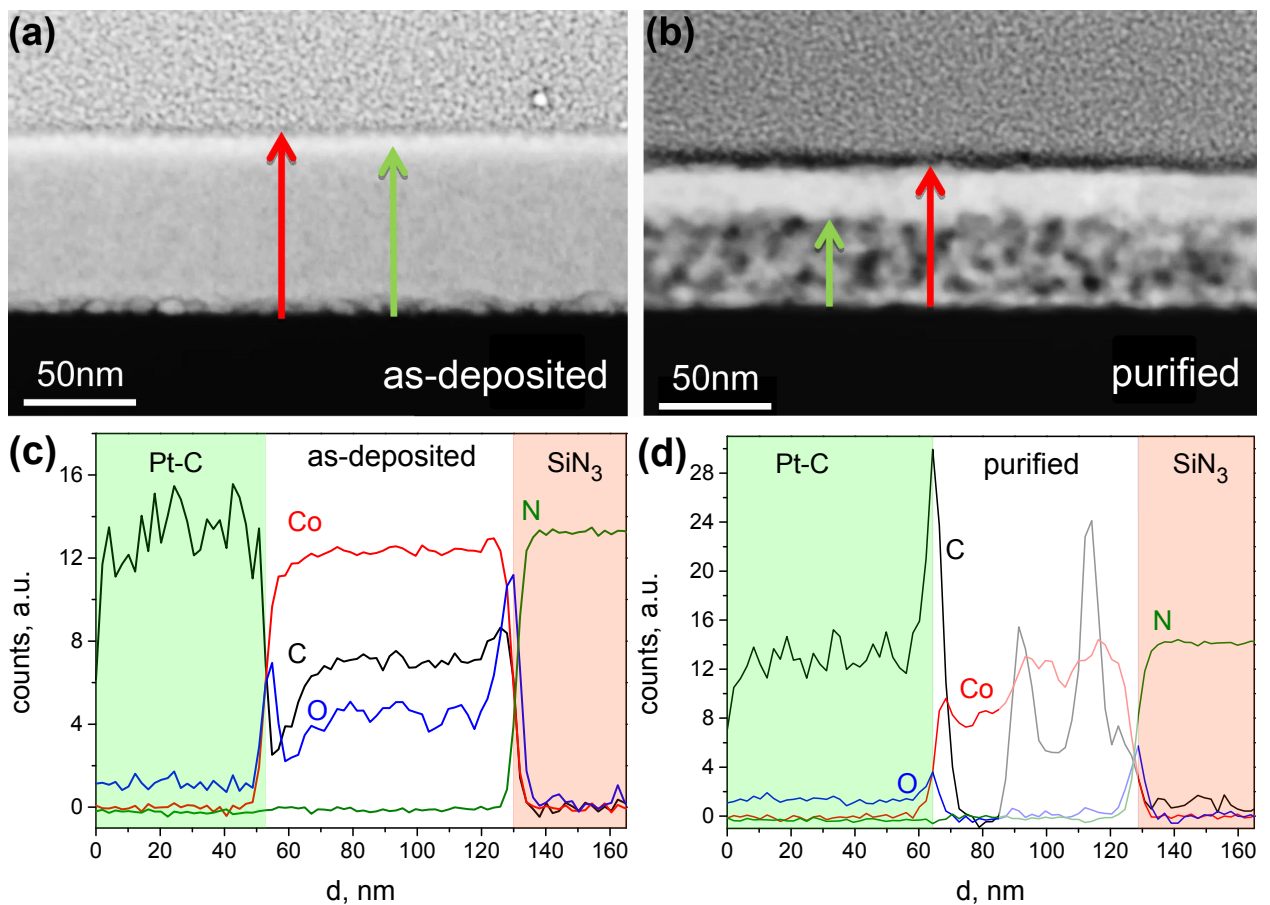


Figure 6.16: Cross-sectional TEM micrographs of (a) as-deposited and (b) purified Co-FEBID samples. Corresponding EELS-STEM spectrograms for (c) as-deposited and (d) purified Co-FEBID samples. Pt-C denotes the protective layer, while SiN₃ is the top layer of the substrate.

Conductivity

The electrical resistance was measured as a function of temperature in the standard 4-probe geometry in the DC current mode. The $\rho(T)$ for the as-deposited and purified samples was found to be significantly different (see Fig. 6.17). For the first one [Fig. 6.17(a)] a very weak metallic behavior is revealed that gradually develops a localization-induced increase below about 70 K. Its high resistivity value ($\rho_{280\text{K}} = 280 \mu\Omega\text{cm}$) is caused by a large degree of grain boundary scattering as well as the high carbon content. The inset of Fig. 6.17(a) presents the square-root temperature dependence of the normalized conductivity. The curve shows a linear behavior in the temperature range from about 3 K up to 28 K. This behavior is in agreement with the transport theory for ordered granular metals in the strong intergrain coupling regime proposed by Beloborodov *et al.* [205, 206]. Similar temperature-dependent data were also reported for nanogranular Pt–C samples prepared by FEBID, where $\sigma \sim T^{0.5}$ was observed in the same temperature range [65].

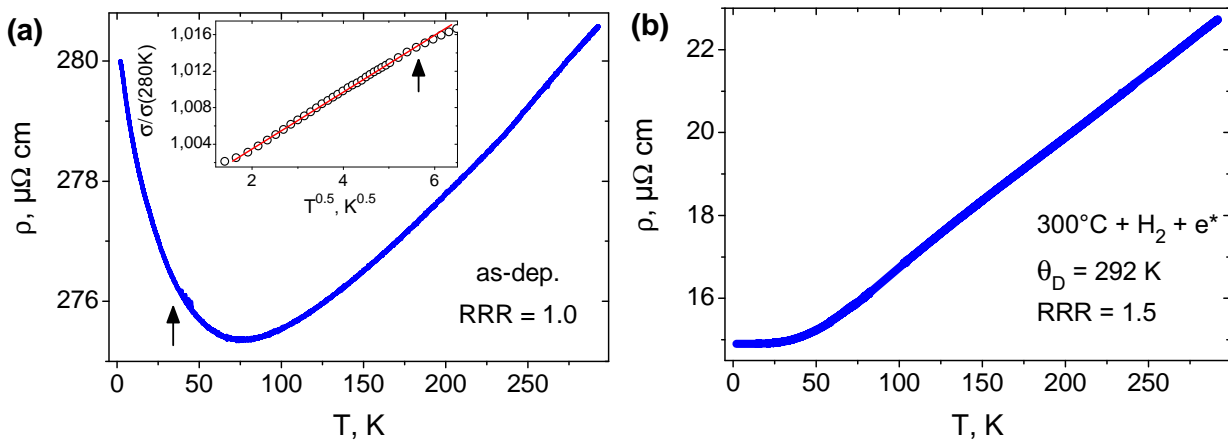


Figure 6.17: Cooling curves for as-deposited (a) and purified (b) samples, as indicated. Inset: Low-temperature conductivity data in σ vs $T^{0.5}$ representation. The solid line is a fit to the law $\sigma \propto T^{0.5}$, while the arrows mark the temperature where the data begins to deviate from this law.

In contrast, the purified sample [Fig. 6.17(b)] exhibits improved electrical conductive properties, as indicated by the drop in resistance by a factor of 1.5 while cooling down. The resistivity value of the purified sample is more than one order of magnitude smaller than that of the as-deposited sample, but it is a factor of 4 larger than the reference bulk value of $5.8 \mu\Omega\text{cm}$ for Co [76]. Taking into account the results of the TEM examinations (the double-layered morphology), resistivity corrections can be applied, providing an upper resistivity value for pure Co of $14 \mu\Omega\text{cm}$. The $\rho(T)$ curve for the purified sample nicely follows the Bloch–Grüneisen behavior (2.14) (see chapter 2, subsection 2.1.2) with a power law exponent $n = 5$, which implies that the resistance is due to electron–phonon scattering, while

electron–magnon contributions ($\propto T^2$) are small. The obtained Debye temperature is 292 K. Interestingly, this value is very close to the value of Θ_D obtained for Co/Pt heterostructures (see section 6.3 of this chapter).

Magnetoresistance and Hall effect

In the MR and Hall effect measurements, very different results were observed for the as-deposited and purified samples, evidencing their different microstructural properties.

A small positive magneto-resistance was observed for the as-deposited sample. The TEM measurements revealed that this sample is a granular metal, and positive magnetoresistance can be attributed to the influence of the magnetic field on the wave function attenuation length for the electronic surface states of the Co grains that are subject to tunnel coupling to neighboring grains. For granular Pt-FEBID structures, it was shown that the wave function shrinkage model (which predicts a reduction of the attenuation length with increasing magnetic field), can account for the observed positive MR [207]. In contrast, a noticeable, one-order-of-magnitude higher, negative magnetoresistance has been observed for the purified sample. It is formed by a pure anisotropic MR (AMR) signal which originates from anisotropic electron scattering due to spin-orbit coupling. This is further confirmation that the purified sample is constituted mostly of pure, metallic Co.

In Hall effect measurements for the as-deposited sample, the signal was formed only by the anomalous Hall contribution. By contrast, the Hall signal for the purified sample demonstrated distinct ordinary and anomalous contributions with different signs. In addition, a notable hysteresis was revealed in this sample. The observed difference in the Hall data can be explained in terms of the microstructural peculiarities of the samples. The significant anomalous Hall contribution for the as-deposited sample can be interpreted as a granular metal with magnetic grains in the strong-coupling limit (resulting in Co grains in the superparamagnetic state). At the same time, if for the purified sample the transport is mainly limited by the topmost, pure, Co layer, observations of a dirty, polycrystalline ferromagnet in Hall effect data are expected. Moreover, given the lateral size and thickness of this sample, it should be in a multidomain state [208] and show hysteresis effects.

Driving elements of the purification process

A post-growth in situ purification approach to obtain pure, Co-FEBID, nano-strip structures relies upon the following three effects: (i) Electron-assisted transformation of the amorphous carbon matrix; (ii) Annealing-assisted microstructural modifications of the cobalt clusters;

(iii) Hydrogen-assisted removal of carbon due to the catalytic activity of cobalt. In the following, a more detailed mechanistic explanation of these physico-chemical processes is proposed.

This first issue to address is to understand which modifications can be introduced by electron irradiation. It should be noted that the as-deposited sample is a nanogranular material made of metallic grains embedded in a dielectric carbon matrix. The transport mechanism in this sample is mediated by electron tunneling between grains through the potential barrier induced by the dielectric matrix. The transport properties of the sample can be tuned by varying the size of the grains in the matrix and by changing the properties of the matrix itself, as it has been reported for electron irradiated Pt-FEBID structures [65, 66]. This effect was explained [65, 66] by microstructural changes associated with (i) a size increase of the metallic nanocrystallites with subsequent coalescence and (ii) a transformation of the amorphous carbon in as-deposited structures into a dielectric matrix with more graphite-like, near-range order. This implies an increased transmission in the tunneling processes in the treated structures. In addition, in Ref. [51] it was reported that by adjusting the nanoparticle sizes and the distances between them, it is possible to tune the magnetic properties of Co-C deposits.

Except for the irradiation step, the annealing-assisted microstructural modifications of the cobalt clusters take place in parallel. It is expected that the microstructural changes are invoked by the presence of the H₂ atmosphere in conjunction with the high temperature. Indeed, an improvement of the conducting properties of Co_xC_{1-x} thin films from the insulating regime for as-grown films to the metallic regimes for films annealed at a temperature of 600°C was reported in Ref. [209]. In this way, for the purified sample, the improved conducting properties can be in part attributed to the thermally-invoked coarsening of the Co nanogranules. These granules tend to form a percolating network. It should be noted that the annealing process takes place in the presence of hydrogen, whereby the purification processes may be driven by a Fischer-Tropsch-like reaction [199]. In this catalytic reaction, hydrogen acts as a reducing agent and the reaction products are hydrocarbons and water which effectively oxidize the carbon. Hence, it is assumed that the reduction of the carbon and oxygen content is caused by the formation of volatile CO. Here, high temperature acts to speed up the reaction. This is an additional effect that stimulates purification.

By combining the driving elements of the purification process for the Co-FEBID deposits described above and applying them simultaneously, the following major effects can be obtained: (i) a reduction of the deposit thickness, (ii) an increase of the metal content with a clear tendency for reduction of the O and C content in the topmost layer (which can be as

thick as 20 nm), (iii) an improvement of the electrical conductivity, and (iv) transition to the ferromagnetic state.

6.6.2 Post-growth purification of Pt-FEBID

The second basic step in the preparation of the Co/Pt heterostructures was the purification of the Pt-FEBID layers. The purification mechanism of the Pt-C deposits fabricated by FEBID was developed in our group by Roland Sachser [75]. Later, different applications were found for this technique, and Co/Pt heterostructures are a particular example. An explanation of the purification mechanism is presented in this subsection, where a more extensive discussion can be found in Ref. [75].

The as-deposited Pt-FEBID layers are nanogranular metals. The purification mechanism for Pt-FEBID structures relies upon the catalytic activity of Pt [200] in an oxygen atmosphere and does not need a parallel electron irradiation process to function (if the O₂ exposure is pulsed). This is in contrast to the purification of Co-FEBID structures, where electron irradiation is one of the driving elements of the purification process.

Details of the deposition process of Pt-FEBID layers can be found in section 6.1 of this chapter. After the deposition, the as-deposited layers were heated up to 150 °C over a ramp time of 60 minutes in the same SEM where they were fabricated without breaking the vacuum. The temperature versus time plot is depicted in Fig. 6.18 (left axis). A special custom-built SEM sample holder allows temperature control of the sample in the range from room temperature to 350 °C, and it is combined with an in situ conductance measurement setup. Details of the setup are presented in chapter 3, section 3.3.

Once heated, the as-fabricated Pt-based deposits were subject to the oxygen flux let into the SEM vacuum chamber up to a pressure of 1.5×10^{-5} mbar through a custom-built GIS with a capillary of 0.5 mm in diameter, and a distance of 100 μ m and an angle of 15° to the sample surface. The samples were subject to 12 cycles of oxygen flux switched on for 5 minutes interrupted by 5-minute turn-offs.

The in situ recorded changes in the electrical conductivity of the samples during the oxygen flux pulsing with fixed exposure period are shown in Fig. 6.18 (right axis). The conductance of the sample was measured under a fixed voltage bias of 10 mV resulting in a small electric field of less than 10 V/cm between the outer contact pads. The recorded $I(t)$ curve can be divided into two sections. The AB section corresponds to the changes in the sample conductance during the heating phase, while the BC section corresponds to the changes in the sample conductance due to the effect of purification. As can be seen from

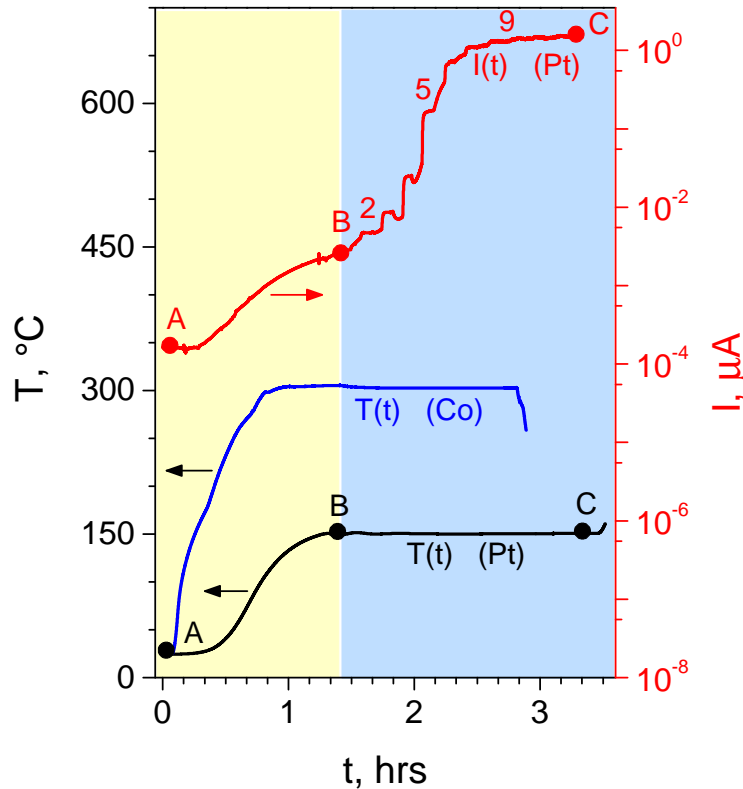


Figure 6.18: Left axis: Temperature logs for the Pt and Co purification processes. Right axis: In situ recorded changes in the electrical current driven by a DC voltage of 10 mV through the Pt-FEBID structure during the cycled oxygen flux at 150 °C. The whole process consists of 12 cycles with a total duration of about 115 min. The AB segments of the recorded curves correspond to the heating time, while the BC segments correspond to the purification time.

the BC section, during the first two cycles, the conductance shows a slight increase during oxygen exposure and saturates when the oxygen supply is switched off. For the third cycle, a different behavior is observed. After a slight increase during oxygen flow, the conductance increases by about 50% after stopping the oxygen supply before saturation occurs. In the later cycles, one can even observe a decrease of the conductance during the oxygen flow, followed by an increase in the flow-off state. After approximately 10 oxygen cycles, one can see in Fig. 6.18 that the resistance of the samples is saturated and it is virtually independent of the oxygen flow state.

The material composition in the as-purified samples was inferred from EDX spectroscopy in the same SEM, without exposure of the deposits to air. The EDX parameters were 5 kV and 1.6 nA. For comparison, the EDX spectra for as-deposited and as-purified Pt-FEBID samples are represented in Fig. 6.19(a). The EDX spectra demonstrate peaks of four elements: Pt, C, O and Al. The peak corresponding to Al arises due to the relatively thin sample thickness, and a contribution from the topmost layer of the substrate (Al_2O_3) cannot be avoided. Also, for this reason, the content of O can not be evaluated adequately since

this element is present in both the Pt-FEBID deposit and substrate. However, it is expected (in accordance with Ref. [75]) that no O would be found in purified Pt-FEBID samples. The comparison of the relative intensities of the Pt M, Pt N and C K lines for the as-deposited and as-purified Pt-FEBID structures suggests that the purification strategy results in very clean Pt. The ratio of Pt/C for the as-deposited samples is 20/80, whereas it is 96/4 for the purified samples. The Al and O peaks were excluded from the quantification. It is worth noting that for the structures with high Pt metal content examined by EDX spectroscopy with excitation energies of 5 keV, low energy X-ray lines from transitions into the N shell of Pt become visible at about 240 eV. These lines must not be ascribed to the K line of C at 277 eV.

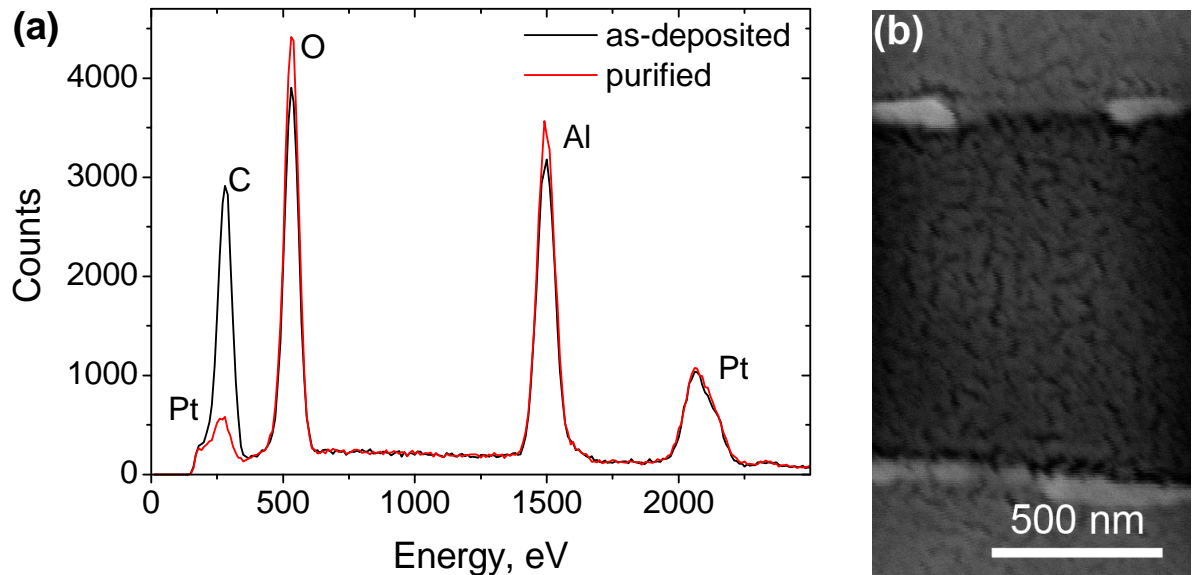


Figure 6.19: (a) EDX spectra of as-grown and purified Pt-FEBID samples. (b) Magnified SEM image of a Pt-FEBID deposit after the purification procedure, illustrating the nanoporous morphology.

Very interesting modifications in the morphology of the as-purified samples take place in comparison to the as-deposited samples. The initial thickness of the 50 nm-thick deposits is reduced by about a factor of 5 as a consequence of the volume reduction effect. The post-treatment thickness of the pure Pt samples is 11 nm, as deduced from AFM measurements. An SEM image of one of the purified samples is shown in Fig. 6.19(b). It reveals a nanoporous morphology. From a greyscale threshold analysis of the SEM image, the void volume fraction of the purified Pt-FEBID samples can be roughly estimated, which yields a value of 0.31 ± 0.07 [75].

In this work, the $\rho(T)$ measurements were not performed alone on the purified Pt-FEBID samples, since these samples were used exclusively for the preparation of Co/Pt heterostruc-

tures. However, some remarks about the transport properties of the purified Pt-FEBID structures can be made in accordance with Ref. [75]. A clear metallic behavior was observed. The residual resistance ratio is $RRR = 1.57$. The room temperature resistivity value is $\rho_{300K} \approx 80 \mu\Omega\text{cm}$, which is about a factor of eight larger than that of bulk Pt ($\rho_{300K} = 10 \mu\Omega\text{cm}$) [201]. The rather small RRR and high ρ_{300K} are most likely due to strongly enhanced diffusive surface scattering contributions considering the small thickness of 11 nm and the nanoporous morphology. The Debye temperature deduced from the fits of the $\rho(T)$ curve by the Bloch–Grüneisen formula (2.14) was about 200 K. For bulk Pt Θ_D is 215 K, which suggests that due to the nanoporous morphology, no significant changes in the electron–phonon scattering channel occur.

To summarize, the major effects observed in the purified Pt-FEBID sample can be reported as follows: (i) a significant reduction of the deposit thickness, (ii) very clean Pt samples are obtained, and (iii) an improvement of the electrical conducting properties. But what is the source for these improvements?

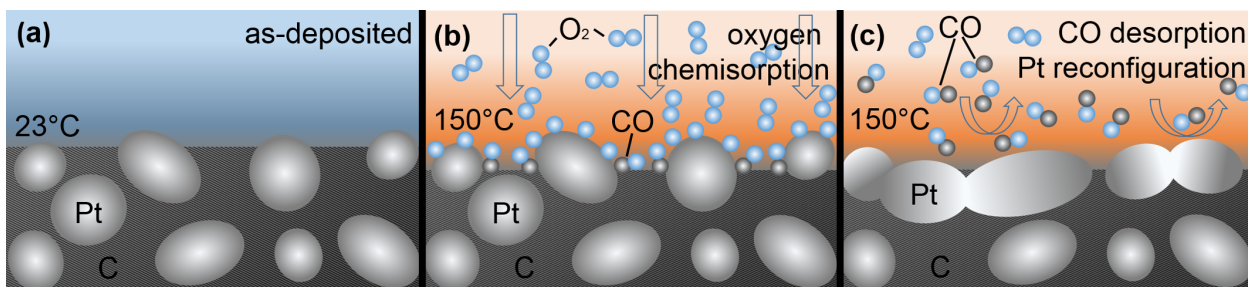


Figure 6.20: Schematic representation of the purification process of the Pt-FEBID samples. (a) A typical cross-section of the as-deposited Pt-FEBID structure consisting of metallic particles of a few nm in diameter embedded in a carbonaceous matrix. (b) Pt-FEBID structure heated to 150 °C accompanied by O_2 flux let close to the deposit surface. The catalytic properties of Pt enable molecular oxygen to dissociatively chemisorb on the surface of the metallic particles leading to formation of CO at the Pt/C interface. The desorption of CO, however, is sterically hindered by chemisorbed oxygen. (c) Switching off the oxygen flux is necessary to enable the CO molecules to desorb. Simultaneously, reorganization and coalescence of Pt nanocrystallites occurs by surface diffusion, resulting in a nanoporous morphology. The chart is build in accordance to Ref. [75].

A mechanistic explanation of the Pt-FEBID purification process under pulsed oxygen conditions can be given as follows. The purification mechanism for Pt-FEBID structures relies upon the catalytic activity of Pt in an oxygen atmosphere [75, 200]. Namely, when delivered close to the deposit surface, molecular oxygen is dissociatively chemisorbed on the surface of the metallic Pt particles. Since the process takes place at 150 °C, a thermally activated oxidation of carbon at the Pt/C interface occurs, leading to the formation of CO and reorganization and coalescence of Pt nanocrystallites by surface diffusion. The latter,

in turn, results in a nanoporous morphology, which is clearly seen in the SEM images of the Co/Pt heterostructures in Fig. 6.2 and pure Pt structure in Fig. 6.19(b). A schematic representation of the purification process of the Pt-FEBID samples used in this work is depicted in Fig. 6.20.

Chapter 7

FEBID superconductor for proximity effect investigations in nanowires

First results of the approach to use a FEBID-based superconductor for the study of the superconducting proximity-effect in normal metal are presented in this chapter. The main purpose of the approach is to evaluate, whether a FEBID-based superconductor can be used for investigations of the long-ranged spin-triplet superconductivity in ferromagnets. Perspectively, the non-invasive deposition of the superconductor by FEBID as compared to FIBID will allow for a better control of magnetic inhomogeneities. In this first experiment an Au nanowire in contact with a Pb-based, superconducting inducer-electrodes prepared by FEBID (Pb-FEBID) was used. A pronounced proximity effect below the T_c of the inducer-electrodes ($T_c \approx 7$ K) was found. The effect is highly sensitive to the current density passing through the nanowire, as well as the applied magnetic field. Moreover, indications of room temperature alloying between Au and Pb, leading to the formation of a new intermetallic compound of these two materials, were found.

7.1 Sample preparation

The investigated samples are Au and Pb-based nanowires, which will be referred to as Au-NW and Pb-FEBID, respectively. Pb-FEBID was prepared for reference purposes.

The 150 nm-wide Au-NW was fabricated from a 60 nm-thick Au film by a combination of photo- and e-beam lithography in conjunction with lift-off (see chapter 3, subsections 3.1.2 and 3.1.3). The Au film was DC magnetron sputtered at room temperature on a Si/SiO₂(10 nm)/Si₃N₄(100 nm) substrate on top of a 2 nm-thick Cr buffer layer. Before sputtering, the sputter chamber was evacuated down to 7.6×10^{-8} mbar. During the deposition the voltage was 430 V resulting in a DC current value of 10 mA at a process pressure

of 1.4×10^{-2} mbar, while the sputtering rate was about 0.3 nm/s.

The Pb-based nanowire was prepared by FEBID (see chapter 3, subsection 3.1.4) on the same substrate after fabrication of the Au-NW in a high-resolution SEM (FEI Nova NanoLab 600). FEBID of Pb was also used for the deposition of the Pb-based, superconducting voltage inducer-electrodes to the Au-NW for the PE investigations. Recently it was found [64] that by using optimized deposition parameters Pb-FEBID structures demonstrate a stable superconducting phase with a T_c of 7.2 K, which is known for bulk lead [210]. In the FEBID process, the precursor was tetraethyl lead $(\text{CH}_3\text{CH}_2)_4\text{Pb}$, the beam parameters were 10 kV/13 pA, the pitch was 10 nm, the dwell time was 5 μs , and the process pressure was 8.85×10^{-6} mbar. Before deposition the chamber was evacuated down to 3.6×10^{-6} mbar. The precursor (kept at room temperature) was introduced into the SEM chamber via a thin capillary with a diameter of 0.5 mm angled at 22° relative to the substrate surface. The capillary was placed 140 μm away from the electron impact area in lateral direction as well as 90 μm away from the substrate. In preliminary tests it was found that in order to obtain submicron Pb-FEBID structures, the FEBID process should be performed in SEM high-resolution mode, while the initial raster pattern should be set not to “rectangle”, but rather to “line”, that is the rastering process takes place along one single line. In this way, the width, w , of the deposit is equivalent to the beam diameter, while the length, l , is equivalent to the length of the pattern. This approach was associated with a significant broadening of the resulting deposits, which likely takes place due to the very rapid dissociation of the precursor gas and, as a consequence, increase in the speed of the deposition process. The Pb-FEBID deposits with the width of $w \approx 100$ nm and the thickness of $d \approx 150$ nm (as revealed by AFM measurements) were prepared in a rectangular, nanowire-shaped form.

An overview of the geometry used for the study of the PE-induced superconductivity is shown in Fig. 7.1(a). This geometry was used to realize a multi 4-probe structure where several voltage electrodes made of FEBID superconductor are attached to the nanowire at different positions. This has allowed simultaneously to induce the superconducting phase into the nanowire and to probe the nanowire resistance changes associated with the PE for the selected nanowire section. For this, 16 μm long Au-NW was divided into 200 nm, 400 nm, 700 nm, 1 μm , 1.5 μm , 2 μm , 2.5 μm and 4 μm measuring sections. Every single electrode was used for two adjacent sections. The current leads for the Au-NW were its extensions which then turn into the outer Cr/Au auxiliary electrodes. An SEM image of the fabricated sample is shown in Fig. 7.1(b). As can be seen, a considerable amount of co-deposit is formed around the Pb-FEBID structures, which is one of the major drawbacks of Pb-FEBID and should be addressed in future experiments.

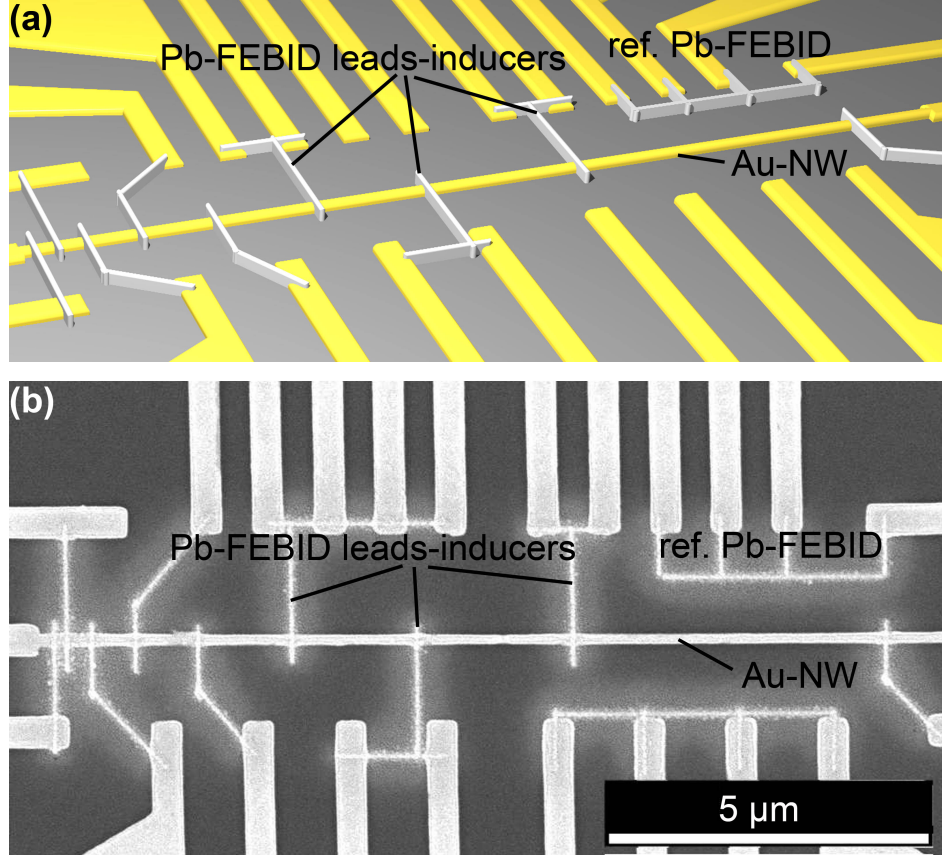


Figure 7.1: (a) Sample layout for electrical resistance measurements. Superconducting Pb-based voltage electrodes are attached to the Au-NW at different positions thus allowing superconductivity to be induced while simultaneously probing the PE over different lengths. (b) SEM micrograph of the sample.

The material composition of the Au-NW and Pb-FEBID structures was evaluated by means of EDX spectroscopy in the same SEM. The probed areas were $100 \times 100 \text{ nm}^2$, and the EDX parameters were 5 kV and 1.6 nA. The EDX analysis made on the Au-NW has showed 98 at. % of Au and 2 at. % of C. Presumably, the small amount of C is arisen from residual gases in the SEM chamber. The composition of the Pb-FEBID was similar to that reported in Ref. [64], namely 45 at. % of Pb, 25 at. % of O, and 30 at. % of C, within the error of the EDX measurement. The structural and compositional parameters of the samples are presented in Tab. 7.1 and Fig. 7.2.

Sample	Cross-section, $w \times d, \text{ nm}^2$	Micro- structure	L, nm	L ₂₀₀ , nm	L ₄₀₀ , nm	L ₇₀₀ , nm	L ₁₀₀₀ , nm	L ₁₅₀₀ , μm	L ₅₀₀₀ , μm
Au-NW	150×60	undefined	×	200	400	700	1000	1.5	5
Pb-FEBID	100×150	nanogranular	1000	×	×	×	×	×	×

Table 7.1: The structural parameters of the Au-NW and Pb-FEBID inducer-electrodes. w : width; d : thickness.

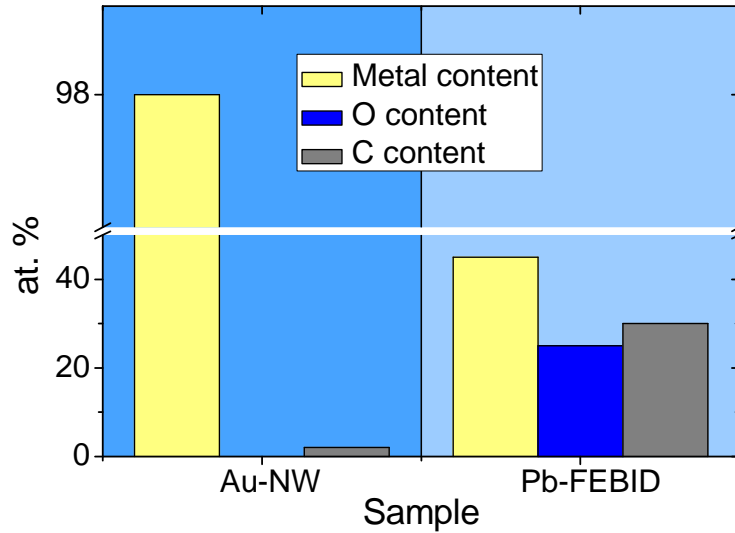


Figure 7.2: Quantified material composition in the Au-NW and Pb-FEBID inducer-electrodes.

7.2 Transport measurements

Transport measurements were performed in a helium-flow cryostat equipped with a 12 T superconducting solenoid. The electrical resistance was measured as a function of temperature in the standard 4-probe geometry, iteratively connecting all sections of the Au-NW. The distances between the voltage electrodes L_i are compiled in Tab. 7.1. All measurements were performed in the DC-current mode¹.

7.2.1 Magneto-transport properties of Pb-FEBID nanowire

The low-temperature resistance data for the reference Pb-FEBID nanowire are shown in Fig. 7.3(a). The $R(T)$ measurements were performed at a current value of 1 nA, corresponding to a current density of 6.7 A/cm^2 . The resistivity of the Pb-FEBID nanowire at 9 K is $\rho_{9\text{K}} \approx 2500 \mu\Omega\text{cm}$, which is two orders of magnitude higher than the resistivity of Pb-FEBID deposits (at the same temperature) reported in Ref. [64] ($\rho_{9\text{K}} \approx 15 \mu\Omega\text{cm}$). The reason for this abnormally high resistivity value is unclear. One potential explanation is that it is increased due to the significantly reduced sample dimensions in both the width and thickness in comparison to those reported in Ref. [64]. Moreover, considering that the metal content of the nanowire is only about 45 at. % of Pb, whereas the rest constitutes the nonconducting elements, the high resistivity value reflects a suppressed conducting channel primarily due to inhomogeneously percolated Pb “islands” across the wire.

¹The current was fed from a Keithley 2400 source meter, while the voltage was measured by a Agilent 34420A nanovoltmeter.

At ≈ 7 K the Pb-FEBID nanowire exhibits a superconducting transition. Here, one noticeable difference in contrast to Ref. [64] is the shape of the transition. It is a relatively broad, that is the onset of the superconducting transition is followed by a long nonzero resistive tail before the zero resistance state at $T \approx 4.75$ K is reached. This tail can be attributed to the previously mentioned structural inhomogeneity of the Pb-FEBID deposits which may lead to spatially varying Josephson coupling energies between those regions which are already fully superconducting [64].

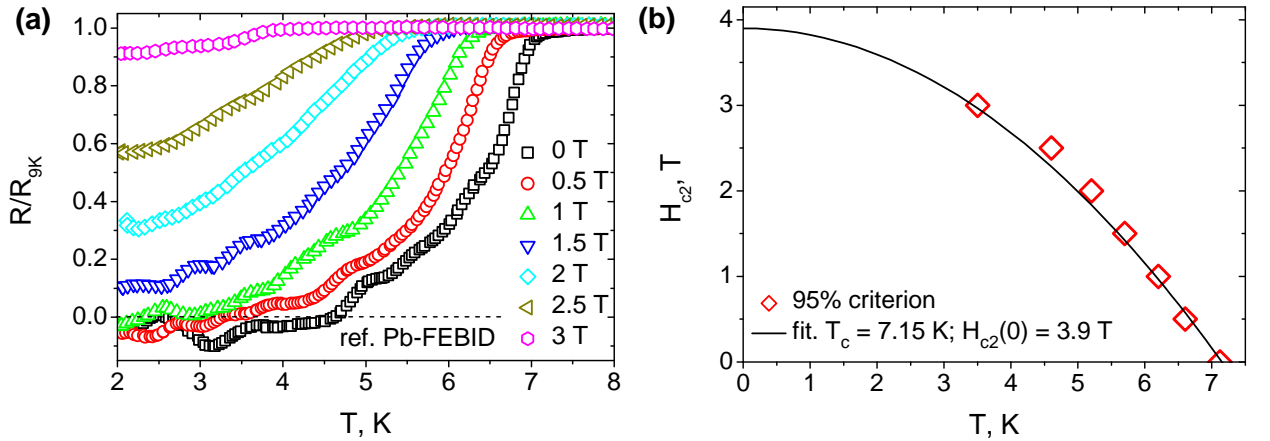


Figure 7.3: (a) Temperature dependences of the normalised resistance of the Pb-FEBID nanowire for a set of applied magnetic fields from 0 to 3 T with a step width of 0.5 T. (b) Temperature dependence of the magnetic field H_{c2} corresponding to the onset of the resistance drop in the $R(T)$ curves in (a). The solid line is a fit to Eq. 7.1 with $H_{c2}(0) = 3.9$ T. The onset temperature of the superconducting transition was determined by using a 95% criterion for the resistance drop.

Measurements of $R(T)$ as a function of the magnetic field were done to deduce the value of the upper critical field H_{c2} for the superconducting Pb-FEBID. Figure 7.3(a) shows the dependence of the normalized resistance as a function of temperature for a set of applied magnetic fields from 0 to 3 T with a step width of 0.5 T. In these measurements, the magnetic field was directed perpendicular to the sample axis. It can be clearly seen that with increasing magnetic field the temperature where the initial resistance begins to decrease shifts towards lower temperatures. By employing a 95% criterion to determine the onset temperature of the superconducting transition and plotting the magnetic field values versus this onset temperature, it was found that the data points $H_{c2}(T)$ nicely follow the empirical law [193]:

$$H_{c2}(T) = H_{c2}(0)[1 - (T/T_c)^2], \quad (7.1)$$

where $H_{c2} = 3.9$ T is the upper critical field and $T_c = 7.15$ K is the superconducting transition temperature of the Pb-FEBID nanowire. The resulting dependence $H_{c2}(T)$ accompanied by

a fit to Eq. (7.1) is shown in Fig. 7.3(b).

It should be noted that the obtained value of $T_c = 7.15$ K for the Pb-FEBID is almost the same as the value of $T_c = 7.2$ K for the more massive Pb-FEBID samples reported in Ref. [64] (which in turn is identical to T_c of bulk lead [210]). Therefore, the T_c of the deposit is not significantly influenced by the presence of carbon and oxygen or by its reduced dimensions.

In principle, both the superconducting properties (T_c and H_{c2}) and the normal conducting properties (metal–insulator transition) of the Pb-FEBID structures are strongly dependent on the deposition parameters, as has been reported in Ref. [64]. Furthermore, optimal deposition parameters for the fabrication of submicron high resolution Pb-FEBID structures are still to be identified.

7.2.2 Proximity effect-induced superconductivity in the Au-NW

Due to problems with the contacts, it was not possible to measure all sections of the Au-NW described in section 7.1. In particular, results for the sections L_{2000} and L_{2500} were not reliable and are not presented.

The low-temperature resistance data for the different sections L_i of the Au-NW are presented in Figs. 7.4 – 7.7. Measurements of $R(T)$ of the Au-NW under magnetic fields up to 4 T were performed with the magnetic field directed perpendicular to the nanowire axis. Measurements were performed at a current value of $1 \mu\text{A}$, corresponding to a current density of 11 kA/cm^2 . The resistivity of all measured Au-NW sections at 9 K, i.e. in the normal state just above T_c of Pb-FEBID, is $\rho_{9\text{K}} \approx 5 \pm 0.5 \mu\Omega\text{cm}$, which is two orders of magnitude higher than the resistivity of bulk gold at the same temperature ($\rho_{9\text{K}} = 0.0226 \mu\Omega\text{cm}$) [211]. Nevertheless, this resistivity value is in agreement with the results reported for gold nanowires of submicron diameter [212]. At these dimensions, finite-size effects, such as the electron scattering from the wire surface and at the grain boundaries, are no longer negligible. In fact, the increased resistivity value in comparison to the bulk material can be explained by taking into account these additional effects.

In Fig. 7.4 the temperature dependence of the normalised resistance for the L_{200} and L_{400} sections of the Au-NW are presented. When T is decreased from 9 to 7 K, a residual plateau is maintained, while with further reduction of T a rapid resistance drop occurs. This is followed by a zero resistance state due to the superconducting PE for both nanowire sections and remains so down to 2.3 K, which was the lowest temperature attainable in the experiment. The measurement was repeated for different current densities, namely $0.2 \mu\text{A} \hat{=}$

2.2 kA/cm² and $5 \mu\text{A} \hat{=} 55 \text{ kA/cm}^2$. As can be seen, the PE effect is strongly dependent on the current density. Namely, for the L₂₀₀ section, the increased current density leads to the reinforcement of the PE effect [see Fig. 7.4(a)]. Conversely, for the L₄₀₀ section, suppression of the zero resistance state can be observed with a higher current density [see Fig. 7.4(b)]. In addition, a negative undershooting of the resistance for the L₄₀₀ section is appeared in the temperature range of $T = 4.5 - 6.5 \text{ K}$, which may be caused by the manifestation of quasi-particle imbalance effects [213].

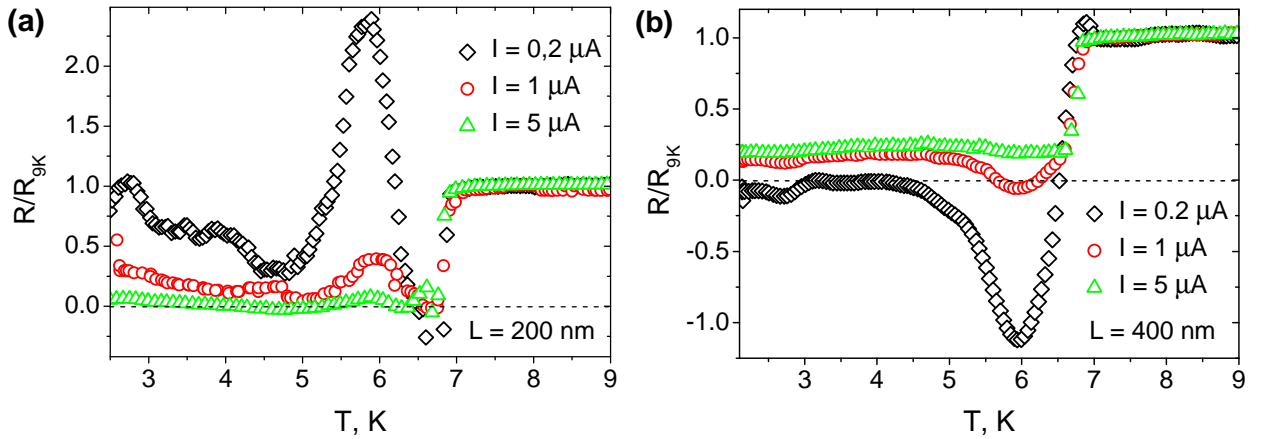


Figure 7.4: Temperature dependence of the normalised resistance for the L₂₀₀ (a) and L₄₀₀ (b) sections of the Au-NW for a set of different currents.

A similar behavior of the $R(T)$ dependence was found for the L₇₀₀ section, namely, a residual plateau followed by a rapid resistance drop and zero resistance state. Measurements of $R(T)$ as a function of magnetic field were done to deduce the value of the upper critical field, H_{c2} , for the L₇₀₀ section. The dependence of the normalised resistance for a set of applied magnetic fields from 0 to 3 T with a step width of 0.5 T are presented in Fig. 7.5(a,b). The measurements were performed with the magnetic field directed perpendicular [Fig. 7.5(a)] and parallel [Fig. 7.5(b)] to the nanowire axis. As can be seen, the PE-induced superconductivity results in the complete extinction of the resistance over the whole nanowire section. The same approach which was applied to the Pb-FEBID nanowire in subsection 7.2.1 was used to determine T_c and H_{c2} of the induced superconductivity for the L₇₀₀ section. By plotting the $H(T)$ dependence and fitting the data with Eq. 7.1, as shown in Fig. 7.5(c), values of $T_c = 7 \text{ K}$ and $H_{c2}^\perp(0) = 3.7 \text{ T}$ and $H_{c2}^\parallel(0) = 4.6 \text{ T}$ were obtained for the magnetic field directed perpendicular (\perp) and parallel (\parallel) to the nanowire axis, respectively. The ratio of H_{c2} values is 1.24. The angular dependence of the upper critical field was theoretically predicted by Saint-James and de Gennes which is the thin film effect type of H_{c2} anisotropy and $H_{c2}^\parallel/H_{c2}^\perp \approx 1.69$ [214, 215], whereas experimental confirmations of this effect can be

found in Refs. [216, 217]. A slight reduction of the T_c value in comparison with the T_c of the Pb-FEBID reference nanowire is expected since the PE can weaken the superconductivity near the S/N interface [38].

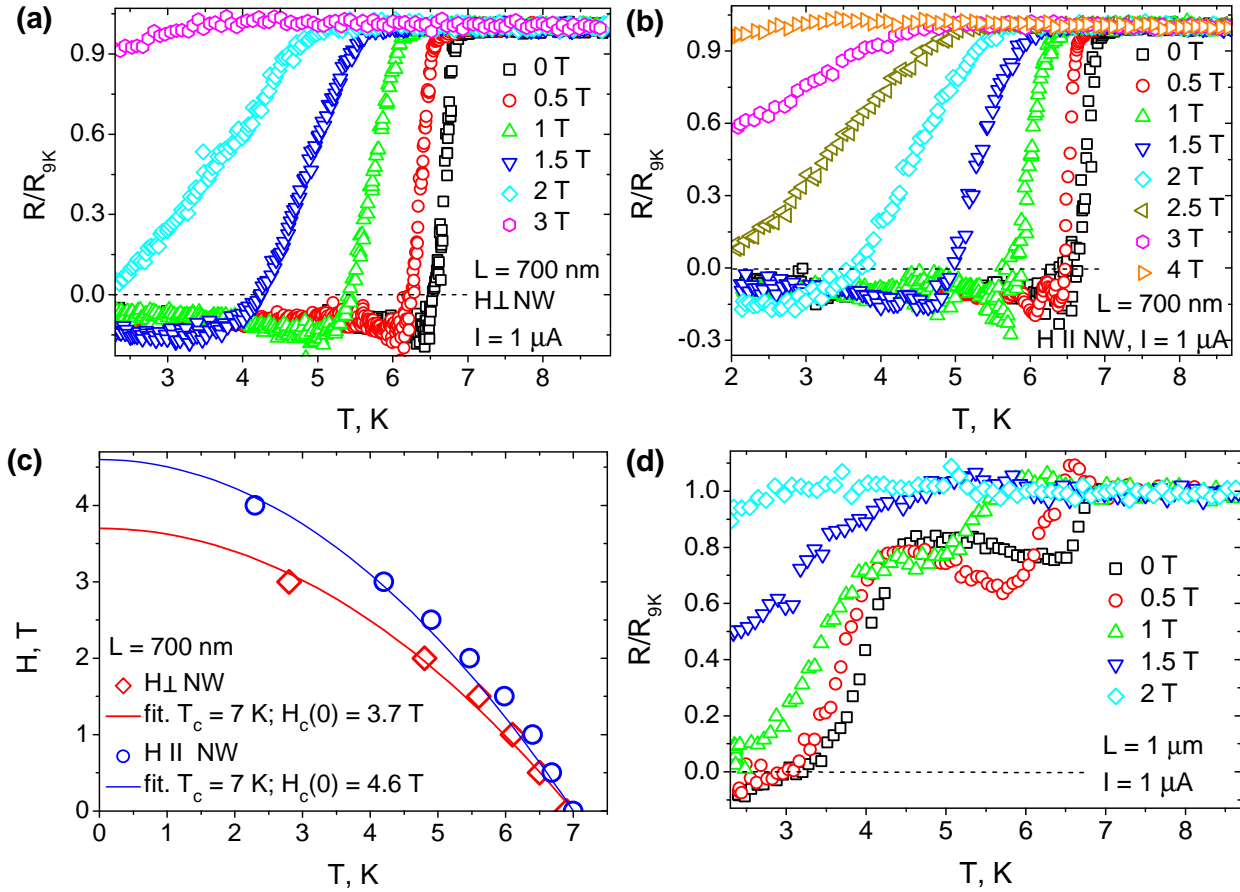


Figure 7.5: Temperature dependence of the normalised resistance of the L_{700} Au-NW section for a set of applied magnetic fields directed perpendicular (a) and parallel (b) to the nanowire axis. (c) Temperature dependence of the magnetic field H_{c2} corresponding to the onset of the resistance drop in $R(T)$ curves of the Au-NW for the two cases shown in panels (a) and (b). (d) Temperature dependence of the normalised resistance of the L_{1000} Au-NW section for a set of applied magnetic fields with a strongly marked two-step transition.

The main feature of the L_{1000} section is that the resistance drop is not as obvious and occurs in two steps, as shown in Fig. 7.5(d). In the first step (between 6.5 – 7 K), the resistance is reduced sharply to 80% of its normal state value, followed by a slight increase to 90% at ≈ 4.5 K, followed by a slow decrease until ≈ 3.3 K where it completely vanishes. The two-step transition shifts to lower temperatures with increasing magnetic field and merges into one transition at about 1.5 T, whereas the superconductivity of the nanowire is fully suppressed at about 3 T. The appearance of the second transition is probably associated with formation of the AuPb₂ intermetallic compound resulting from alloying between Au and Pb at the room temperature. This effect is considered in more detail in the next section.

In contradistinction to the above reported Au-NW sections, the relative resistance drop for the L_{1500} section is only about 17% with respect to its normal state value [see Fig. 7.6(a)]. The induced superconductivity in this section is fully suppressed at a magnetic field value of ≈ 2.5 T. It is worth noting that the magnetic field value required to suppress the PE in the nanowire is lower than the critical field of the superconducting inducer-electrode. Moreover, with increasing length of the nanowire section, smaller magnetic field values are required to see this regularity. The resistance versus magnetic field $R(H)$ dependence measured at a fixed temperature of 5 K is shown in Fig. 7.6(b). In the $R(H)$ curves, the superconducting transition is clearly seen, as well as symmetric oscillations of the magnetoresistance at ± 1.5 T. These oscillations are similar to those that have been observed for the Cu nanowire in contact with the W-based superconductor (see chapter 4, section 4.6), and presumably can be caused by (i) the induced superconductivity in the nanowire by means of the PE (ii) accompanied by the generation and movement of superconducting vortices in response to the increasing perpendicular magnetic field across the wire. Nevertheless, this effect must remain for future elaborations.

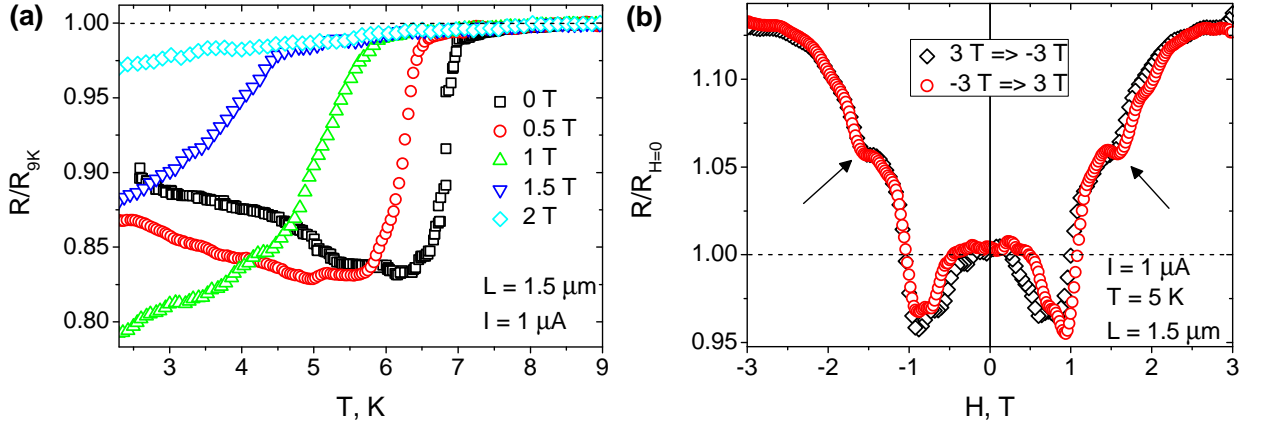


Figure 7.6: (a) Temperature dependence of the normalised resistance of the L_{1500} Au-NW section for a set of applied magnetic fields. (b) Magnetoresistance of the L_{1500} Au-NW section measured at fixed $T = 5$ K.

Results for the longest measured Au-NW section L_{5000} are presented in Fig. 7.7. A new feature was observed for this section. Instead of the anticipated resistance decrease, a sharp resistance jump of about 10% relative to the normal state value was observed at the superconducting onset temperature of the inducer electrodes. This is followed by a slowly decreasing resistance tail until 5.5 K. Applying of a magnetic field leads to the shift of the resistance jump to the lower temperatures followed by its disappearance at higher applied magnetic fields. Moreover, a significant increase of the signal noise ratio after the superconducting onset temperature of the inducer electrodes has been observed.

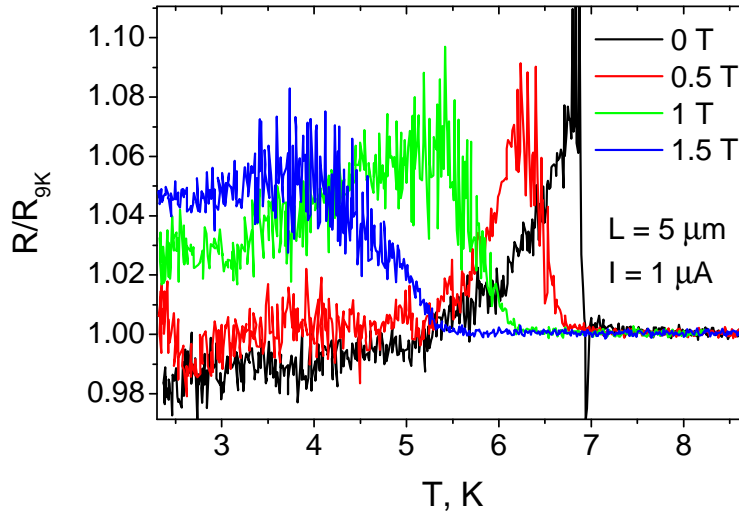


Figure 7.7: Temperature dependence of the normalised resistance of the L_{5000} Au-NW section for a set of applied magnetic fields.

7.3 Room temperature alloying at the Au/Pb interface

It is well known that when two metal films made of two different materials are brought in contact and this double layer is annealed, diffusion will occur at the interface. The result is the formation of either a solid solution or an intermetallic compound [218]. The interdiffusion depth, which is usually controlled by the motion of the reaction boundary, follows a parabolic law $x^2 = D't$ [219], where x is the distance moved by the boundary from the initial interface in time t , and D' is the diffusion coefficient for the boundary. The diffusion coefficient, D' , is a function of temperature in accordance with the Arrhenius equation, $D' = D'_0 \exp(-E/RT)$, where E is the activation energy of diffusion, R is the universal gas constant and T is the temperature. Interestingly, for some diffusion processes high temperatures are not required, and interdiffusion takes place even at room temperature [220]. This scenario is applicable to the AuPb system [221], which in the present case can be formed at the Au/Pb interface of the PE junction during and after the contacting of the Au-NW with the Pb-FEBID electrodes.

The interdiffusion effect between Au and Pb is comprehensively addressed in Refs. [218] and [222]. In this section, the most relevant properties of the AuPb system for the present work are considered. According to the AuPb binary phase diagram [221], shown in Fig. 7.8, several intermetallic compounds are formed in the bulk. These are AuPb_2 , AuPb_3 and Au_2Pb . In fact, all of these three compounds are superconductors with different T_c (for example, vapor deposited thin films of AuPb_2 and AuPb_3 have T_c of 4.30 K and 4.25 K, respectively [221]). The formation of AuPb_2 at room temperature was identified by Weaver *et al.* [222], and it is the only compound which can be formed upon diffusion rapidly after

deposition of the Pb layer on the Au film. It has been shown that only 20 min is required for Au to diffuse 500 Å into Pb. Later, Caswell [223] reported on the superconducting properties of AuPb₂ with $T_c = 4.3$ K. In the extensive investigations performed by Marinkovic *et al.* [220] it was shown that two other compounds can be also formed at room temperature. Depending on the Au/Pb ratio and the time passed after deposition, both AuPb₂ and AuPb₃ can be formed either separately or simultaneously. This is in contrast to Au₂Pb which is not formed immediately after deposition, but is produced somewhat later through a structural transformation from AuPb₂. Moreover, the variation of the thickness ratio of the Au and Pb films can be used to preferentially form a desired intermetallic phase, where each intermetallic phase is characterized by its own transition temperature T_c and energy gap Δ [224].

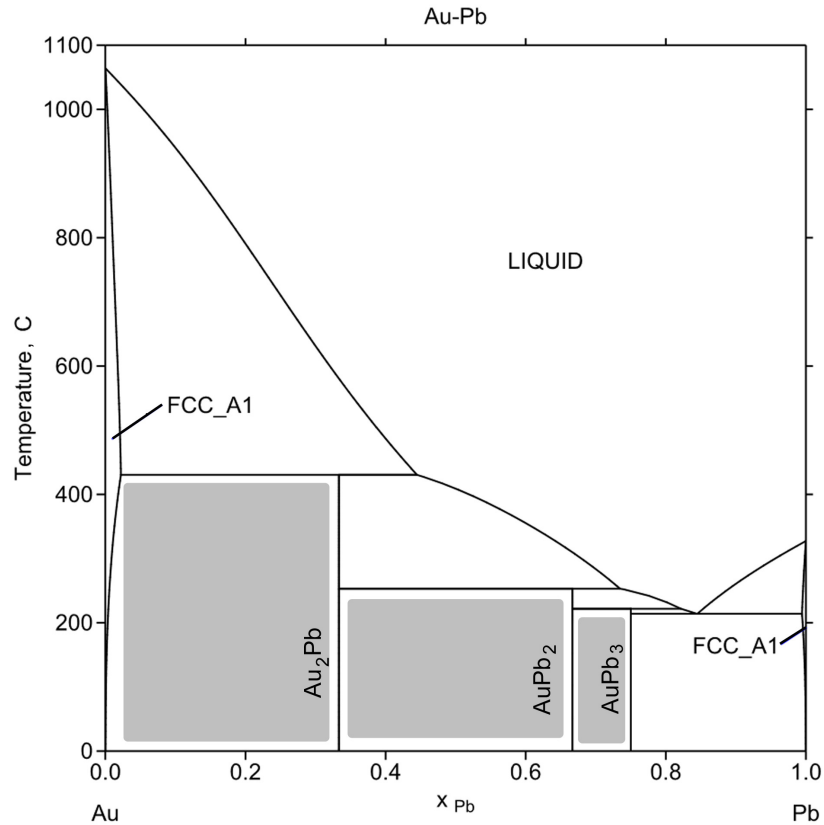


Figure 7.8: The AuPb binary phase diagram (reproduced after Okamoto *et al.* [221]).

To summarize, based on the results on AuPb intermetallic compounds described above and taking into account the thickness ratio of the Au-NW and the Pb-FEBID electrodes, it is expected that AuPb₂ can be formed at the Au/Pb interface. This is in line with $R(T)$ measurements performed on the L_{1000} section of the Au-NW reported in Fig. 7.5(d). For this section of the nanowire, the sharp resistance drop at 7 K due to the PE-induced superconductivity in the Au-NW is followed by a second drop at ≈ 4.25 K. The temperature at which the second drop takes place is close to the T_c of AuPb₂ reported in Ref. [223].

Chapter 8

Conclusions

One of the focuses of this work was to experimentally study the proximity-effect-induced superconductivity by electrical resistance measurements in single diamagnetic and ferromagnetic nanowires. Specifically, the following materials were used for this study: two, single crystal, high-quality Cu nanowires with a resistivity close to that of the bulk material, one polycrystalline Co nanowire grown in heavy-ion-track-etched polycarbonate templates, one rectangular nanowire-shaped, finely dispersed, nanogranular, Co structure prepared by focused electron beam induced deposition (FEBID), and finally, one rectangular-shaped nanowire fabricated from a Au film by e-beam lithography in conjunction with lift-off. In this work, amorphous W-based and nanogranular Pb-based superconductors were prepared by focused ion (FIBID) and electron beam-induced deposition (FEBID), respectively. These were directly attached to the nanowires and were used as superconducting inducer electrodes. In this way, marked drops (although different in magnitude) in the nanowire resistance $R(T)$ have been observed when sweeping the temperature below the T_c of the superconducting inducer.

The different microstructural properties of the samples allowed us to qualitatively investigate different cases of proximity-induced superconductivity coexisting with other effects. In particular, a large resistance contribution from the ion-beam-damaged regions (for the high-quality Cu nanowires) was identified and quantified as well as a localization-like, low-temperature transport in the polycrystalline Co nanowire owing to the large resistivity of the grain boundaries, and strong pair-breaking effects due to the wave function symmetry-altering scattering in the finely dispersed, nanogranular, Co structure. In all the cases, proximity-induced superconductivity became apparent via resistance drops just below the transition temperature of the W-based (5.2 K) and Pb-based (7 K) superconducting inducer electrodes. By using a simple resistance model it was possible to successfully quantify the proximity lengths as a function of temperature in all the samples. It was observed that in

the polycrystalline Co nanowire the proximity effect is long-ranged, with a proximity length on the order of $1\ \mu\text{m}$ at 2.4 K, which is amongst the largest reported to date. Moreover, this long-ranged effect is insusceptible to magnetic fields up to 11 T, limited only by the critical field of the superconducting electrode. A strong magnetic inhomogeneity of the system is believed to be caused by both the presence of antiferromagnetic Co_3O_4 at grain boundaries and the employed nanoprocessing by FEBID. These are all indications of the spin-triplet nature of the observed proximity effect in the polycrystalline cobalt, although an extensive comparison of the proximity effect in metallic and ferromagnetic nanowires remains for future elaboration on a large number of samples. Interestingly, the same effect was not observed in the nanogranular Co nanowire structure, most likely due to the enhanced pair-breaking effects by the wave function symmetry-altering scattering at the boundaries of nanograins. Quantitatively, the temperature dependence of the superconducting proximity length in the single-crystal Cu and the polycrystalline Co could be fitted very well to an expression of the form $\xi(T) \propto \sqrt{1/T}$ over a wide temperature range. This is in good agreement with the theoretical predictions for the temperature dependence of the superconducting proximity length in the diffusive limit. Finally, the proximity length seems to be larger than the average grain size of the polycrystalline Co. This indicates that the induced, long-range triplet state is a rather robust feature of the ferromagnetic Co nanowires, an aspect of great relevance for applications.

Additionally, it is worth noting that great care should be paid when choosing materials for the investigation of the superconducting proximity effect. Thus, despite the promising application of FEBID for fabrication of Pb-based, high-resolution, superconducting structures, the choice of the AuPb system was in general not suitable. A significant room-temperature inter-diffusion process was found to take place between these two metals, leading to formation of intermetallic compounds. These compounds possess their own superconducting properties, which introduces difficulties in the interpretation of the obtained data.

The second focus of this work was the study of materials with controllable magneto-transport properties. The ability to switch the magnetization is a basic property needed for tuning the local magnetic inhomogeneity of ferromagnets on the lateral mesoscale. This is highly relevant for basic research in micro-magnetism and spin-dependent transport. According to theoretical predictions, it is particularly required for inducing and subsequently supporting triplet superconductivity in superconductor/ferromagnet heterostructures. After numerous investigations, an approach allowing the controllable tuning of the magnetic properties of Co/Pt nano-stripe, layered heterostructures with high resolution on the lateral mesoscale prepared by FEBID was presented. By means of post-growth irradiation and

heating of the Pt- and Co-based nano-stripes (as well as by predefining thicknesses of each layer) it has been demonstrated that the magnetic response of the nano-stripes can be locally tuned from the soft-magnetic properties of Co to the hard ferromagnetic response of the CoPt L1₀ phase formed at the interface between two layers. Furthermore, controllable magnetic properties are combined with the high conducting properties. Based on the lateral resolution capability of the FEBID technique employed, coercive field and remanence tuning down to the 30 nm regime are anticipated.

It is quite obvious that a direct-write approach of structures by FEBID on the nanometer scale can greatly benefit applications in mesoscopic physics. Many novel phenomena not seen in bulk material often manifest themselves in systems of reduced dimensionality. Also reported in this work is the possibility to control the magneto-transport properties of Co nanowires and Co/Pt heterostructures fabricated by FEBID. Their combination with mesoscopically resolved, Pb-based FEBID superconductor may be of interest in topics such as spintronics. The opportunity to combine the dissipationless supercurrents of superconductors with the spin alignment of ferromagnets via exotic spin-triplet pairing is of great potential for new spin-based applications. Perhaps in the near future, the new devices proposed by theorists such as spin switches, spin valves, spin pumps or spin filters, in combination with superconductivity, will find proper practical application in electronics, in analogy with SQUIDs half a century ago.

Appendices

A Determination of crystallite sizes in Co_3O_4

The broadening of the Co_3O_4 peaks in the X-ray diffractogram (see chapter 3 subsection 3.2.2) can be attributed to the presence of sub-micrometer crystallites and, thus, analyzed on the basis of the Scherrer equation:

$$\tau = \frac{K\lambda}{\Delta(2\theta) \cos \theta}, \quad (8.1)$$

where τ is the lower limit for the crystallite size, $K = 0.9$ for the assumed round shape of the crystallites, $\lambda = 0.1542$ nm is the $\text{Cu}_{K\alpha}$ wavelength, $\Delta(2\theta)$ is the peak broadening at half maximum intensity (in radians), and θ is the Bragg angle.

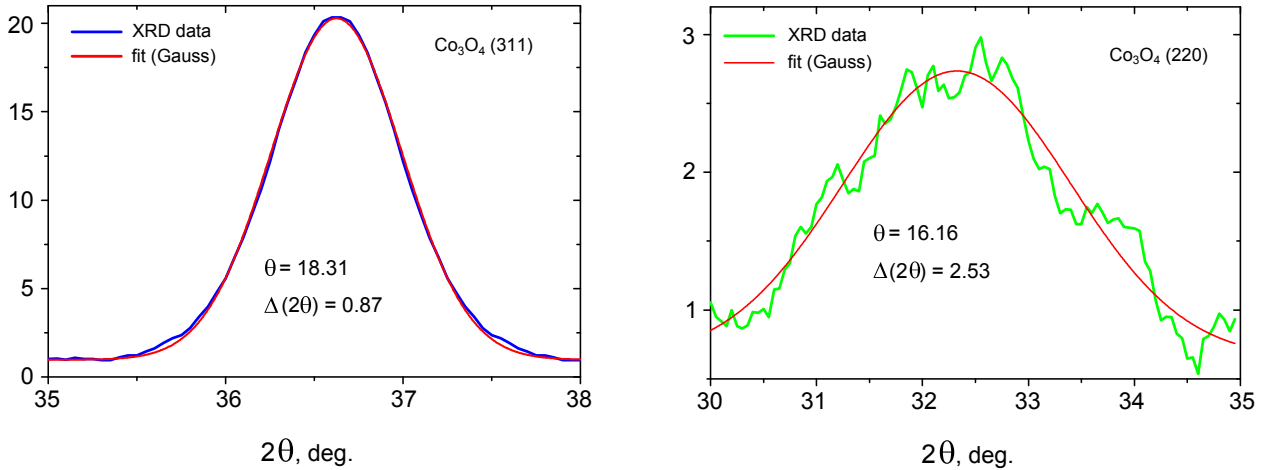


Figure 8.1: XRD data in the vicinity of Co_3O_4 peaks accompanied by Gaussian fits.

Substituting the values deduced from fitting the XRD data in Fig. 8.1 to gaussian distributions, the deduced crystallite sizes are within 5-10 nm. Therefore, we assumed that an oxide layer with a thickness of 10 nm has been formed at the Co crystallite boundaries. The thus estimated thickness of the Co_3O_4 layer was used in the Monte Carlo simulation of the penetration of electrons in the Co nanowire.

B Quantification of the resistance contribution of ion-damaged areas

Quantification of the resistance contribution of the ion-damaged areas associated with application of FIBID for contacting the Cu-NW2 (see chapter 4 section 4.4) is based on the

model electrical circuit shown in Fig. 8.2. The entire nanowire can be considered as a series of serial resistors. There are three types of the resistors. The first one, R_{NW} , corresponds to the intact segments of the nanowire, the second one, R^* , corresponds to the nanowire segment underneath of the W-FIBID electrode, and the third one, R^{**} , corresponds to the nanowire segments underneath of the Pt-FIBID electrodes. Each resistor has its own resistivity, that is ρ_{NW} , ρ^* and ρ^{**} , respectively. According to the electrical circuit shown in Fig. 8.2, one can write the following system of equations:

$$\begin{cases} R_1 = R_{NW1} + R^* \\ R_2 = R_{NW2} + R^* + 2R^{**}, \\ R_3 = R_{NW3} + R^* + 4R^{**} \end{cases} \quad (8.2)$$

where R_1 , R_2 and R_3 are the measured resistances of the corresponding nanowire sections.

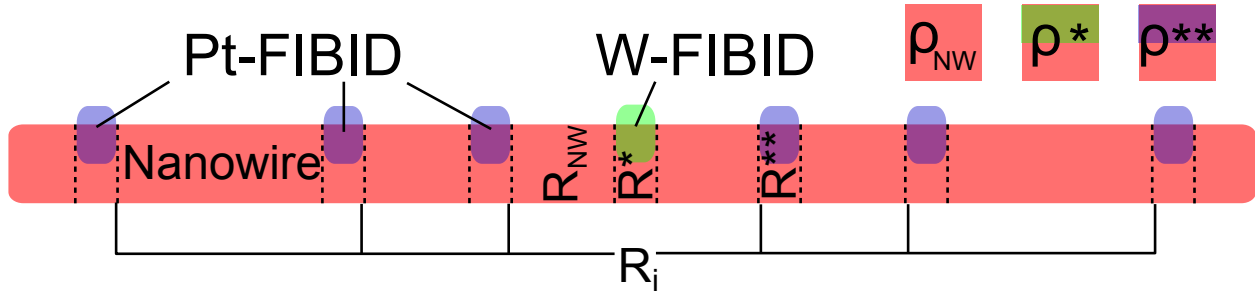


Figure 8.2: Model electrical circuit used for the quantification of the resistance contribution of the ion-beam-damaged areas.

Using Pouillet's law ($R = \rho L/S$) this system of equations can be rewritten as follows:

$$\begin{cases} R_1 = \frac{\rho_{NW}(L_{NW1} - L_W)}{S} + \frac{\rho^* L_W}{S}, \\ R_2 = \frac{\rho_{NW}(L_{NW2} - L_W - 2L_{Pt})}{S} + \frac{\rho^* L_W}{S} + 2\frac{\rho^{**} L_{Pt}}{S}, \\ R_3 = \frac{\rho_{NW}(L_{NW3} - L_W - 4L_{Pt})}{S} + \frac{\rho^* L_W}{S} + 4\frac{\rho^{**} L_{Pt}}{S}, \end{cases} \quad (8.3)$$

where L_{NW1} , L_{NW2} and L_{NW3} are the length of the corresponding measured nanowire sections, L_W and L_{Pt} are the width of the contact segments for W-FIBID and Pt-FIBID, respectively, and S is the cross sectional area of the nanowire. From this simple system of equations (with three unknowns) ρ_{NW} , ρ^* and ρ^{**} can be easily obtained.

C CoPt binary alloy phase diagram, crystal structure and magnetic properties

The CoPt binary alloy phase diagram, shown in Fig. 8.3, is characterized by the A1 phase in the range of complete solid solubility at high temperatures [225]. Co and Pt are mutually miscible and form homogeneous solid solutions over the entire range of composition. The crystal structure of the A1 phase is disordered fcc over the whole solid solution range, in which Co and Pt atoms statistically occupy the crystallographic sites. The high temperature fcc phase is practically useless for permanent magnet applications because it does not show magnetic ordering. Only at $T \approx 1100$ °C on the Co-rich side a magnetic transformation takes place, namely the system orders ferromagnetically, but stays disordered atomically. Below $T = 825$ °C, a disorder-order transition takes place. At this temperature formation of CoPt L₁₀ from the fcc structure occurs. Also, at $T \approx 750$ °C on the Pt rich side formation of another ordered phase, namely CoPt₃ L₁₂, occurs.

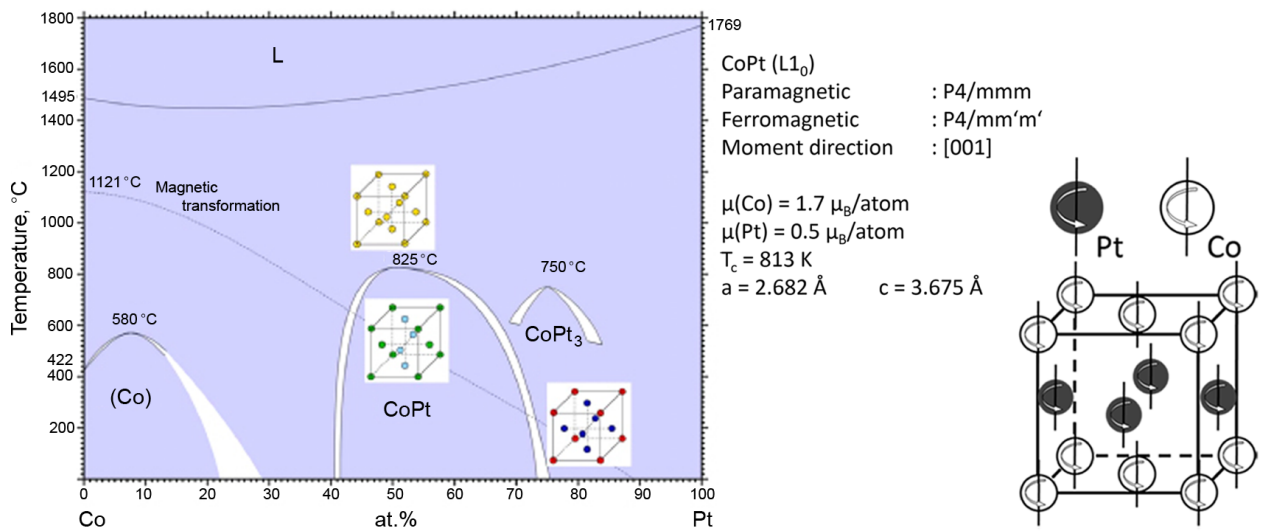


Figure 8.3: CoPt binary alloy phase diagram (reproduced from Ref. [226]).

The CoPt L₁₀ phase (Co_xPt_{1-x} alloy with $x \approx 0.5$) is of interest for this work. It is an ordered superstructure with Pt at the $(0, 0, 0)$ and $(\frac{1}{2}, \frac{1}{2}, 0)$ sites and Co at the $(\frac{1}{2}, 0, \frac{1}{2})$ and $(0, \frac{1}{2}, \frac{1}{2})$ sites. This phase is magnetically hard with a high saturation magnetization and a large magnetocrystalline anisotropy field (≈ 12.3 T). The easy axis of magnetization is oriented along the c -axis [227, 228]. Also, it has a paramagnetic (gray) symmetry of $P4/mmm$. The addition of the magnetic moments yields the lower symmetry of $P4/mm'm'$.

Bibliography

- [1] T T Hongisto and A B Zorin. Single-charge transistor based on the charge-phase duality of a superconducting nanowire circuit. *Phys. Rev. Lett.*, 108:097001, Feb 2012.
- [2] J S Lehtinen, K Zakharov, and K Yu Arutyunov. Coulomb blockade and Bloch oscillations in superconducting Ti nanowires. *Phys. Rev. Lett.*, 109:187001, Oct 2012.
- [3] M Tian, J Wang, J Snyder, J Kurtz, Y Liu, P Schiffer, Th E Mallouk, and M H W Chan. Synthesis and characterization of superconducting single-crystal Sn nanowires. *Appl. Phys. Lett.*, 83(8):1620, 2003.
- [4] J Langer and V Ambegaokar. Intrinsic resistive transition in narrow superconducting channels. *Phys. Rev.*, 164(2):498–510, Dec 1967.
- [5] C Lau, N Markovic, M Bockrath, A Bezryadin, and M Tinkham. Quantum phase slips in superconducting nanowires. *Phys. Rev. Lett.*, 87(21), Nov 2001.
- [6] A Gupta, L Créteinon, N Moussy, B Pannetier, and H Courtois. Anomalous density of states in a metallic film in proximity with a superconductor. *Phys. Rev. B*, 69(10), Mar 2004.
- [7] P G de Gennes. Boundary effects in superconductors. *Rev. Mod. Phys.*, 36(1):225–237, Jan 1964.
- [8] G Deutscher and P G de Gennes. *Proximity effects*. Dekker, NY, 1969.
- [9] A Buzdin. Proximity effects in superconductor-ferromagnet heterostructures. *Rev. Mod. Phys.*, 77(3):935–976, Sep 2005.
- [10] Yu N Chiang, O G Shevchenko, and R N Kolenov. Manifestation of coherent and spin-dependent effects in the conductance of ferromagnets adjoining a superconductor. *Low Temp. Phys.*, 33(4):314–320, 2007.

- [11] J Aumentado and V Chandrasekhar. Mesoscopic ferromagnet-superconductor junctions and the proximity effect. *Phys. Rev. B*, 64:054505, Jul 2001.
- [12] F S Bergeret, A Volkov, and K Efetov. Long-range proximity effects in superconductor-ferromagnet structures. *Phys. Rev. Lett.*, 86(18):4096–4099, Apr 2001.
- [13] F S Bergeret, A Volkov, and K Efetov. Odd triplet superconductivity and related phenomena in superconductor-ferromagnet structures. *Rev. Mod. Phys.*, 77(4):1321–1373, Nov 2005.
- [14] J Wang, M Singh, M Tian, N Kumar, B Liu, Ch Shi, J K Jain, N Samarth, T E Mallouk, and M H W Chan. Interplay between superconductivity and ferromagnetism in crystalline nanowires. *Nature Phys.*, 6(5):389–394, Mar 2010.
- [15] M Kompaniets, O V Dobrovolskiy, C Neetzel, F Porrati, J Brötz, W Ensinger, and M Huth. Long-range superconducting proximity effect in polycrystalline Co nanowires. *Applied Physics Letters*, 104(5):052603, 2014.
- [16] M Eschrig and T Löfwander. Triplet supercurrents in clean and disordered half-metallic ferromagnets. *Nature Phys.*, 4(2):138–143, Jan 2008.
- [17] M Eschrig. Spin-polarized supercurrents for spintronics. *Physics Today*, 64(1):43, 2011.
- [18] R S Keizer, S T B Goennenwein, T M Klapwijk, G Miao, G Xiao, and A Gupta. A spin triplet supercurrent through the half-metallic ferromagnet CrO₂. *Nature*, 439(7078):825–827, Feb 2006.
- [19] J W A Robinson, J D S Witt, and M G Blamire. Controlled injection of spin-triplet supercurrents into a strong ferromagnet. *Science*, 329(5987):59–61, Jul 2010.
- [20] M S Anwar, F Czeschka, M Hesselberth, M Porcu, and J Aarts. Long-range supercurrents through half-metallic ferromagnetic CrO₂. *Phys. Rev. B*, 82:100501, Sep 2010.
- [21] V I Zdravkov, J Kehrlé, G Obermeier, D Lenk, H-A Krug von Nidda, C Müller, M Yu Kupriyanov, A S Sidorenko, S Horn, R Tidecks, and et al. Experimental observation of the triplet spin-valve effect in a superconductor-ferromagnet heterostructure. *Phys. Rev. B*, 87(14), Apr 2013.
- [22] T S Khaire, Mazin A Khasawneh, W P Pratt, and N O Birge. Observation of spin-triplet superconductivity in Co-based Josephson junctions. *Phys. Rev. Lett.*, 104:137002, Mar 2010.

- [23] D Sprungmann, K Westerholt, H Zabel, M Weides, and H Kohlstedt. Evidence for triplet superconductivity in Josephson junctions with barriers of the ferromagnetic Heusler alloy Cu_2MnAl . *Phys. Rev. B*, 82:060505, Aug 2010.
- [24] M Giroud, H Courtois, K Hasselbach, D Mailly, and B Pannetier. Superconducting proximity effect in a mesoscopic ferromagnetic wire. *Phys. Rev. B*, 58(18):R11872–R11875, Nov 1998.
- [25] I Sosnin, H Cho, V Petrashov, and A Volkov. Superconducting phase coherent electron transport in proximity conical ferromagnets. *Phys. Rev. Lett.*, 96(15), Apr 2006.
- [26] B Almog, S Hacoen-Gourgy, A Tsukernik, and G Deutscher. Long-range odd triplet order parameter with equal spin pairing in diffusive Co/In contacts. *Phys. Rev. B*, 80(22), Dec 2009.
- [27] V Petrashov, I Sosnin, I Cox, A Parsons, and C Troadec. Giant mutual proximity effects in ferromagnetic/superconducting nanostructures. *Phys. Rev. Lett.*, 83(16):3281–3284, Oct 1999.
- [28] V T Petrashov, I A Sosnin, I Cox, A Parsons, and C Troadec. Ferromagnetic nanowires with superconducting electrodes. *J. Low Temp. Phys.*, 118(5/6):689–698, 2000.
- [29] S A Wolf. Spintronics: A spin-based electronics vision for the future. *Science*, 294(5546):1488–1495, Nov 2001.
- [30] I Zutíć and S Das Sarma. Spintronics: Fundamentals and applications. *Rev. Mod. Phys.*, 76(2):323–410, Apr 2004.
- [31] J Linder, T Yokoyama, A Sudbo, and M Eschrig. Pairing symmetry conversion by spin-active interfaces in magnetic normal-metal-superconductor junctions. *Phys. Rev. Lett.*, 102(10), Mar 2009.
- [32] M Houzet and A I Buzdin. Long range triplet Josephson effect through a ferromagnetic trilayer. *Physical Review B*, 76(6):060504, 2007.
- [33] Th Mühge, N Garif’yanov, Yu Goryunov, G Khaliullin, L Tagirov, K Westerholt, I Garifullin, and H Zabel. Possible origin for oscillatory superconducting transition temperature in superconductor/ferromagnet multilayers. *Phys. Rev. Lett.*, 77(9):1857–1860, Aug 1996.

- [34] L Lazar, K Westerholt, H Zabel, L R Tagirov, Yu V Goryunov, N N Garifyanov, and I A Garifullin. Superconductor/ferromagnet proximity effect in Fe/Pb/Fe trilayers. *Physical Review B*, 61(5):3711, 2000.
- [35] I Garifullin, D Tikhonov, N Garif'yanov, L Lazar, Yu Goryunov, S Khlebnikov, L Tagirov, K Westerholt, and H Zabel. Re-entrant superconductivity in the superconductor/ferromagnet V/Fe layered system. *Phys. Rev. B*, 66(2), Jul 2002.
- [36] V V Ryazanov, V A Oboznov, A Yu Rusanov, A V Veretennikov, A A Golubov, and J Aarts. Coupling of two superconductors through a ferromagnet: Evidence for a π junction. *Physical review letters*, 86(11):2427, 2001.
- [37] V Zdravkov, A Sidorenko, G Obermeier, S Gsell, M Schreck, C Müller, S Horn, R Tidecks, and L Tagirov. Reentrant superconductivity in Nb/Cu_{1-x}Ni_x bilayers. *Phys. Rev. Lett.*, 97(5), Aug 2006.
- [38] J Wang, Ch Shi, M Tian, Qi Zhang, N Kumar, J Jain, T Mallouk, and M Chan. Proximity-induced superconductivity in nanowires: Minigap state and differential magnetoresistance oscillations. *Phys. Rev. Lett.*, 102(24), Jun 2009.
- [39] H Liu, Z Ye, Zh Luo, K D Rathnayaka, and W Wu. Long-range superconducting proximity effect in template-fabricated single-crystal nanowires. *J. Phys.: Conf. Ser.*, 400(2):022136, Dec 2012.
- [40] L Tagirov. Low-field superconducting spin switch based on a superconductor/ferromagnet multilayer. *Phys. Rev. Lett.*, 83(10):2058–2061, Sep 1999.
- [41] A Volkov, F Bergeret, and K Efetov. Odd triplet superconductivity in superconductor-ferromagnet multilayered structures. *Phys. Rev. Lett.*, 90(11), Mar 2003.
- [42] M Kompaniiets, O V Dobrovolskiy, C Neetzel, E Begun, F Porrati, W Ensinger, and M Huth. Proximity-induced superconductivity in crystalline Cu and Co nanowires and nanogranular Co structures. *Journal of Applied Physics*, 116(7):073906, Aug 2014.
- [43] C Neetzel, M Rauber, and W Ensinger. Preparation of multilayered nanowires with well-defined segments of constant lengths in ion track etched polymer templates. *Trans. Mat. Res. Soc. Japan*, 36:301–304, 2011.
- [44] C Neetzel, F Münch, A Schachtsiek, and W Ensinger. Copper nanowires, nanotubes, and hierarchical nanopatterns: One-dimensional architectures using ion track etched templates. *Trans. Mat. Res. Soc. Japan*, 37:213–218, 2012.

- [45] K Muthukumar, H O Jeschke, R Valenti, E Begun, J Schwenk, F Porrati, and M Huth. Spontaneous dissociation of $\text{Co}_2(\text{CO})_8$ and autocatalytic growth of Co on SiO_2 : A combined experimental and theoretical investigation. *Beilstein J. Nanotech.*, 3:546–555, 2012.
- [46] I Enculescu, M E Toimil-Molaes, C Zet, M Daub, L Westerberg, R Neumann, and R Spohr. Current perpendicular to plane single-nanowire GMR sensor. *Appl. Phys. A*, 86(1):43–47, Nov 2006.
- [47] M E Toimil-Molaes, V Buschmann, D Dobrev, R Neumann, R Scholz, I U Schuchert, and J Vetter. Single-crystalline copper nanowires produced by electrochemical deposition in polymeric ion track membranes. *Adv. Mater.*, 13(1):62–65, Jan 2001.
- [48] M E Toimil-Molaes. Characterization and properties of micro- and nanowires of controlled size, composition, and geometry fabricated by electrodeposition and ion-track technology. *Beilstein J. Nanotechnol.*, 3:860–883, 2012.
- [49] H Kronmüller and M Fähnle. *Micromagnetism and the Microstructure of Ferromagnetic Solids (Cambridge Studies in Magnetism)*. Cambridge University Press, 2003.
- [50] S P Parkin, M Hayashi, and L Thomas. Magnetic domain-wall racetrack memory. *Science*, 320(5873):190–194, Apr 2008.
- [51] M Gabureac, L Bernau, I Utke, and G Boero. Granular Co-C nano-Hall sensors by focused-beam-induced deposition. *Nanotechnology*, 21(11):115503, Mar 2010.
- [52] A Fernández-Pacheco, J M De Teresa, R Córdoba, M R Ibarra, D Petit, D E Read, L O’Brien, E R Lewis, H T Zeng, and R P Cowburn. Domain wall conduit behavior in cobalt nanowires grown by focused electron beam induced deposition. *Appl. Phys. Lett.*, 94(19):192509, 2009.
- [53] D A Allwood. Magnetic domain-wall logic. *Science*, 309(5741):1688–1692, Sep 2005.
- [54] Y K Takahashi, K Hono, S Okamoto, and O Kitakami. Magnetization reversal of FePt hard/soft stacked nanocomposite particle assembly. *J. Appl. Phys.*, 100(7):074305–1–7, 2006.
- [55] L O’Brien, D Petit, E R Lewis, R P Cowburn, D E Read, J Sampaio, H T Zeng, and A-V Jausovec. Tunable remote pinning of domain walls in magnetic nanowires. *Phys. Rev. Lett.*, 106:087204, Feb 2011.

- [56] M Velez, J I Martin, J E Villegas, A Hoffmann, E M Gonzalez, J L Vicent, and I K Schuller. Superconducting vortex pinning with artificial magnetic nanostructures. *J. Magnet. Magn. Mater.*, 320(21):2547 – 2562, 2008.
- [57] O V Dobrovolskiy, M Huth, and V A Shklovskij. Anisotropic magnetoresistive response in thin Nb films decorated by an array of Co stripes. *Supercond. Sci. Technol.*, 23(12):125014–1–5, 2010.
- [58] I Utke, P Hoffmann, and J Melngailis. Gas-assisted focused electron beam and ion beam processing and fabrication. *J. Vac. Sci. Technol. B*, 26(4):1197, 2008.
- [59] M Huth, F Porrati, Ch Schwalb, M Winhold, R Sachser, M Dukic, J Adams, and G Fantner. Focused electron beam induced deposition: A perspective. *Beilstein J. Nanotechnol.*, 3:597–619, Aug 2012.
- [60] T Liang, E Frennberg, B Lieberman, and A Stivers. Advanced photolithographic mask repair using electron beams. *J. Vac. Sci. Technol. B*, 23(6):3101–3105, 2005.
- [61] A Fernandez-Pacheco, L Serrano-Ramn, J M Michalik, M R Ibarra, J M De Teresa, L O’Brien, D Petit, J Lee, and R P Cowburn. Three dimensional magnetic nanowires grown by focused electron-beam induced deposition. *Sci. Rep.*, 2:1492, 2013.
- [62] Ch Danelon, Ch Santschi, J Brugger, and H Vogel. Fabrication and functionalization of nanochannels by electron-beam-induced silicon oxide deposition. *Langmuir*, 22(25):10711–10715, 2006. PMID: 17129050.
- [63] Ch H Schwalb, Ch Grimm, M Baranowski, R Sachser, F Porrati, H Reith, P Das, J Müller, F Völklein, A Kaya, and et al. A tunable strain sensor using nanogranular metals. *Sensors*, 10(11):9847–9856, Nov 2010.
- [64] M Winhold, P M Weirich, Ch H Schwalb, and M Huth. Superconductivity and metallic behavior in $Pb_xC_yO_\delta$ structures prepared by focused electron beam induced deposition. *Applied Physics Letters*, 105(16):162603, 2014.
- [65] R Sachser, F Porrati, Ch H. Schwalb, and M Huth. Universal conductance correction in a tunable strongly coupled nanogranular metal. *Phys. Rev. Lett.*, 107:206803, Nov 2011.
- [66] F Porrati, R Sachser, Ch H Schwalb, A S Frangakis, and M Huth. Tuning the electrical conductivity of Pt-containing granular metals by postgrowth electron irradiation. *J. Appl. Phys.*, 109(6):063715, 2011.

- [67] L Bernau, M Gabureac, R Erni, and I Utke. Tunable nanosynthesis of composite materials by electron-impact reaction. *Angewandte Chemie International Edition*, 49(47):8880–8884, Oct 2010.
- [68] E Begun, O V Dobrovolskiy, M Kompaniets, R Sachser, Ch Gspan, H Plank, and M Huth. Post-growth purification of Co nanostructures prepared by focused electron beam induced deposition. *Nanotechnology*, 26(7):075301, 2015.
- [69] A Botman, J J L Mulders, and C W Hagen. Creating pure nanostructures from electron-beam-induced deposition using purification techniques: a technology perspective. *Nanotechnology*, 20(37):372001, Sep 2009.
- [70] S Mehendale, J J L Mulders, and P H F Trompenaars. A new sequential EBID process for the creation of pure Pt structures from MeCpPtMe₃. *Nanotechnol.*, 24(14):145303, 2013.
- [71] H Plank, J H Noh, J D Fowlkes, K Lester, B B Lewis, and Ph D Rack. Electron-beam-assisted oxygen purification at low temperatures for electron-beam-induced Pt deposits: Towards pure and high-fidelity nanostructures. *ACS Applied Materials & Interfaces*, 6(2):1018–1024, Jan 2014.
- [72] B Geier, Ch Gspan, R Winkler, R Schmied, J D Fowlkes, H Fitzek, S Rauch, J Rattenberger, Ph D Rack, and H Plank. Rapid and highly compact purification for focused electron beam induced deposits: A low temperature approach using electron stimulated H₂O reactions. *J. Phys. Chem. C*, 118(25):14009–14016, Jun 2014.
- [73] M Winhold, Ch H Schwalb, F Porrati, R Sachser, A S Frangakis, B Kämpken, A Terfort, N Auner, and M Huth. Binary Pt-Si nanostructures prepared by focused electron-beam-induced deposition. *ACS Nano*, 5(12):9675–9681, Dec 2011.
- [74] F Porrati, E Begun, M Winhold, Ch H Schwalb, R Sachser, A S Frangakis, and M Huth. Room temperature L₁₀ phase transformation in binary CoPt nanostructures prepared by focused-electron-beam-induced deposition. *Nanotechnology*, 23(18):185702, May 2012.
- [75] R Sachser, H Reith, D Huzel, M Winhold, and M Huth. Catalytic purification of directly written nanostructured Pt microelectrodes. *ACS Applied Materials & Interfaces*, 6(18):15868–15874, Sep 2014.
- [76] Ch Kittel. *Introduction to Solid State Physics*. Wiley, 2004.

- [77] C M Hurd. Hall effect in metals and alloys. 1972.
- [78] N Nagaosa, J Sinova, Sh Onoda, A H MacDonald, and N P Ong. Anomalous Hall effect. *Reviews of Modern Physics*, 82(2):1539, 2010.
- [79] I Campbell. Hall effect and resistivity anisotropy in Ni alloys. *Physical Review Letters*, 24(6):269–271, Feb 1970.
- [80] T R McGuire and R I Potter. Anisotropic magnetoresistance in ferromagnetic 3d alloys. *Magnetics, IEEE Transactions on*, 11(4):1018–1038, 1975.
- [81] A Gerber, A Milner, A Finkler, M Karpovski, L Goldsmith, J Tuillon-Combes, O Boisson, P Mélinon, and A Perez. Correlation between the extraordinary Hall effect and resistivity. *Phys. Rev. B*, 69(22), Jun 2004.
- [82] A Gerber and O Riss. Perspective of spintronics applications based on the extraordinary Hall effect. March 2008.
- [83] A Fert and O Jaoul. Left-right asymmetry in the scattering of electrons by magnetic impurities, and a Hall effect. *Physical Review Letters*, 28(5):303, 1972.
- [84] L Berger. Side-jump mechanism for the Hall effect of ferromagnets. *Physical Review B*, 2(11):4559, 1970.
- [85] N P Ong and W-L Lee. *Geometry and the anomalous Hall effect in ferromagnets*, chapter 28, pages 121–126.
- [86] J Kötzler and W Gil. Anomalous Hall resistivity of cobalt films: Evidence for the intrinsic spin-orbit effect. *Phys. Rev. B*, 72:060412, Aug 2005.
- [87] S Andreev and P Dimitrova. Anisotropic-magnetoresistance integrated sensors. *J. Optoelec. Advanced Materials*, 7(1):199–206, 2005.
- [88] J Nickel. *Magnetoresistance overview*. Hewlett-Packard Laboratories, Technical Publications Department Palo Alto, CA, USA, 1995.
- [89] S Tumanski. *Thin film magnetoresistive sensors*. CRC Press, 2010.
- [90] K Mohamadabadi. *Anisotropic Magnetoresistance Magnetometer for inertial navigation systems*. PhD thesis, Ecole Polytechnique X, 2013.
- [91] J M Ziman. *Electrons and Phonons*. Clarendon Press, Oxford, 1960.

- [92] A Bid, A Bora, and A K Raychaudhuri. Temperature dependence of the resistance of metallic nanowires of diameter ≥ 15 nm: Applicability of Bloch-Grüneisen theorem. *Phys. Rev. B*, 74:035426–1–8, Jul 2006.
- [93] Ph B Allen, J R Chelikowsky, and S G Louie. Quantum theory of real materials. *Klüwer, Boston*, pages 219–250, 1996.
- [94] C Durkan and M E Welland. Size effects in the electrical resistivity of polycrystalline nanowires. *Physical review B*, 61(20):14215, 2000.
- [95] K Fuchs. The conductivity of thin metallic films according to the electron theory of metals. In *Mathematical Proceedings of the Cambridge Philosophical Society*, volume 34, pages 100–108. Cambridge Univ Press, 1938.
- [96] E Hi Sondheimer. The mean free path of electrons in metals. *Advances in physics*, 1(1):1–42, 1952.
- [97] AF Mayadas, M Shatzkes, and JF Janak. Electrical resistivity model for polycrystalline films: the case of specular reflection at external surfaces. *Applied Physics Letters*, 14(11):345–347, 1969.
- [98] A F Mayadas and M Shatzkes. Electrical-resistivity model for polycrystalline films: the case of arbitrary reflection at external surfaces. *Physical Review B*, 1(4):1382, 1970.
- [99] J Bardeen, L Cooper, and J Schrieffer. Microscopic theory of superconductivity. *Phys. Rev.*, 106(1):162–164, Apr 1957.
- [100] J G Bednorz and K Al Müller. Possible high T_C superconductivity in the Ba-La-Cu-O system. *Zeitschrift für Physik B Condensed Matter*, 64(2):189–193, 1986.
- [101] K B Efetov, I A Garifullin, A F Volkov, and K Westerholt. Proximity effects in ferromagnet/superconductor heterostructures. In *Magnetic Heterostructures*, pages 251–290. Springer, 2008.
- [102] V P Mineev, K Samokhin, and L D Landau. *Introduction to unconventional superconductivity*. CRC Press, 1999.
- [103] Y Maeno, Sh Kittaka, T Nomura, Sh Yonezawa, and K Ishida. Evaluation of spin-triplet superconductivity in Sr_2RuO_4 . *J. Phys. Soc. Jpn.*, 81(1):011009, Jan 2012.

- [104] D Jerome, A Mazaud, M Ribault, and K Bechgaard. Superconductivity in a synthetic organic conductor $(\text{TMTSF})_2\text{PF}_6$. *Journal de Physique Lettres*, 41(4):95–98, 1980.
- [105] F S Bergeret, A F Volkov, and K B Efetov. Odd triplet superconductivity in superconductor ferromagnet structures: a survey. *Applied Physics A*, 89(3):599–601, 2007.
- [106] H Courtois, P Charlat, Ph Gandit, D Mailly, and B Pannetier. The spectral conductance of a proximity superconductor and the reentrance effect. *Journal of low temperature physics*, 116(3-4):187–213, 1999.
- [107] F K Wilhelm. Transport in mesoscopic proximity systems: A quasiclassical perspective. *Physica C: Superconductivity*, 341-348:2569–2572, Nov 2000.
- [108] V Petrashov, R Shaikhaidarov, I Sosnin, P Delsing, T Claeson, and A Volkov. Phase-periodic proximity-effect compensation in symmetric normal/superconducting mesoscopic structures. *Phys. Rev. B*, 58(22):15088–15093, Dec 1998.
- [109] J Clarke. The proximity effect between superconducting and normal thin films in zero field. *J. Phys. Colloques*, 29(C2):C2–3–C2–16, Feb 1968.
- [110] A C Mota, P Visani, and A Pollini. Magnetic properties of proximity-induced superconducting copper and silver. *J Low Temp Phys*, 76(5-6):465–512, Sep 1989.
- [111] P Visani, A Mota, and A Pollini. Novel reentrant effect in the proximity-induced superconducting behavior of silver. *Physical Review Letters*, 65(12):1514–1516, Sep 1990.
- [112] S Gueron, H Pothier, N Birge, D Esteve, and M Devoret. Superconducting proximity effect probed on a mesoscopic length scale. *Physical Review Letters*, 77(14):3025–3028, Sep 1996.
- [113] L Cooper. Superconductivity in the neighborhood of metallic contacts. *Physical Review Letters*, 6(12):689–690, Jun 1961.
- [114] P G De Gennes and E Guyon. Superconductivity in “normal” metals. *Physics Letters*, 3(4):168–169, Jan 1963.
- [115] N Werthamer. Theory of the superconducting transition temperature and energy gap function of superposed metal films. *Phys. Rev.*, 132(6):2440–2445, Dec 1963.

- [116] L P Gorkov. Theory of superconducting alloys in a strong magnetic field near the critical temperature. *JETP*, 37:998, 1960.
- [117] P Fulde and R A Ferrell. Superconductivity in a strong spin-exchange field. *Physical Review*, 135(3A):A550, 1964.
- [118] AI Larkin and Iu N Ovchinnikov. Inhomogeneous state of superconductors (Production of superconducting state in ferromagnet with Fermi surfaces, examining Green function). *Soviet Physics-JETP*, 20:762–769, 1965.
- [119] T Kontos, M Aprili, J Lesueur, and X Grison. Inhomogeneous superconductivity induced in a ferromagnet by proximity effect. *Physical review letters*, 86(2):304, 2001.
- [120] J S Jiang, D Davidović, Daniel H Reich, and C L Chien. Oscillatory superconducting transition temperature in Nb/Gd multilayers. *Physical review letters*, 74(2):314, 1995.
- [121] T Kontos, M Aprili, J Lesueur, F Genet, B Stephanidis, and R Boursier. Josephson junction through a thin ferromagnetic layer: negative coupling. *Physical review letters*, 89(13):137007, 2002.
- [122] A Bauer, J Bentner, M Aprili, M L Della Rocca, M Reinwald, W Wegscheider, and Ch Strunk. Spontaneous supercurrent induced by ferromagnetic π junctions. *Physical review letters*, 92(21):217001, 2004.
- [123] AI Buzdin, L N Bulaevskii, and S V Panyukov. Critical-current oscillations as a function of the exchange field and thickness of the ferromagnetic metal (F) in an SFS Josephson junction. *JETP Lett*, 35(4):178–180, 1982.
- [124] Z Radović, M Ledvij, L Dobrosavljević-Grujić, AI Buzdin, and J R Clem. Transition temperatures of superconductor-ferromagnet superlattices. *Physical Review B*, 44(2):759, 1991.
- [125] A Buzdin and I Baladie. Theoretical description of ferromagnetic π junctions near the critical temperature. *Physical Review B*, 67(18):184519, 2003.
- [126] P G De Gennes. Superconductivity of metals and alloys, 1966. *New York*, page 126, 1966.
- [127] G Eilenberger. Transformation of Gorkov’s equation for type II superconductors into transport-like equations. *Zeitschrift für Physik*, 214(2):195–213, 1968.

- [128] K D Usadel. Generalized diffusion equation for superconducting alloys. *Physical Review Letters*, 25(8):507, 1970.
- [129] K Halterman and O T Valls. Proximity effects at ferromagnet-superconductor interfaces. *Physical Review B*, 65(1):014509, 2001.
- [130] A Kadigrobov, R I Shekhter, and M Jonson. Quantum spin fluctuations as a source of long-range proximity effects in diffusive ferromagnet-super conductor structures. *EPL (Europhysics Letters)*, 54(3):394, 2001.
- [131] M G Blamire and J W A Robinson. The interface between superconductivity and magnetism: understanding and device prospects. *Journal of Physics: Condensed Matter*, 26(45):453201, 2014.
- [132] Ya V Fominov, A F Volkov, and K B Efetov. Josephson effect due to the long-range odd-frequency triplet superconductivity in SFS junctions with Néel domain walls. *Physical Review B*, 75(10):104509, 2007.
- [133] A F Volkov and K B Efetov. Odd triplet superconductivity in a superconductor/ferromagnet structure with a narrow domain wall. *Physical Review B*, 78(2):024519, 2008.
- [134] Gábor B Halász, J W A Robinson, J F Annett, and M G Blamire. Critical current of a Josephson junction containing a conical magnet. *Physical Review B*, 79(22):224505, 2009.
- [135] F S Bergeret, A F Volkov, and K B Efetov. Manifestation of triplet superconductivity in superconductor-ferromagnet structures. *Physical Review B*, 68(6):064513, 2003.
- [136] A F Andreev. Thermal conductivity of the intermediate state of superconductors. *Zh. Eksperim. i Teor. Fiz.*, 46, 1964.
- [137] G E Blonder, M Tinkham, and T M Klapwijk. Transition from metallic to tunneling regimes in superconducting microconstrictions: Excess current, charge imbalance, and supercurrent conversion. *Physical Review B*, 25(7):4515, 1982.
- [138] M J M De Jong and C W J Beenakker. Andreev reflection in ferromagnet-superconductor junctions. *Physical review letters*, 74(9):1657, 1995.
- [139] R Landauer. Spatial variation of currents and fields due to localized scatterers in metallic conduction. *IBM J. Res. & Dev.*, 1(3):223–231, Jul 1957.

- [140] R J Soulen, J M Byers, M S Osofsky, B Nadgorny, T Ambrose, S F Cheng, Pr R Broussard, C T Tanaka, J Nowak, J S Moodera, et al. Measuring the spin polarization of a metal with a superconducting point contact. *Science*, 282(5386):85–88, 1998.
- [141] R Meservey and P M Tedrow. Spin-polarized electron tunneling. *Physics Reports*, 238(4):173–243, 1994.
- [142] C Neetzel. Formkontrollierte Herstellung von mikro-/nanostrukturierten Kupfer-und Eisenverbindungen sowie Anwendungsbeispiele. *Dissertation*, 2014.
- [143] T Gao, G Meng, Y Wang, Sh Sun, and L Zhang. Electrochemical synthesis of copper nanowires. *J. Phys.: Condens. Matter*, 14(3):355–363, Dec 2001.
- [144] M E Toimil Molares, E M Höhberger, Ch Schaefflein, Robert H Blick, R Neumann, and C Trautmann. Electrical characterization of electrochemically grown single copper nanowires. *Applied Physics Letters*, 82(13):2139–2141, 2003.
- [145] Ju Hun Lee, Jun Hua Wu, Hong Ling Liu, Ji Ung Cho, Moon Kyu Cho, Boo Hyun An, Ji Hyun Min, Su Jung Noh, and Young Keun Kim. Iron-gold barcode nanowires. *Angewandte Chemie International Edition*, 46(20):3663–3667, May 2007.
- [146] Ch-L Cheng, J-S Lin, and Y-F Chen. Fabrication and growth mechanism of metal (Zn, Sn) nanotube arrays and metal (Cu, Ag) nanotube/nanowire junction arrays. *Materials Letters*, 62(10-11):1666–1669, Apr 2008.
- [147] D M Davis and E J Podlaha. CoNiCu and Cu nanotube electrodeposition. *Electrochem. Solid-State Lett.*, 8(2):D1–D4, 2005.
- [148] L Liu and S Park. Direct formation of thin-walled palladium nanotubes in nanochannels under an electrical potential. *Chemistry of Materials*, 23(6):1456–1460, Mar 2011.
- [149] M Paunovic and M Schlesinger. *Fundamentals of Electrochemical Deposition*. John Wiley & Sons., 2006.
- [150] M E Toimil Molares. Fabrication and characterisation of copper nanowires electrochemically deposited in etched ion-track membranes. *Dissertation*, 2001.
- [151] S Kumar, S Kumar, and S K Chakarvarti. Electrochemical synthesis of copper nanotubules in etched ion tracks in polycarbonate. *Journal of Materials Science*, 39(9):3257–3259, May 2004.

- [152] P J Kelly and R D Arnell. Magnetron sputtering: a review of recent developments and applications. *Vacuum*, 56(3):159–172, Mar 2000.
- [153] A Anders. A structure zone diagram including plasma-based deposition and ion etching. *Thin Solid Films*, 518(15):4087–4090, May 2010.
- [154] O V Dobrovolskiy and M Huth. Crossover from dirty to clean superconducting limit in dc magnetron-sputtered thin Nb films. *Thin Solid Films*, 520(18):5985–5990, Jul 2012.
- [155] W F van Dorp and C W Hagen. A critical literature review of focused electron beam induced deposition. *Journal of Applied Physics*, 104(8):081301, 2008.
- [156] S Lipp, L Frey, C Lehrer, E Demm, S Pauthner, and H Ryssel. A comparison of focused ion beam and electron beam induced deposition processes. *Proceedings of the 7th European Symposium on Reliability of Electron Devices, Failure Physics and Analysis*, 1996.
- [157] J D Fowlkes, S J Randolph, and P D Rack. Growth and simulation of high-aspect ratio nanopillars by primary and secondary electron-induced deposition. *J. Vac. Sci. Technol. B*, 23(6):2825, 2005.
- [158] J J L Mulders, L M Belova, and A Riazanova. Electron beam induced deposition at elevated temperatures: compositional changes and purity improvement. *Nanotechnology*, 22(5):055302, Dec 2010.
- [159] L Serrano-Ramón, R Córdoba, L A Rodríguez, C Magén, E Snoeck, Ch Gatel, I Serrano, M I R Ibarra, and J M De Teresa. Ultrasmall functional ferromagnetic nanostructures grown by focused electron-beam-induced deposition. *ACS Nano*, 5(10):7781–7787, Oct 2011.
- [160] A Fernández-Pacheco, J M De Teresa, R Cordoba, and M R Ibarra. Magnetotransport properties of high-quality cobalt nanowires grown by focused-electron-beam-induced deposition. *J. Phys. D*, 42(5):055005, Mar 2009.
- [161] O V Dobrovolskiy, E Begun, M Huth, and V A Shklovskij. Electrical transport and pinning properties of Nb thin films patterned with focused ion beam-milled washboard nanostructures. *New J. Phys.*, 14(11):113027, Nov 2012.

- [162] P M Weirich, C H Schwalb, M Winhold, and M Huth. Superconductivity in the system $\text{Mo}_x\text{C}_y\text{Ga}_z\text{O}$ prepared by focused ion beam induced deposition. *Journal of Applied Physics*, 115(17):174315, May 2014.
- [163] A Fernández-Pacheco, J M De Teresa, R Córdoba, and M R Ibarra. Metal-insulator transition in Pt-C nanowires grown by focused-ion-beam-induced deposition. *Phys. Rev. B*, 79:174204, May 2009.
- [164] E S Sadki, S Ooi, and K Hirata. Focused-ion-beam-induced deposition of superconducting nanowires. *Appl. Phys. Lett.*, 85(25):6206, 2004.
- [165] W F van Dorp, J D Wnuk, J M Gorham, D H Fairbrother, T E Madey, and C W Hagen. Electron induced dissociation of trimethyl (methylcyclopentadienyl) platinum (IV): Total cross section as a function of incident electron energy. *Journal of Applied Physics*, 106(7):074903, 2009.
- [166] P L Pauson, J P Stambuli, Teh-Chang Chou, and Bor-Cherng Hong. Octacarbonyldicobalt. *Encyclopedia of Reagents for Organic Synthesis*, pages 1–26, Apr 2001.
- [167] Y M Lau, P C Chee, J T L Thong, and V Ng. Properties and applications of cobalt-based material produced by electron-beam-induced deposition. *J. Vac. Sci. Technol. A*, 20(4):1295, 2002.
- [168] I Utke, J Michler, Ph Gasser, Ch Santschi, D Laub, M Cantoni, C Jiao, P Hoffmann, et al. Cross section investigations of compositions and sub-structures of tips obtained by focused electron beam induced deposition. *Advanced Engineering Materials*, 7(5):323–331, 2005.
- [169] E Nikulina, O Idigoras, P Vavassori, A Chuvilin, and A Berger. Magneto-optical magnetometry of individual 30 nm cobalt nanowires grown by electron beam induced deposition. *Appl. Phys. Lett.*, 100(14):142401, 2012.
- [170] D Seyferth. The rise and fall of tetraethyllead. 2. *Organometallics*, 22(25):5154–5178, Dec 2003.
- [171] Wuxia Li, J C Fenton, Yiqian Wang, D W McComb, and P A Warburton. Tunability of the superconductivity of tungsten films grown by focused-ion-beam direct writing. *Journal of Applied Physics*, 104(9):093913, 2008.

- [172] S B Knapp. *Kinetics of Thermal Decomposition of Tungsten Hexacarbonyl*. Oregon State University, 1966.
- [173] Dallas T Hurd and Eugene O Brimm. Tungsten hexacarbonyl. *Inorganic Syntheses*, pages 135–138, Jan 1957.
- [174] R Schneider. Energy-dispersive x-ray spectroscopy (EDXS). *Surface and Thin Film Analysis*, pages 293–310, Apr 2011.
- [175] J J Friel. *X-ray and Image Analysis in Electron Microscopy*. Princeton Gamma-Tech, 2004.
- [176] D Drouin, A R Couture, D Joly, X Tastet, V Aimez, and R Gauvin. CASino v2.42 - a fast and easy-to-use modeling tool for scanning electron microscopy and microanalysis users. *Scanning*, 29(3):92–101, May 2007.
- [177] C F Macrae, I J Bruno, J A Chisholm, P R Edgington, P McCabe, E Pidcock, L Rodriguez-Monge, R Taylor, J van de Streek, and P A Wood. Mercury CSD 2.0 - new features for the visualization and investigation of crystal structures. *J Appl Cryst*, 41(2):466–470, Mar 2008.
- [178] S Sharma, A Barman, M Sharma, L R Shelford, V V Kruglyak, and R J Hicken. Structural and magnetic properties of electrodeposited cobalt nanowire arrays. *Solid State Communications*, 149(39):1650–1653, 2009.
- [179] Zuwei Liu, Pai-Chun Chang, Chia-Chi Chang, Evgeniy Galaktionov, Gerd Bergmann, and Jia G Lu. Shape anisotropy and magnetization modulation in hexagonal cobalt nanowires. *Advanced Functional Materials*, 18(10):1573–1578, 2008.
- [180] R Reichelt. Scanning electron microscopy. *Science of Microscopy*, pages 133–272, 2007.
- [181] Stephen J Pennycook and Peter D Nellist. *Scanning transmission electron microscopy: imaging and analysis*. Springer, 2011.
- [182] A D Beyer, M Koesters, K G Libbrecht, and E D Black. Macroscopic coherence effects in a mesoscopic system: Weak localization of thin silver films. *Amer. J. Phys.*, 73(11):1014–1019, 2005.
- [183] M Kompaniets, O V Dobrovolskiy, C Neetzel, W Ensinger, and M Huth. Superconducting proximity effect in crystalline Co and Cu nanowires. *J Supercond Nov Magn*, 28(2):431–436, Aug 2014.

- [184] K Arutyunov, D Presnov, S Lotkhov, A Pavolotski, and L Rinderer. Resistive-state anomaly in superconducting nanostructures. *Phys. Rev. B*, 59(9):6487–6498, Mar 1999.
- [185] M Park, M Isaacson, and J Parpia. Resistance anomaly and excess voltage near superconducting interfaces. *Phys. Rev. Lett.*, 75(20):3740–3743, Nov 1995.
- [186] C Strunk, V Bruyndoncx, B Burk, C J Chien, C Haesendonck, V V Moshchalkov, Y Bruynseraede, and V Chandrasekhar. Resistance anomalies in mesoscopic superconducting al structures. *Czech. J. Phys.*, 46(S4):2335–2336, Apr 1996.
- [187] I Landau and L Rinderer. Comment on “Intrinsic resistance fluctuations in mesoscopic superconducting wires”. *Phys. Rev. B*, 56(10):6348–6351, Sep 1997.
- [188] H Courtois, Ph Gandit, and B Pannetier. Proximity-induced superconductivity in a narrow metallic wire. *Phys. Rev. B*, 52(2):1162–1166, Jul 1995.
- [189] O K Soroka, V A Shklovskij, and M Huth. Guiding of vortices under competing isotropic and anisotropic pinning conditions: Theory and experiment. *Phys. Rev. B*, 76:014504–1–12, Jul 2007.
- [190] J P Biersack and M D Ziegler. *SRIM – The Stopping and Range of Ions in Matter*. James Ziegler, 2008.
- [191] P Sigmund. *Particle Penetration and Radiation Effects: General Aspects and Stopping of Swift Point Charges*. Springer, Berlin-Heidelberg-New York, 2006.
- [192] M Singh, J Wang, and Yi Sun. *Superconductivity in nanoscale systems*. INTECH Open Access Publisher, 2012.
- [193] W Buckel and R Kleiner. *Superconductivity (Physics)*. Wiley-VCH, 2004.
- [194] L He and J Wang. Periodic magnetoresistance oscillations induced by superconducting vortices in single crystal Au nanowires. *Nanotechnology*, 22(44):445704, Oct 2011.
- [195] Y Henry, K Ounadjela, L Piraux, S Dubois, J-M George, and J-L Duvail. Magnetic anisotropy and domain patterns in electrodeposited cobalt nanowires. *Eur. Phys. J. B*, 20(1):35–54, Mar 2001.
- [196] Xiao-Ping Shen, Hua-Juan Miao, Hui Zhao, and Zheng Xu. Synthesis, characterization and magnetic properties of Co₃O₄ nanotubes. *Appl. Phys. A*, 91(1):47–51, Apr 2008.

- [197] The stopping of the Ga ions in the nanowires was simulated with the help of SRIM software available under <http://www.srim.org/>.
- [198] O V Dobrovolskiy, M Kompaniiets, R Sachser, F Porrati, Ch Gspan, H Plank, and M Huth. Tunable magnetism on the lateral mesoscale by post-processing of Co/Pt heterostructures. *Accepted by Beilstein Journal of Nanotechnology*, 2015.
- [199] R B Anderson. *The Fischer-Tropsch Synthesis*. Academic Pr, 1984.
- [200] J Wintterlin, T Zambelli, J V Barth, and G Ertl. Complex pathways in dissociative adsorption of oxygen on platinum. *Nature*, 390(6659):495–497, Dec 1997.
- [201] N W Ashcroft and N D Mermin. Solid state physics. itps thomson learning, 2000. Technical report, isbn 0-03-083993-9.
- [202] A Hubert and R Schäfer. *Magnetic Domains: The Analysis of Magnetic Microstructures*. Springer, 2008.
- [203] C Chappert, H Bernas, J Ferré, V Kottler, J-P Jamet, Y Chen, E Cambril, T Devolder, F Rousseaux, V Mathet, et al. Planar patterned magnetic media obtained by ion irradiation. *Science*, 280(5371):1919–1922, 1998.
- [204] R Córdoba, J Sesé, J M De Teresa, and M R Ibarra. High-purity cobalt nanostructures grown by focused-electron-beam-induced deposition at low current. *Microel. Engin.*, 87(5-8):1550–1553, May 2010.
- [205] I Beloborodov, K Efetov, A Lopatin, and V Vinokur. Transport properties of granular metals at low temperatures. *Phys. Rev. Lett.*, 91(24), Dec 2003.
- [206] I Beloborodov, A Lopatin, V Vinokur, and K Efetov. Granular electronic systems. *Rev. Mod. Phys.*, 79(2):469–518, Apr 2007.
- [207] F Porrati, R Sachser, and M Huth. Magnetoresistance of granular Pt-C nanostructures close to the metal-insulator transition. *J. Phys.: Condens. Matter*, 26(8):085302, Feb 2014.
- [208] M Jaafar, L Serrano-Ramón, O Iglesias-Freire, A Fernández-Pacheco, M R Ibarra, J M De Teresa, and A Asenjo. Hysteresis loops of individual Co nanostripes measured by magnetic force microscopy. *Nanoscale Research Letters*, 6(1):407, 2011.

- [209] H Weinforth, C Somsen, B Rellinghaus, A Carl, E F Wassermann, and D Weller. Structural, electrical and magnetic properties of $\text{Co}/\text{sub } x/\text{C}/\text{sub } 1-x/$ granular films. *IEEE Trans. Magn.*, 34(4):1132–1134, Jul 1998.
- [210] J P Franck and Douglas L Martin. The superconducting transition temperature of lead. *Canadian Journal of Physics*, 39(9):1320–1329, Sep 1961.
- [211] R A Matula. Electrical resistivity of copper, gold, palladium, and silver. *Journal of Physical and Chemical Reference Data*, 8(4):1147–1298, 1979.
- [212] S Karim, W Ensinger, T W Cornelius, and R Neumann. Investigation of size effects in the electrical resistivity of single electrochemically fabricated gold nanowires. *Physica E: Low-dimensional Systems and Nanostructures*, 40(10):3173–3178, 2008.
- [213] F Hübler, J Camirand Lemyre, D Beckmann, and H v Löhneysen. Charge imbalance in superconductors in the low-temperature limit. *Physical Review B*, 81(18):184524, 2010.
- [214] D Saint-James and P G de Gennes. Onset of superconductivity in decreasing fields. *Physics Letters*, 7(5):306–308, 1963.
- [215] D Saint-James. Angular dependence of the upper critical field of type II superconductors; theory. *Physics Letters*, 16(3):218–220, 1965.
- [216] J P Burger, G Deutscher, E Guyon, and A Martinet. Angular dependence of the upper critical field of type II superconductors; experiments. *Physics Letters*, 16(3):220–221, 1965.
- [217] L Tovazhnyanskii, V G Cherkasova, and N Ya Fogel. Angular dependence of the critical field of superconducting superlattices: experiment. *Zh. Eksp. Teor. Fiz*, 93(4):1384–1393, 1987.
- [218] H Schopper. Die optische untersuchung der diffusion von metallen ineinander. *Zeitschrift für Physik*, 143(1):93–117, 1955.
- [219] J S Kirkaldy, D Weichert, and Zia-Ul Haq. Diffusion in multicomponent metallic systems: VI. Some thermodynamic properties of the D matrix and the corresponding solutions of the diffusion equations. *Canadian Journal of Physics*, 41(12):2166–2173, 1963.

- [220] Ž Marinković and V Simić. Room temperature interactions in Au/metal and Al/metal thin film couples. *Thin Solid Films*, 75(3):229–235, 1981.
- [221] H Okamoto and T B Massalski. The Au-Pb (gold-lead) system. *Bulletin of Alloy Phase Diagrams*, 5(3):276–284, 1984.
- [222] C Weaver and L C Brown. Diffusion in evaporated films of gold-lead. *Philosophical Magazine*, 8(92):1379–1393, 1963.
- [223] D Seraphim, F d’Heurle, and W Heller. Free energy of composite wires in the superconducting state. *Reviews of Modern Physics*, 36(1):323, 1964.
- [224] A F Hebard. Tunneling studies of the formation of intermetallic compounds in gold-lead films. *Journal of Vacuum Science and Technology*, 10(5):606, Sep 1973.
- [225] M Tech Manvendra Singh Khatri. *Structure, microstructure and magnetic properties of electrodeposited Co and Co-Pt in different nanoscale geometries*. PhD thesis, University of Technology, 2010.
- [226] V Mukundan, B N Wanjala, R Loukrakpam, J Luo, J Yin, C J Zhong, and O Malis. Limited grain growth and chemical ordering during high-temperature sintering of Pt-NiCo nanoparticle aggregates. *Nanotechnology*, 23(33):335705, 2012.
- [227] O Ersen, V Parasote, V Pierron-Bohnes, M C Cadeville, and C Ulhaq-Bouillet. Growth conditions to optimize chemical order and magnetic properties in molecular-beam-epitaxy-grown CoPt/MgO (001) thin films. *Journal of Applied Physics*, 93(5):2987, 2003.
- [228] M Abes, O Ersen, E Elkaim, G Schmerber, C Ulhaq-Bouillet, A Dinia, P Panissod, and V Pierron-Bohnes. Magnetic anisotropy and microstructure in sputtered CoPt (110) films. *Catalysis Today*, 89(3):325–330, Mar 2004.

Acknowledgments

Although only one name of Maksym Kompaniets is appeared on the title page of this thesis, many people have made contributions to its becoming. These contributions were of different kind and matter and their significance is hard to overestimate. I am heartily thankful and grateful to all these people, the most pleasant memories of which will always remain in my mind. Dear colleagues and friends, thank you so much for your great support!!!

First of all, I would like to acknowledge and thank my research advisor Prof. Dr. Michael Huth. Michaels warm welcome in the working group at the beginning of my post-graduate activities gave me a significant confidence in subsequent research years. His striking inexhaustible ideas supported by great motivation were inspiring me over and over again. The atmosphere created by Michael in the working group was so friendly and comfortable, that I can confidently say that the “Dünne Schichten und Nanostrukturen” group was for me like a second family. I am proud that I could work with Michael and learn from him many not only scientific, but also vital things.

Secondly, I would like to thank my co-promotor Dr. Oleksandr Dobrovolskiy for the professional support in a scientific life. Thank you Oleksandr for many fruitful and interesting discussions, scientific suggestions and ideas which were very helpful for our collaboration and which are resulted in plenty nice publications.

I would like to thank the entire Michaels group “Dünne Schichten und Nanostrukturen”: Dr. Fabrizio Porrati, Roland Sachser, Dirk Klingenberg and Evgenia Begun for very valuable help at laboratories, Jörg Franke for versatile technical support. Special thanks to Mr. Bernhard Klug for reliable and willingly help in a clean room and with a bonding machine.

Of course my special gratitude I sent to my dear colleagues Dr. Christian Schwalb and Marcel Winhold. Your positive and full of humor attitude to life had helped me a lot, regardless of whether we were in a laboratory or doing mountain biking marathon. It is thanks to you I was able to understand and integrate to German culture, learn German language and people, which I find extremely important and helpful for my family today. Many times I was asking for help, and you were always open. Herzlichen Dank, Jungs! I hope our friendship will continue regardless of where we are and what we do. I wish you all the best!

I am very grateful to Prof. Dr. Wolfgang Ensinger and Dr. Cornelia Neetzel from the Department of Materials Science of TU Darmstadt for the productive collaboration and joint publications. Special thanks to Cornelia for reliable preparation and providing with

nanowires and carrying out of XRD measurements.

Also, I would like to acknowledge Beilstein-Institut Frankfurt/Main for the financial support during the years 2009 to 2013 of my research activity within the framework of the collaboration project NanoBiC.

Finally, I would like to thank my wife Olga and my parents Gennady and Olga Kompaniets. Your moral support, inspiration and understanding during the whole PhD time and especially in the last time during the writing of this thesis have played a very important role for me. Thank you dears for your love, patience and believing in me. I will try not to disappoint you in the future!!!

Best regards,

Maksym Kompaniets

List of publications

- [1] *Long-range superconducting proximity effect in polycrystalline Co nanowires*, M. Kompaniets, O. V. Dobrovolskiy, C. Neetzel, F. Porrati, J. Brötz, W. Ensinger, and M. Huth, **Applied Physics Letters** **104** (5), 052603 (2014);
- [2] *Proximity-induced superconductivity in crystalline Cu and Co nanowires and Co nanogranular structures*, M. Kompaniets, O. Dobrovolskiy, C. Neetzel, E. Begun, F. Porrati, W. Ensinger, M. Huth, **Journal of Applied Physics** **116**, 073906 (2014);
- [3] *Superconducting proximity effect in crystalline Co and Cu nanowires*, M. Kompaniets, O. V. Dobrovolskiy, C. Neetzel, W. Ensinger, M. Huth, **Journal of Superconductivity and Novel Magnetism** **28**(2), 431 (2014);
- [4] *Post-growth purification of Co nanostructures prepared by focused electron beam induced deposition*, E. Begun, O. Dobrovolskiy, M. Kompaniets, R. Sachser, Ch. Gspan, H. Plank, M. Huth, **Nanotechnology** **26**(7), 075301 (2015);
- [5] *Tunable magnetism on the lateral mesoscale by post-processing of Co/Pt heterostructures*, O. V. Dobrovolskiy, M. Kompaniets, R. Sachser, F. Porrati, Ch. Gspan, H. Plank, M. Huth, **Beilstein Journal of Nanotechnology**, accepted (2015).

Communications to scientific conferences

- [1] *Mesoscopically Resolved Tunable Magnetism in Co/Pt Heterostructures*, M. Kompaniiets, O. V. Dobrovolskiy, F. Porrati, R. Sachser, M. Huth, **5th Workshop on Focused Electron Beam Induced Processing – FEBIP-2014**, (Frankfurt am Main, Germany, 2014), p. 181;
- [2] *Superconducting proximity effect in crystalline Cu and Co nanowires*, M. Kompaniiets, O. V. Dobrovolskiy, C. Neetzel, J. Brötz, W. Ensinger, M. Huth, **4th International Conference on Superconductivity and Magnetism – ICSM-2014**, (Turkey, Antalya, 2014), p. 667;
- [3] *Proximity effect induced superconductivity in Cu nanowires*, M. Kompaniiets, C. Neetzel, F. Porrati, W. Ensinger, M. Huth, **DPG Spring Meeting**, (Regensburg, Germany, 2013), TT 12.46, p. 429;
- [4] *Proximity effects in Cu and Co nanowires in contact with a FIBID-based superconductor*, M. Kompaniiets, C. Neetzel, W. Ensinger, M. Huth *in Proc. NanoBiC Fellows Meeting Beilstein-Institut*, (Frankfurt am Main, Germany, 2013);
- [5] *Electrical transport and tunnel measurements on pure copper nanowires*, M. Kompaniiets, D. Klingenberger, F. Porrati, O. Dobrovolskiy, O. Foyevtsov, C. Neetzel, M. Rauber, M. E. Toimil-Molares, W. Ensinger, Ch. Trautmann, and M. Huth, **76th Annual Conference of the DPG** (Berlin, Germany, 2012), TT 13.20, p. 429.

Curriculum vitae

Personal information

Name: Maksym Kompaniets

Date of Birth: 13 January 1986

Place of Birth: Mariupol, Ukraine

Citizenship: Ukrainian

Marital status: married

Address: Physikalisches Institut,
Goethe-Universität
Max-von-Laue-Str. 1
60438 Frankfurt am Main, Germany

Tel.: +49(069)-798-47263

E-mail: kompaniets@physik.uni-frankfurt.de



Education and academic degrees

2010–2015: Ph.D. student (granted within the research collaboration *NanoBiC*, financially supported by the Beilstein Institute) Physical Institute, Johann Wolfgang Goethe University, Frankfurt am Main, Germany

2003–2007: M.Sc. degree in Applied Physics, Department of Physics and Technology, V. N. Karazin Kharkiv National University, Kharkiv, Ukraine

2007–2009: B.Sc. degree in Applied Physics, Department of Physics and Technology, V. N. Karazin Kharkiv National University, Kharkiv, Ukraine

2003–2007: Mariupol high school No. 67, Mariupol, Ukraine